Analysis of mechanical and optical brain injury from optogenetic implants.

John Exton, BSc MSc

Doctor of Philosophy (PhD)

Mechanical Engineering

School of Engineering

Newcastle University

Abstract

Deep brain stimulation (DBS) technology has become an effective clinical tool for treating symptoms of a range of conditions including Parkinson's disease, epilepsy, treatment-resistant depression, and others. The electrical signal from a DBS electrode penetrates a limited distance through brain tissue and must be precisely placed to target the location of interest. Current DBS electrodes are prone to several complications including mistargeting (requiring revision), mechanical trauma, and glial scar formation leading to impaired implant function.

Optogenetics is a relatively novel technology with the potential to reduce or overcome many of the issues with DBS electrode implants. Optogenetic implants use optical rather than electrical stimulation, targeting neurons modified to express light-reactive channelrhodopsin proteins.

The optical signals used in optogenetics have the potential to travel further through brain tissue than do electrical signals. Multiple wavelengths can be employed to stimulate or suppress separate neural populations from the same implant, and implant placement need not be as precise since only modified neurons will be affected. Channelrhodopsins have been engineered to produce a wide range of behaviours unavailable via electrical stimulation including stimulation, suppression and switchable activity.

To successfully bring an optogenetic implant to clinical practice, it is necessary to determine its safety compared to existing techniques; optrodes could cause trauma to patient tissue via mechanical, thermal and optical mechanisms. To establish an effective regulatory framework for optogenetic implants, tools must be available to measure these effects in patient tissue.

This study critically assesses the use of atomic force microscopy as a tool for measuring the mechanical properties of brain tissue, investigates cell-derived extracellular matrix models as tools for probing the mechanisms of brain tissue remodelling after injury and measures toxicity in brain tissue from exposure to optical wavelengths and intensities typical for optogenetic applications.

Here, we (i) showed that measurement of acute brain slices with atomic force microscopy is significantly influenced by osmotic swelling and should be performed rapidly at low temperatures to mitigate these effects, (ii) found that cell-derived extracellular matrix possesses several properties that make it unconducive to mechanical measurement with atomic force microscopy or rheological tools and (iii) developed an experimental method for measuring optical toxicity in brain tissue that could be used to establish regulatory limits for clinical devices. Further investigation will yield additional improvements to these techniques, facilitating development of safer optogenetic implant technologies.

Covid-19 Impact Statement

During the period of the COVID-19 lockdowns, I was unable to access laboratory facilities for several months. This substantially affected my ability to carry out experiments. In lieu of experimental work during this period, I carried out the literature search for (and wrote most of) Chapter 3.

During the period of the pandemic, it was necessary for me to live away from my normal home as my partner is immunologically vulnerable. These altered living circumstances severely affected my ability to work whilst I adapted to the new situation.

In addition, in September 2022 I contracted COVID-19, suffering relatively severe symptoms and was unable to work for ~2 weeks. "Long COVID" symptoms - specifically fatigue and loss of focus - have affected me since, though these symptoms have by this point largely resolved. These symptoms combine particularly poorly with symptoms of ADHD (which I was diagnosed with in late 2021 and began to receive medication for in mid-2022).

Without these impacts on my work, I would have expected to have expanded my optical toxicity work to include additional wavelengths and would have utilised the conclusions obtained from chapter 5 to perform AFM analysis of light-exposed brain tissue samples in comparison to unexposed tissue.

Declaration of Work

I declare that this thesis is based on my own work and has not been submitted in any form for another degree at any university or any other tertiary education. Information derived from published and unpublished work of others has been acknowledged in the text and the list of references given in the bibliography.

Acknowledgements

Firstly, I would like to thank the EPSRC for funding this project. My thanks to Dr. Jinju Chen for her supervision and to Prof. Jonathan Higgins for same, as well as his generosity with advice, laboratory space, equipment and consumables throughout the project and extremely thorough proofreading and feedback during the thesis writing process.

I am extremely grateful to Prof. Patrick Degenaar for teaching me the principles of optogenetics and working with me to form the narrative of this thesis and the experiments in Chapter 6. I'm extremely grateful to Prof. Andrew Trevelyan for generous access to his laboratory, equipment, reagents, mice, advice and time. Many thanks to Dr. Ethan Cohen for discussions and advice on optogenetics and brain slice experiments, Dr. Suzanne Madgwick for tissue sharing and advice throughout the project, Dr. Tyrell Cartwright for his guidance on Western Blot and ELISA, Dr. Laura Alberio and Dr. Faye McLeod for their help learning acute brain slice techniques and other advice, Jack Dawson for his guidance on using the OCT system and Xin Xu for teaching me the operation of the microtome, cryostat and other histological methods.

I'm hugely grateful to my partners; Cat, Rowan and Pyrrha. Without their support, belief, love and patience I would have been hard-pressed to make it through this project. I'm glad you put up with me.

I am hugely indebted to my dearest and closest friend Ias, without whom I would literally have been unable to access the laboratory for much of the project and who has provided constant and unwavering support and companionship. Jenny, I cannot understate how much your incredibly generous work to make sure I had easy and delicious meals during my write-up has helped me get through this. Dragon, thanks so much for listening whenever I couldn't wrap my head around something; having you to help make sense of things was incredibly valuable.

Massive thanks to my parents and sister. You've believed in and supported me throughout all my life, and I couldn't have come this far without your love and guidance.

Finally, thank you to my cats, Beatrix and Celes. You've kept me sane, and I am privileged to have been able to give you a home and a family.

Contents

List of figures

List of tables

Chapter 1. Introduction

1.1. Thesis overview

In this first chapter, the literature review will outline the key factors involved in optogenetics and the principles behind both deep brain stimulation implants and the types of complications that may arise from use of such devices in clinical practice. This will explain the need for better understanding of the brain's response to optrode implantation (both mechanical and cellular) and phototoxic effects in brain tissue, providing the rationale behind this project.

Next, a review of the current understanding of mechanical, photothermal and photochemical trauma in brain tissue arising from optogenetic implants is covered, revealing some of the gaps in understanding and areas that require additional exploration. Some brief attention is given to principles of designing an optrode device for clinical use. Finally, an explanation of the principles behind mechanical measurement of biological (and particularly brain) tissues is given, including description of types of mechanical measurement that might be used on such samples and what methods exist to perform such measurements.

This thesis will then describe the methods and materials used throughout the course of the project in **Chapter 2**. Following this, **Chapter 3** contains a review of existing literature in which mechanical analysis of healthy mouse brain was performed, including a comparison of the findings of these studies and a critical analysis of the quality and reliability of these data.

Chapter 4 details efforts to produce cell-derived extracellular matrix from astrocyte cells, with the intent of using these matrices as models for brain tissue mechanical properties. This chapter also describes analysis of the mechanical properties of these samples using atomic force microscopy and shear rheology.

Chapter 5 presents experiments undertaken to establish whether acute mouse brain slices remain mechanically stable after they are obtained, and for how long. The chapter explores the optimal conditions for mechanical analysis of such samples if the results are to be reliable and comparable across different studies.

Chapter 6 involves work on optical toxicity in brain tissue; exposing acute mouse brain slices and cultured astrocytes to visible light of intensity comparable to that used in optogenetic devices and measuring the amount of cell death that results. Multiple methods are explored for detecting cell death in these samples, and the effect of 470 nm light on both cultured immortalised astrocytes and on acute mouse brain slices is described.

In **Chapter 7**, the results of earlier chapters are summarised and discussed, and their implications for the field of clinical optogenetics is argued. Suggestions are made for future work that should be carried out in this field.

1.2. Clinical opportunities for optogenetics

Neural stimulators are a type of medical implant used therapeutically to stimulate a targeted group of neurons for the purpose of inducing or suppressing motor activity, conveying sensory information, reducing pain or otherwise modulating neural activity to mitigate symptoms of disease or injury[1].

In brain, neural stimulator implants have seen great clinical success in applications including suppression of tremor in Parkinson's disease, treatment-resistant depression, dystonia, epilepsy and several other conditions. Treatments are also being developed for chronic pain, Tourette syndrome, cluster headache and more[1–7].

Deep-brain stimulation (DBS) electrode implants utilise a thin wire electrode that conducts electrical current into the neural population of interest, triggering action potentials in nearby neurons. The amplitude, pulse pattern and duration of the stimulation can be adjusted to produce desirable outcomes. Often, these settings must be discovered for a specific patient via a process of trial and error, varying substantially from patient to patient.

Unfortunately, such implants produce a variety of complications including mechanical trauma along the insertion track, the development of glial scar tissue around the implant – potentially insulating the implant and reducing function over time – and electrochemical damage to tissue due to long-term ion exchange and electrode degradation. In some cases, these issues worsen over the lifespan of the implant, eventually requiring removal and reimplantation along a new route (revision)[8–10].

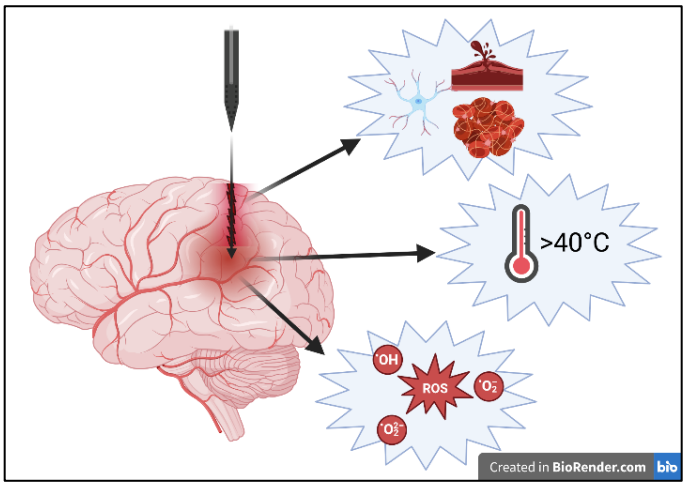

Figure 1: Insertion of optogenetic implants can cause a range of complications, including mechanical, thermal and photochemical toxicity.

Optogenetic implants are a relatively new technology, involving stimulation of neurons that have been modified to express light-reactive ion channels, using an implanted light source[11,12]. This technology has several potential advantages over conventional electrode implants; light can be transmitted through glial scar more readily than electrical signals[13–15], multiple wavelengths may be employed to stimulate several populations in different ways simultaneously[16], implants can be inserted in a more shallow position due to the higher distance along which light can penetrate through tissue, there is no risk of electrochemical damage[17,18] and neurons can be both stimulated and suppressed, depending on the target protein used[16].

Because of these features, optogenetic implants offer the same potential for novel treatments as electrical deep-brain implants, with further scope for more precise targeting and more nuanced control of regions of interest. However, optogenetic implants introduce the risk of new types of trauma for the patient (Figure 1).

1.3. The Optogenetic Mechanism

Optogenetic devices utilise the channelrhodopsin (ChR) protein family originally discovered in *Chlamydomonas reinhardtii*, a photosynthetic alga. Several members of this family have been discovered in nature and many cloned variants have been produced[19].

ChRs are transmembrane light-gated ion channels; in the presence of sufficient light of a frequency band specific to the protein, there is a conformational change causing the channel to open, allowing ions in or out of a cell (depending on the local ionic gradient). Most ChRs are non-specific cation channels (allowing H^+, Na^+, Ca^{2+} and K^+ ions to pass), though anion-transmitting ChRs also exist[20].

When ChRs embedded in the cell membrane are opened, cations are allowed to flow into the neuron. This moves the (negative, resting) membrane potential towards zero, triggering voltage-gated ion channels nearby to do the same and resulting in a large, rapid increase in (positive) transmembrane potential as cations flood into the cell. This process continues rapidly along the axon, conveying the signal towards the synapse and from there on to connected neurons. Once the transmembrane potential becomes sufficiently positive, the membrane polarity reverses, causing the open ion channels to close. Cations are actively transported out of the cell, resetting the membrane potential to its resting state[11].

ChRs have been adopted as a tool for rapidly inducing action potentials in neurons since 2005[11] due to the high speed at which they open and close, allowing millisecond-timescale control of neural activity using optical signals. Genetic engineering of the protein has allowed for development of variants with much-reduced recovery times – enabling control over smaller timescales – and variants that open with one wavelength and close with another, enabling channels to be kept open or closed without requiring constant illumination[19,21].

In brain, neurons are genetically modified via viral vectors to express ChRs, allowing site-specific reactivity and enabling the technology to be used in mature organisms. Once the target population has been transduced, an optrode (*ta optiká* + *hodos* – Greek, “appearance, look” + “way”[22,23]) implant is inserted surgically into the tissue, providing a source of illumination. Optrode implants are still in early stages of development, requiring optimisation in terms of material selection, miniaturisation, improved thermal performance and introduction of features such as multi-wavelength sources and biocompatible coatings.

1.4. Light traversal through tissue

Since optogenetics relies on optical signals reaching modified neural populations, it is important to understand how these signals travel through tissue; the distance at which neurons of interest may be stimulated with an implant emitting light of a given wavelength and intensity is a major factor in optogenetic implant design and development.

Since brain tissue is not substantially pigmented (containing only small amounts of neuromelanin[24,25]), absorption of light by pigment molecules is not a major concern compared to – for example – skin, where melanin is much more abundant. Depending on the wavelength used, absorbance by haemoglobin from red blood cells in capillaries throughout the tissue may affect transmission, however the primary mechanism by which light passage through brain tissue is attenuated is via scattering[13–15,26].

When light (or any wave) enters a material at an oblique (not perpendicular to the boundary between the materials) angle, it will change direction unless the refractive index of the two materials is the same (Figure 2). The greater the difference in refractive index, the greater the change in direction. In brain tissue, a wide variety of molecules exist possessing different refractive indices. In particular, proteins and lipids have significantly higher refractive indices than that of water (1.33); the

refractive index of dehydrated brain tissue has been estimated at ~1.50, resulting in multiple scattering events as light passes between the aqueous medium and the biomolecules throughout the cytoplasm and extracellular matrix[27].

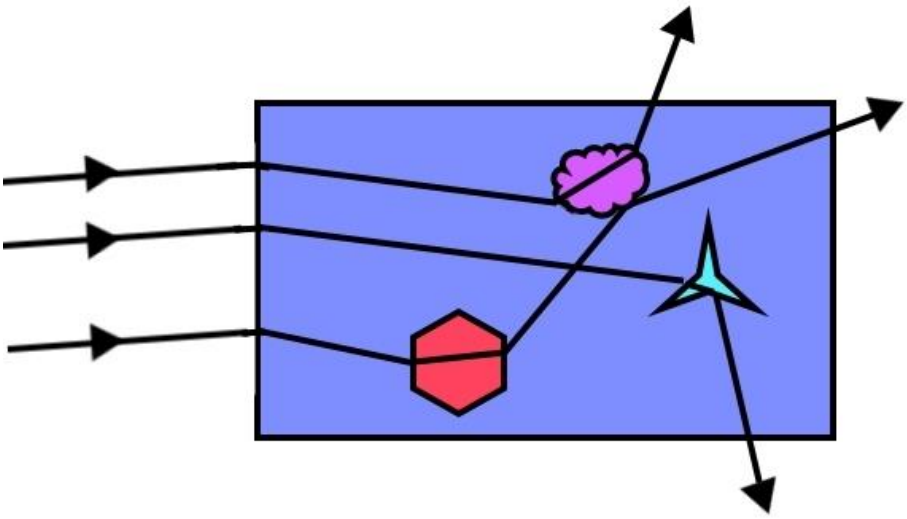

Figure 2: Non-perpendicular light entering cytosol (RI ~1.33) from air (RI ~1.00) will change direction. Proteins, lipids and other biomolecules (varied RI but average ~1.5) will cause additional changes in direction, resulting in scattering.

The above explanation of light scattering is sufficient in most cases, however Lichtman et al. (2015) provide a more detailed explanation that covers the underlying physics more comprehensively[28]. Light scattering occurs in any material; the only instance in which scattering does not occur is in a vacuum. When light interacts with the electrons around an atom, it can result in one of three outcomes: fluorescent emission (if sufficient energy is imparted to cause a jump to a higher energy level), ionization (if even more energy is imparted, sufficient to remove the electron from the atom) or elastic scattering. In elastic scattering, the electron is caused to vibrate temporarily, but most of the energy is re-emitted as a spherical wave (akin to a circular ripple in water, but in 3 dimensions) at the same frequency at which it was absorbed. The amount of time that the energy was “stored” in the vibrating electron varies according to the material and causes a tiny (around a femtosecond in scale) delay in the progression of the light. The greater this delay, the greater refractive index the material is said to have. As the density of the material increases (and

therefore the number of electrons that can be interacted with), the ability of the electrons to absorb energy increases, as does the refractive index.

In a material with very tightly packed, homogeneous atoms (such as glass, water, or air), the atoms are arranged closer together than the wavelength of the light that interacts with them. Because of this, for every wave that is emitted by one atom, another will be emitted that is out of phase to it. This results in destructive interference in all directions where the light is propagating apart from directly ahead of the wave, where due to the slight delay before the next atoms are excited, the waves are in phase with one another and interact constructively. Because of this, the light will only propagate forwards.

Tissue and other light-scattering systems differ from this example because the electron density (and the electrons' ability to absorb energy) of each type of molecule is different, and these different molecules are not homogeneously distributed. Because of this, not all waves emitted by one molecule will be completely cancelled by those emitted from another, and light will be emitted perpendicularly to the original direction of the wave.

Since the energy of higher-frequency, shorter-wavelength light is higher, the amplitude of the re-radiated wave from each particle is greater. This results in larger amounts of energy being re-emitted in directions perpendicular to the original direction, causing greater scattering for short wavelengths than long. In optical imaging of tissue, near-infrared and infrared wavelengths are often employed due to their long wavelength, allowing for reduced scattering and thus deeper penetration of light through the subject[29].

This would imply that for optogenetics, it is desirable to use as long a wavelength as possible to stimulate the target cells. However, several other considerations affect this decision: whilst many ChRs have been developed, there are limited options for

stimulatory wavelengths[19]. Additionally, longer wavelengths may cause greater thermal effects in the tissue and carry less energy per photon (requiring greater photon flux from the emitter to achieve the required number of ChR activations). Finally, current LED technology produces emitters that are brightest in certain wavelengths, requiring more expensive or bulkier devices to achieve equivalent emission from less effective wavelengths.

1.5. Types of optogenetic device

Optogenetic devices have taken a range of forms in the literature to date. The simplest devices directly illuminate the transduced tissue – either illuminating channelrhodopsin-expressing retinal neurons directly through the eye or illuminating modified cortical neurons via “brain windows” installed through the skull and dura[30–37]. Whilst therapeutic devices have been developed to treat blindness via this method, it has little potential for clinical brain stimulation due to the inability to reach deep within the tissue and the necessity for a chronically implanted window.

Other approaches utilise arrays of LEDs, often simply placed onto the surface of the brain between the dura and the target tissue. Generally these devices cannot deliver light deeply, however some examples incorporate optical fibres or waveguides to deepen their reach[38–43].

Devices utilising optical fibres have the advantages of simplicity (since the illumination source can be mounted externally) and small diameter (reducing mechanical trauma from insertion). Most optical fibres are too stiff for chronic implantation however; an issue that may be avoided by using novel materials instead of glass - one such device employs a flexible silk-based fibre[44]. Early optic fibre-based implants were not sharpened like DBS electrodes, leading to increased mechanical trauma – however methods for producing sharp optical fibres have been developed and have the additional benefit of increasing the diameter of the fibre’s

emission cone[45–50]. Fibre implants with addressable emission points have been developed by micro-machining of the fibre surface[51].

Alternative delivery structures involve waveguides, which can be manufactured from a wide range of materials (many of which are softer than glass, easier to manufacture, or have other advantages), and have been integrated into LED arrays to produce devices capable of illuminating large regions of tissue deeply. Similarly to optical fibre arrays however, the multiple insertions this approach entails significantly increases the mechanical trauma experienced by the tissue[52–57].

Finally, as advancements in micro-LED technology become available, devices that directly integrate LEDs into the probe itself (rather than guiding light from external arrays) have been developed. These devices can be implanted deeply, often incorporate multiple LEDs of different wavelengths and can be implanted using methods similar to existing DBS protocols. Downsides of these devices include greater heat generation at the target site and the need for greater miniaturisation before they approach the diameter of existing electrodes[58–63].

1.6. Probe insertion and complications

As with any surgically implanted medical device, the process of penetrating an object through tissue carries with it the consequence of physical trauma. Surgeons must produce a route from the external environment to the target neurons via the skull, meninges and intervening non-target brain tissue.

Neural stimulators are employed to stimulate a wide range of targets (for example common targets for treatment of Parkinsons disease tremors include the subthalamic nucleus or globus pallidus). To facilitate accurate and precise implantation of these implants, stereotactic equipment is employed: an apparatus (that may have a rigid frame or be frameless) is held stationary relative to the patient and holds precisely adjustable mounts for surgical tools and the probes themselves, allowing them to be

introduced into tissue at a specific angle, depth and speed. In conjunction, a stereotactic atlas and x-ray monitoring serve as references for the surgeon to select a route to the target site[64]. Use of this approach minimises trauma to neighbouring brain tissue that might arise through manual implantation.

The precise site of implantation can vary by 1-2 mm between patients; most DBS implants are carried out in a “proprietary” manner (i.e. the insertion route is determined individually for each patient), with the final position of the electrode determined by *in situ* electrophysiological measurement via microelectrodes prior to the final electrode insertion. This process is particularly vulnerable to complication; it has been estimated that between 15-34% of DBS electrodes are removed or their placement revised after initial insertion[65] and that up to 48.5% of these revisions may be due to improper placement[8,66,67]. It is best practice to minimise the number of insertions and the amount of revision, since insertion and manoeuvring of insertion cannulae, microelectrodes and DBS electrodes contributes to mechanical trauma and the likelihood of complication.

In the case of optogenetic neural stimulators, two invasive steps are required: injection of the viral vector required to transform the target neurons and insertion of the optrode itself. Whilst optogenetic implants may not need to be implanted as close to their target site (due to the increased distance that light may penetrate compared to electrical stimulation, and the improved specificity of that signal to stimulate only the target tissue), the injection channel must still reach the region of interest directly.

Whilst the needle used for virus injection can be much thinner than a “conventional” DBS electrode (on the scale of 0.1-0.3mm vs 1-2mm in diameter respectively), this still produces trauma and increases the risk of complication. Targeting the viral injection requires a similar level of precision to that of a DBS electrode, necessitating the support of microelectrode measurements and imaging to confirm the final site and that targeting a particular site will produce positive clinical outcomes. However,

use of cell type-specific vectors reduces this need, allowing specific neural subpopulations to be targeted via use of selected genetic promoters and tailoring of the genetic payload[68]. These modifications are still in their infancy and have the potential to substantially reduce the need for high mechanical precision of the injection site.

Provided the viral vector is properly delivered, however, the precision of optrode placement required to successfully target the transduced cells may be lower than that required for a DBS electrode.

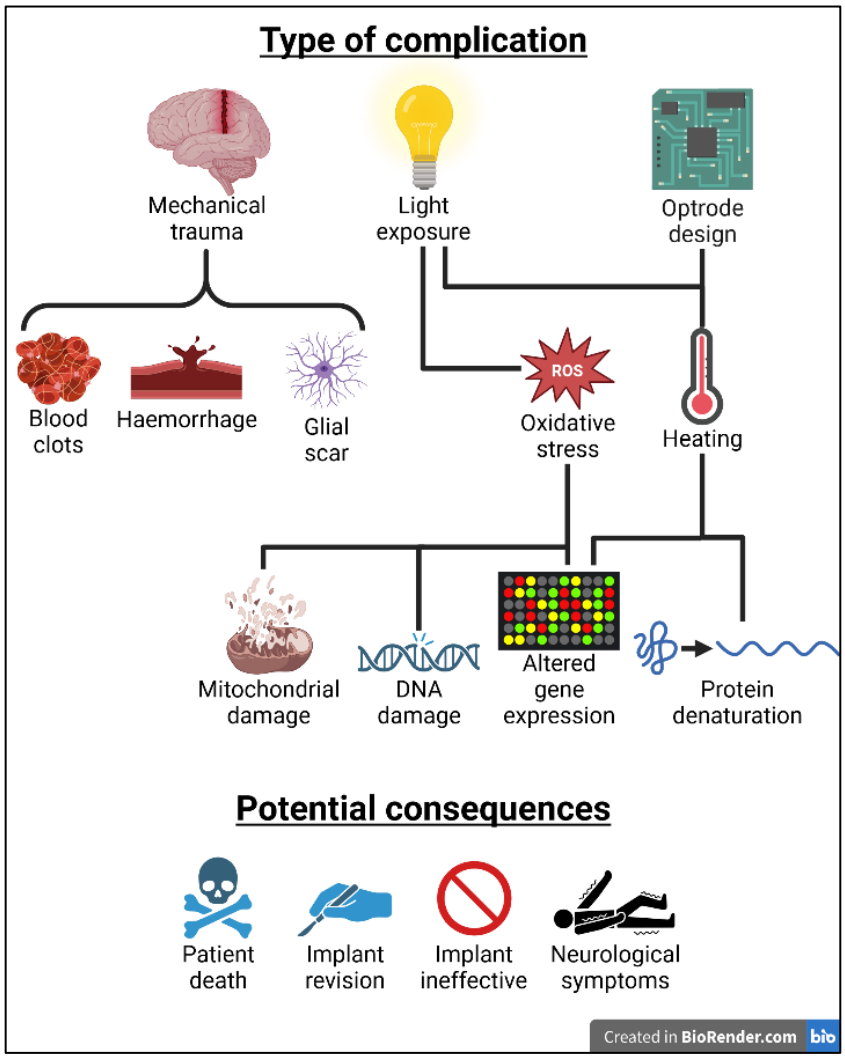

Figure 3: Optogenetic implants could potentially cause complications in patients via several mechanisms including mechanical trauma, thermal effects and photochemical damage. Trauma from these mechanisms risks serious consequences for patients ranging from ineffective treatment to death.

1.7. Mechanisms for tissue damage

Several types of trauma are possible during the insertion and long-term use of an optogenetic implant including mechanical, thermal (both from the device electronics and photothermal effects) and chemical (from implant materials and photochemical effects) – illustrated in Figure 3.

1.7.1. Mechanical damage

Several acute complications may occur in the immediate aftermath of DBS device implantation, resulting in temporary or permanent neural deficit and exacerbation or emergence of new symptoms; direct neural damage, oedema (tissue swelling), intracerebral haemorrhage (stroke), blood vessel infarction (blockage) and seizures resulting from the above or other causes[8].

Direct neural damage is perhaps the most obvious mechanism of mechanical trauma from implantation; the relatively stiff electrode must pass through soft brain tissue *en route* to its target, causing tearing and crushing of neurons, glial cells and extracellular matrix. By minimising the diameter of objects introduced into the tissue, the number of insertions and the amount of adjustment required, this type of damage can be minimised.

If the DBS implant or other probes cause mechanical trauma to blood vessels, infarction (collapse or blockage) or haemorrhage (bleeding) and subsequent clotting can restrict flow of blood to surrounding regions of tissue and cause increased pressure – this is known as a “stroke”. The severity and scale of this complication can vary substantially, potentially resulting in widespread tissue damage through compression and/or ischemia[8,69].

DBS implantation can also result in longer-term complications including glial scarring[70,71] and infection[8].

Glial scar formation is an inflammatory process involving activation and recruitment of astrocytes and microglia to the injured site. This process results in a region surrounding the implantation trajectory and probe tip that contains dense populations of glial cells and heavily modified extracellular matrix (ECM), composed mainly of vimentin, collagen IV and laminin (all of which are components of the basement membrane)[72,73]. Many ECM components that are upregulated in glial scar formation act as inhibitors (and paradoxically, stimulators) of neural regeneration[74–76].

Once implanted, complications can arise from the implant hardware itself; infection remains a risk for the lifespan of the implant, electrode migration can occur due to external forces on the anchor site, electrodes and leads can fracture and electrical faults may develop in the hardware. As hardware design improves, this type of complication is becoming less common – however it remains a concern for any chronically implanted device.

1.7.2. Photochemical damage

Photoexcitation of chemicals can result in photochemical effects; chemical reactions whose activation energy is provided not by (or not solely by) thermal effects but by absorbance of photons. When a photon is absorbed by a molecule, an electron is raised to a higher energy level from the highest occupied molecular orbital (HOMO) to the lowest unoccupied molecular orbital (LUMO) or higher. Depending on the specifics of the absorption event, this energy is released either by internal conversion (resulting in thermal emission) or emission of a photon via fluorescence or phosphorescence. Because the excited molecule has empty space in a low energy orbital, it is more susceptible to oxidative processes; the remaining electron is less stable and more easily removed via oxidative reactions. Conversely, since the molecule has an electron in a high-energy orbital it is also more reducing, meaning that excited molecules are more prone to both types of electron transfer reaction[77].

Intracellular oxygen in biological systems exists as molecular oxygen (O_2), occurring in a triplet state. Usually, triplet molecules cannot react with those in a singlet state; because of this oxygen is relatively unreactive with other molecules in a system. When a molecule is excited via photon absorption, the excited electron enters either the S^1 (excited singlet) or T^1 (excited triplet) state in which reaction with triplet oxygen is possible.

There are two types of reaction that can result: Type-I and Type-II. Type-I reactions are between the excited molecule and a substrate molecule; these produce free radicals (molecules with at least one unpaired valence electron). Type-II reactions are between the excited molecule and molecular oxygen, producing a reactive oxygen species (singlet oxygen, hydroxyl radicals and superoxide ions). The radicals produced by Type-I reactions typically react with molecular oxygen immediately, producing ROS – as such the consequence of both pathways is similar. ROS are highly cytotoxic due to their ability to react with a wide range of biomolecules[78,79].

This phenomenon has been harnessed for clinical applications – particularly in treatment of tumours, acne, wet age-related macular degeneration, psoriasis, atherosclerosis, and other conditions. This treatment is known as photodynamic therapy and involves introducing a molecule that is particularly susceptible to excitation from a particular wavelength (a “photosensitiser”) to the patient and targeting tissue for destruction with highly focused laser light. Photosensitisers can be selected for a tendency to accumulate in the target tissue, allowing highly focused destruction of undesirable tissues whilst keeping surrounding tissue intact[80]. The same effect can cause undesirable damage to patient tissue when drugs given for other purposes unintentionally behave as photosensitising agents[81].

In optogenetic applications, phototoxicity is an undesirable side effect; many endogenous molecules are chromophores that can act as photosensitisers and result in damage to healthy tissue. In particular, the mitochondrion expresses many

chromophores and can be thought of as the principal site at which photochemical toxicity may occur in optogenetic applications[82]. Because the mitochondrion is a site rich in oxygen – and which already suffers substantial oxidative stress during normal function – it is a particularly vulnerable target for photochemical damage, easily resulting in activation of apoptotic pathways and cell death[83]. Nevertheless, a range of other potential targets are expressed throughout mammalian cells, including nucleic acids, some proteins, lipofuscin and others[84,85].

Ageing is a major risk factor for accumulation of reactive oxygen species[86–88] and of some photosensitisers including lipofuscin[85,89], as well as mitochondrial degradation[90]. Additionally, mitochondrial dysfunction can itself cause production and accumulation of lipofuscin, meaning that ageing, photochemical damage and mitochondrial dysfunction are interlinked factors[91]. Since DBS patients – particularly for Parkinsons disease – tend to be older, this emphasises the importance of mitigating or preventing photochemical effects arising from optogenetic implants. Additionally, neurons and glial cells have a particularly high concentration of mitochondria due to their high energy needs; this potentially makes them more susceptible to phototoxic effects than cell types from other tissues such as skin[92,93].

Since photochemical damage is reliant on absorption of photons by chromophores, wavelength is a major factor in phototoxicity in optogenetic applications; wavelengths that are absorbed by a wider range of biomolecules are likely to produce greater phototoxicity than those with few highly absorptive targets. Similarly, phototoxicity requires photons of sufficient energy to excite electrons in their target to the S1 or T1 positions; since longer wavelength photons contain less energy, it follows that photochemical effects are more prevalent with shorter wavelengths. Whilst it is possible for two longer wavelength photons to be absorbed simultaneously, such “two-photon” excitations are very rare, requiring much higher photon flux than typically exhibited in optogenetic devices to occur in with significant frequency[94–96].

1.7.3. Photothermal damage

The energy absorbed by light-excited molecules is not only released via photon emission (fluorescence and phosphorescence, as discussed above), but also via non-emissive relaxation in the form of thermal energy.

Heating of tissue can cause cell death and dysfunction; a temperature of 42-45 °C can cause structural changes to proteins and breakage of hydrogen bonds. Higher temperatures can result in enzyme inactivation, conformational changes to proteins, disruption of cell membranes, coagulation and – in extreme cases – boiling, steaming and carbonisation[97].

In practice, optogenetic implants are unlikely to cause such extreme heating, however even small changes to tissue temperature can cause pathological disruptions. Normal brain activity in response to environmental stimuli can produce temperature changes as high as 2-3 °C[98], however at temperatures of 40 °C or more, irreversible changes to mitochondrial structure and function, cell division and survival begin to occur[99]. As such, an approximate increase in brain temperature of >3 °C may be considered an appropriate threshold for cell damage.

Since humans routinely tolerate temperatures in excess of 40 °C for short periods without substantial tissue damage, it can be assumed that this threshold is true only for extended exposures; optogenetic sources are commonly pulsed to allow for thermal dissipation between exposures; the maximum temperature recorded at the surface of exposed tissue is strongly related to the duty cycle of exposure[100].

In addition to damaging effects of temperature change, possible effects on the electrical behaviour of neurons should be considered. Changes in temperature affect ion channel conductance, amplitude and length of action potentials, and opening of temperature-sensitive ion channels that may affect ionic potential across the cell membrane, conceivably leading to unexpected neural behaviour[101].

1.7.4. Existing regulations – skin and retina

The EU maintains regulatory guidance regarding light-induced tissue damage[102]. This guidance focuses on the eyes and skin as these are the tissues that are typically exposed to light. Both tissues are adapted to tolerate light exposure (with increased melanin expression in the case of skin[103] and Müller glial cells in the case of retina[104], as well as various enzymatic and antioxidant molecules that are expressed in both[96,105–107]).

Rather than discussing safety from the perspective of irradiance on a given area of tissue, these regulations provide guidance based on the type of emitter – a more practical approach in many instances since the typical user of a light-emitting device will vary the distance from which they are exposed. They separate devices according to wavelength (discussing ultraviolet, visible and infrared light separately), and coherent (laser) light exposure is treated as its own category (as compared to non-coherent sources such as LEDs), due to the relatively small focal point of most laser devices, increasing risk of exposure on a very small region of tissue that could cause very rapid damage.

Hazard functions are expressed in the form of the maximum average irradiance on a tissue over a period of 10,000 seconds should not exceed 100 Wm^{-2}, after weighting for wavelength (Figure 4). Each wavelength is assigned a spectral weighting function (a dimensionless value) that scales the risk of photochemical damage from that wavelength. Similarly, photothermal damage regulations assign a weighting function for each wavelength, allowing the safe average intensity threshold over a 1000 second period to be determined for a given emitter.

Since brain tissue is not commonly exposed to light, these regulations can only provide theoretical upper limits for brain tissue exposure. Further work is required to establish similar action spectra for brain tissue, allowing regulatory agencies to make informed decisions about optogenetic implants in clinical practice.

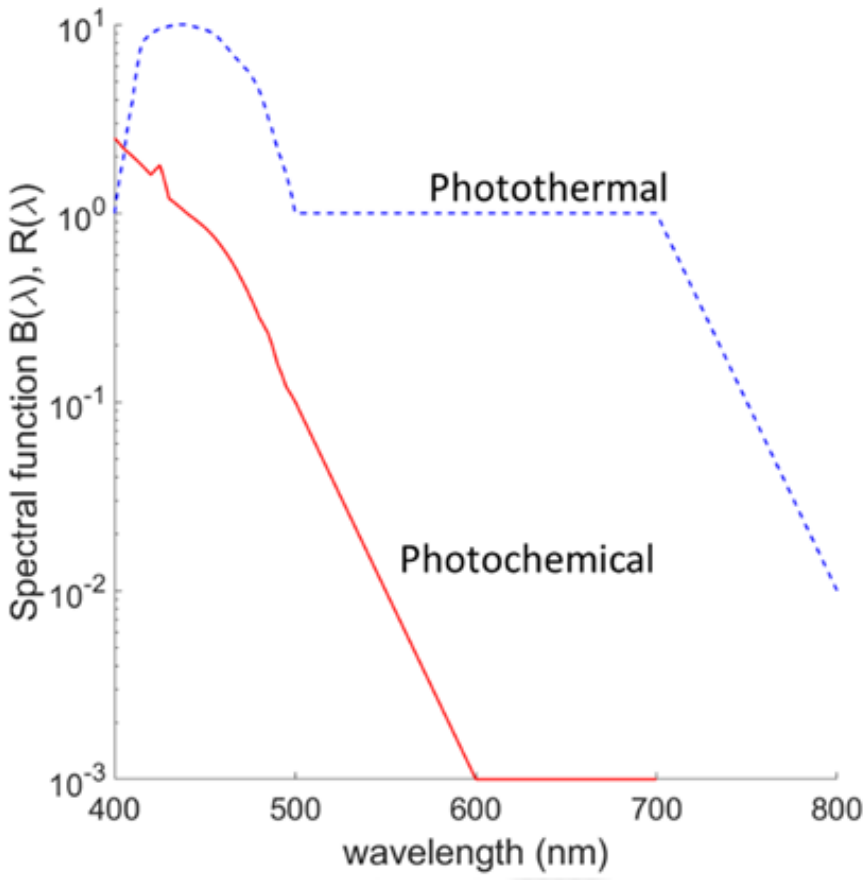

Figure 4: Action spectra for photothermal and photochemical damage in EU regulations on visible radiation exposure. Note that since the photothermal and photochemical action spectra are used in different safety calculations, they are not directly comparable to each other. Data taken from Directive 2006/25/EC of the European Parliament.

1.8. Experimental evidence

In this section, existing evidence regarding the various types of damage that could be caused by optogenetic deep brain stimulation devices is summarised. Discussion of mechanical trauma primarily relies on clinical data concerning conventional DBS electrodes; these complications are likely to be similar to those seen in any optogenetic device that reaches clinical use, since both technologies require physical penetration of a device through patient brain tissue. Since no optogenetic brain implant has yet seen clinical use in animals or humans, discussion of photothermal and photochemical damage is limited to evidence from academic studies of optogenetics in laboratory animals, *in vitro* cultured samples and *in silico* simulations. The relationship between toxicity and exposure intensity, duration, wavelength and duty cycle are discussed, as well as potential strategies and design approaches to minimise these types of damage.

1.8.1. Tissue damage from mechanical trauma

Use of DBS electrode implants for the treatment of Parkinson's disease was approved by the US FDA in 2002. However, DBS electrode implantations have been carried out clinically since the mid-1970s, originally for analgesic purposes[1,108].

Implantation of DBS devices carries a risk of several complications arising from mechanical trauma: haemorrhage, infarct and neural damage that can cause a wide variety of symptoms peri- and post-operatively, including tremor, palsy, behavioural changes, dysarthria, gait changes, partial or complete loss of visual field, seizure and more[8] (representative CT scans of these injuries are shown in Figure 5). It is difficult to determine whether many of these symptoms arise due to mechanical trauma from the implantation process or from subsequent electrical stimulation. However, it is reasonable to assume that complications that are detected prior to commencement of electrical stimulation – or which do not resolve after alteration of stimulation parameters – were likely the consequence of mechanical damage to brain tissue.

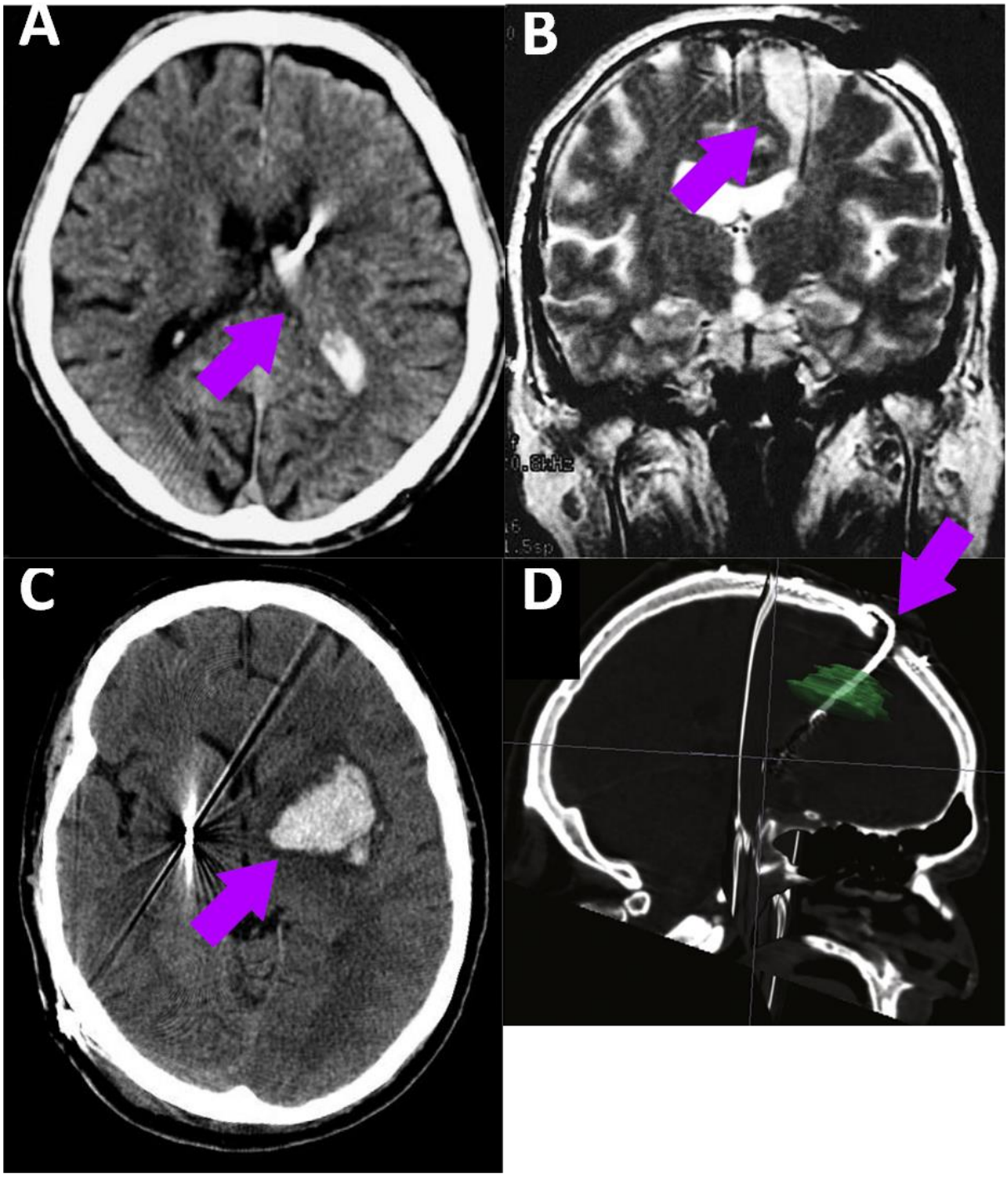

Figure 5: Representative computed tomography images of mechanical trauma in DBS electrode implant patients.

A: Image from Terao et al. (2003). Shows an intraventricular haemorrhage (arrow) caused by DBS electrode penetration.

B: Image from Umemura et al. (2003). Shows a lesion (arrow) caused by infarction around the DBS implant site.

C: Image from Binder et al. (2005). Shows a lesion (arrow) resulting from penetration of a microelectrode through the choroidal fissure.

D: Image from Deogaonkar et al. (2011). Shows a computer reconstruction of peri-lead hypodense tissue (green) indicating oedema around the DBS electrode (arrow).

Table 1 shows incidence of complications likely to have been caused by implantation of DBS electrodes in clinical practice, taken from 28 reports of procedures carried out between 1995 and 2022[9,10,109–134]. A list of keywords and sites used for the literature search is included in the appendix.

The rate of complications from mechanical trauma is relatively low for electrode implantation, and it is generally considered to be a safe procedure; complications associated with electrode malposition are substantially more common (it has been estimated that between 15.2 and 34% of DBS electrodes require later removal or revision) and hardware malfunction or wear occurs eventually with most implants, at a rate of approximately 8% annually per electrode[8]. However, the rate of complications from mechanical trauma increases with each additional trajectory, and electrode removals have a higher rate of haemorrhage than do insertions, making the relative risk of mechanical complication per-patient substantially higher due to the high revision rate required[135,136].

Additionally, the rate of neurological complications from mechanical trauma may be underestimated when recorded perioperatively; 4-year follow up of DBS patients reports a substantially higher rate of these issues, with 47.8% of patients showing implant-associated adverse events that did not resolve with adjustment of stimulation parameters, suggesting that they arose from mechanical trauma that developed over time, either due to shifting of the implant or inflammatory effects and scarring of the trajectory[137].

Complication	No. of Procedures	% Rate per Procedure
ICH	9132	4.42
Infarct	705	1.55
NS	2810	3.40
Seizure	6594	6.87

Number and rate of various types of complication arising from DBS electrode lead implantations reported in clinical literature. Seizure is the most common complication of lead implantation, followed by ICH, NS and infarct.

Data were taken from 28 studies from 1998 to 2022. Number of procedures may be underestimated as not all sources cite number of leads implanted or whether procedures were unilateral, bilateral or revisions.

Definitions = ICH: Intracranial haemorrhage. Includes all peri- and postoperative symptomatic and non-symptomatic intracerebral & intraventricular haemorrhage and haematoma. Infarct = Includes all reports of peri- and postoperative stroke and infarct. NS = Neurological symptoms. Includes peri- and postoperative tremor, palsy, behavioural changes, dysarthria, gait changes and other neurological symptoms. Does not include confusion or pain as these are difficult to distinguish from surgical discomfort or confusion from age, pre-existing conditions or anaesthesia. Excludes symptoms which resolved after electrical stimulation was adjusted. Seizure: Peri- and postoperative seizures prior to commencement of electrical stimulation. Listed separately to NS as it is relatively common compared to other symptoms and more commonly reported.

Table 1: Rate of complications arising from mechanical trauma related to DBS electrode implantations.

Incidence of these types of complications has decreased since the procedure was originally introduced, due to a combination of improved implant design (primarily reducing the diameter of the electrodes[126]), more experienced surgeons[119] and use of real-time MRI guidance rather than (or in conjunction with) CT or microelectrode-guided placement[114], though the benefit of MRI guidance over these methods is controversial[8].

Many factors of mechanical trauma arising from these procedures are poorly understood; the source of peri- and postoperative oedema along the electrode trajectory has not been firmly identified, though it may relate to cyst formation that has been observed in some MRI-monitored procedures[138–144] and, whilst it has generally been considered a rare complication, this may be due to insufficient monitoring; recent estimates suggest a rate of as much as 35.8% for asymptomatic cases, with a 3.1% rate of symptomatic peri-lead oedema[145].

Whilst no optogenetic implant is currently approved for clinical application (and studies in nonhuman primates and rodents tend to be concerned only with increased light scattering and opacity caused by haemorrhage of vessels at the brain's surface[30]), several inferences can be made from rates of mechanical trauma in extant DBS technologies. At present, optogenetic devices tend to be larger in diameter than conventional electrodes; a property associated with increased rates of haemorrhage[126]. Similarly, optogenetic treatments require an injection into the target site as well as a (potentially shallower) optrode trajectory. Since the rate of complication increases with number of insertions, this may increase risk of mechanical trauma – but delivery of agents such as viral inoculations have been suggested to have lower risk than electrode insertions[135]. However, since optrodes need not necessarily be implanted as deeply or precisely as a DBS electrode so long as the viral injection site was correct, the risk of implant deflection may be reduced and the need for adjustment, revision and re-implantation could be substantially lower.

Some investigation has been made into optogenetic methods utilising two- or even three-photon illumination[146–148] – though practically, these methods achieve depths suitable only for DBS in rodents, can illuminate only very small regions and the high intensity of illumination exacerbates heating and photochemical effects. Similarly, techniques such as nanoparticle up-conversion of NIR light to visible wavelengths may further reduce the required depth of penetration, though such techniques have thus far been demonstrated only in rodent and smaller models[149,150].

1.8.2. Photochemical trauma in brain

The first study of optical toxicity in a rodent model was carried out by Noell *et al.* in 1966. The study investigated retinal damage in rats using broad-spectrum light between 490 and 580 nm, as well as 500 nm (green) and UV wavelengths over a 24 hour exposure, finding retinal damage in all three conditions[151]. This paper kindled the first interest in phototoxic effects *in vivo*.

The vast majority of studies into visible light phototoxicity in the absence of exogeneous photosensitising agents have been in retina, and are usually limited to white (simulating sunlight or residential light sources) or blue (~400-500 nm) light, with very few investigating green (~500-540 nm) wavelengths[152]. Longer wavelengths between 540 and 800 nm tend to be neglected in studies of phototoxicity, with "visible" light tending to be a shorthand for "blue" in most cases. Studies of near-infrared and infrared light (>800 nm) are more common; however, these wavelengths tend to cause photochemical effects only in the presence of exogeneous photosensitising agents or in multiphoton applications.

Photochemical damage is cumulative with increasing exposure time above an injurious threshold. The intensity threshold required for damage depends on a range of factors, including the tissue/cells being exposed, the wavelength of the light and the pulse pattern[107]. Peak power appears to be less important than average power across the duty cycle – this is particularly important during applications such as

multiphoton stimulation, where pulsed lasers are successfully employed at much higher peak power than continuous-wave sources can achieve[94,146,148].

Blue light

Light of between ~400-500 nm is most closely associated with phototoxic effects from "visible" light. Photochemical damage has been observed in a range of animal models and tissue types – chiefly retinal epithelial or neural cells[82,153–157], but also cortical neurons and glial cells[158–161]. In experiments using "white" light, it has generally been suggested that the blue component is the biggest contributor to toxicity[157,162,163]. More recent studies have suggested that existing intensity thresholds recommended by regulatory agencies may be overestimated, and that diagnostic equipment used by opticians and even consumer lighting products produce blue light in intensities sufficient to cause retinal damage[164–166].

Even in the absence of cell death or damage, blue light exposure has been demonstrated to cause changes in gene expression, calcium signalling and reactive oxygen levels – which can affect signalling pathways in the exposed tissue[159,167–169]. Indeed, this response has been utilised to investigate the role of ROS in cell signalling via optogenetic stimulation[170].

Blue light phototoxicity is thought to be chiefly associated with mitochondrial oxidative stress and damage[82,83,153,160,161,171], and it has been suggested that the major mode of cell death from photochemical damage is not the classic caspase-mediated apoptotic pathway, but is instead triggered by a variety of other mechanisms including lysosomes, apoptosis inducing factor, mitochondrial damage and other routes[157,160]. Despite this, caspase-mediated apoptosis has been observed in phototoxicity experiments[156] and it has been suggested that the primary mode of cell death may vary between pulsed and continuous-wave illumination[172]. Whilst mitochondrial stress is thought to be the main consequence of blue light phototoxicity, mitochondrial DNA and nuclear DNA damage have been observed[153].

Several endogenous photosensitisers have been implicated in retinal visible light phototoxicity, chiefly opsins[157], oxidation products of retinal pigments such as N-retinylidene-N-retinylethanolamine, kynurenine and melanin[156,163], retinoids[173] and components of lipofuscin[174]. Many of these molecules are not expressed in brain tissue, and phototoxicity from blue light has been demonstrated in microglia without expression of opsins[159].

The context in which cells and tissue are exposed to light is important; several studies have pointed at components of cell culture media and their photo-oxidation products as a source of toxicity, however since phototoxicity occurs *in vivo* as well as *in vitro*, claims that this is the sole source of photochemical hazard cannot be the whole picture[158,169,175,176]. Similarly, hyperosmolar conditions have been associated with increased blue light toxicity[155].

Clinically, it is important to recognise that exogeneous photosensitising agents may place patients at risk; drugs with a tricyclic or heterocyclic structure or other visible-light absorbing chromophores may amplify phototoxic effects, and if such drugs are capable of crossing the blood-brain barrier (such as many lipophilic and amphiphilic small molecules), could cause complications for patients with optogenetic implants. Some relatively common drugs have been associated with drug-induced phototoxicity, including non-steroidal anti-inflammatory drugs and many antibiotics[81,96,163].

Phototoxicity has been known as an issue in live-cell microscopy for some time, and reduction of exposure duration and intensity combined with increasing the wavelength of stimulatory light are commonly recommended to avoid such issues when imaging live samples. Fluorophores and stains used in microscopy can often act as photosensitising agents, and targets which require illumination with blue light are particularly common – for example fluorescein[177–180].

Green light

Photochemical damage from green (~500-540 nm) light has been much less thoroughly investigated than blue. Noell *et al.* (1966)[151] used broad-spectrum green light (peaking at 500 nm), however the substantial overlap with the blue range and relatively crude measurements of injury make it difficult to draw conclusions based on wavelength.

A narrow band of green light (500-520 nm) has been associated with single-strand DNA breaks and “slowly developing alkali-labile sites” in human teratoma P3 cells, however the action spectrum shows dramatic increases in this type of damage as wavelength shortens[181]. This small band corresponds to the upper end of the absorption spectrum of riboflavin, which is a potent photosensitising agent at shorter wavelengths (though also behaves as an antioxidant[182]) and is present throughout the body (though this effect is ameliorated by ascorbate and flavonoids)[183,184]. Riboflavin supplementation has been investigated as a potential treatment for Parkinson’s disease[185,186], so there may be potential of green light-induced phototoxicity in Parkinson’s patients fitted with optogenetic implants.

Green light has been demonstrated to cause photoreceptor cell death in rats; the light used is described as “intense” but was several orders of magnitude less bright than values seen in optogenetic applications (intensity values in lux are adjusted according to sensitivity of the human eye; the 3.5 KLux used is approximately equivalent to 0.005 mW/mm^2, assuming a monochromatic light at 555nm. Since the light used was not monochromatic this is not an exact conversion, however this is the maximum possible value since the conversion factor is greatest at 555 nm). Despite this, 12 h of exposure resulted in death of 3.5% of the subject’s photoreceptor cells and a corresponding increase in caspase-1 immunoreactivity, indicating an increase in the rate of apoptosis[187].

Similarly, Organisciak *et al.* (1999) found that green light (490-580 nm, ~8 mW/mm^2) in dark-reared albino rats resulted in a ~40% receptor cell death rate after 3 h of exposure, and the same rats raised under cyclic light conditions (which were less susceptible to light-induced damage) showed a 50% loss after a 24 h exposure[188]. Antioxidant supplementation protected against this damage, suggesting that light-mediated ROS generation was involved; the likely photosensitiser was rhodopsin[157], which is not common in brain and thus may not be relevant to optogenetic applications – though a brain-expressed rhodopsin has been associated with circadian function in *Drosophila melanogaster*[189].

It is also possible that brain tissue expresses chromophores that absorb green wavelengths equally or more efficiently than rhodopsin or riboflavin. However, until further studies of green light are carried out on brain tissue or cultures this cannot be determined.

Yellow-orange light

Exposures of macaque retinas to orange light (~3800 mW/mm^2 at 568 nm) for 15 minutes resulted in complete loss of retinal pigment epithelial cells in the exposed region, and intensities ~3x this value also caused cell death in the photoreceptor layer. Calculated exposure thresholds for photodamage in retina from this wavelength were an order of magnitude lower than those previously calculated by Ham *et al.* (1979) and were no different with scanned exposure at high peak intensity or continuous exposure at lower peak, suggesting that average intensity was more important. The mechanism of this damage was suggested to likely be photochemical in nature, as modelled temperature increases for the exposure were >1.5 °C[190].

Whilst this exposure was at substantially higher intensities than are normally used for optogenetics, the threshold was not precisely determined, only concluding that the previously described injury threshold for retina at this wavelength is inaccurate. The duration of exposure was brief; since photochemical damage is cumulative, a

chronically implanted optrode has the potential to cause similar effects over time. Morgan *et al*. (2008) suggest that the damage they saw may be the result of lipofuscin photooxidation, and as such the same potential hazard may exist in brain tissue[190].

Red, near-infrared and infrared light

Light approaching the upper limit of the visible spectrum is generally considered to be safe with regards to photochemical hazard; the low energy per photon combined with low level of scattering in tissue has made development of a channelrhodopsin which absorbs near infra-red (NIR) light an attractive target. The most red-shifted ChRs in nature are the RubyACRs, discovered in *Hondaea fermentalgiana,* with an action spectrum approaching 610 nm at its top-end[19]. At present, NIR optogenetic stimulation must be achieved via less direct methods, such as upconversion via fluorescent nanoparticles[149,150].

Whilst NIR light is not readily absorbed by most biomolecules, it is still capable of producing single-photon photochemical effects in a small range of molecules, including haemoglobin (though almost two orders of magnitude less efficiently than it absorbs blue light)[95]. Single-photon phototoxicity has been seen in applications using red and NIR light, though these are typically seen in optical tweezers or confocal microscopy where the intensity is much higher than those used in optogenetic applications (though at very low exposure times – on the order of 2 µs per 0.4 μm^2 pixel in one case). This photodamage has been observed to correlate with mitochondrial damage. However, unlike in most phototoxicity studies, the damage appears to be dependent on peak power rather than average intensity[191,192].

Some red and NIR wavelengths are also capable of directly exciting molecular oxygen to produce singlet oxygen with single-photon absorptions. This effect has generally been reported at the very high intensities used in optical tweezing or

microscopy, though again exposure times in these applications are much shorter than those used in optogenetics[95].

Whilst direct photochemical damage from red and NIR light appears to require very high intensities, modification of biological activity – particularly in the mitochondria – appears to occur with exposures of much lower intensity. A wide range of effects including alterations to mitochondrial morphology, DNA synthesis, redox activity and oxygen consumption have been reported at intensities between 0.48 – 3000 mW/mm^2. In neurons – which have a higher number of mitochondria than most cell types – alteration to mitochondrial behaviour could be significant[84].

Lipofuscin as a common photosensitiser in retina and brain

Lipfuscin is a type of pigment granule containing a mixture of lipid-containing residues of lysosomal digestion. These granules cannot be removed and excreted, instead accumulating in cells including retinal pigment epithelial cells and neurons[89].

Lipofuscin has been identified as a major photosensitiser in visible light damage to the retina[107]. In particular, one of the more abundant components of lipofuscin – docosahexaenoate – has been demonstrated to form oxidation products that act as potent photosensitisers[154,174,193].

Lipofuscin-derived phototoxicity can cause damage to a range of cellular components, including mitochondrial and nuclear DNA[85,153]. Mitochondria trigger the production of lipofuscin when stressed, so producing a self-driving cycle; photochemical stress to the mitochondria from lipofuscin triggers the production of more lipofuscin, making the cell more susceptible to further photochemical injury[91].

Lipofuscin levels also accumulate with age (whilst expression of antioxidants and protective enzymes decreases in retina[163]), making older animals more susceptible to phototoxicity. Since many studies use young animals (for convenience, to avoid

variation between animals that can accumulate with age, or for ethical reasons), it is possible that age is a major confounding factor in studies of phototoxicity[89].

Lipofuscin can be excited fluorescently with wavelengths ranging from 488 to 550 nm (though this range varies with lipofuscin composition, which is not consistent), and can be photobleached by these same wavelengths[193]. Photobleaching of fluorescent molecules has been directly associated with ROS generation, so light from this wavelength range is potentially hazardous to brain tissue, with an increase in risk as levels of lipofuscin accumulate[173,180].

Photo-oxidation products of lipofuscin components are often fluorescent, thus photo-oxidation of lipofuscin can increase, decrease or shift the wavelength of fluorescence in lipofuscin granules[193]. This can be seen in fluorescent microscopy, where lipofuscin autofluorescence can been observed increasing or decreasing depending on the illumination wavelength, intensity and duration[180,193].

Changes to lipofuscin autofluorescence have been associated with retinal damage, and in particular autofluorescence photobleaching in retina has been used as a diagnostic criterion for various retinal diseases[194,195]. It is likely that changes in lipofuscin autofluorescence will serve as a similar marker of photo-oxidative damage in brain tissue.

When investigating phototoxicity in brain tissue, lipofuscin appears to be a major target of interest. Because optogenetic implants are likely to be installed in older patients (primarily sufferers of Parkinson's disease, who tend to be older) and lipofuscin accumulation – and thus photochemical risk – increases with age, studies of lipofuscin-associated photodamage should use older animals where possible.

1.8.3. Optogenetics intensity requirements

Channelrhodopsins require a minimum intensity of illumination to activate; this is referred to as the “activation threshold”. Concrete values for the activation threshold of a given ChR are impractical to determine, since the intensity required to achieve an action potential depends on a combination of the efficiency of the ChR being used at the illumination wavelength, the level of expression of that ChR in the target cells, the location of ChR expression in those cells and various other factors[196].

Light propagation through brain tissue results in substantial losses with increased depth; at wavelengths between ~470-640 nm, 0.5 mm of mouse brain tissue causes approximately an order of magnitude reduction of intensity, decreasing by another order of magnitude at 1 mm and 2 mm from the emitter[12,197]. As light is scattered in tissue, lateral diffusion occurs, increasing the illuminated region such that the diameter of the illuminated region is similar to the depth of penetration[197]. Due to the much larger volume of primate brains compared to e.g. rodent models, much larger regions must be illuminated to cause behaviourally relevant effects with optogenetic stimulation[46,100,198]. To illuminate such volumes of tissue without substantially increasing the size of the optrode (and thus increasing mechanical trauma), illumination must originate from a larger distance than in organisms with smaller brains, requiring substantially higher intensity to exceed the activation threshold of the channelrhodopsin being used. As such, a ChR-expressing cell requiring a 1 mW/mm^2 activation threshold when illuminated directly would necessitate an optrode emitting approximately $100mW/mm^2$ when separated by 1 mm of brain tissue. Additional losses can be caused by factors such as nearby blood vessels or haemorrhage, as haemoglobin is a strong absorber of light in the wavelength range ~450-600 nm[12]. Because of these factors, a wide range of illumination intensities are employed across the optogenetics literature; it is thus reasonable to consider illumination intensities over 2-3 orders of magnitude when investigating phototoxic effects in optogenetic devices intended for clinical use.

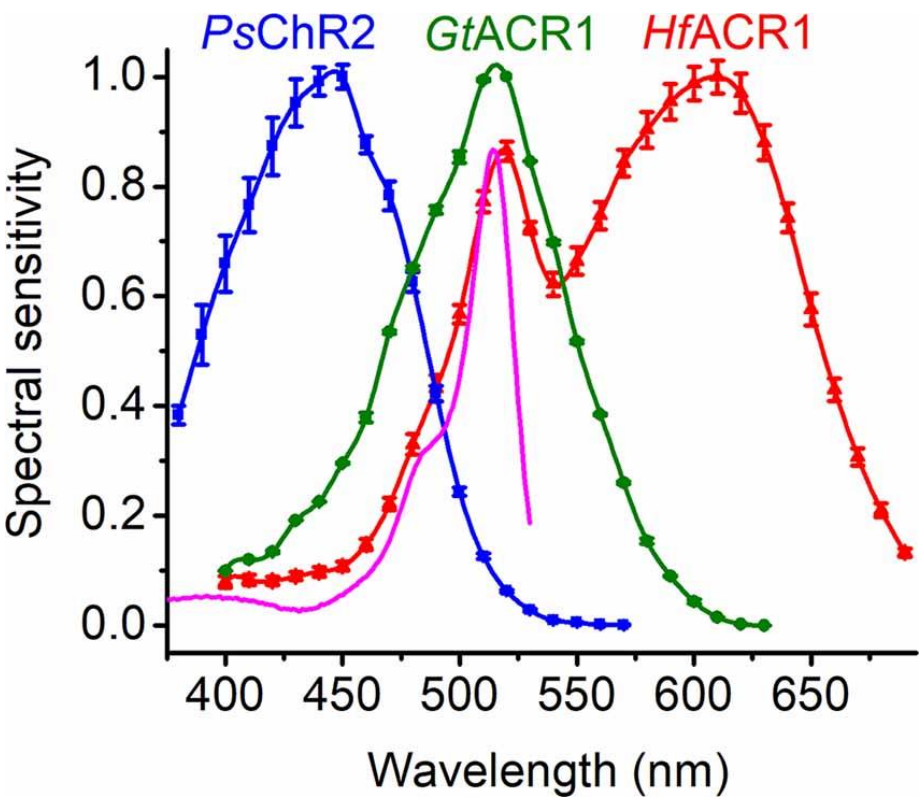

Figure 6: Taken from Govorunova et al, 2022. The action spectra of photocurrents generated by representative ChRs tagged with enhanced yellow fluorescent protein. The magenta line shows the absorption spectrum of EYFP.

PsChR2: Platymonas subcordiformis channelrhodopsin 2. GtACR1: Guillardia theta anion channelrhodopsin 1. HfACR1: Hondaea fermentalgiana anion channelrhodopsin 1.

Whilst absorption peaks of these ChRs differ substantially (~450 nm, ~510 nm and ~610 nm respectively), there is heavy overlap between the absorption spectra, meaning that in multi-wavelength applications each would be partially activated by wavelengths intended for other opsins.

Whilst great effort has been made to develop red- and blue-shifted channelrhodopsin molecules, there still exists substantial spectral overlap between the available options, with adequate spectral separation only possible from either end of the available range[19] (Figure 6). In theory, there exist natural rhodopsins with absorption peaks as high as 700 nm, though these have not yet been characterised or their chromophores identified[199]. These shifts in absorption wavelength often result in decreased sensitivity or changes to kinetics, requiring higher intensity stimulation or making them unsuitable for some applications. This spectral overlap necessarily requires short-spectrum visible light (400-480 nm) to be used if multispectral applications are required, making the phototoxic effects of blue light relevant for any such application until more wavelength-specific channelrhodopsin proteins are discovered or developed (Figure 7[200]). One recent candidate — NeoR — has been identified in *Rhizoclosmatium globosum* and has an absorbance maximum of 690 nm and a narrow absorption band (a modified variant has also been produced with an absorbance peak at 759 nm). However, NeoR has a second (albeit lower intensity) absorption band broadly around 400 nm, making its use in multispectral applications difficult. In addition, NeoR only exhibits photoreactivity when co-expressed with two other rhodopsins; RGC1 and RGC2. Further, its NIR-photoreactivity requires activation with UVA light, complicating use in optogenetic applications[201].

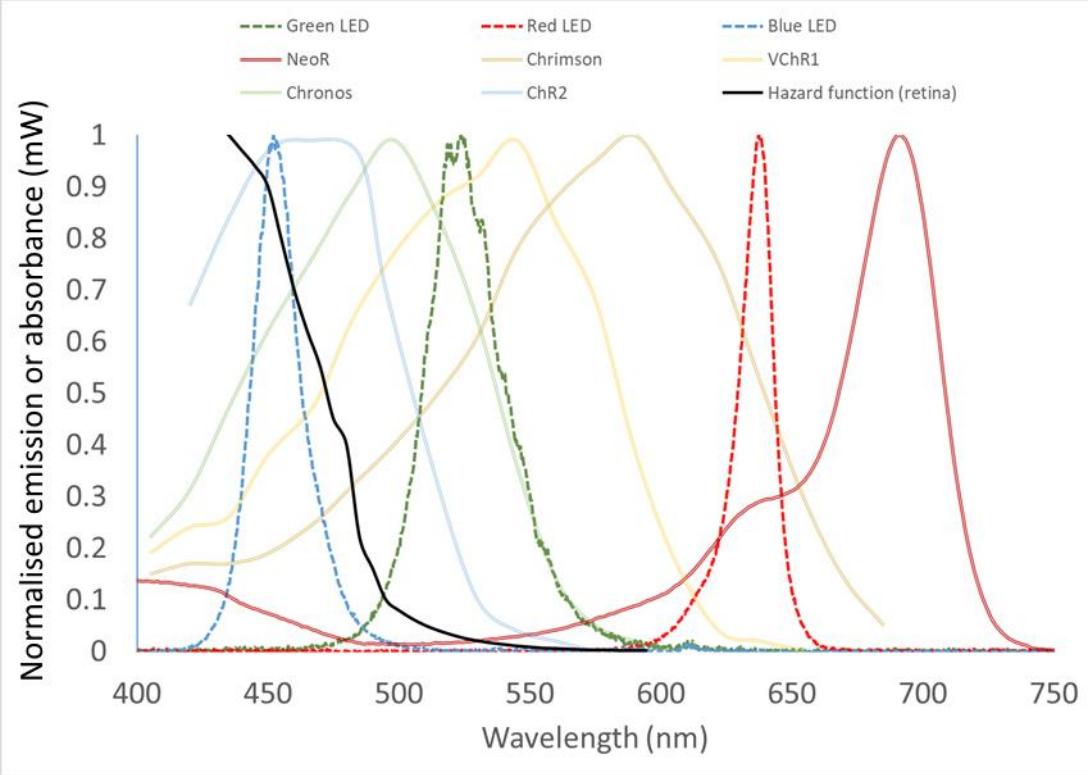

Figure 7: Normalised LED emission spectra (dotted lines) and normalised absorption spectra from a range of opsins (solid lines).

Also shown is the ICNIRP photochemical hazard function for retina (black line), indicating the normalised exposure intensity at which photochemical hazard would be expected in retina depending on wavelength.

1.8.4. Tissue damage from thermal effects

Whilst temperature increases of >3 °C can be treated as a reasonable threshold for expected tissue damage, values as high as 10 °C have been proposed in the literature[96]. Understanding of the risks of photothermal damage in tissue has evolved over the last few decades, leading to concerns that existing clinical technologies such as vitrectomy probes are at risk of causing damage to patient retinas[166].

Part of this evolution of understanding is an increased awareness of the effects of heating on tissue; cell death after heating can be substantially delayed and – as with photochemical damage - tends to be cumulative[96]. Additionally, hazards beyond direct cell death have been identified; increases in temperature below levels that would cause cell death have been demonstrated to alter neuronal function[197] including suppressing firing rates even in the absence of opsin expression at intensities within the range typically used for optogenetic applications[202].

Another potential reason for changes to our understanding of thermal damage to tissue – and in particular brain tissue – is evolution of temperature-measurement tools. In 1966, Noell *et al.* used rectal temperature readings to infer retinal temperature, assuming that retinal temperature was closely related to general body temperature. Since then, our understanding of energy confinement and thermal transfer through tissue has developed; local temperature of very small areas of tissue can rise substantially higher than that of bulk tissue if more energy is added to that region than can leave in a given time period[96].

Common methods for measuring temperature increases in tissue include thermocouples (which must be physically inserted into the sample close to the target region and are sensitive to temperature changes in the millimetre resolution) and thermal imaging cameras (which require unobstructed line of sight to the stimulated area and have a resolution of approximately 50 µm). Neither of these methods can measure localised temperature increases inside living brain tissue after insertion of

an optrode, though thermal imaging is capable of measuring at the brain's surface[203]. More recently, temperature-sensitive fluorescent nanoparticles have been used to measure temperature increases at a high spatial and temporal resolution[203].

Induced heating with light exposure is used clinically to destroy precise target regions of tissue without harming surrounding healthy cells. For example, transpupillary thermotherapy uses red lasers to locally heat tumour or vascular lesions, causing temperature increases to ~45-65 °C. Generally, this method is used in conjunction with more conventional chemotherapy or radiotherapy[107,204,205]. The intensity used in these treatments far exceeds that used in optogenetics, however.

Several models of heating in optogenetic applications have been developed; both *ab initio* computational models (Monte Carlo simulations of random photon movement through homogeneous media approximating brain) and empirical models using data from animal models to predict temperature changes more closely under different lighting conditions. The accuracy of such models can be skewed by the effect of vascularisation (which can affect both light scattering and remove heat via blood flow), variation in brain tissue density and structure and the presence of the optrode itself (since most experimentally-derived models use optical fibres to deliver light to the target area, which will have different optical and thermal properties to an optrode implant)[206,207]. These models also tend to be developed using mouse tissue, which can differ from human brain in many respects.

Two-photon illumination in optogenetics experiments has the potential to induce heating due to high intensity light, however strategies to reduce this effect have been proposed, including short illumination times, reduction of pulse frequency and more sensitive opsins. Temperature-sensitive fluorescent nanoparticles were used to measure temperature increases at a high spatial and temporal resolution[203].

Most studies of photothermal effects in brain have been carried out in mice using optical fibre delivery of light. Optrode-delivery of light in deep brain regions of primates must account for heat emission of the optrode itself, as well as substantially higher intensities of light needed to illuminate sufficiently large areas of tissue. Heating effects are thus of substantially more concern when considering optogenetic devices for clinical application.

Temperature generation during optogenetic stimulation is reliant on several interconnected factors; photon energy (wavelength), absorbance of the target tissue, pulse duration and frequency and intensity of exposure. Simulations have predicted increases in a range from 1-4 °C at an intensity of 10 mW, depending on wavelength and illuminated area[206], and studies of laser illumination of brain tissue at 445 nm, 0.6-16 mW showed increases in temperature of up to ~6 °C in all conditions[208]. Pulse durations longer than 100 ms have been observed to cause substantial heating, as thermal energy cannot dissipate sufficiently rapidly through the tissue to avoid temperature increases[202].

Experimental investigations of photothermal effects in brain have reached widely variable outcomes. Some studies have shown histologically visible tissue damage from exposures of infrared light (1000-3000 nm) at intensities ranging from 0.3 to 0.66 J/cm^2, though these values were obtained under a range of pulse patterns[209,210] – other studies have detected no damage at substantially higher values[211]. One study observed that ~318 mW/mm^2 of 450 nm light increased temperature by an average of 6.35 °C (e.g. >43 °C *in vivo*), well above the ~40 °C threshold for damage[207] - another showed <0.9 °C increases at intensities as high as 600 mW/mm^2, and observed that the heating effect is the same for all conditions where the product of the intensity and duty cycle are the same – which aligns with the same observation for photochemical hazard[100].

Due to the wide range of wavelengths, duty cycles, intensities and other conditions used in these studies, there is no clear relationship between these variables and induced temperature increases in brain tissue. It is clear, however, that photothermal effects can and have been observed under conditions representative of optogenetic applications, and as such care must be taken to ensure that chronic temperature increases remain below ~3 °C by controlling duty cycle, pulse duration and intensity.

1.9. Optrode design considerations

High light intensity is typically achieved using laser illumination or high-power LEDs coupled to optical fibres. These fibres can have diameters as small as common DBS electrodes (~100-400 µm). Most optical fibres used in optogenetic applications have blunt tips that cause substantially more tissue trauma than equivalent-diameter electrodes[12], though there has been success in producing sharp optical fibres in more recent studies[51,198]. Whilst multi-fibre arrays have been developed to overcome this issue, this makes avoidance of blood vessels more difficult and effectively produces a greater number of insertion trajectories, increasing the potential for mechanical trauma and hardware failure. Additionally, incorporating such optical fibres into clinical optogenetic devices would require external LED light sources with bulky heat-sinks. Since optrode size is a critical factor in their development as medical devices, a balance between illumination intensity, heat generation and size is required.

LED light sources use a variety of semiconducting materials to produce different wavelengths of light – alternatively, phosphor coatings can be employed to absorb one wavelength (usually blue) and emit the desired wavelength. Different semiconductor chemistries are more or less efficient, allowing larger amounts of light to be emitted with lower input current. Whilst theoretically most LEDs can be made to emit intensely enough for optogenetic applications, increased current produces greater thermal losses. As such, it is desirable to use efficient LED wavelengths to avoid the need for large heat-sinks, reduce possible thermal trauma and allow for use

of smaller LEDs to reduce implant size. In 2012, LEDs produced by Philips were most efficient in red and blue, followed by red-orange, cyan and green (Table 2)[212].

Colour	Wavelength range (nm)	Typical efficiency coefficient
Red	620 < λ < 645	0.39
Red-orange	610 < λ < 620	0.29
Green	520 < λ < 550	0.15
Cyan	490 < λ < 520	0.26
Blue	460 < λ < 490	0.35

Table 2: LED colours and efficiency coefficients as produced by Philips, 2012.

Since 2012 higher-efficiency LEDs have been developed however red and blue remain the most efficient wavelengths that are commercially available, though a wide variety of novel chemistries and designs have been trialled experimentally. Efficiency values are typically obtained in laboratory environments where the LED is kept cool, and as such lower efficiencies can be assumed in the insulating, warm environment of the brain.

1.10. Measuring mechanical properties of mouse brain

1.10.1. Why measure brain mechanical properties?

Many cell types are sensitive to the mechanical properties of their environment, or alter their own properties in response to external factors. Fibroblasts alter their gene expression – including production of extracellular matrix components – in response to mechanotransduction of tension, expression and shear forces through cytoskeletal and adhesive structures[213,214]. Similarly, cancerous cells have been observed to both respond to and modify the mechanical properties of their surroundings, affecting their ability to metastasise[215]. Pathological errors in mechanotransduction can lead to conditions such as tissue fibrosis, myopathies, developmental disorders and atherosclerosis[215]. It is becoming increasingly clear that most cell types are influenced in one way or another by their mechanical environment[216].

External insults (such as traumatic injury, radiation or chemical exposure and metabolic challenge from toxins) can trigger cells to modify or interact differently with their mechanical environment. Glial scarring in the brain has been demonstrated to result in a reduction of tissue elastic modulus that has downstream effects on neural regeneration[217]; radiotherapy causes increased elastic modulus, nuclear size and F-actin fibre accumulation in human umbilical vein endothelial cells[218]; and chemotherapeutic drugs are capable of altering cancer cell stiffness, morphology, roughness and adhesion[219]. Similarly, the mechanical properties of the cell substrate (usually the extracellular matrix, but often observed *in vitro* on synthetic hydrogels) have been shown to influence the behaviour of cells grown on them[220–222].

In the context of optogenetic brain implants, these mechanosensory pathways are relevant to a number of design considerations; implant diameter affects the size of the wound channel and the magnitude of strain that is applied to tissue surrounding the insertion path[126], implant coatings can affect cellular responses to chronic implantation[223–226] and the high rate of revision (e.g. repositioning in the case of an off-target implantation, side effects or malfunction) of deep brain stimulation implants

risks a high level of mechanical disruption of tissue[65]. Identifying the mechanical factors that affect brain tissue during and after optrode implantation can contribute to a better understanding of the overall impact of these devices on patient health in an acute and chronic timeframe.

1.10.2. Mechanics of biological tissues

Biological samples present a set of particular challenges and characteristics that affect mechanical measurement.

Firstly, almost all biological materials are “viscoelastic”; when they are deformed, they respond with a combination of “viscous” and “elastic” behaviour. In a perfectly elastic (“Hookean”) material, deformation in response to a stress and relaxation (return to original dimensions after removal of a stress) are almost instantaneous; they happen at the speed of sound in that material. The *elastic* (or “storage”) component of viscoelasticity describes elements of the biomaterial that store energy when deformed and recover their original shape — releasing the stored energy — when the strain imposing the deformation is removed (unless the material is deformed beyond its plastic threshold). The *viscous* (or “loss”) component of viscoelasticity describes elements of the biomaterial that resist and delay deformation via frictional forces, causing that energy to be lost in the form of heat[227].

In simple terms, this means that when a stress (a force) is applied to a biomaterial, the resultant change in shape will be delayed and some thermal energy released. When the stress is removed, the material will return to its original shape after some delay.

When measuring purely elastic materials, time is a relatively unimportant factor (because all strains can be assumed to occur immediately). In viscoelastic materials, time is an important variable because the delay caused by the viscous component

can provide information about the molecular structure and interactions in the material.

Since most models for viscoelasticity assume that the material is in the linear regime (i.e. where the response of the sample is linearly correlated with the stress put on the sample), measured values tend to only be predictively useful if measured under small strains[228]. Practically, the definition of a “small strain” varies from sample to sample but should usually be <1% - that is, the strain should be smaller than 1% of the total dimension of the sample in the direction of load[229,230]. In practice, extensions of 10% are considered normal in mechanical exploration of brain tissue[231], with some values going as high as 60%[232,233]; there is no broad consensus on the maximum acceptable strain.

Most biomaterials experience strains much larger than 1% during normal function. It is important to remember that whilst values for storage or loss moduli obtained at larger strains may usefully reflect real-world scenarios, they are unlikely to be *accurate* when using models that assume small strains are being applied.

Since water is commonly a large component of biomaterials, it is commonly assumed that the “Poisson’s ratio”† of biomaterials is 0.5, the same as water – that is, that the material is incompressible. Dehydrated samples or those with unusual fibrous arrangements or cavities may not follow this assumption.

Mechanical properties of most materials usually vary with temperature; at higher temperatures both the storage and loss moduli of the material will typically decrease, with the storage modulus decreasing at a higher rate; the material becomes more fluid-like. At lower temperatures materials tend to become stiffer, with elastic

† The ratio at which stretch of a material in one dimension changes its other dimensions; essentially, how much thinner a material becomes as it is stretched in a perpendicular direction.

properties increasing more quickly than viscous; the material will behave more like a Hookean material. Whilst most materials follow this general trend, specific properties of a given material may alter its mechanical relationship with temperature. For example, at temperatures higher than ~40 °C, protein denaturation and other thermochemical effects alter the structure of biological tissues, tending to cause a permanent increase in stiffness[234].

It is generally recommended to measure biological materials at physiological temperatures; this range provides the most relevant data for normal functioning of the tissue. In a biological material, temperature change may influence hydration, conformation and chemical bonding/interaction, introducing or removing relaxation processes in unpredictable ways. Data collected from biomaterials at different temperatures are thus incomparable.

Almost all biomaterials are non-isotropic; their structure and organisation means that their mechanical properties will vary depending on the direction of the stress applied[235,236]. Unless a sample is highly disorganised (and measurements are sufficiently gross in resolution that local variation of structure is irrelevant), care should be taken that sample orientation is consistent across measurements and that this is specified in published data.

1.10.3. Definitions of mechanical properties

Young's modulus

Equivalent terms: Elastic modulus, storage modulus, stiffness, elastic component, E'

Inappropriate terms: Hardness, strength, geometric stiffness, toughness.

Unit: Pascals (Pa)

Young's modulus describes the force per unit area required to deform a material linearly (i.e., through extension or compression). It uses the Pascal as a unit, which represents force per unit area. Young's modulus is a very commonly published value for biomaterials and is often referred to as the "stiffness" of the material.

Changes in stiffness of tissue may block or encourage cell migration (or metastasis), act as a mechanical signal to up- or down-regulate factors, provide increased durability to a tissue (for example in scar tissue), may be an indicator of changes in tissue hydration or of changes in tissue organisation (more highly organised tissue tends to be stiffer).

Young's modulus can be measured directly using extension or compression equipment, stretching or squashing a sample and measuring the resistive force. It must be separated from the viscous component of such resistance.

In an isotropic material, Young's modulus values can be derived (or in a non-isotropic material such as most biomaterials, can be approximated) from indentation experiments using mathematical formulae that account for the geometry of the indenter, or from shear modulus values obtained from rheology or similar techniques.

Young's modulus and shear modulus can be converted between each other provided the Poisson ratio of the material is known:

$$G = \frac{E}{2(1+v)}$$

Where G = shear modulus, E = Young's modulus and v = Poisson's ratio.

This means that in most biomaterials (where the Poisson's ratio is 0.5[237]), the Young's modulus is 3x the shear modulus.

Energy that is expended to deform a purely elastic material is stored as potential energy in interatomic bonds in the material. In a viscoelastic material the elastic component is referred to as the "storage modulus" (E') because it represents energy stored in interatomic bonds.

Bulk modulus

Equivalent terms: K, B, Volume modulus

Units: Pascals (Pa)

This value represents a material's resistance to compression from all directions. Water is commonly described as an incompressible fluid. This is not strictly accurate; water (and other fluids) will compress if surrounded by sufficient force‡.

‡ The bulk modulus of water is approximately 2.2GPa, meaning that it must be surrounded by approximately 22MPa of force on all sides to compress by 1% of its volume.

Nevertheless, the bulk modulus of water (and most solids) is too high to be meaningfully relevant in investigations of biomaterials in most cases; it is mentioned here to clarify this point and to disambiguate the term.

Shear modulus

Equivalent terms: G', S

Units: Pascals (Pa)

The shear modulus measures the force required to deform a sample in the plane of two opposing forces across the sample (effectively "skewing" the sample). It represents the force required to "skew" a sample by an angle in radians from its original position; since this angle is a dimensionless number, shear modulus has the same units as Young's modulus[238].

Similarly to Young's modulus, shear modulus in a purely elastic material represents energy stored in interatomic bonds in the material, and in a viscoelastic material represents the "elastic component" of the measured forces as the "shear storage modulus" (G').

The shear modulus is of interest for the same reasons as the Young's modulus; it is simply another method of obtaining similar information. As with Young's modulus measurements, sample orientation is important when measuring shear modulus.

Shear modulus values are commonly obtained via use of a plate-plate rheometer. Whilst these instruments will often report a Young's modulus value derived from the shear modulus, it is important to recognise that in a biological material this is often inaccurate due to anisotropy.

Viscosity

Equivalent terms: E” (for linear viscosity), G” (for shear viscosity), loss modulus, η, μ.

Inappropriate terms: Thickness.

Units: Pascal-second (Pa·s)

The viscosity of a material represents the material’s resistance to deformation in response to a stress due to frictional forces in the material, at a given strain rate.

Energy that is expended to deform a purely viscous material is released as heat. In a viscoelastic material the viscous component is referred to as the “loss modulus” (E”) or “shear loss modulus” (G”) because it represents energy lost as heat[238].

Complex modulus

Equivalent terms: Dynamic modulus, G*

A measure of material stiffness (overall resistance to deformation, whether elastic or viscous) obtained from the ratio of stress to strain under vibratory conditions. The complex modulus is a combination of storage and loss moduli.

Phase angle

Equivalent terms: δ, phase shift

Units: Degrees (°)

A measurement of how much the phase of the strain (response) curve in a dynamic (vibratory/oscillatory) experiment lags behind the stress (input) curve. This value acts as a descriptor for how “elastic-dominant” or “viscous-dominant” the material is. A low value (closer to 0°) indicates that the strain occurs quickly in response to stress; the

elastic structure of the material is intact and dominates the response. A high value (closer to 90°) indicates that there is a large lag between the stress and the strain, characteristic of a material with dominant viscous effects or whose elastic structure has failed and is undergoing plastic deformation[238].

Loss tangent

Equivalent terms: Tanδ

The ratio of loss modulus to storage modulus in a dynamic (vibratory/oscillatory) experiment. A higher value indicates more damping by the viscous component and a lower value indicates less damping. A value above 1 indicates that damping effects exceed storage effects and below 1 the opposite[238].

This is of particular interest in “frequency sweep” experiments; as the frequency of oscillation between 0 and maximum strain approaches the relaxation period of a specific component of the material, that component’s ability to damp energy increases, peaking when the frequency matches its relaxation rate.

In a complex viscoelastic composite (such as many biomaterials) this allows identification of different components and their contribution to the viscous properties of the material: as the frequency sweep approaches the relaxation period of each component, a stepped increase in the loss modulus is seen.

1.10.4. Types of mechanical measurement

Transient experiments

Transient experiments apply a single stress or strain to a sample and measure the response. These experiments have the advantage of being very simple and requiring less specialised equipment than dynamic experiments, but at the disadvantage of providing less information about the properties of the sample.

The two most common types of transient experiment are the “creep” experiment and the “stress-relaxation” experiment.

In a “creep” (or “cold flow”) experiment, a sample is loaded with a constant stress and the change in strain over time is observed; this displays a curve demonstrating the delay in strain caused by the viscous component of the material.

The simplest example of a creep experiment is to hang a weight (providing a constant stress) off the sample and to observe lengthening of the sample over time.

In a “stress-relaxation” experiment, a constant strain is applied to the sample, applying as much stress as is required to maintain this strain. Initially, this stress will be very high (as both the elastic and viscous component of the sample will resist the strain) however over time the contribution of the viscous component will reduce.

Different parts of the sample with different viscosities will contribute a characteristic “relaxation period” to this curve; in a transient experiment the resulting stress-relaxation curve is a function of all of these individual relaxation processes combined.

Dynamic experiments

In a dynamic experiment, stress or strain (most commonly strain) is applied to a sample in an oscillatory fashion – usually a sinusoidal curve, as this is relatively simple to process mathematically.

These experiments have two major uses:

- **Separating viscous and elastic contributions:** At the point of highest strain rate (i.e. the moment when the change in strain per unit time is highest – this is usually the point on the curve where strain is zero), the viscous component of the sample is at its maximum.

At the point of lowest strain rate (i.e. at the peak of the curve, when the sample has been extended to maximum strain), the elastic component is at its greatest. Because of this, dynamic experiments allow both contributions to be separated from each other – often, rheology software will do this automatically.

- **Identifying individual relaxation processes:** When the period of the oscillation is very short, there is insufficient time for any relaxation process to take place in the sample. The sample behaves more like a glassy, Hookean solid when the frequency of the oscillation is very short.

As the oscillations become longer, the amount of relaxation a given process can undergo increases, up to a maximum of the relaxation period of that portion of the sample. Because of this, dynamic experiments can be set up to gradually increase or decrease the frequency of oscillation (“frequency sweep” experiments); when the frequency matches the relaxation time of a process, a “step” in the viscous component can be observed in the data, since that process cannot contribute any more to the energy loss to viscous processes.

From this type of experiment, it is possible to identify the range of relaxation processes occurring in the sample (though care must be taken, since processes with a substantially similar relaxation time may not be distinguishable from each other).

This is especially valuable in biomaterials, which contain hundreds or thousands of components that could contribute to the sample's viscoelastic behaviour.

In a dynamic experiment, the phase angle or loss tangent can be used to describe whether the material behaves more like an elastic solid or a viscous fluid. Typically, biomaterials will have a value somewhere between these two points, with a combination of elastic and viscous elements.

1.10.5. Methods for mechanical measurement of biological tissues

There are a wide range of techniques and experimental setups that can be employed to measure the viscoelastic properties of biomaterials. These methods vary in how directly they measure these properties, their spatial resolution, cost and whether they are capable of transient experiments, dynamic experiments or both.

Shear (Plate-plate) rheology

This method employs two surfaces ("geometries") between which the sample is placed. The distance between geometries is calibrated such that axial load (compressive force between geometries) is very low and the sample is trimmed so that it does not protrude beyond the geometries.

The sample is deformed via rotation of the geometries relative to each other; the fact that the sample has been trimmed to the same size as the geometries allows precise strains to be applied (by rotating the geometries a precise amount). The resistance forces exerted on the geometries are measured via a force transducer on the device's spindle[238].

The geometries vary substantially in size, shape and surface treatment; many are textured to improve friction between the sample and testing rig. Larger geometries are needed for softer samples, since this will increase the measured shear modulus sufficiently to be in the detectable range. Similarly, some geometries are optimised for measurement of particular sample types or purposes (such as the “cone and plate”, which generates a uniform shear rate across the sample)[239].

Compared to some of the other methods described below, plate-plate rheology requires large sample volumes. Care should be taken when deciding sample orientation and interpretation of the results; values obtained from such equipment are from shear loads and cannot usually be directly translated into linear elastic values given the anisotropy of biomaterials. If samples are to be compared, their orientation should take into account structures such as fibres so that measurement conditions are consistent between samples[240].

Plate rheology has an advantage over indentation-based methods since the latter relies on mathematical models (such as Hertz, Sneddon or Maugis) that assume measurements are taken in the linear regime (with small deformations). Plate rheology is not subject to this restriction and thus measurements taken at larger deformations can be used more readily (whilst still taking into account anisotropy and the risk that large deformations may cause plastic deformation or otherwise alter the viscoelastic behaviour of the material)[241,242].

Indentation, nanoindentation and atomic force microscopy

These methods calculate mechanical properties by pushing a probe of known dimensions into the sample and measuring the resistance forces. Probes are available in a wide range of shapes including sharp (pyramidal), cylindrical, conical, colloidal (spherical) or flat. The main difference between the three methods is the scale of the probe; indentation probes may be on the order of millimetres wide, micro- or nanoindenters fractions of a millimetre and atomic force microscope probes

are available ranging from micron scale spherical probes to nanometre-diameter sharp tips[243–248].

Since material is not displaced in a solely axial direction, sample anisotropy can have substantial effects on the results of these experiments; a highly organised biological sample may resist deformation substantially more in one dimension than another, and since indentation experiments displace in all directions to various degrees this must be taken in to account.

Different probe geometries use different mathematical calculations to produce elastic modulus values; a limitation when analysing biological samples is that these equations usually assume isotropic samples of infinite thickness. Interferences can arise from inhomogeneous samples, thin samples or samples mounted on a surface of substantially higher stiffness (for example plastic or glass culture plates).

Sharp indenters are often unsuitable for soft biological samples; they tend to penetrate the sample with very little resistance and thus provide little sensitivity. It is generally recommended to use colloidal indenters for particularly soft tissues such as brain, though this will impair spatial resolution; a compromise is needed.

Depending on the strain applied, plastic deformation of samples is common during indentation; small strains and larger probes should be used to avoid this and to keep strains in the linear range as much as possible.

AFM indentation methods are not capable of carrying out dynamic experiments, however creep and strain-relaxation experiments are common. Conventional micro- or nano-indenters (such as ferrule-top indenters) may have this capability however. The main advantages of these techniques over plate-plate rheology is that most of the force applied is axial (offering a more direct calculation of elastic modulus compared to the shear values obtained from the latter) and that spatial resolution is

orders of magnitude higher; an atomic force microscope can be used to obtain values from sub-micron regions of a sample, allowing mapping of a sample's elastic modulus by taking hundreds or thousands of readings in a grid.

Force spectroscopy maps equip the researcher with the ability to both acquire low spatial resolution readings that give a general picture of bulk stiffness and viscosity (by taking the mean storage and bulk modulus of each point in a region) and to map variation in these properties at high resolution.

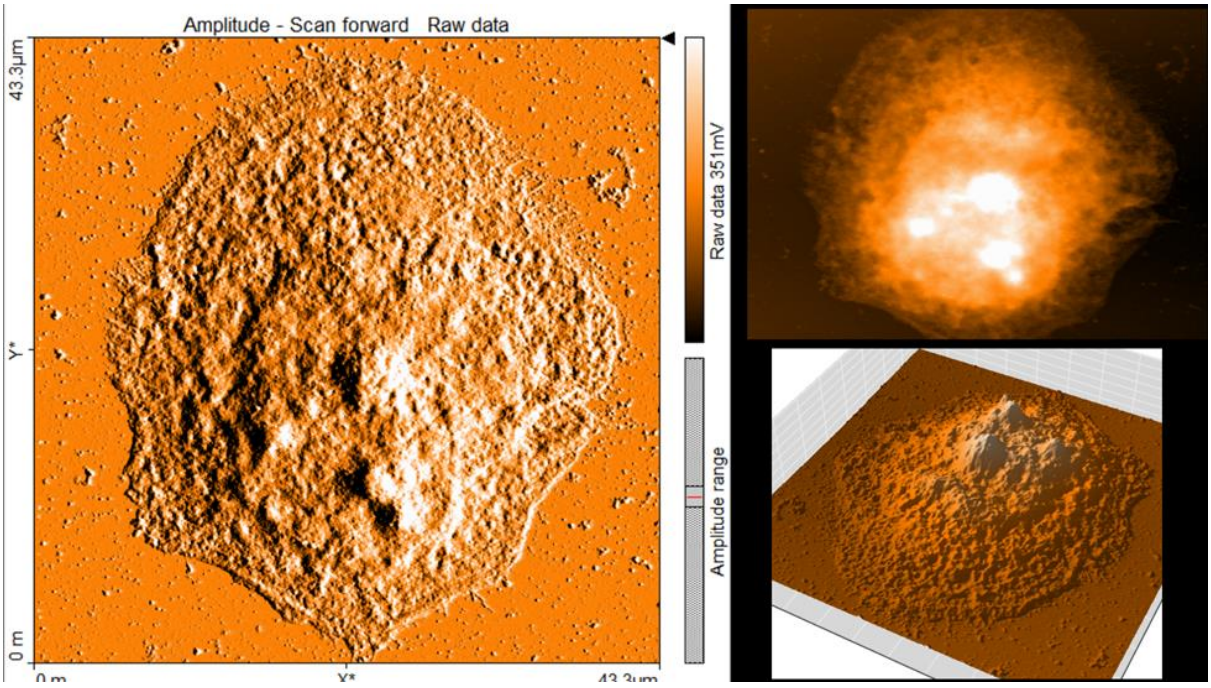

Figure 8: Topographical images of U2-OS Fucci cells on a Nanosurf AFM instrument. Cells were fixed in methanol and dehydrated with hexamethyldisilazane.

Impact indentation

Impact indentation is also sometimes referred to as "dynamic" indentation. This terminology can be confusing, as unlike the "dynamic" experiments carried out in shear rheology, these experiments do not impose strains in an oscillatory manner, instead applying a single deformation at a high strain rate. In these methods, a probe is used to deliver a transient force to a sample and afterwards is allowed to move freely[249,250].

Typical impact indentation setups include a probe mounted on a low-friction pivoting pendulum. The probe can have forces delivered to it via an electromagnet, allowing it to be accelerated to a specific speed (and therefore force) without a mechanically-coupled force transducer.

After the probe has impacted the sample, the displacement of the pendulum over time and changes in volume to the sample can be measured to provide information about the hardness of the sample at the relevant impact speed, as well as the ability of the material to dissipate energy. The elastic modulus of the sample can also be calculated.

Magnetic resonance elastography

Magnetic resonance elastography (MRE) is a non-invasive technique that is capable of high spatial and temporal resolution. It uses rapid magnetic resonance images synched to rapid, low-amplitude vibrations of a sample, tracking waves of deformation through the sample to calculate viscoelastic properties[251].

Typical frequencies of vibration are in the hundreds to low thousands of hertz, with amplitudes of tens to hundreds of microns. These vibrations were originally transduced through the skull of the subject (originally mice) via direct coupling (via an embedded pin or cyanoacrylate adhesive on the exposed skull) – this was determined to be too invasive and the majority of MRE experiments now use a mandibular connection (essentially a mouthguard-type device inserted into the subject's mouth, transducing the signal through the jaw). This is substantially less invasive, less stressful for the subject and lends itself better to longitudinal studies.

MRE has several other advantages: the high frequency makes measurement of elastic modulus easier since viscous processes do not dominate the reactive forces (though conversely this may result in limited viscous data), the technique is applicable to live subjects and an entire brain may be imaged at once. Additionally,

due to the mandibular signal transduction, samples must always be oriented in the same direction relative to the scanner, increasing consistency of measurements between laboratories.

Disadvantages include the inability to measure from other orientations and high cost; the magnetic resonance instruments required to image small animals typically cost hundreds of thousands of dollars (or more, depending on supplier), are expensive to operate (due to cryogen costs, electricity and maintenance), require a dedicated laboratory space (due to the size of the instrument and the risk of magnetic interference with other devices) and the additional MRE equipment is still in its early stages of development and thus must either be manufactured in-house or purchased from a very limited number of suppliers.

Hydration measurements

Whilst not a direct method of measuring viscoelastic properties, hydration measurements are often used to *imply* relative stiffness of samples. It is generally true that tissues with a higher level of (bound, static) hydration tend to be softer; low-hydration tissues such as cartilage and bone are much stiffer than – for example – muscle or fat, which have high levels of hydration[252–258]. Fluctuations in tissue hydration due to age or disease lead to alterations in the tissue's mechanical behaviour, for example stiffening of muscles and tendons due to age[259–261].

Highly hydrated tissue also demonstrates more prominent viscous behaviour as demonstrated in creep[255,262] and stress relaxation tests [259,263].

Similarly, a given tissue will become stiffer as it is dried out; this can be readily demonstrated by taking a tissue sample and dehydrating it completely. The original sample will be pliable and soft, whilst the dehydrated sample will be brittle and hard.

Hydration measurements cannot be used to compare the stiffness of two different tissue types; the presence of different proteins and other structural components makes such comparisons useless. It can however be used to compare two samples from the same type of tissue that have undergone a treatment (for example, a drug-treated muscle sample and a control sample of the same muscle).

In these situations, both samples are dried slightly (sufficient to eliminate surface-bound water and free-flowing water, both of which can introduce error), weighed at high precision, dried fully over the same timeframe and then weighed again. Any difference in hydration is *relative* (and thus does not reflect the absolute hydration of the tissue) and may indicate a difference in stiffness.

These measurements are ideally used as an initial method of comparison between samples to indicate whether further investigation is warranted; the technique is inexpensive, quick and requires essentially no reagents and very little equipment. It cannot however be used alone to claim mechanical differences.

Chapter 2. General Methods

2.1. Literature search: Mechanical properties of healthy mouse brain

The following keywords were used for the literature search. Words in brackets indicate that the search was carried out with said word included and omitted. Quotation marks and a slash between two words indicates that these words were both used in the displayed context in separate searches. Papers were searched for with the “review only” settings on and off, if available. “AND” operators were used to ensure that studies were relevant to mouse models only (e.g. “[Term] AND Mouse”) and “OR” operators were applied in order to make the search more rapidly by searching for multiple terms simultaneously. To avoid potential issues with formatting, some terms were used in fragments (e.g. where a slash or hyphen is present in a term, multiple searches might be carried out with variations on the term: “BALB”, “BALB C”, “BALB-C” etc).

- Mouse / murine
- C57BL/6
- BALB-C
- ICR
- CD-1
- Brain
- Mechanical (properties)
- (“Elastic / shear / storage / loss”) (modulus)
- (“nano / micro / dynamic / impact”) indentation
- (“shear / plate”) rheology
- MRE
- (“Magnetic resonance / Shear wave”) elastography
- “Cortical / Cortex”
- “Cerebellar / Cerebellum”
- “Hippocampal / Hippocampus”
- Stiffness
- Fixation
- (Para)formaldehyde
- Formalin
- PFA
- Deformation
- Strain (“% / percentage”)
- Frequency
- Tan“δ / delta”
- Viscoelastic(ity)
- aCSF

2.2. CRL2541 astrocyte culture

CRL2541 mouse cerebellar immortalised astrocytes were obtained from ATCC (catalogue no. C8-D1A). They were cultured in T75 polystyrene culture flasks using Dulbecco's modified Eagle's medium (DMEM) supplemented with 10% foetal bovine serum (FBS) and penicillin/streptomycin at 100 I.U/ml concentration.

Cells were passaged at 90-100% confluence. The flask was emptied of medium and washed gently with phosphate-buffered saline. Trypsin enzyme was warmed to 37°C in a water bath and ~1ml was introduced to the flask and incubated in a 37°C incubator for ~3 min or until cells were loosened. Cells were detached with gentle tapping of the flask, and 6 ml of DMEM/FBS was added to inactivate the trypsin. Cells were centrifuged for 4 min at 650 g and the supernatant discarded. The pellet was resuspended in DMEM/FBS and distributed among fresh T75 flasks as required.

For storage, aliquots of CRL2541 were stored at <-130°C via liquid nitrogen. Frozen cells were suspended in 80% FBS + 10% DMSO.

CRL2541 cells were not cultured beyond P12.

2.3. CRL-2541 cell-derived ECM

2.3.1. ECM production

CRL-2541 cells were cultured in matrix medium (High-glucose Dulbecco's modified Eagle medium [DMEM] supplemented with 10% foetal bovine serum, 100 U/ml penicillin 100 µg/ml streptomycin and 50 µg/ml L-ascorbic acid sodium salt [Sigma]) on either coated (with either 0.2% gelatin or 5 µg/ml fibronectin [Sigma] for 1 h at 37 °C) or uncoated (to facilitate later removal of ECM) 35 mm polystyrene culture dishes until 80% confluent.

After 12-18 hrs, medium was carefully aspirated from cells and replaced with fresh matrix medium with ascorbic acid increased to 50 µg/ml. Half of the medium was replaced with freshly made matrix medium containing 100 µg/ml ascorbic acid every two days to achieve a total of 50 µg/ml ascorbic acid, for a total of 9 days.

2.3.2. Decellurisation

When ECM had grown to >10 µm thick (~ 9 days), medium was carefully aspirated and dish was rinsed twice with DPBS- (Dulbecco's phosphate-buffered saline lacking CaCl2 and MgSO4), placing the pipette against the dish wall to minimise damage to the ECM and discarding the DPBS- after rinsing.

Cells were removed with pre-warmed (37°C) extraction buffer (Dulbecco's phosphate-buffered saline, Ca++ and Mg++ free; containing 0.5% Triton X-100, 20 mM NH4OH) and lysis observed using an inverted light microscope. Sample was incubated at 37°C until no intact cells could be seen (~3 to 5 min). Cellular debris was diluted with 2-3 ml DPBS− and left overnight at 4 °C. Debris was partly aspirated and re-diluted three times, avoiding drying of the ECM.

ECM was treated with 1 ml benzonase solution (7ul benzonase [Sigma] in 1000ul 10mM TRIS buffered saline) for 30 min at 37 °C. Samples were then washed twice with DPBS+ (Dulbecco's phosphate-buffered saline containing 1 mM CaCl2, 1 mM MgSO4) and were stored in DPBS+ supplemented with 100 U/ml penicillin, 100 µg/ml streptomycin and 0.25 µg/ml amphotericin B (Sigma) at 4 °C until use.

2.4. Mice

Four strains of mouse were used: unmodified C57BL/6, unmodified CD-1 (tissue from these mice was taken from *ex-vivo* animals immediately after sacrifice under a tissue sharing agreement – sacrifice was carried out via cervical dislocation by the Newcastle University Comparative Biology Centre), HALO (a mouse genetically modified to express a halorhodopsin/enhanced yellow fluorescent protein fusion in

cre recombinase expressing cells[264]) and EMX-ChR (a mouse genetically modified to express a channelrhodopsin/enhanced yellow fluorescent protein fusion in cre recombinase expressing cells[265]).

EMX-ChR mice express cre recombinase in approximately 88% of the neurons of the neocortex and hippocampus, and in the glial cells of the pallium[264].

HALO mice have been bred such that cre recombinase expression is primarily limited to pyramidal neurons, however since male cre-expressing mice have been used for subsequent maintenance of the line it is possible that cre recombination in germ cells may have impacted the cell-specificity of this expression (resulting in expression in non-target cells in addition to pyramidal neurons)[266].

For CD-1 Mice, All animals were handled in accordance with ethics approved by the UK Home Office Animals Scientific Procedures Act 1986. However, given that mice did not undergo a ‘procedure’ as defined by the Act, the project did not require Home Office Licensing. The reason for animal use was instead approved and governed by Newcastle University’s Comparative Biology Centre Ethics Committee; Study Plan Reference Number 699; AWERB Approval Reference Number 663. Tissue in this project was waste tissue from other experiments. Mice were originally purchased with funds from a MRC Career Development Award to Dr. Suzanne Madgwick [MR/T010789/1].

For other mice, all experiments were performed in accordance with the Animals (Scientific Procedures) Act 1986 and with protocols and guidelines approved by the Institutional Animal Care and Use Committee (UvA-DEC) at Newcastle University operating under standards set by EU Directive 2010/63/EU and was performed in accordance with appropriate guidelines. This study is reported in accordance with Animal Research: Reporting In Vivo Experiments (ARRIVE) guidelines. Efforts were made to only use the necessary number of animals. The reason for animal use was

approved and governed by Newcastle University's Comparative Biology Centre Ethics Committee; AWERB Approval Reference Number 712.

Effort was made to use mice intended for culling (either for population reduction or when animals were exceeding breeding age) where possible, following the "three Rs" principles. As such, animals ranged from 2-12 months in age - depending on the reason for culling – and both male and female mice were used. Animals were all healthy, housed in a 26 ± 2 °C room with food and water ad libitum.

2.5. Mouse brain dissection

Schedule 1 procedure was carried out via cervical dislocation, followed immediately by decapitation. Fine, sharp-tipped scissors were used to cut the scalp sagittally from the neck to the nose, exposing the skull. The skull was first cut across the bridge of the nose followed by a cut from the rear of the skull to the nose. Fine tweezers were then used to snap the top of the skull away, exposing the brain. Finally the brain was removed with a spatula, scooping from the hindbrain and taking care to not apply pressure to the cortex.

Removed brains were placed immediately into chilled cutting solution bubbled with carbogen whilst slicing was prepared.

2.6. Acute brain slice preparation

Slices were prepared and handled as described by Papouin and Haydon[267]. Briefly, the brain was trimmed with a scalpel and adhered to the cutting platform with cyanoacrylate adhesive, taking care to not compress the tissue. The cutting platform was inserted into the tissue slicer (either a a Campden Instruments Vibroslice vibrating-blade tissue slicer or a Leica VT1200S vibratome) and covered in near-frozen cutting solution bubbled with carbogen. The vibratome was set to a frequency of 65-70 Hz with 0.75-1 mm amplitude (in the Leica instrument; the Vibroslice cannot adjust amplitude) and an advance speed of approximately 0.1 mm/s.

Slices were taken coronally (from approximately the septo-striatal to caudal diencephalon[268]) at the desired thickness and trimmed with a scalpel to isolate the cortex, before being transferred to a recovery chamber containing aCSF bubbled with carbogen at room temperature (20-22 °C) for 45 min.

2.7. Artificial cerebrospinal fluid (aCSF)

300 mOsm/l aCSF consisted of 2 mM $CaCl_2$, 1 mM $MgCl_2$, 126 mM NaCl, 2.6 mM $NaHCO_3$, 3.5 mM KCl, 1.26 mM NaH_2PO_4, 10 mM glucose.

400 mOsm/l aCSF consisted of 2.66 mM $CaCl_2$, 1.33 mM $MgCl_2$, 168 mM NaCl, 3.46 mM $NaHCO_3$, 4.66 mM KCl, 1.68 mM NaH_2PO_4, 13.33 mM glucose.

Solutions were checked with a freezing-point osmometer to confirm their osmolarity. For both 300 mOsm/l aCSF and 400 mOsm/l aCSF, their pH was 7.4. To produce ChABC-supplemented aCSF, 0.1 unit/ml ChABC (Scientific Laboratory Supplies, C2905) was added to 300 mOsm aCSF.

For cutting, $CaCl_2$ was omitted and $MgCl_2$ was increased to 3 mM. Cutting solution was cooled until partially-frozen and mixed into a slush immediately before cutting.

2.8. Western blotting

For western blotting, tissue was homogenised with an ice-cold Dounce homogeniser containing lysis buffer (RIPA) supplemented with freshly prepared phosphatase and protease inhibitors (Complete, Roche), and centrifuged at 13,000 g at 4°C for 10 min. Then, 5× sample buffer was added to the supernatants and was boiled at 100°C for 5 min.

Protein samples were run on SDS-PAGE using a standard protocol and were transferred to nitrocellulose membrane using Mini Trans-Blot® apparatus (Bio-Rad). The blot was blocked in 3% bovine serum albumin (BSA) for 1 h and incubated overnight with primary antibody.

Primary antibodies used were: tubulin (Abcam, ab6160), vinculin (Cell Signaling Technology, #13901), p53 (Sigma Aldrich, P5813), cleaved caspase-3 (Cell Signaling Technology, Asp175) and GFAP (Abcam, ab222279).

After washing twice with TBST (TBS containing 0.05% Tween-20) for 15 min each and once with TBS for 10 min, the blot was incubated with the corresponding secondary antibodies for 1 h. This was again followed by washing the blot in TBST and TBS as earlier, and the proteins were then detected using an iBright® Western Blot imaging system (Invitrogen) after incubation with chemiluminescence substrate for 5 min.

Secondary antibodies used were: Abcam goat anti-rat HRP-conjugated - ab97057, Abcam goat anti-rabbit – ab6721, Abcam goat anti-mouse - ab6708, Abcam paired detector antibody ab222279.

2.9. AFM nanoindentation measurements

Sample elastic modulus was measured using atomic force microscopy (Nanosurf FlexAFM instrument). Unless otherwise specified, a spherical probe with a diameter of 10 µm and spring constant of 0.01 N/m was used, with a maximum force of 700 pN and a loading rate of 2 µm/s.

For a spherical indenter, the following Hertz model is commonly used [269]:

$$F = \frac{4}{3}\frac{E_a}{1-\nu^2}\sqrt{R}\delta^{3/2} \qquad (1)$$

where F is the reaction force of the indenter, δ is indentation depth, and v is Poisson's ratio. E_a is the apparent cell modulus as a rigid indenter was used. R is the radius of the spherical indenter. However, the Hertz model only works for very small strains without adhesive contact between indenter and material. When indenting very soft tissues like brain, it is necessary to have a relatively large indentation depth (or

strain) relative to the probe tip diameter to eliminate the surface roughness effect of tissue slices. Furthermore, adhesive contacts were evident. Therefore, data analysis was done by combining Sneddon's model for the sphere[270] and the Maugis' model of adhesive contact[269], as shown in equation (2). Curve fitting was performed using the open source software AtomicJ software[271].

$$F = \frac{3aK}{2}\left(\frac{R^2+a^2}{4a}\ ln\frac{R+a}{R-a} - \frac{R}{2} - \sqrt{\frac{8\pi aw}{3K}}\right) \qquad (2a)$$

Where F is the indentation force, w is the Dupre energy of adhesion, a is the radius of contact, R is the tip radius.

K is given by:

$$K = \frac{4}{3}/\left(\frac{1-v^2}{E} + \frac{1-v'^2}{E'}\right) \qquad (2b)$$

Where v and v' are the Poisson's ratio for the sample and indenter, respectively. The E and E' are the Young's modulus of the sample and sample and indenter, respectively. As the indenter used is 6 orders of magnitude stiffer than the brain tissues tested, the equation (2b) can be reduced to:

$$K = \frac{4E}{3(1-v^2)} \qquad (2c)$$

For brain tissue, it is reasonable to assume that its Poisson's ratio is close to 0.5[237].

In principle, soft tissues like brain also exhibit viscoelastic characteristics. Therefore, we also attempted to use a Prony series model for soft tissue viscoelasticity to account for stress-relaxation of the tissue during the loading period[272] using in-house developed Python code. However, indentation curves were too noisy for high quality curve fitting, with substantially higher failure rate for the curve-fitting and a greatly lengthened processing time per curve. Furthermore, for the curves successfully fitted,

the results are similar to those determined using the elastic model. This suggests that the viscous effect is not very significant in the test conditions of this study.

2.10. Primary mouse astrocyte isolation – original and improved protocols.

2.10.1. Original protocol

Tissue was placed in an appropriate volume (1-2 ml) of 0.05% trypsin and Hank's buffered salt solution (HBSS). Using a Pasteur pipette, tissue was gently dissociated by pipetting up and down for 15 mins. Sample was then centrifuged at 400 g for 5 mins, the supernatant discarded and fresh 0.05% trypsin HBSS solution was added. The sample was resuspended and allowed to dissociate for 15 mins before being centrifuged again at 400 g for 5mins.

The supernatant was discarded and the pellet resuspended in HBSS containing 0.01% benzonase, incubating at RT (~20-22 °C) for 30-40 min. Supernatant was collected and centrifuged at 400 g for 7 min, resuspended in DMEM/F-12 with 10% FBS (Thermo Fisher) and plated in a T75 culture flask. Medium was changed after 24 hrs, and then every two days afterwards for 2 weeks total. From the third week onwards, FBS concentration was increased to 20%.

2.10.2. Improved protocol

Tissue was cut into small pieces with a sterile scalpel and incubated in 0.05% trypsin in HBSS for 15 min at 37 °C. Trypsin was aspirated gently and replaced with 5 mg/ml papain solution (Sigma), incubating at 37 °C for 15 min. Samples was gently washed twice with sterile HBSS with 0.01% benzonase, removing as much fluid as possible between washes whilst not disturbing the settled tissue. Tissue was resuspended in 3 ml DMEM/F-12 and triturated 30 times up and down with a 25 ml pipette, repeating with a 10 ml and 5 ml pipette. Sample was resuspended in DMEM/F-12 and plated in a T75 culture flask. Medium was changed after 24 hrs, and then every two days afterwards for 2 weeks total. From the third week onwards, FBS concentration was increased to 20%.

2.11. Tissue hydration measurements

After acute brain slice preparation, samples were immersed in either 300 mOsm, 400 mOsm or cABC-supplemented 300 mOsm aCSF. Samples were incubated for 0.5, 1.5 and 4 h, then pooled into pre-weighed weighing boats and excess aCSF wicked away gently with a soft-bristled paintbrush. Slices were weighed before being air-dried at 37°C for 48 h and weighed again. Hydration was calculated from the wet and dry values.

To establish whether a 48 h drying time was sufficient, test samples were dried at 37°C and weighed twice daily until no further weight change was observed (this was achieved at ~32 h. A safety factor was added, resulting in the final 48 h drying time used).

2.12. Tissue swelling measurements

Acute brain slices were immersed in the appropriate aCSF formulation and bubbled with carbogen. A frame was mounted above the plate to allow a camera to take images at a fixed distance. The carbogen supply was briefly removed when taking images, to avoid disruption from bubbles. Images were taken every 0.5 h for 4 h. XY area of the slices measured using Fiji image analysis software[273], and converted to approximate volume by raising to a power of 3/2 based on the assumption of isotropic swelling.

2.13. Acute brain slice light exposure

After the recovery period, acute mouse brain slices were transferred to a perfusion chamber held at 37°C, in which aCSF bubbled with carbogen was flowed continuously over and around them. Slices were placed on microscopy lens tissue to permit passage of aCSF on all sides.

A 400 µm diameter glass optical fibre was brought to the surface of the slice via a stereotactic holder, aided with a widefield microscope. When the tip of the fibre contacted the meniscus of the aCSF, it was retracted until the moment that the

meniscus broke contact, providing headroom for slices to swell during the experiment without physically contacting the fibre.

Slices were exposed to 470 nm light emitted by a Thorlabs M470F3 fibre-coupled LED. At the distance used, emitted light was approximately collimated with an approximate incident spot size of 400 µm. Total light intensity at the tip of the fibre was measured via an integrating sphere. Slices were illuminated with 0, 6, 9 or 12 mW total emission, with a pulse length of 100 ms and a 50% duty cycle for 1 h. Some slices were illuminated with different intensities, wavelengths, pulse patterns or durations (as noted in the relevant results section).

2.14. CRL2541 astrocyte light exposure

CRL2541 immortalised mouse cerebellar astrocytes (ATCC) were cultured until ~90% confluent. Medium was aspirated, washed off with phosphate buffered saline (PBS) and replaced with aCSF bubbled with carbogen immediately before light exposure.

Cells were exposed to 470 nm light at 12 mW via the bottom of polystyrene petri dishes to minimise risk of contamination. A 400 µm diameter optical fibre delivered the light, contacting the bottom of the dish at 90° to the dish surface. Cells were exposed for a range of durations with either a 50% duty cycle (100 ms pulse length) or continuously. After exposure, aCSF was aspirated off, washed with PBS and replaced with serum-free DMEM to arrest cell division.

Cells were allowed to rest in the incubator for various times before staining with Live/Dead Fixable NIR and fixation with ice-cold paraformaldehyde for 15 min. Cells were then washed with distilled water for 3 min, air-dried and mounted under cover slips with ProLong Glass Antifade Mountant with NucBlue (Thermo Fisher Scientific).

Dishes were imaged using a Zeiss AxioImager upright fluorescent microscope with Colibri 7 illumination source, 10x (NA 0.3) and 20x (NA 0.8) objectives and a Flash4 camera. Images were acquired with Zeiss blue software.

2.15. Tissue & cell fixation, mounting and staining

Acute brain slices were fixed with 4% paraformaldehyde in PBS for 15 min at 4°C before sectioning and mounting, with the exception of samples visualised with live stains, which were either not fixed or were fixed after staining (see specific protocols).

After fixation, slices were immersed in 30% sucrose in PBS until they sank in the solution, indicating that it had fully perfused the tissue.

Slices were cut into 30 µm thick sections with a Leica CM1900 cryostat (-16°C; tissue was embedded and frozen in a 50/50 mixture of 30% sucrose in PBS and OCT cutting solution prior to cutting) before being mounted and air-dried on Epredia SuperFrost Plus adhesion slides. Samples were rehydrated in staged ethanol dilutions (100, 80, 50, 0%) in Tris-buffered saline (TBS) for 10 min per stage before staining.

CRL2541 cell samples on Fisherbrand Unbreakable cover slips (made from pressed polyvinyl chloride) were fixed with 4% paraformaldehyde for 15 min at 4°C. Cells were stained on the cover slips and mounted to Epredia SuperFrost slides after staining.

2.15.1. TUNEL staining

Cells were stained with Abcam TUNEL Assay Kit - FITC ab66108, following the manufacturer's instructions.

Tissue sections were stained with a modified protocol; TBS was supplemented with 0.1% TWEEN 20 detergent (TBS-T)_ for rehydration steps, and reagents were

introduced to samples via micropipette in 40 µl volumes and incubated in a humidity box to prevent desiccation.

TUNEL-stained samples were mounted using ProLong Diamond antifade mountant.

2.15.2. DAPI staining

Samples to be stained with DAPI were either immersed in a 1 µg/ml solution of DAPI stain in a Coplin jar for 20 min, or were incubated with 40 µl of the same solution in a humidity box for the same duration. DAPI staining was performed after all other stains had been applied.

2.15.3. Autofluorescence suppression treatments

Samples that utilised autofluorescence suppression were treated with either Sudan black B (solvent black 3), eriochrome black T or potassium permanganate.

Sudan black B was prepared at 0.3% in 70% ethanol. The solution was dissolved on an orbital shaker for 3 hrs and was centrifuged at 3000 RPM for 30 mins to remove clumps before use. Samples were incubated in the solution for 10 min and washed in TBS-T for 5 min.

Eriochrome black T was prepared at 1.65% in DI water and samples incubated for 5 min before washing with TBS-T for 5 min.

Potassium permanganate was prepared at 0.06% in DI water and samples incubated for 10 min before washing with DI water for 5 min.

2.15.4. FFPE sections: rehydration

Formalin-fixed, paraffin embedded (FFPE) tissue samples were rehydrated before staining. Paraffin was removed via 2x 10 min washes in xylene, followed by

rehydration in staged dilutions of ethanol in TBS-T (100, 95, 85, 75, 50%, 3 min each) followed by a 5 min incubation in TBS-T.

2.15.5. Antigen retrieval

FFPE sections were subjected to antigen retrieval after rehydration and prior to staining. Slices were immersed in 1x citrate buffer (0.1 M, pH 6, 0.0825 M sodium citrate dihydrate, 0.0175 M citric acid, 0.1% TWEEN-20 in DI water) and heated in a microwave until boiling was initiated. Slices were then allowed to cool for 30 min.

2.15.6. General antibody staining protocol

Slices and cell samples were generally stained with the following protocol, adjusted to fit specific stains as required. Steps were either carried out in Coplin jars or applied in ~40 µl volume via pipette in a humidity tray:

- 3x dH2O, 5 min, room temperature.
- Blocking (TBS-T/5% normal goat serum OR 5-10% BSA), 1 hr, room temperature.
- Primary antibody in diluent and concentration recommended by manufacturer or determined in-house, overnight at 4°C.
    - 4-hydroxynonenal (Abcam, ab46545): 1/500
    - p53 (Cell Signalling Technology, #9282): 1/1000
    - Phospho-Histone H2AX (Cell Signalling Technology, #9718): 1/1000
    - Cleaved caspase-3 (Cell Signalling Technology, #9661): 1/1000
    - 8-OXO-DG (R&D Systems, 4354-MC-050): 1/1000
- 3x TBS-T, 5 min.
- Secondary antibody in diluent and concentration recommended by manufacturer or determined in-house (typically 1/2000), 1 hr, room temperature.
- 3x TBS-T, 5 min.
- 1x dH2O, 5 min.

- Air-dry and mount (ProLong Gold, ProLong Diamond or Histomount depending on stains used).

2.15.7. Fluoro-jade C staining

Avantor fluoro-jade C ready-to-dilute staining kit was used for brain tissue sections, following the manufacturer's instructions.

Fluoro-jade C stained samples were mounted using ProLong Gold.

2.15.8. Propidium iodide staining

In fixed cells/tissue, propidium iodide was applied as a nuclear counterstain at a concentration of 100 µg/ml for 20 min, followed by a wash in TBS-T for 5 mins.

In living cells/tissue, propidium iodide was introduced into growth medium/oxygenated aCSF at a concentration of 100 µg/ml and allowed to incubate for 20 min before live-imaging.

2.15.9. Calcein-AM (green and orange) staining

Calcein-AM (Thermo Fisher, C34852 green and C34851 red-orange) vials were diluted in 50 µl DMSO to produce a 1 mM stock solution. 2 µl of this stock solution was added to 1 ml oxygenated aCSF to produce a 2 µM solution that was used within 1 day. Samples were incubated for 10-60 min and returned to aCSF without calcein-AM for 15-60 min before imaging.

2.15.10. Live/Dead Fixable NIR staining

Live/Dead Fixable NIR stain (Thermo Fisher, L34975) vials were diluted in 50 µl DMSO to produce a 1 mM stock solution. 1 µl was added to 1 ml oxygenated aCSF to produce a working solution. Samples were transferred from the perfusion chamber into this solution and incubated for 30 mins at 4°C before paraformaldehyde fixation.

2.16. Fluorescence microscopy

Widefield fluorescence images were obtained using a Zeiss AxioImager upright fluorescent microscope with Colibri 7 illumination source, 10x (NA 0.3) and 20x (NA 0.8) objectives and a Flash4 camera. Images were acquired with Zeiss blue software.

Confocal images were obtained using a Leica SP8 DLS confocal microscope with HyD detectors, 10x (NA 0.4), 20x (NA 0.75) and 40x (NA 0.55) objectives and Leica Las X software. To ensure images were comparable, samples were imaged with identical settings unless otherwise indicated.

2.17. Optical coherence tomography

300 µm-thick acute mouse brain slices were chilled to 4°C on ice immediately after light exposure and transported to the OCT instrument (Thorlabs Ganymede). Samples were placed in a black weighing boat filled with chilled, oxygenated aCSF and scanned as quickly as possible to avoid tissue swelling.

Chapter 3. Mechanics of Healthy Mouse Brain Tissue in the Literature: A Systematic Review

Whilst inclusion of healthy controls is generally recommended in any experiment involving biological tissues, there is also a place for reference data in the literature; these numbers enable researchers to identify when their work substantially differs from established values due to experimental error, unusual samples or differences in analytical methodology.

Data on healthy brains can be incorporated into *in silico* models: simulations of traumatic brain injury are increasingly valuable both in academia and in industry (for example in the design of more effective impact-resistant helmets for sports and hazardous environments). Without accurate data on the viscoelastic properties of brain these simulations cannot be developed.

Measurements of healthy brain also highlight differences between measurement techniques, animal strains, sex, age and other potential confounding factors.

A review was carried out of existing data for elastic modulus of healthy mouse brain in the scientific literature with the goal of assessing the consistency with which various factors are reported or controlled for. The following factors are discussed: animal strain; age; sex; size of mechanical strain and frequency used; sample temperature and orientation; and the medium in which samples are immersed during storage and measurement, along with their potential impact on the data and comparability between studies.

This review focuses on studies concerning mouse brain since this is the species with which I carried out my experiments during this project. A variety of other species are commonly used in brain mechanics experiments including porcine, bovine and rat brains. It is important to note that brain does not have equivalent mechanical properties between species – for example human brain has been measured as 29-

40% stiffer than porcine brain[274]. In addition, larger brains are often treated very different to those from mice prior to measurement; it is common practice to acquire such tissue from abattoirs, with delays of hours or days after death before measurements are taken – during which time the tissue is often stored whole in unoxygenated iced water or buffer rather than oxygenated artificial cerebrospinal fluid (aCSF), allowing substantial degradation of tissue condition prior to measurement[236,237,250,274–277]. Due to the large potential variability in measurements of brain from different species handled in this manner, it was judged that limiting review to a single species would be appropriate.

For some techniques or variables there is a paucity in available data, so only limited conclusions can be raised.

Much of the data were extracted from published graphs via use of "WebPlotDigitiser"[278] when raw data are not readily available. Whilst this will have produced some numerical inaccuracy, variation from the original data is very small. Accuracy of WebPlotDigitizer depends on several factors; the resolution of the image in pixels (higher resolution means it is possible to more precisely indicate the centre of a point on the graph), the dimensions that are depicted on the axis (small variations in larger numbers are less significant) and whether the axis are linear or nonlinear (a nonlinear scale such as a log scale will exaggerate error).

Values from Figure 13 were extracted from an image of the graph (3225 x 2411 px) with WebPlotDigitizer and compared to the original data. Several points in the original graph were sufficiently similar to each other that they differed by < 1px and were indistinguishable; the extracted value was duplicated for each of these points for purposes of comparison. X-axis values differed by an average of 0.048 ± 0.65 Hz on a scale of 500 to 2000 Hz (in the worst case where the variation is largest, this would be less than 0.087% of the smallest X-axis value on that graph), and a paired T-test comparing the original X values to those obtained from WebPlotDigitizer output p =

0.77, indicating that the values are not significantly different. Similarly, Y-axis values differed by an average of $2.3^{e-5} \pm 6.63^{e-4}$ degrees (a maximum of ~0.25% variation from the smallest Y value) and a paired T-test comparing the original Y values with those obtained from WebPlotDigitizer output p = 0.89, indicating that the Y values are also not significantly different.

These results indicate that WebPlotDigitizer is capable of extracting data from graphs at extremely high precision provided the user is careful to precisely place each point correctly.

A total of 24 studies that reported values for elastic modulus and other mechanical properties was found[231,251,276,279–299] – a full search methodology is included in Chapter 2.

3.1. Elastic modulus

Reported elastic modulus values for healthy mouse brain vary by several orders of magnitude across the literature, from 0.03 to 105.4 kPa[291,295] (Figure 9). Magnetic resonance elastography produces the highest mean value across all studies[251,279–284,286,287,296] (29.5 ± 17.4 kPa), followed by dynamic indentation[231,298,299], nanoindentation[289–297] and shear rheology[276,288], whose mean values are in relative agreement (3.6 ± 2.3 kPa, 1.7 ± 7.3 kPa and 1.5 ± 1.1 kPa respectively). The chief reason for the large discrepancy between MRE and the other methods is likely to be the substantially higher frequency at which these measurements are made – discussed below.

The large range of values within each method points to a lack of standardisation in animal properties, sample handling, measurement method and environmental conditions between studies.

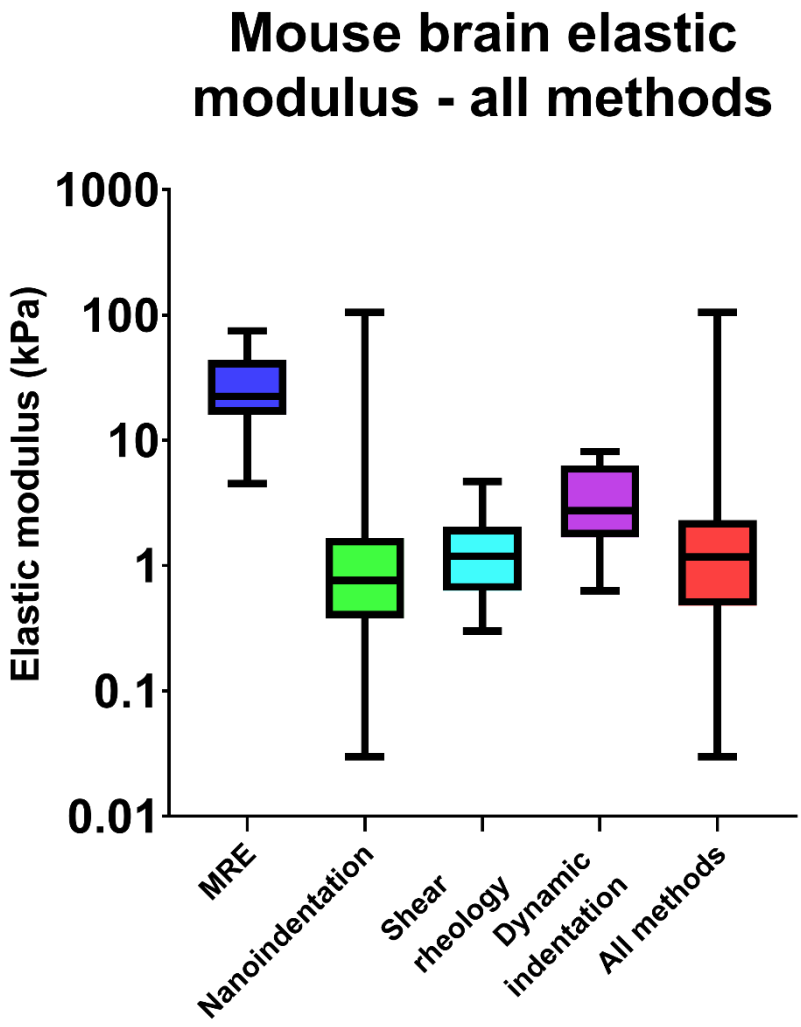

Figure 9: Elastic modulus values for healthy mouse brain vary substantially across the literature.

3.2. Mouse strain

The strain of mouse used in viscoelastic experiments is variable; C57BL/6 black laboratory mice are the most common model, however BALB/c albino and ICR mice are also used (Table 3[231,251,276,279–299]). Whilst the differences between these subspecies have not been explored, more concerning is the number of studies which neglect to state the mouse type they use at all, or that use the term “wild type” – a phrase that means little without knowing the type of mouse being used.

	MRE	Plate rheology	Nanoindentation	Dynamic indentation	Total
C57BL/6	6	1	5	0	12
BALB/c	2	0	0	0	2
ICR	0	0	2	0	2
Unknown	2	1	2	3	8

Table 3: Distribution of mouse strains used for mechanical studies across the literature.

There are few data available that would allow comparison of viscoelasticity in different mouse strains – certainly insufficient to state definitively that significant differences exist – however this also means that the risk of such differences cannot be discounted and that data from different or unreported strains cannot be directly compared in an absolute sense; only relative comparisons can be made and even then only whilst acknowledging that different strains may respond differently to a given treatment.

Whilst there is not a large enough dataset available to make conclusive statements on the effect of mouse strain on storage modulus, values taken from C57BL6 and

BALB/c mice do seem to have different viscoelastic properties; if a simple linear regression is carried out on each mouse strain, a two-tailed T-test comparing the slopes of the resulting curves returns $P < 0.0001$, indicating that the slopes are significantly different. It is likely that the slopes would be better fit with a more complex regression, however given the small number of frequency values for the C57BL/6 mice a simple linear regression was judged more appropriate. Figure 10 shows that C57BL/6 appears to have a much more pronounced increase in storage modulus as frequency increases; the BALB/c curve is substantially flatter[251,279–284,286,287,296]. From this graph it can also be surmised that the two values reported as coming from “wild type” mice are likely to be C57BL6 – though insufficient values are available to test this statistically. Data are unlikely to differ due to methodological differences, as MRE experiments are carried out on live sedated mice (avoiding error from tissue damage and sample handling) and MRE devices tend to be extremely similar, with little variability in structure or design.

Since mouse strain is often neglected in viscoelasticity studies, there is a need for further investigation into potential differences between mouse strains.

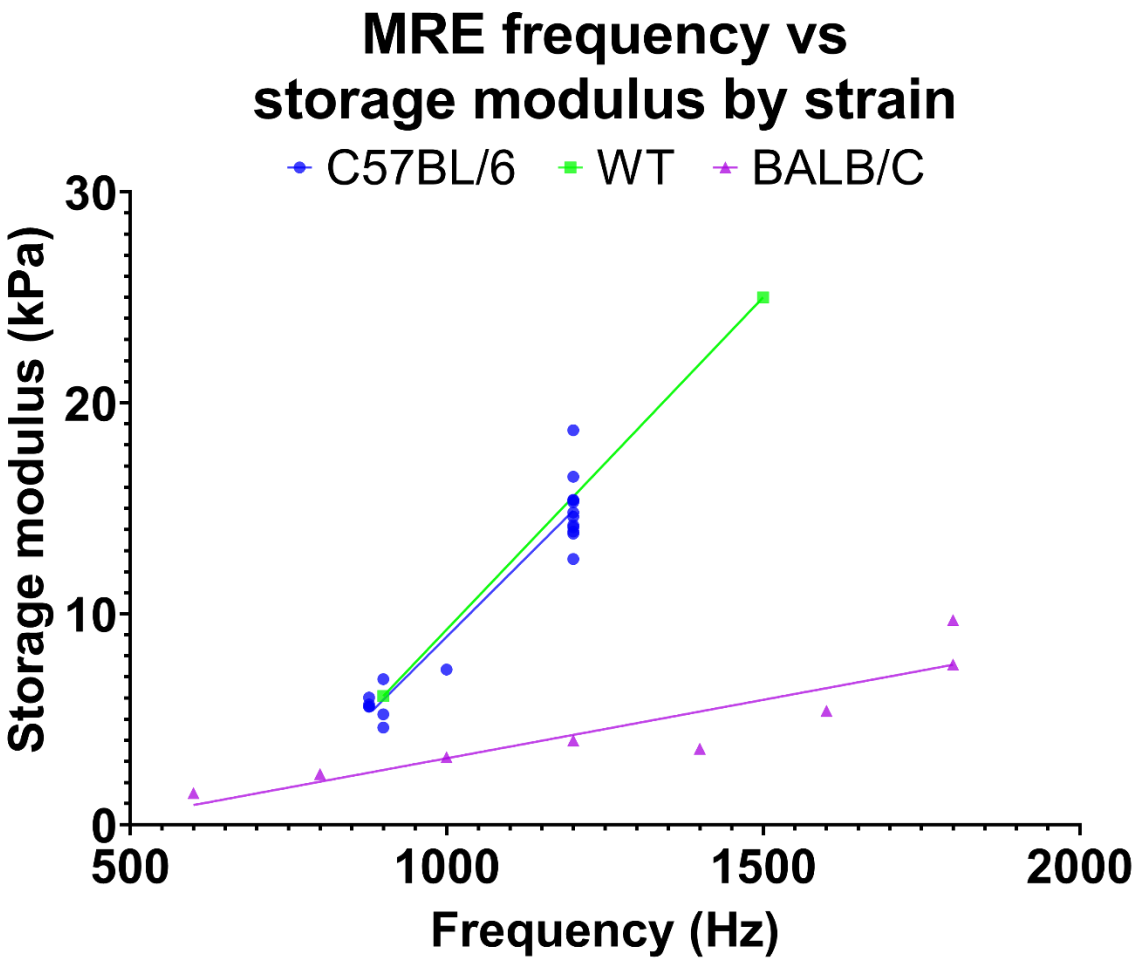

Figure 10: Storage modulus of healthy mouse brain samples increases with measurement frequency in MRE experiments. C57BL/6 brains appear to be stiffer overall than BALB/C mouse brains, and have a more pronounced increase in storage modulus with frequency.

3.3. Age

Animal age has been demonstrated to be a major factor affecting brain viscoelasticity in other species; thus, it is important to keep in mind when comparing data from the literature that the age of mice used can vary significantly and may lead to substantial differences in measured stiffness.

The National Institute on Aging (USA)'s strain information[300] states that 75% of C5BL6 mice reach 22-24 months of age (median lifespan 21.5 months). BALB/c mice have widely variable lifespans, with pronounced sexual dimorphism[301]; a lack of consistency in mouse strain and sex reporting makes correlation of age with viscoelastic differences in brain tissue difficult to predict.

Mean animal age across the papers investigated (with mice from different experimental cohorts counted separately) is 5 ± 6.17 months; the high variation being due to the very large range of ages used (embryonic mice were in this case recorded as 0.1 months). Ages ranged from embryonic to 26.1 months. No clear trend of stiffness can be seen with mouse age; it is likely that the other confounding variables described in this review make extracting such a trend near impossible (Figure 11[231,251,276,279–299]).

Out of the 24 studies examined, 9 did not report the age of one or more mouse cohorts.

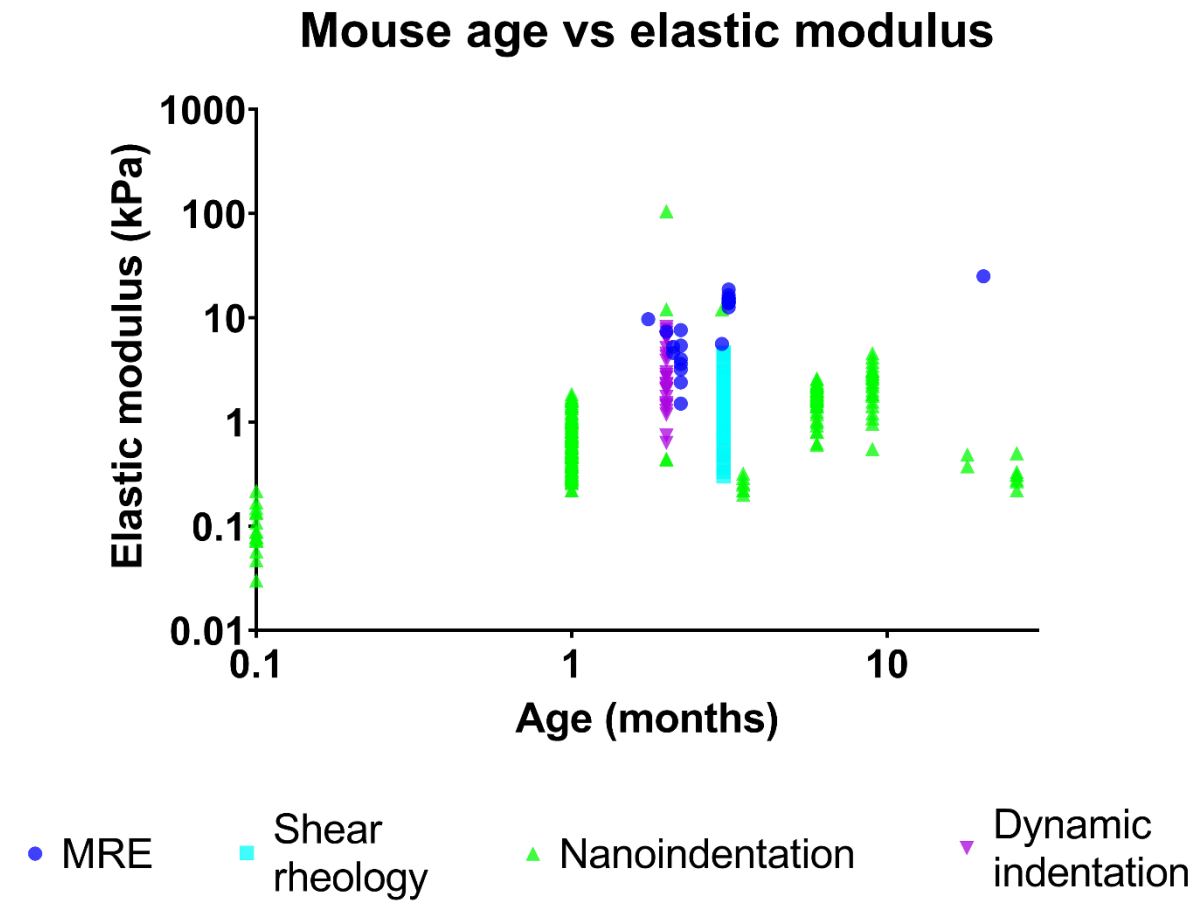

Figure 11: Age of all mouse cohorts plotted against their elastic modulus. No clear relationship of age to elastic modulus can be discerned - likely due to confounding factors.

3.4. Mechanical strain

The size of strain that is appropriate when investigating brain viscoelasticity depends on the topic under study and the method being employed; if the goal of a study is to investigate brain at the extremes of *in vivo* performance – some studies use values as high as >40%[237,302] – then it may be desirable to employ large strains. If one is not interested in the *largest* strains that brain might experience, but instead *common* strains, substantially lower values may be warranted; a study investigating the effects of injury or collision may warrant larger strains than one looking at the effects of – for example – age-related cognitive decline in the absence of traumatic injury.

If the method being employed to measure viscoelastic properties employs a model reliant on small strains – such as the very common Hertz or Sneddon models – then deformation should be kept below 1% where possible.

MRE employs very small strains that were – in all papers discussed – less than 1%. Shear rheology does not mathematically rely on strains being small. Nanoindentation and impact indentation, however, require small strains to remain within the linear regime.

Whilst shear rheology is not reliant on models assuming linearity, it is important to be aware that at high (approaching 50%) strains in very soft nonlinear samples, the measurement can change the mechanical properties of the sample[303,304].

Despite these limitations, many of the nanoindentation, AFM and impact indentation studies in the literature regularly employ strains of 2-14%[231,292,293,296] or do not report the magnitude of strain imposed on the tissue at all. Care should be taken when designing these studies that indentation depth does not exceed 1% of total sample thickness.

It might be desirable to employ large strains to reduce the impact of finite tip radius in some models (e.g. Sneddon), since this is more pronounced in smaller indentations[305] however it would be more appropriate to implement a model that is less sensitive to these effects – such as the Maugis model[269].

3.5. Frequency

The frequency of dynamic measurements significantly affects measured storage and loss moduli. Since the behaviour of a non-linear material such as brain can vary unpredictably with frequency, any two datasets can only be meaningfully compared when the frequency range utilised overlaps.

Indentation techniques – used primarily for transient measurements – are also sensitive to frequency, since the ramp speed of the indenter can be adjusted. A higher or lower ramp speed may be used to avoid measurement error (for example adjusting ramp speed to compensate for drag forces in a fluid environment[247]). The indentation curve of a transient AFM measurement can be thought of as a single oscillation from a dynamic experiment (this property has been exploited to extract viscoelastic data from AFM readings[246]). A higher ramp speed will tend to produce higher elastic modulus readings than a lower value due to a more limited opportunity for relaxation events to occur during the measurement[247,306–308].

AFM measurement of brain is challenging and adjustments to ramp speed may be necessary for reliable measurements. However, where possible ramp speed should be matched to existing values in the literature to permit comparison of data.

Shear rheology papers tend to employ low frequencies (0.32 - 9.87 Hz[276,288]). Reported frequencies from AFM experiments lie in a similar range – between 1 and 10 Hz[289–297], and the one dynamic indentation study found that reported a frequency value was also similar (30 Hz[231]). Impact indentation studies also employ various strain rates (strain rate can be considered an analogous variable to frequency –

higher strain rates produce larger elastic modulus readings, as would be expected with higher frequency measurements) however converting these values in a way that allows them to be directly comparable to frequency-controlled methods is non-trivial[309].

There is a general upward trend of elastic modulus with frequency across all nanoindentation, shear rheology and dynamic indentation studies – though this relationship is unclear due to low overlap between most datasets (Figure 12).

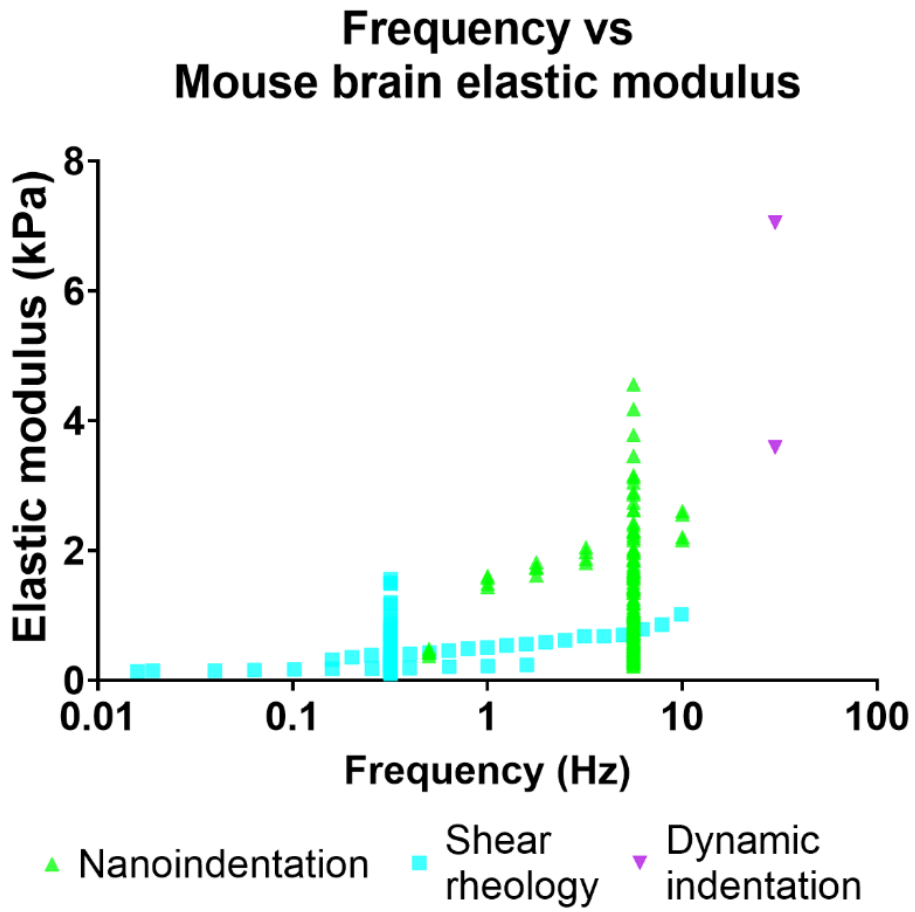

Figure 12: Deformation frequency vs. mouse brain elastic modulus for all nanoindentation, shear rheology and dynamic indentation studies.

In comparison, MRE employs frequencies that are substantially higher than other methods (600-1800Hz[251,279–284,286,287,296]). Both storage and loss moduli increased with frequency (Figure 13[251,279–284,286,287,296]), though a combination of sparse data and confounding variables means that whilst the ratio of storage to loss modulus appears to increase with frequency, a clear relationship of frequency to Tanδ cannot be confirmed.

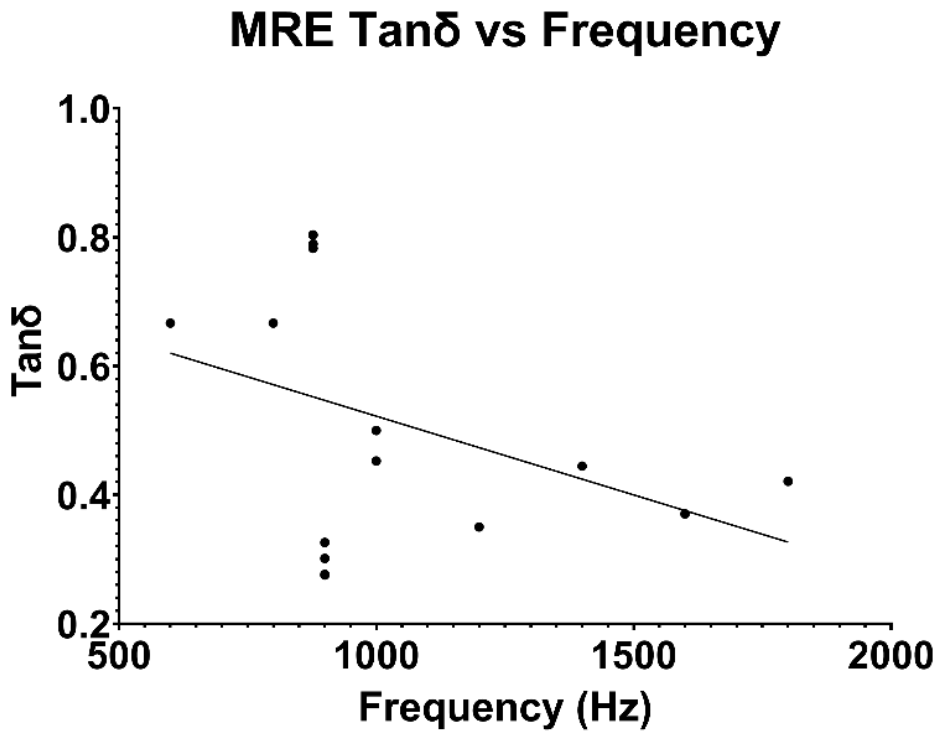

Figure 13: Tanδ of all mouse brain samples from MRE studies plotted against the deformation frequency.

Storage modulus values for healthy mouse brain across all MRE papers range from 1.5 to 25 kPa; a larger range than other methods (excluding a single unusually high value from the nanoindentation literature). Since these values are in shear, they are equivalent to elastic moduli of 4.5 to 75kPa; substantially higher than values acquired with other methods. The very large range of elastic moduli could be explained by the wide range of frequencies employed in MRE experiments.

3.6. Temperature

If a study aims to replicate *in vivo* conditions faithfully, temperature is an important variable: viscoelastic properties of materials tend to vary by temperature, with elastic factors generally dominating at lower temperatures and viscous relaxation becoming more prevalent as temperature increases[234,310,311].

The body temperature of a mouse varies between 36.5 and 38°C[312]. Despite this, 10/14 studies (excluding MRE since it is carried out primarily on living animals at 37°C) investigating the viscoelasticity of healthy mouse brain performed measurements at room temperature (20 - 25°C) for one or more animal cohorts. 3/14 studies carried out all experiments at 37°C and 1/14 studies did not report the temperature used.

Maintaining samples at body temperature can pose technical challenges; samples in air will desiccate in a heated chamber and fluid immersion requires a temperature management solution such as a heated bath, chamber or platform to maintain a consistent temperature throughout the measurement. For techniques such as rheology this functionality is included in most equipment. However, in AFM the scan head of the instrument can heat up substantially, making it difficult to operate at a consistent temperature.

Temperature selection is particularly complex for measurement of *ex vivo* samples, where lower temperatures can delay tissue death and resultant osmotic (Donnan) swelling but will also alter material properties of the sample[313,314]. In these cases, it may be preferable to standardise mechanical measurement of living tissues at 4°C to prevent cell death, which can have a substantial effect on tissue elastic modulus (chapter 5).

3.7. Slice orientation

There is no obvious convention for orientation of brain samples during mechanical measurement; excluding MRE (where all brains are in the same orientation due to the orientation of the sedated animal relative to the detector), 7/14 papers do not report the orientation at which brain is sliced (Table 4).

Whilst brain is typically assumed in the literature to be a homogenous and isotropic material, this appears to be for convenience rather than accuracy; like many tissues[235], brain is highly structured and mechanically anisotropic[315,316]. In healthy brain, axonal fibres and blood vessels run in polarised orientations through the tissue[317], whilst diseased brain can possess anisotropy in myelination, fibre arrangement, axonal integrity, cellular composition and axoglial contacts[318,319]. Depending on the brain region in question and the measurement method used, orientation of the tissue sample may impact measured mechanical values. Since there are few studies with reported sample orientation, it is not possible to establish whether such an effect may exist in reports of healthy mouse brain mechanical properties.

Sample orientation	**Horizontal**	**Coronal**	**Radial**	**Unknown**	**Total**
Number of studies	2	4	1	7	14

Table 4: Distribution of mouse brain slice orientation relative to the whole brain across all studies.

3.8. Sample buffer composition and oxygenation

Immediately following sacrifice, mouse brain tissue requires a supply of oxygen, nutrients and ions in an appropriately buffered environment. Artificial cerebrospinal fluid (“aCSF”) is a commonly used solution developed for electrophysiological studies to keep acute *ex vivo* brain tissue viable and maintain normal neural electrical activity, designed to provide these factors. aCSF is typically oxygenated via bubbling with carbogen, a 95% CO_2, 5% O_2 mixture.

Only two studies stored their acute brain samples in aCSF prior to and during mechanical measurement (Table 5[231,276,281–299]). One additional study instead stored their tissue in “Hibernate-A media” (Thermo Fisher) – a medium intended for long-term storage of brain tissue and cells.

The most common solution in which to store samples was phosphate-buffered saline (PBS). This buffer is used in mammalian cell culture for washing, staining and other procedures that require a solution with osmolarity compatible with mammalian cells (to avoid osmotic swelling or desiccation of cells and tissue). However, PBS does not contain the required nutrients for maintenance of brain tissue for more than a few minutes, and was not oxygenated in any study. Two similar buffers (HEPES buffered extracellular solution and Krebs-Henseleit buffer) were used in other studies, with the same limitations. Dulbecco’s modified Eagle medium (DMEM) is widely used for mammalian cell culture and contains the necessary nutrients to sustain tissue – though not in proportions optimised for whole brain tissue – however no study that used DMEM elected to oxygenate the solution.

Finally, one study reports that their samples were measured in “a liquid environment” with no further detail, and another measured whole mouse brain in air.

The wide range of environments in which *ex vivo* brain tissue samples were stored and measured could contribute to the variability of mechanical properties across these studies; all but three studies used solutions that lack the proper qualities for sustaining live brain tissue, making it likely that most samples were partly or fully dead by the point of measurement, and would therefore have experienced significant osmotic (Donnan) swelling.

Medium	Glucose/sucrose?	Oxygenated?	Number of studies
Dulbecco's modified Eagle medium (DMEM)	Y	N	2
Hibernate-A media	Y	N	1
HEPES buffered extracellular solution	Y	N	1
Phosphate-buffered saline	N	N	5
Artificial cerebrospinal fluid (aCSF)	Y	Y	2
Krebs-Henseleit buffer modified	Y	N	1
"A liquid environment"	?	?	1
Air	N	Y	1

Table 5: Media in which samples were stored, handled and measured in literature concerning healthy mouse brain mechanical properties.

3.9. Tissue fixation

Fixation of tissue with paraformaldehyde is a standard method for preserving tissue architecture for future analysis. Paraformaldehyde cross-links proteins and DNA in tissue via formaldehyde monomers, preventing enzymatic and metabolic activity and avoiding decomposition from external contaminants.

Fixation with paraformaldehyde has been demonstrated to affect tissue elastic modulus, increasing stiffness in all tissue including brain[320–323]. Out of the studies discussed (excluding MRE, which uses live animals), 2/14 carried out fixation with 4% paraformaldehyde prior to mechanical measurements[295,296].

3.10. Shear wave elastography

Shear wave elastography is an uncommon technique using ultrasonic waves to measure brain elastic modulus in a similar manner to magnetic resonance elastography. I could find only one study that acquired elastic modulus values for healthy mouse brain using this method. Five live, sedated Male MitoCFP mice were used for the sham (healthy) group (age unknown) and cortical measurements were taken from each hemisphere of the sham mice's brains. The reported values were 5.14 ± 1.03 kPa for one hemisphere and 5.19 ± 0.93 kPa for the other[324].

Chapter 4. Results: Characterisation of Astrocyte Extracellular Matrix

4.1. Introduction

4.1.1. Astrocytes

Astrocytes (also referred to as astroglia) are a type of cell found in the central nervous system. Their name is derived from their star-shaped morphology ("astro"); "activated" astrocytes possess multiple long projections that are largely symmetrical in direction and length, thus loosely resembling a star.

Multiple astrocyte subtypes have been described, including *fibrous* (typically found in white matter), *protoplasmic* (grey matter) and *radial* (a progenitor type that produces neurons and astrocytes as well as directing their migration)[325–328].

Protoplasmic astrocytes are the most common subtype in the brain (radial astrocytes being primarily found in developing brain)[329]. However, it has historically been difficult to produce *in vitro* populations of astrocytic cells that are definitively fibrous or protoplasmic; a plurality of environmental, chemical, and mechanical signals govern the transition between the subtypes and numerous variations have been observed. An early attempt at classifying astroglia separated them into two subtypes (type 1 and type 2) based on the expression of various markers. However, the study was carried out on astrocytes derived from progenitor cells from immature rat optic nerve, and may have limited relevance to human astrocytes, or cells isolated from brain tissue[330].

A more useful identifying factor for astrocytic cells for *in vitro* work is the presence of glial fibrillary acidic protein (GFAP). Whilst not exclusively produced by astrocytes, this marker serves as a useful tool for identifying astrocytic populations in neural cultures[331].

Astrocytes perform a wide range of roles in the brain, including (but not limited to)[332]:

- Metabolic and nutritional support to neurons (by providing, clearing or otherwise manipulating supply of neurotransmitters, nutrients and glycogen to neurons).
- Structural (acting as a physical support for neurons and synapses).
- Producing and maintaining extracellular matrix and the blood-brain barrier.
- Modulating the action of other nearby cells (including myelination by oligodendrocytes, firing of neurons and inflammatory responses).
- Repair of neural tissues (a complex process; astrocytes fill spaces in injured brain tissue, promote and suppress regrowth of neurons).

4.1.2. Mechanical factors in glial scar

It was assumed until recently that glial scar is stiffer than the original brain tissue; most scar tissue contains large amounts of collagen I and resists cellular penetration, resulting in a less functional tissue after healing[333–338]. The assumption that glial scar is stiffer than healthy brain implies that neurons are mechanically restricted from the injured site.

Recent research suggests that the opposite may be true; glial scar tissue is substantially softer than healthy brain, meaning that it cannot be acting as a physical barrier to healing[71,339]. Neurons, microglia and astroglia are affected by mechanical cues in their environment (neural axons grow longer in softer substrates but grow fewer dendrites[340], axons of dorsal root ganglion cells grow better on stiffer substrates *in vitro, Xenopus* retinal ganglion cell (RGC) axons grow faster in stiffer environments[341]), which could contribute to the dysregulated growth and migration seen in glial scar.

Neural stem cells proliferate in injured tissue, preferentially differentiating into glial cells on softer substrates and into neurons on stiffer substrates[342]. Manipulating this

property by restoring normal tissue stiffness following brain injury may result in better health outcomes; it is possible that species capable of regenerating brain tissue (such as newts and axolotls) experience different mechanical changes following injury, leading to higher neural growth and reduced glial scar formation[339].

Cultured cortical astroglia also soften during glial scar formation — a phenomenon reversible by blocking ATP-mediated ion channels[343]. Whether there is a link between cell-softening and ECM-softening in glial scarring is currently unknown.

Glial scar production can be inhibited by treating tissue with cell cycle inhibitors, slowing astrocyte proliferation[344,345]. However, inhibition of cell division would also prevent differentiation of neural progenitors into new neurons and a complete suppression of glial scar formation may result in inadequate repair of the blood-brain barrier.

If astrocyte proliferation could be controlled by manipulating tissue stiffness, it may be possible to inhibit glial scar formation whilst continuing to allow differentiation of neurons from progenitors. By adjusting brain tissue stiffness appropriately, it may be feasible to allow sufficient astrocyte proliferation to repair the blood-brain barrier whilst minimising inhibition of neural regrowth.

Olomoucine and Mdivi-1 have both been employed as treatments to prevent astroglial proliferation, and could be used as a positive control in experiments investigating the effect of drug treatments on proliferation rate of primary astrocytes during reactive gliosis[344,346,347].

Several ECM components are upregulated after traumatic brain injury: vimentin, collagen IV, glial fibrillary acidic protein (GFAP) and chondroitin sulphate proteoglycans (CSPGs)[339]. Vimentin has been observed as a marker of immature glial cells and neural stem cells[348,349] and as such may not be directly related to

mechanical changes to ECM. Collagen IV is associated with the basal laminae; inhibition of its production may prevent blood-brain barrier repair[350]. CSPGs are highly branched neuroinhibitory molecules. Due to their branched structure, CSPGs tend to be highly hydrated[351].

Since tissue hydration is closely linked to mechanical stiffness, CSPGs may be a viable target for manipulating brain tissue stiffness; possibly via digestion by chondroitinase enzyme[351]. CSPG synthesis inhibitors have been developed, offering a potential small-molecule treatment that could be used to alter brain tissue stiffness after traumatic brain injury[352].

4.1.3. Producing an in vitro model of brain ECM

The ECM is a complex structure with substantial variation depending on the specific functional needs of a given tissue. It provides structural support for cells via a dense, interconnected matrix of proteins whilst being permissive to nutrient diffusion. The ECM contributes to the mechanical properties of a tissue, acting as a structure to which cells can anchor via focal adhesions[353–355].

The ECM is formed of fibrous protein (chiefly collagen and elastin) and glycoprotein (proteoglycans and laminins) molecules which vary in ratio and interact with each other to produce conditions that support cellular growth and structure. A wide range of additional molecules are sequestered and stored in the ECM for the purposes of nutrition, signalling and binding (for example heparin will bind to growth factors, proteases and chemokines whilst maintaining function and presenting bioactive sites for binding by cells).

Tissues which require a high degree of structural strength have distinctly different ECM to those requiring the ability to remodel rapidly (cartilage contains CSPGs to provide compressive strength, tendons form linear fibrous structures for tensile strength). Brain tissue ECM is rich in glucosaminoglycans, has low levels of type-1

collagen and elevated concentration of type 4 collagen — a more highly branched variant), leading to a soft and flexible ECM compared to many other tissues[353].

ECM composition is influenced by many biological processes; immune cell migration is facilitated during inflammation by triggering an influx of fluid into tissue (reducing tissue stiffness). Conversely, solid tumours have been shown to rearrange collagen fibres into linear bundles that permit more rapid cell metastasis[356,357].

To successfully simulate ECM, molecular composition, architectural structure and mechanical characteristics must be matched to the tissue of interest. It is not sufficient to simply mix major ECM components in the correct ratios; ECM contains functional modifications for binding and signalling, small molecules such as cytokines or growth factors and a wide array of other substances[353]. ECM may feature specific arrangements of component fibres — which may not necessarily be replicated by a simple mixture[358]. The mechanical properties of ECM are influenced by factors such as arrangement of collagen fibres — affecting tensile strength — and the amount of bound water, which contributes to both compressive strength and elastic modulus[359,360].

ECM from decellularised tissue

One approach to producing a realistic ECM model is to decellularise an *ex vivo* tissue sample, permitting new cells to be seeded into the cell-depleted structure[361]. This approach has been successful in tissue engineering applications such as the growth of artificial organs, by stripping cells from an organ and using the remaining ECM "skeleton" as a scaffold on which to grow cells of the desired type (e.g. taking a porcine heart, stripping the cells from it and growing human cardiomyocytes on the ECM to enable transplant into a human patient)[362].

Whilst this approach is likely to retain much of the molecular variety of ECM *in vivo*, cell stripping utilises proteases and chemical treatments that may damage ECM

components and strip out small molecules. Additionally, whole cells or lysed fragments may persist in the stripped ECM structure, causing contamination. Unlike synthetic or cell-derived ECM models, decellularised ECM scaffolds cannot be freely synthesised or grown; the requirement for whole tissue may present a manufacturing bottleneck.

Synthetic ECM mixtures

Artificial ECM models can be approximated using synthetic or purified proteins. Several suppliers now offer purified collagen and fibronectin extracted from animal sources (e.g. rat tail collagen), used commonly to improve cell adhesion to culture substrates. These individual components can be used to form mixtures matching the ratio of major ECM components. Such synthetic models lack specialised architectural features that require more complex compositions, or that form as a result of cellular action[363].

With improved understanding of ECM fibrogenesis, it is possible that specialised ECM analogues could be tailored to different tissues by adjusting the specific composition of the mixture[358]. By using either serial or simultaneous incubation of ECM components together it is possible to control stacking and formation of fibres with heterogeneous components. At present, this type of process is labour intensive and does not produce large amounts of material[358].

Commercial ECM products

Several companies offer commercial ECM analogues, either for the coating of cell culture substrates in thin layers for monolayers, hydrogels for the culture of cells in 3 dimensions or products intended for tissue engineering and clinical use. These range from purified ECM proteins such as collagen, synthetic hydrogels with added biological components, decellularised tissue or synthetic structures modified with functional motifs. Many of these models have been engineered to allow enzymatic degradation, improved binding, specific signalling behaviour and other functions that

mimic those of natural ECM. Whilst none of these options are likely to be a perfect match for ECM *in vivo*, they offer high consistency and a reduction in workflow compared to generating ECM analogues in-house[364–366].

For brain-specific ECM, Cultrex basement membrane extract is a commercially available soft ECM gel that contains a higher type-4 collagen and lower type-1 collagen concentration than other products[366].

ECM from decellularised monolayer culture

By growing a monolayer culture of cells from the tissue of interest and stimulating them with appropriate growth factors, thin layers of cell-derived ECM can be produced and decellularised in a similar fashion to tissue-derived ECM scaffolds[367]. This method has the advantage of requiring a less intensive decellularization process that does not require solubilisation of the ECM, thereby retaining architectural features that would otherwise be lost[368]. With a less intensive cell removal process, small molecules and globular proteins are more readily retained.

Cell-derived ECM models have been produced from a wide range of immortalised and primary cell types including haematopoietic and mesenchymal stem cells, epi- and endothelial cells, fibroblasts, osteoblasts, hepatic and lung cells[367]. Whilst monolayer culture of a single cell type may produce different ECM to that of a more complex tissue, co-culture of multiple cell types has been employed to produce more complex ECM models[361,369–372].

4.1.4. Removal of cells from ECM samples

To measure the mechanical properties of an ECM sample, cells covering the surface must first be removed.

Protease enzymes are commonly employed for decellularization; cell-ECM connections are digested by enzymes such as trypsin and the loosened cells are

rinsed off with a buffer solution such as phosphate-buffered saline. Protease treatment is relatively broad in its action however; ECM components would be damaged by this approach, potentially altering the results of any mechanical measurement[368].

Alternatively, detergent treatments such as Triton x-100, sodium dodecyl sulphate and sodium deoxycholate can be used to remove cells via disruption of cell membranes and dissociate cellular components. Whilst this approach does not directly cleave proteins like a protease-based decellularization method, it is still capable of denaturing proteins and is liable to leave residue from both detergent and lysed cells in the resulting ECM gel[373–375].

Commonly, ethylenediaminetetraacetic acid (EDTA) is used in conjunction with trypsin, acting as a chelating agent to sequester calcium and magnesium ions. Cadherins and integrins (which are calcium- and magnesium dependent respectively) treated with EDTA will bind less strongly, loosening cultured cells from the ECM. Many ECM components are EDTA-soluble[376], however an EDTA-based protocol may be less destructive than a detergent or protease-based approach[377].

Individual cells could be removed via mechanical interaction using a micromanipulator; microinjection or AFM instruments can be used to mechanically displace cells with their needle or cantilever tip, and optical tweezers are capable of exerting forces on cellular or subcellular targets non-invasively. This approach is laborious and risks mechanical disruption to the ECM structure, however unlike chemical cell-removal approaches there is no risk of ECM components being washed away. The risk of probe fouling and contamination of the ECM with cellular debris is quite high, and the strong adhesion forces exerted by biological samples risk damage to a relatively delicate AFM cantilever or micromanipulator[378].

There is currently no optimal solution for decellularization of cell-derived ECM; each approach risks contamination, damage to ECM components and disruption of architectural features. Each method will have varying levels of success depending on the tissue or culture that is to be decellularised; an approach that works well for tendon is unlikely to be directly applicable to liver. Each method should therefore be considered individually or in combination to produce a tailored protocol for each application.

4.1.5. Weaknesses of current ECM models

Current ECM models each have specific weaknesses:

- Decellularised tissue tends to contain contaminants from cells or loses ECM components due to over-harsh cell removal methods. ECM architecture tends to be lost due to cleaving and solubilising of ECM fibres by proteolytic action.
- Crude mixtures of ECM components lack the complete complement of components that ECM possesses *in vivo* and does not exhibit the same fibrous architecture.
- Synthetic ECM fibres possess a more accurate architectural structure and can be tweaked to match particular ECM types but lack molecular variety, and are labour-intensive to produce.
- Synthetic hydrogels enable easy adjustment of mechanical properties and can even be modified to contain similar functional domains to real ECM, but are fundamentally made from different components and do not simulate ECM as accurately as other methods.
- Cell-derived ECM produces the most molecularly and architecturally accurate ECM but only produces a thin layer and so do not simulate bulk ECM properties.

Of the above, cell-derived ECM appeared to have the fewest drawbacks and was be used as the starting point for the ECM model in this project. Cell-derived ECM produced from astrocyte culture has not been described in the literature; a protocol for producing cell-derived ECM was adapted from literature concerning other cell types.

4.2. Aims and objectives.

This project aimed to investigate the relationship between brain injury, astrocyte activation, tissue softening and factors that affect neural regeneration in an *in vitro* context, and to assess potential methods to suppress tissue softening in injured brain and thus reduce scar formation.

Objectives of this project were to:

- Develop an ECM analogue that closely matches the chemical and architectural content of brain ECM *in vivo*.
- Produce a methodology that allows the analysis of mechanical properties of this ECM model before and after astrocyte activation, without interference or contamination from the astrocyte itself.
- Apply this methodology to better understand the effect of surgical, photochemical and thermal trauma from optogenetic brain implants and identify potential targets that can be used to mitigate these effects.

4.3. Results and discussion

4.3.1. Selection of an astrocyte model

Most experiments in literature related to reactive gliosis, glial scarring and ECM changes during traumatic brain injury are either carried out *in vivo*, *ex vivo* with cultured tissue or *in vitro* with primary astroglia.

Primary cells are difficult to obtain (requiring extraction from brain tissue and separation from other cell types), expensive to purchase commercially and difficult to maintain; commercial primary astroglial lines advertise between 4 and 10 division cycles before the cells begin to degrade. This makes them unsuited to early-stage experimentation whilst methods are developed and risk of waste is higher.

It is therefore desirable to make use of an immortalised astroglial cell line; several such lines exist commercially and others have been produced independently by research groups[379,380].

Since these cell lines have been modified and may have undergone many generational cycles, it is possible that their behaviour has diverged from that of primary astroglia. It is therefore important to establish desirable traits for such a cell line and to select the option that best exhibits as many of these traits as possible.

The presence of these traits does not guarantee that cultured immortalised astrocytes will behave like primary astrocytes or those *in vivo*; indeed, primary *in vitro* cultured astrocytes have been observed to be substantially different from astrocytes *in vivo* despite being perceived as the “gold standard” for *in vitro* astrocyte experiments[381]. However, the presence of these traits should indicate a greater similarity to astrocytes *in vivo*.

The most important marker for an astroglial cell line is the presence of glial fibrillary acidic protein (GFAP)[382]. This protein is the key indicator that a cell has progressed down the astrocytic lineage from neural precursors rather than becoming a neuron or a microglial cell. Any cell line that lacks robust GFAP expression was rejected.

An astroglial cell line suitable for these experiments should be able to be cultured in an quiescent state, and should enter a reactive phenotype under simulated injury conditions; scratch assays, stretch injury, cytokine challenge and other methods have been used to trigger this state in astroglia[383–386].

During glial scar production, the compounds most associated with tissue softening are vimentin, collagen IV, laminin and CSPGs; these compounds should be detectable in immortalised astroglia which have undergone reactive gliosis[339].

Other major markers for astrocytes (as determined by RNA sequencing and comparison to other neural cells) include aquaporin 4 (AQP4), aldehyde dehydrogenase 1 family member L1 (ALDH1L1) and thrombospondin (THBS4)[387]; presence of these markers is not critical, however may indicate a closer match to *in vivo* properties.

8 commercially available cell lines were considered (Table 6):

- ABM Immortalized Human Astrocytes, foetal – hTERT (cat no. T0281)
- ABM Immortalized Mouse Astrocytes - SV40T (IMA2.1) (cat no. T0289)
- ABM Immortalized Human Astrocytes, foetal - SV40 (cat no. T0280)
- ATCC CTX TNA2 (cat no. CRL-2006)
- ATCC DI TNC1 (cat no. CRL-2005)
- ATCC C8-D1A (cat no. CRL-2541)
- ATCC BALB SFME (cat no. CRL-9392) (this line is of particular interest as these are naturally immortal neural stem cells; presence of serum causes cell growth arrest and differentiation into astroglia)
- Creative Bioarray Immortalized Human Astrocytes - foetal-hTERT (cat no. CSC-I9064L)

Cell lines are referred to by their catalogue number going forwards.

All cell lines except CRL-9392 (which is a neural progenitor line) are type-I astroglia, which exhibit multiple short processes (as opposed to two longer processes in type II or none in type III) and are the most common type in mature brain[329].

Cell line	T0281	T0289	T0280	CRL-2006	CRL-2005	CRL-2541	CRL-9392 (differentiated)	CSC-I9064L
THBS4	?	?	?	Yes	?	Yes	?	?
ALDH1L1	?	?	?	?	Yes	Yes	?	?
AQP4	Yes	?	?	No	No	Yes	?	?
CSPG	?	?	?	Yes	?	Yes	?	?
Collagen IV	?	?	?	Yes	?	?	?	?
Vimentin	?	?	?	Yes	Yes	?	Yes	?
Induced gliosis	?	Yes	?	Yes	Yes	Yes	?	?
GFAP	Yes	No	Yes	Yes	Yes	Yes	Yes	?

Table 6: Assessment of commercially available immortalised astrocyte cell lines. Data were collected from manufacturer websites and scientific literature[388–401].

CRL-2006 has been demonstrated to secrete ECM components via proteomic analysis [402].

No reference could be found for CSC-I9064L, and information on the manufacturer website is limited.

Whilst many of the above properties could not be confirmed via literature search, this does not mean that they are not exhibited by the cell line; little information is provided by vendors and as such information about marker expression is typically only available from published experimental data.

CRL-9392 was potentially of interest due to the ability to culture the neural progenitor and differentiate (arresting proliferation) as needed. These cells have not been immortalised, and may behave more like *in vivo* astrocytes than other lines. Unfortunately, this cell line is not exceptionally well documented, and appears to require specialised culture conditions that may be challenging to replicate.

From the “conventional” immortalised lines above, CRL-2006, CRL-2541 or CRL-2005 appear to be the best documented, with confirmed presence of most of the desired properties. The lack of aquaporin-4 is not critical, and other groups have successfully induced its expression via genetic modification[389,392].

Available documentation does not confirm vimentin or collagen IV expression in CRL-2541, however these are both highly associated with astrocytes throughout the literature, and it is likely that they do express these markers[403,404]. Based on communication with Dr. Andras Lakatos (Cambridge University) whose laboratory has experience working with primary astrocytes on similar topics, it was decided to use CRL-2541 for initial experiments, with the intention of moving to primary culture if these are successful.

4.3.2. CRL-2541 cell-derived ECM production

CRL-2541 cells grow readily in high-glucose DMEM supplemented with FBS. They reach confluence in approximately 4-5 days after seeding at ~50% density, halting at 100% confluence due to contact inhibition (Figure 14B).

CRL-2541 was confirmed to produce GFAP via both ELISA and immunocytochemistry (data not shown). Cultured CRL-2541 cells exhibited morphological differences to astrocytes *in vivo*; whilst cells grown at low density exhibit multiple long cellular processes that resemble the “stellate” morphology of astrocytes *in vivo*, they are not as numerous or branched as would be expected (Figure 14A), and these features are not visible at high confluence (Figure 14B). Astrocytes grown in 3D culture tend to form round, bipolar, stellate and perivascular morphologies, however in 2D culture the round morphology dominates[405]. Whilst it is desirable to replicate these morphological characteristics, use of a 3D culture would substantially complicate decellularization and acquisition of intact cell-derived ECM. Supplementation with FGF-2 (which has been demonstrated to restore stellate morphology in primary astrocytes in monolayer culture[406]) did not trigger stellate morphology in CRL-2541 cultures (data not shown).

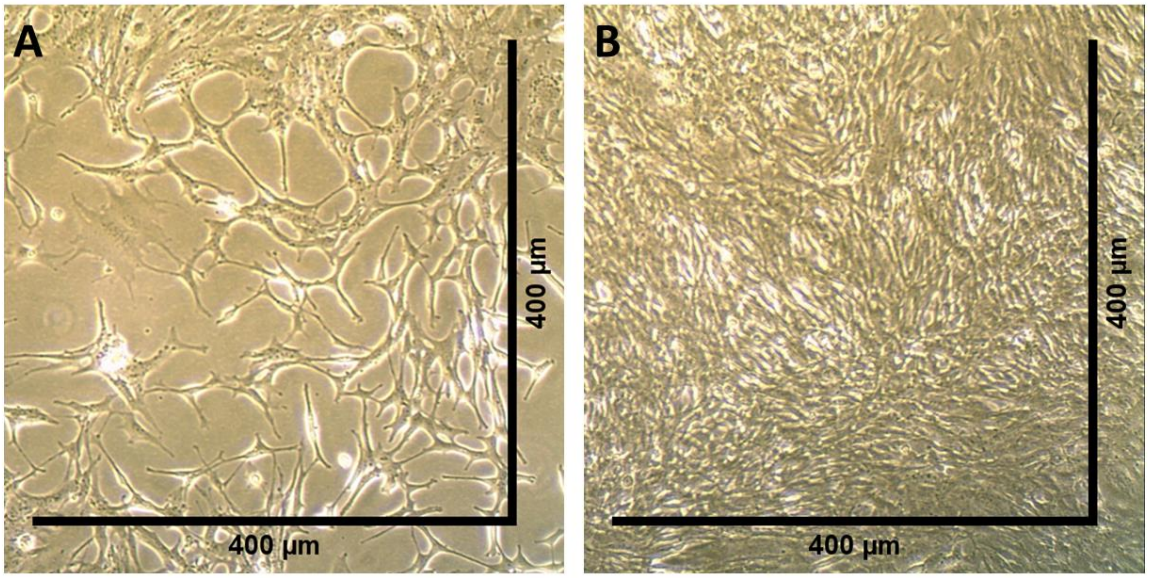

Figure 14: Low (A) and high (B) density cultures of CRL-2541 cells, viewed under an upright phase contrast light microscope.

When stimulated with ascorbic acid, CRL-2541 readily produced a soft, gel-like ECM layer that was slightly thicker than the cell monolayer. This cell-derived ECM was decellularised using a weak detergent solution (0.5% Triton X-100) and treated with benzonase to remove remaining DNA and RNA fragments (full method in chapter 2). To my knowledge, this is the first time that cell-derived ECM has been successfully produced from the CRL-2541 immortalised astrocyte cell line (though cell-derived ECM has been produced from primary astrocyte cultures[407–409]).

If cells are cultured in a plate coated with gelatin or fibronectin, the ECM layer adhered to the plate and could be decellularised without detachment from the vessel (Figure 15) but must be removed by scraping, risking damaging its structure. If cultured on an uncoated vessel, the ECM layer detached upon decellularisation and – over the course of several hours – gathered in a bunched, folded mass.

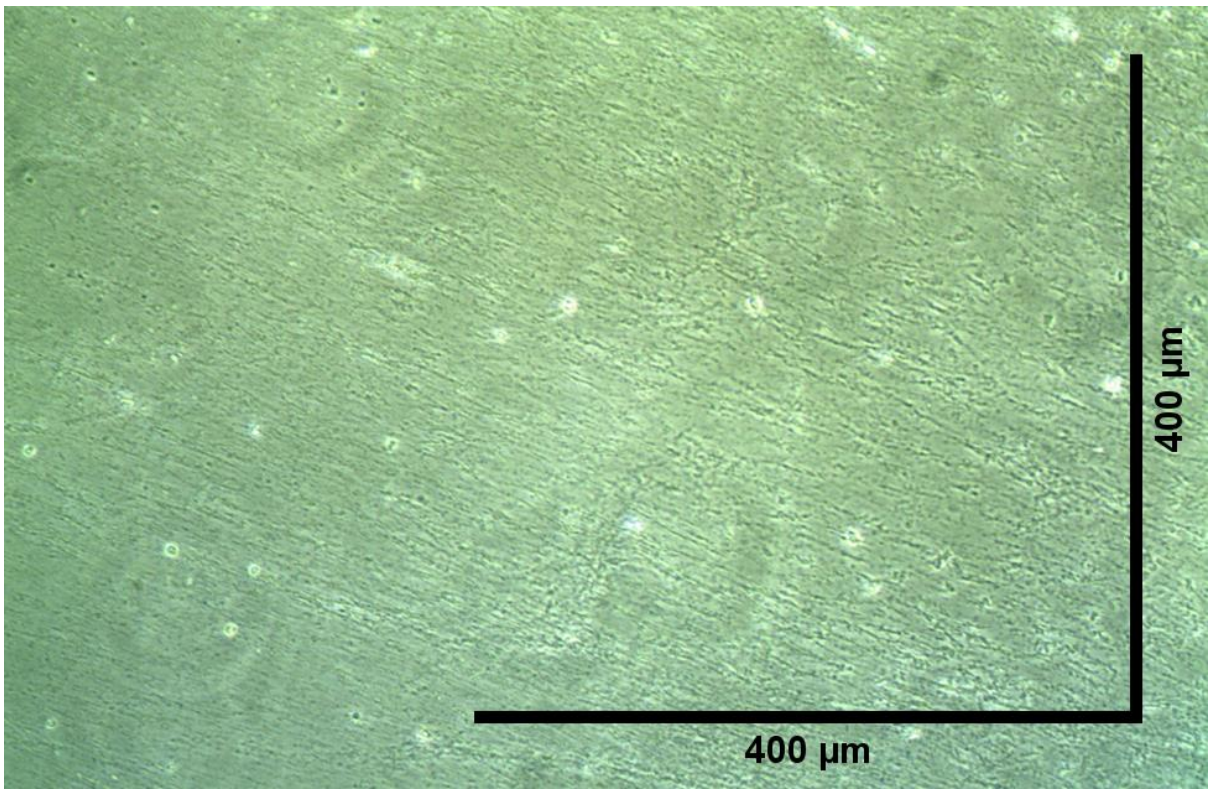

Figure 15: A decellularised ECM gel viewed under an upright phase contrast light microscope

4.3.3. Modulating reactive gliosis in CRL541 cells

To determine whether ECM secreted by quiescent astrocytes differs from that from activated cells, it is necessary to develop methods to suppress or stimulate a reactive phenotype in astrocyte cultures. Several candidates were tested for suppressive or stimulatory effects on CRL-2541 cell cultures: TGF-β, RepSox and FGF-2.

TGF-β – Western Blot

Transforming growth factor beta (TGF-β) is a cytokine implicated in the differentiation, chemotaxis, proliferation, and activation of many immune cell types. Supplementation of primary astrocyte cultures with TGF-β has been shown to stimulate a reactive phenotype[410]. This experiment sought to establish the effective dosage required to trigger reactivity in CRL-2541 cells.

CRL-2541 cells were seeded on 6-well plates and cultured until confluent. Plates were treated with TGF-β1 at either 2, 5 or 10 ng/ml every three days for 3, 6 or 9 days. At the end of the treatment, cultures were lysed and frozen until analysis.

Lysates were analysed using Western Blot with Abcam ab10062 anti-GFAP antibody to determine whether the astrocyte cultures entered a reactive phenotype when treated with TGF-β (Figure 16). If the treatment triggered a reactive phenotype, an increase in GFAP expression would be expected.

Figure 16: Western blot detecting GFAP in CRL-2541 lysates. Cells were treated with TGF-β at 2, 5 or 10 ng/ml for 3, 6 or 9 days.

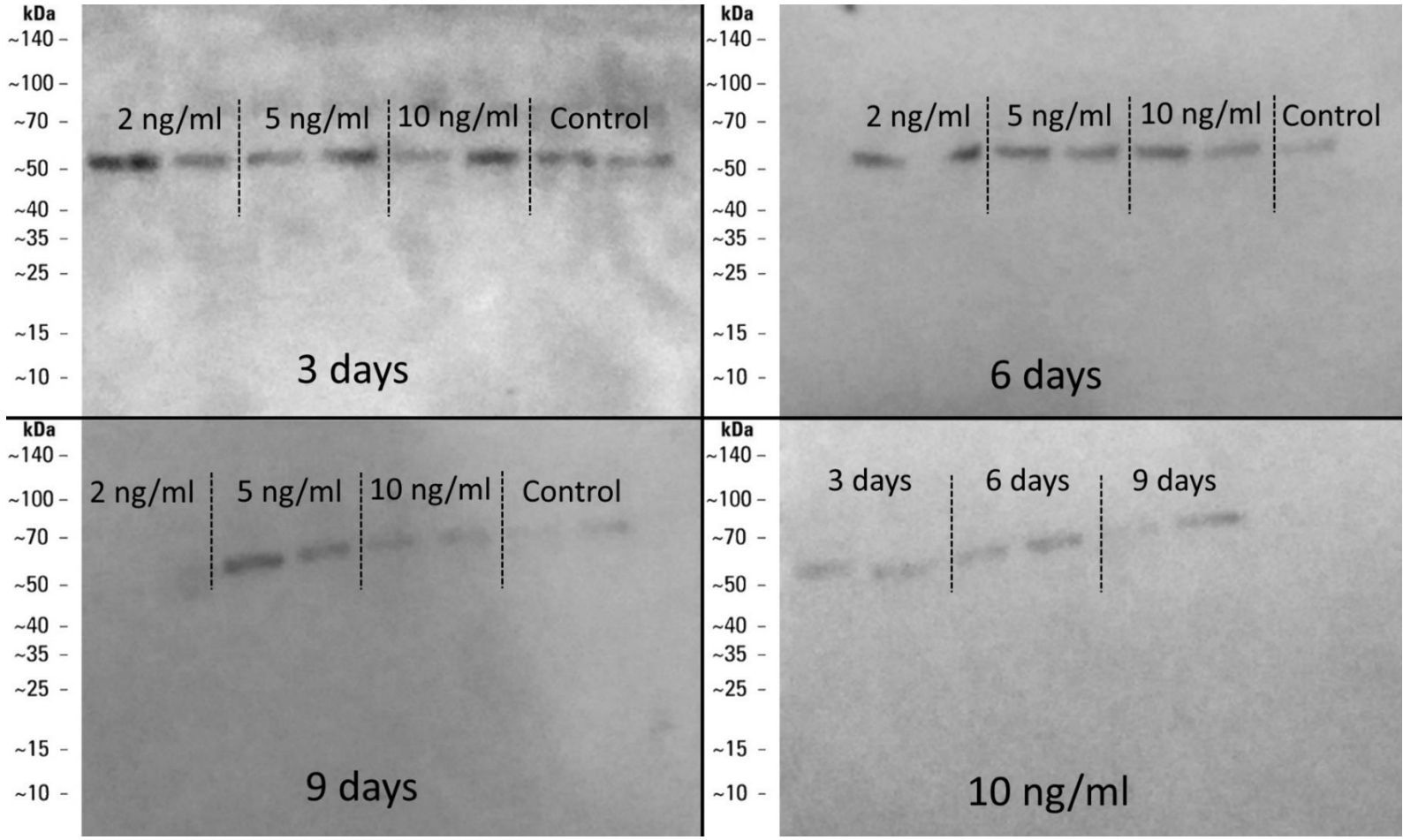

Blots showed a possible increase in GFAP expression when treated with TGF- β that appears most prominent after 3 days of treatment and recedes with longer periods of treatment, however the results are inconsistent and unclear. It is possible that sample inhomogeneity due to high protein concentration introduced errors in loading, or that some portion of the CRL-2541 cultures had entered a reactive phenotype prior to treatment due to handling or other factors. The fact that CRL-2541 cells appear to express GFAP at all concentrations of TGF- β including untreated samples suggests that the cell line may be constitutively activated, and that it may be more productive to explore options for suppressing reactive gliosis rather than stimulating it. It is possible that serum in the growth media contains factors that cause astrocyte reactivity, causing the cells to activate even in the absence of TGF- β treatment.

TGF-β, RepSox and FGF-2 – ELISA

To test the hypothesis that the CRL-2541 cell line is constitutively activated, CRL-2541 cells were cultured to confluence in 6-well plates and treated with either TGF-β1, RepSox (an inhibitor of the TGF-β1 receptor) or fibroblast growth factor 2 (FGF-2; a factor that has been implicated in triggering reactive gliosis in astrocytes[406,411–414]). It was decided that ELISA (enzyme-linked immunosorbent assay) would be a more quantitative method for measuring GFAP expression than Western Blot, allowing differences in expression between samples to be more readily identified. To reduce the potential effect of serum components on cell reactivity and prevent cells from reaching 100% confluence, cells were cultured in serum-free medium. Plates were maintained for either 9 days, replacing medium and treatment every 3 days. Each treatment was repeated 3 times, for a total of 12 wells across all treatments.

GFAP expression was measured using a sandwich ELISA with a paired anti-GFAP antibody kit from GeneTex (GTX500023). GFAP levels were low in the control and RepSox samples (mean absorbance of control = 0.31 ± 0.07, RepSox = 0.22 ± 0.02) and high in the FGF-2 and TGF-β treated samples (FGF-2 = 2.52 ± 0.13, TGF-β = 2.70 ± 0.05). A one-way ANOVA of the results suggests that control and RepSox-treated samples are not significantly different ($p = 0.51$) and FGF-2 and TGF-β treated samples are not significantly different ($p = 0.09$) but that control and RepSox treated samples have significantly lower GFAP expression than TGF-β or FGF-2 treated samples ($p < 0.0001$) – Figure 17.

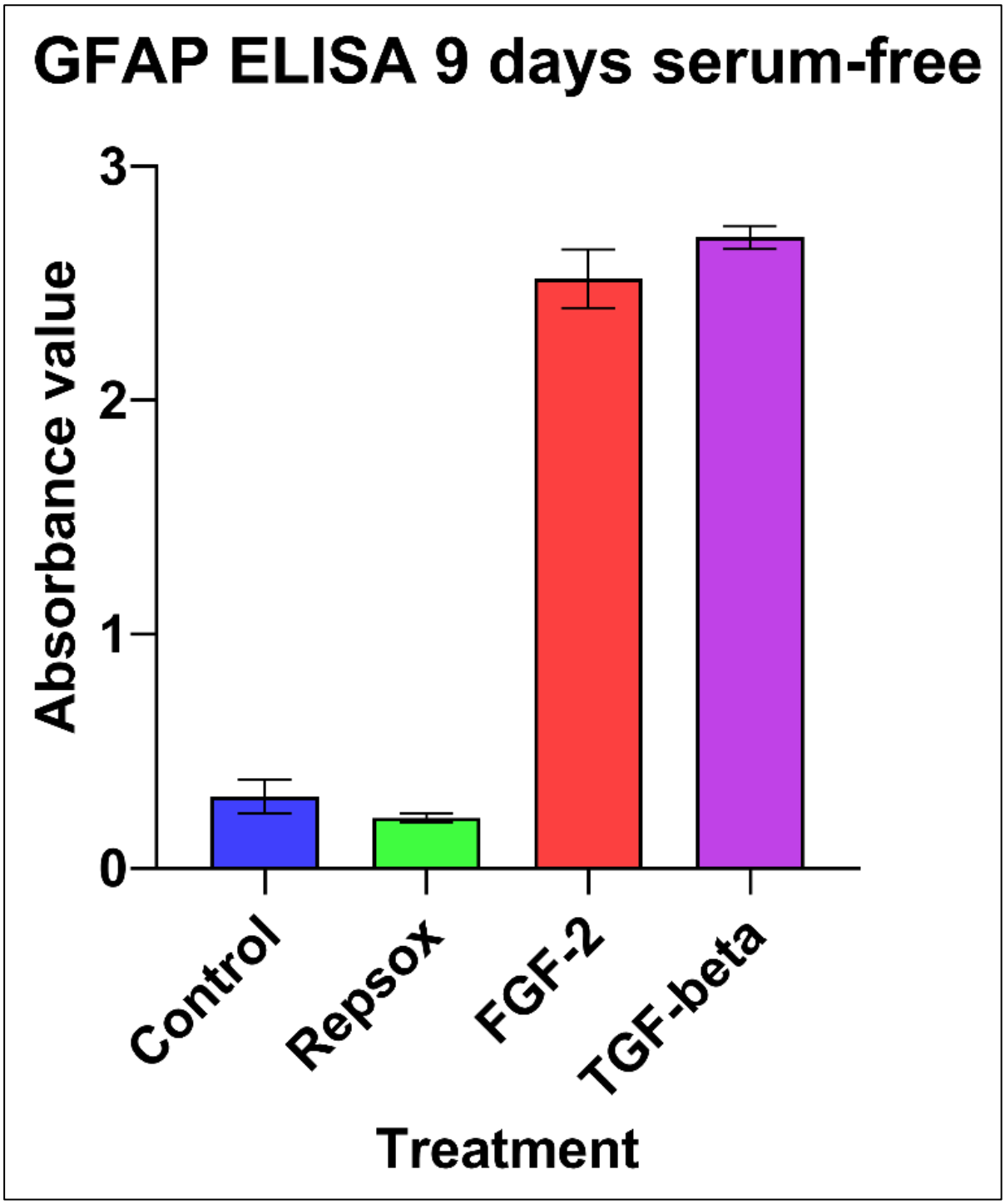

Figure 17: ELISA of CRL-2541 cell lysates. Cells were treated with RepSox, FGF-2 or TGF-beta for 9 days. Bars represent mean absorbance value. Error bars are standard deviation. N = 3 per condition.

Unfortunately, the standard curve generated for these samples was too concentrated, meaning that these results could not be accurately quantified since the standards exceeded the linear detection range of the assay – as such, results may be interpreted qualitatively relative to each other, but absolute values for GFAP concentration cannot be calculated. Nevertheless, the results imply that CRL-2541 cells are not constitutively activated when cultured in serum-free conditions, but can be stimulated to enter an activated state when treated with FGF-2 or TGF-β. Despite this, untreated and treated cells did not appear morphologically distinct; activated astrocytes *in vivo* would be expected to develop more branched and thicker projections but this was not observed, suggesting that whilst CRL-2541 cells might be inducible into a reactive gliosis-like state, this behaviour is not identical to that seen in astrocytes *in vivo*.

4.3.4. Primary culture of mouse cortical astrocytes

Following proof-of-concept ECM production experiments with the CRL-2541 cell line, primary astrocytes would be required to repeat measurements with ECM from a model more similar to brain ECM *in vivo.* A protocol was developed for isolation and culture of primary astrocytes from mouse cortex.

Primary astrocytes are conventionally isolated from P0 to P2 mouse pups[415]; immature astrocytes are more robust than mature cells, enabling higher yields that can be brought to maturity after extraction. Conversely, immature astrocytes differ substantially in behaviour to those from older animals (supporting brain vascularisation, establishment of the blood-brain-barrier and axon pathfinding rather than supporting established neurons and reacting to injury –astrocytes undergo extensive transcriptional alterations during maturation[416]), and the maturation process is time-consuming. The decision was made to isolate cells directly from mature mice using an adjusted protocol to minimise losses.

Isolation was first attempted using a “conventional” protocol from the literature[417], using trypsin combined with mechanical action via Pasteur pipette to dissociate brain tissue, and medium supplemented with Ham’s F12 nutrient mix (a nutrient mixture designed to allow culture of mammalian cells without the inclusion of serum). This method resulted in a low yield of viable astrocytes. Discussion with Dr. Laura Alberio from Prof. Andrew Trevelyan’s laboratory (Neuroscience, Newcastle University) resulted in a modified protocol using papain (a proteolytic enzyme mixture isolated from papaya) and a gentler mechanical dissociation method initially using a 25 ml pipette, moving to a 10 ml and finally 5 ml to more gradually break tissue apart. The new protocol also eliminated centrifugation steps to further reduce mechanical damage. Full protocols are detailed in the chapter 2.

Application of this modified protocol substantially increased yields of viable primary astrocytes (data not shown). However, further optimisation and testing of this protocol were halted by the outbreak of the COVID-19 pandemic, and when laboratory access was restored the decision was made to move to experiments with acute mouse brain slices rather than primary astrocyte culture.

4.3.5. AFM measurement of CRL-2541 cell-derived ECM

Astrocyte-derived ECM possesses a combination of properties that make it a challenging sample to measure with AFM force spectroscopy:

- It is extremely soft. This necessitates a cantilever tip with large surface area; a sharp tip provides insufficient sensitivity. The cantilever must also have a low Young's modulus else contact with the sample will not cause detectable deflection, instead piercing the tip through the sample without deflecting the cantilever.
- It exerts very high adhesive forces. Attempts at analysis of these samples resulted in cantilever adhesion that interfered heavily with measurement, in some cases destroying the cantilever. Additionally, due to the high elasticity of the samples, adhesion persists throughout the range of movement of the cantilever; moving it away from the sample surface pulls the sample with it.
- It must be analysed in a fluid environment to avoid drying out in the warm AFM sample chamber. Drag forces from the fluid environment can cause false-positive measurements or approach attempts if the cantilever is moved too quickly; approach speed must be set very low to minimise drag forces.

A variety of cantilevers were tested on CRL-2541 cell-derived ECM samples; the most successful were 30 µm diameter silica beads adhered to 450 µm long cantilevers with a low force constant (0.2 N/m; TL-CONT from Nanosensors, NanoWorld AG), though due to the increased surface area these cantilevers adhered very strongly to the sample, resulting in failure due to probe fouling or damage after

only a small number of measurements. Probes with smaller diameter tips and higher force constants (such as the CP-FM-Au-C-5 from NanoAndMore GMBH, a 225 µm-long probe with a 9 µm diameter spherical tip and 2.8 N/m force constant) are less susceptible to adhesion – possessing sufficient stiffness to pull away from the sample if moved sufficient distance – but are too stiff and have too small a tip diameter to measure the elastic modulus of the very soft gels.

Use of phosphate-buffered saline (PBS) as the fluid medium neutralises some of the surface charge of the gels, reducing adhesion but not eliminating it. It is possible that coating of the cantilever in a hydrophobic substance may further reduce adhesion, however this was not possible at the time these experiments were performed.

From the few successful measurements performed, the elastic modulus of astrocyte-derived ECM samples was determined to be approximately 80 Pa (measurements were taken at 37 °C, using the Sneddon model of a spherical indenter[270]) – though error from probe fouling, adhesion forces and viscous drag mean that the true value may be substantially different. Elastic modulus values for healthy mouse brain in the literature are highly variable; indentation measurements of healthy mouse brain in the literature show elastic modulus values ranging from 0.03 to 12.07 kPa[231,289–293,298,299], meaning that whilst 80 Pa is within the range of values reported in existing studies, it is firmly on the low end of existing values. This low value may be explained by the absence of cells in the ECM samples; cell-cell connections and the higher stiffness of individual cells compared to their gel substrate are likely to contribute substantially to the net Young's modulus of the composite cell-ECM material.

Due to the very low elastic modulus, high elasticity, and high adhesion of CRL-2541 cell-derived ECM samples, it was decided to attempt bulk measurement via rheology rather than continuing to pursue reliable measurements with AFM.

4.3.6. Rheological measurement of CRL-2541 cell-derived ECM

To measure the mechanical properties of CRL-2541 cell-derived ECM, five ECM samples were produced in uncoated dishes (to allow subsequent removal) and analysed with a Malvern Kinexus Pro + rheometer. Samples were decellularised and detached from the dishes by gently washing with PBS before being gathered into a ball via gentle manipulation with a plastic spatula.

The non-abrasive side of a silicon carbide grinding paper (from Struers online store, 2000 grit) was attached to double sided sticky tape (3M 9084, Double Sided Paper Tape) and 20 mm discs were produced using a punch. These adhesive-backed abrasive discs were placed at the end of the rotating head and the bottom plate of the rheometer to reduce instances of slip between the plate and the ECM sample. Zero gap calibration was carried out with the grit papers attached to both plates and the ECM sample was loaded onto the bottom stage. Excess PBS was removed using tissue paper and gentle pressure. A constant normal force of 0.1 N was applied and the sample was allowed to reach a steady state for at least 60 s, which ensured uniform contact between the top plate and the sample. If required, any excess sample was trimmed to reduce instances of overfill. The sample stage was heated to 37 °C and a solvent trap system was used to keep the samples hydrated for the duration of the measurements. The rheometer was operated in a strain-controlled mode and a 20 mm parallel plate geometry was used for our tests. A constant gap height was maintained for each run, which can vary between 0.7 and 2.2 mm due to the differences in ECM volume harvested (the volume harvested per plate varies substantially between plates). Samples were subjected to a 1% strain at 1 Hz for 22 cycles (Figure 18).

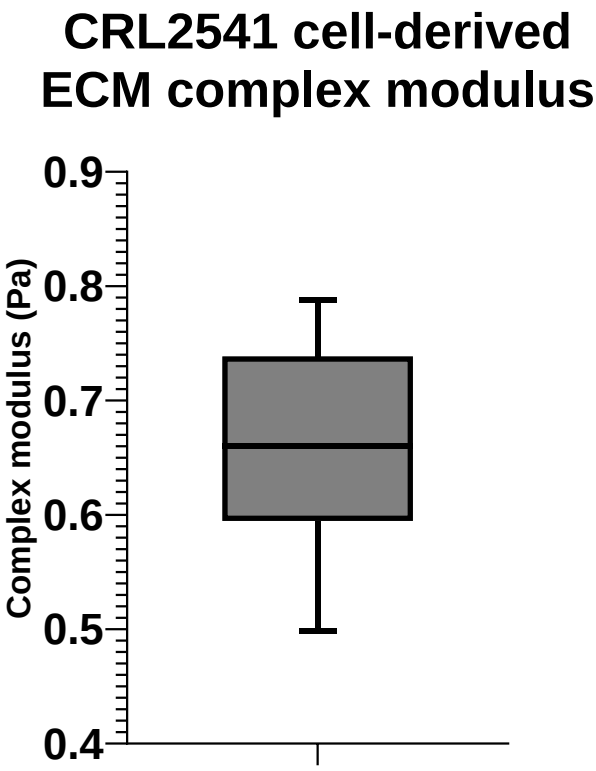

Figure 18: Complex shear modulus of CRL-2541 cell-derived ECM samples, measured with a 1% constant-strain deformation at 1 Hz (N = 5). Central line shows median value. Box shows upper and lower quartiles, and "whiskers" show maximum and minimum values.

As with the AFM measurements, ECM samples were extremely soft (mean complex shear modulus was 0.66 ± 0.08 Pa. Shear modulus values may be converted to elastic modulus by multiplying by 3 in samples where the Poisson ratio is 0.5; the elastic modulus of these samples was 1.98 ± 0.24 Pa compared to ~80 Pa in AFM measurements). Whilst the samples remained difficult to handle due to their high adhesion, stretchiness and softness, the process of rheological measurement was substantially simpler than AFM measurement. Sample trimming was difficult due to the high elasticity; samples would often deform and stretch rather than cutting.

The large difference between elastic modulus values acquired via AFM and shear rheology may be due to a range of factors including size of the AFM cantilever tip, AFM indentation loading rate and whether the AFM cantilever interacted with relatively rigid microstructures in the samples (though this is ameliorated by taking the average measurement from a grid of points on the sample).

Amplitude sweep tests (0.01% to 100%) on an additional 6 ECM samples were performed at 1Hz to investigate how the mechanical properties of the matrix may change with strain (Figure 19). Samples had consistent complex and elastic shear moduli across all strain levels (mean complex modulus across all samples and strains was 0.36 ± 0.18 Pa - Figure 19A). Mean elastic modulus across all samples and strains was 0.35 ± 0.18 Pa (Figure 19B), equivalent to 1.05 ± 0.54 Pa elastic modulus. A one-way ANOVA comparing the complex modulus at each strain point returned $p > 0.9999$, indicating that the complex modulus at each strain level is not significantly different – results were the same for elastic modulus). Loss modulus of the samples was higher at the lowest strains (Mean loss modulus at 0.01% was 0.14 ± 0.12 Pa, at 0.1% was 0.18 ± 0.09 Pa. Loss modulus at 0.2% strain dropped substantially to 0.054 ± 0.055 Pa and remained similar for all further strains. A one-way ANOVA comparing the loss modulus at each strain returns a significant difference between the loss modulus at 0.1% strain to all higher values, with the highest p value returning as $p = 0.007$ – Figure 19C). This change in loss modulus may have resulted from excess PBS being squeezed from the samples during the initial measurements. Similarly, the phase angle of the samples started substantially higher (mean phase angle at 0.01% strain = 27 ± 29.9°, 0.1 = 44.8 ± 33.2°. Phase angle for 0.2% strain drops to 10 ± 5.7° and further drops in larger strains, stabilising from 1% strain where phase angle was 5.4 ± 3.5° and remains similar up to 100% strain. A one-way ANOVA comparing the phase angle at each strain shows a significant difference between the phase angle at 0.1% strain to all higher values, with the highest p value returning as $p = 0.0002$ – Figure 19D).

Figure 19: Complex (A), elastic (B) and loss moduli (C), plus phase angle (D) of CRL-2541 cell-derived ECM samples analysed with a strain-sweep rheological measurement. N = 6, error bars are standard deviation.

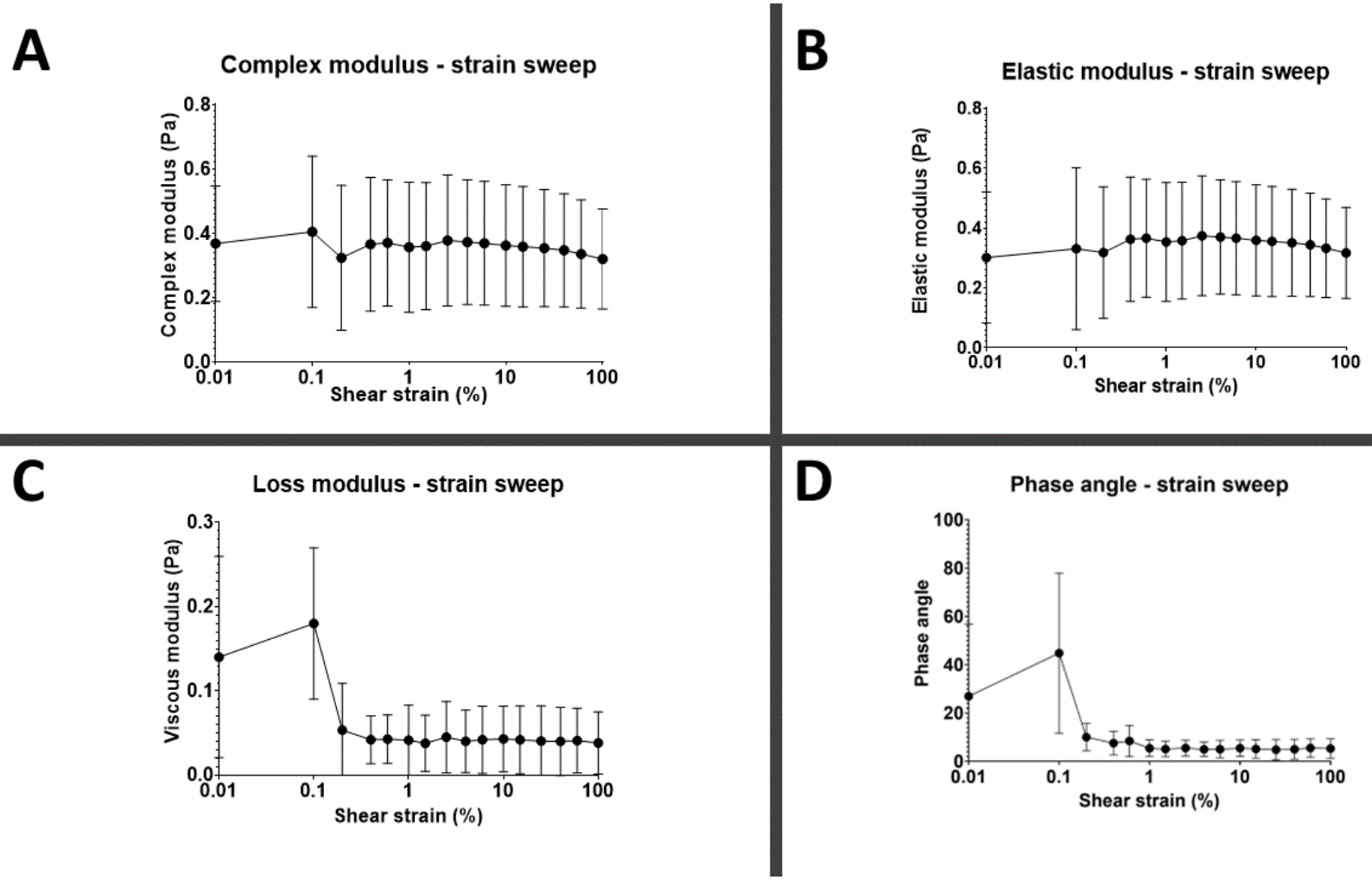

The change in phase angle from relatively high (indicating a more liquid behaviour, with the loss modulus contributing a large proportion of the complex modulus) to very low (indicating a more solid behaviour, with a low contribution from loss modulus) supports the theory that excess PBS was squeezed from the samples during these initial measurements. This was also confirmed visually; samples became more compact and homogeneous as measurements proceeded, and felt substantially less "loose" when removed from the sample plate than prior to measurement.

Mean complex and storage shear modulus values from the strain sweep samples are lower than the fixed-strain samples, however when converted to elastic modulus are still approximately a factor of ten lower than values obtained from whole mouse brain in the literature (ECM values from these experiments were fractions of a Pascal, whereas even the lowest values for whole brain in the literature are in the tens of Pascals).

A single ECM sample was subjected to a frequency sweep measurement. Due to the long duration of these measurements and relatively low importance to the study (most injuries resulting from optrode implant insertion have a very low frequency, unlike – for example – shockwave-induced brain injury from explosives, or collision-induced brain injury in contact sports), only one sample was measured in this way (Figure 20).

The frequency sweep experiment showed an exponential increase in elastic shear modulus from approximately 5 Hz and higher frequency (elastic modulus at 4 Hz was 3.4 Pa, increasing to 9.0 Pa at 5 Hz and peaking at 51 Pa at 10 Hz). This suggests that the relaxation period of most molecules in the ECM sample was ≥0.25 seconds – at higher frequencies, the sample could not relax fully before the next measurement and so appeared to be stiffer.

The frequency-dependent nature of the ECM's mechanical properties may be explained by the deformation frequency outpacing the relaxation period of structures in the sample; when measurements are taken more rapidly than the structure can relax, the storage modulus will appear higher. Alternatively, repeated deformation of the sample may have caused structural rearrangement, producing tangled or interlinked fibrous structures that more strongly resist deformation.

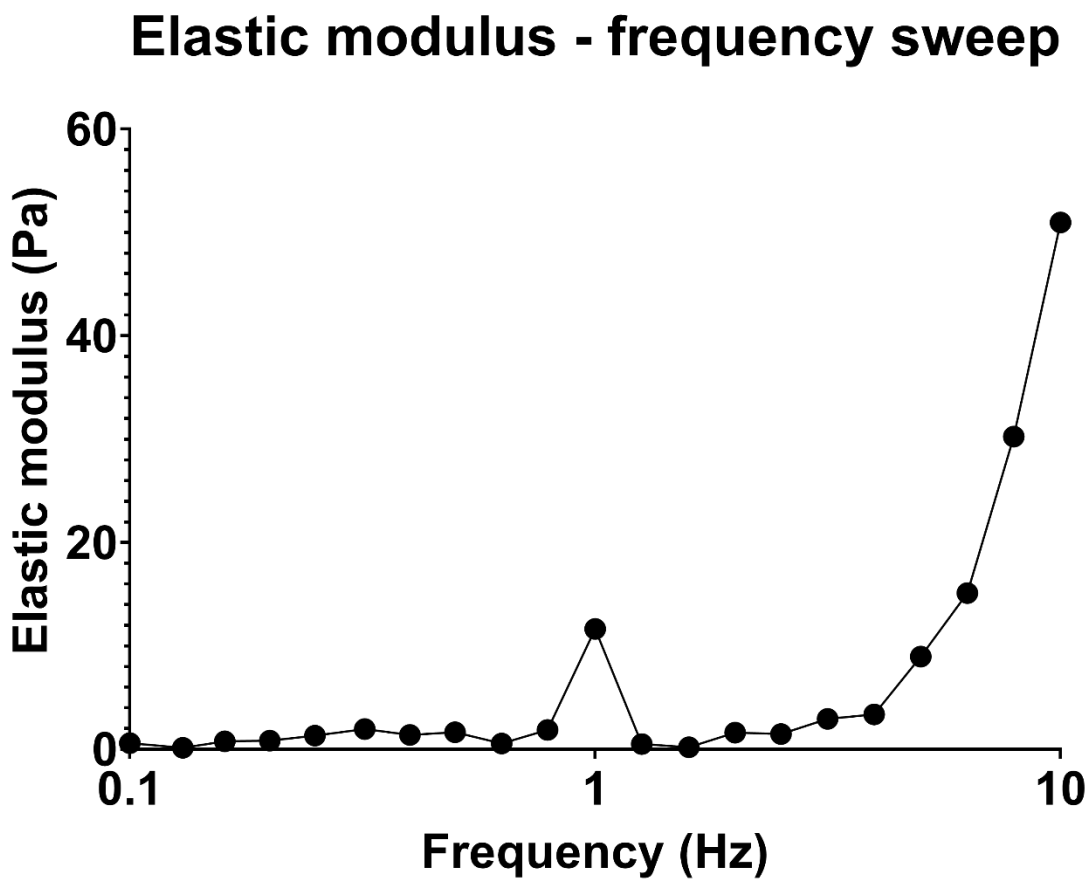

Figure 20: Elastic modulus of a CRL-2541 cell-derived ECM sample analysed with a frequency sweep rheological measurement.

4.4. Conclusion

The results of these rheological measurements suggest that the major contributing elements of mouse brain tissue to stiffness are likely to be cells and cell-cell or cell-ECM connections rather than the ECM itself – though it is possible that this is unique to the CRL-2541 cell line, or that ECM produced by a mixture of cell types *in vivo* may differ significantly from that obtained from monolayer culture from a single cell type. It is also possible that ECM produced in thicker layers (via 3D culture) may better reflect that produced *in vivo*.

This was the first time — to my knowledge — that cell-derived ECM has been produced from CRL-2541 astrocytes, though ECM has been produced from astrocyte primary culture in the past[407–409]. Whilst these experiments were successful in creating and measuring the mechanical properties of CRL-2541 astrocyte-derived ECM samples, they are unlikely to be useful in analysis of stiffness changes resulting from surgical trauma during and after implantation of optogenetic devices. Instead, further experiments should utilise samples more representative of whole brain, such as acute brain slices or organotypic cultures.

Chapter 5. Results: Acute Brain Slice Elastic Modulus Decreases over Time

5.1. Introduction

Elastic modulus measurements of brain tissue have been used to investigate axonal demyelination[289], developmental biology[291], brain tumours[418,419], hydrocephalus[420], glial scar formation after trauma[217] and a wide range of other biological questions. Additionally, data on the mechanical properties of brain tissue are useful in the development of medical products such as electrode implants and personal protective equipment (e.g. helmets).

Measuring elastic moduli of acute brain slices has several advantages over *in vivo* measurements. Firstly, ethical considerations for tissue that is used *ex vivo* are less strict, reducing both welfare concerns and regulatory burden. Additionally, multiple slices may be obtained and measured from the same brain, and access is granted to deeper regions of the tissue; in a living animal it can be difficult to probe mechanical properties below the surface of the tissue with conventional indentation-based techniques. Experimental setup is generally more convenient with acute brain slices, since sedation, brain windows and restraints are unnecessary. Unfortunately, acute brain slice experiments also have limitations: tissue is subjected to mechanical trauma during slicing, raising questions about whether measurements are of healthy or injured regions. Acute brain slices are not subject to the normal intracranial pressure (~4-7 mmHg[421–424] in mice) due to their removal from the skull and lack of cerebrospinal fluid pressure. Additionally, phenomena such as Donnan swelling due to exposure of intracellular charged molecules during slicing have the potential to substantially alter mechanical properties of tissues[313].

Atomic force microscopy (AFM) is a popular method for mechanical analysis of brain tissue although sample softness, fouling of the cantilever, the need for an aqueous environment (that damps cantilever motion and introduces capillary forces) and cantilever fouling all complicate its use in biological samples[244]. AFM cantilevers

typically only penetrate short distances during force spectroscopy measurements, limited by the length of the cantilever tip (typically 2 – 20 µm for AFM cantilevers with spherical tips suitable for measuring soft tissue[425]), meaning that such measurements are almost entirely restricted to the outer layer of a slice where the majority of trauma from slicing, cell debris and Donnan swelling will be located. Measuring at greater depths would necessitate further slicing or scraping of debris from the surface, which is likely to simply produce further trauma and debris. Due to the sensitive nature of AFM, perfusion methods intended to provide acute brain slices with a constant flow of carbogen or fresh artificial cerebrospinal fluid (aCSF) are liable to introduce noise to the AFM results; both interface-type and immersion-type slice chambers introduce aCSF flow and carbogen bubbles[426]. Observations of brain slices immediately post-slicing show substantial debris from the slicing process, whilst slices kept in culture tend to "flatten" onto their substrate – indicating substantial mechanical remodelling[427].

In literature discussing mechanical analysis of brain tissue, it is often asserted that acute brain slices should be measured within 6-8 hours of the experimental animal being sacrificed [231,276,288,292,293,296,298,299,428] with the rationale that, since protein degradation is typically only observed after 8 hours, the tissue's elastic modulus will remain stable during this period [314,429]. This neglects the various factors discussed above that might modify mechanical properties of the tissue. Furthermore, acute slice preparation protocols typically include 45 – 60 min in a "recovery" chamber. This step is designed to improve neural survival and to promote healthy action potentials for electrophysiological analysis, but is a lengthy and often inconsistent period in which Donnan swelling and tissue trauma could substantially affect later measurements[267].

Cerebrospinal fluid (CSF) in healthy mice was reported to be 313 ± 2 mOsm/l[430]. The CSF osmolality of rats has been measured as ~307 mOsm/l[431–433], suggesting that the two species are similar in this regard. By contrast, human CSF values average closer to 260 mOsm/l[434,435]; around 15% lower. Artificial cerebrospinal fluid recipes,

which are largely developed for electrophysiological work and optimised to produce “healthy” action potentials in neurons (not to produce an environment in which brain tissue has stable mechanical properties), call for an osmolality of 280-338 mOsm/l depending on protocol and species[267,427,436]. Whilst this lack of consistency may be of no importance to electrophysiological behaviour, osmotic effects on tissue swelling and hydration could substantially affect mechanical properties.

It has been argued that brain oedema following traumatic brain injury is primarily driven by intracellular fixed charge density (FCD) becoming accessible as injured cells lyse. This would trigger the movement of further fluid into the tissue following the resulting osmotic gradient, causing swelling and ischemia due to increased pressure. Chondroitin sulphate proteoglycans (CSPGs) have been implicated as the source of much of this FCD in brain tissue[275,313,437], and several studies support this by identifying intracellular CSPG content in astrocytes and neurons[438,439]. However, recent understanding of the role of CSPGs in brain tissue suggests that most CSPG content exists extracellularly as part of the ECM, and it is generally considered to be an extracellular molecule and is suggested to form an physical obstacle that serves to repair the blood-brain barrier after traumatic brain injury[440]. Despite this, treatment with chondroitinase ABC (ChABC) has been demonstrated to reduce brain slice swelling in *ex vivo* acute brain slice experiments[275] and *in vivo* mouse models of oedema[437], suggesting involvement of CSPGs in brain tissue osmotic swelling.

It is possible that the FCD contribution from CSPGs is limited solely to CSPGs that are being synthesised or transported out of astrocytes and neurons and so remain intracellular at the time that the tissue is injured. Alternatively, it has been suggested that brain oedema is contributed to by the presence of charged products of brain tissue metabolism that are too large to diffuse readily through brain tissue, and so act to produce an osmotic gradient in a similar way to exposed FCD[441]. Mathematical models of brain tissue oedema support the hypothesis of a combined mechanism, with both exposed intracellular FCD and “trapped” solutes contributing to the osmotic

gradient[442]. Perhaps the presence of CSPGs in brain ECM acts as a mechanical barrier to the transport of these solutes out of the tissue; this would explain why treatment of brain oedema with ChABC is effective despite the relatively low intracellular CSPG content, breaking down the barriers in brain ECM that prevent osmotically active solutes from escaping into the surrounding medium.

Indentation measurements of healthy mouse brain in the literature show elastic modulus values ranging from 0.03 to 12.07 kPa[231,289–293,298,299], with little consistency with regard to animal strain, sex, age, temperature, AFM cantilever properties, indentation (depth, frequency, strain) or slice preparation method. It is thus difficult to compare across the literature to determine the potential effect of time after slicing on measured elastic modulus. In this study, a consistent protocol is used to determine the effect of post-slice time on the mechanical properties of mouse brain slices. Measurements of tissue swelling and hydration — both properties linked to mechanical properties due to osmotic effects — are also performed. Additionally, the effects of modifying aCSF osmolality or of degrading chondroitin sulphate proteoglycans (whether intracellular or extracellular) with chondroitinase ABC enzyme (cABC) are explored.

5.2. Results and Discussion

All animals used were female CD1 mice from Charles River Laboratories between 5 and 8 weeks of age – see chapter 2 for more information.

5.2.1. Protein degradation analysis

It has been asserted that since significant protein degradation does not occur in brain tissue until ~8 h post mortem, and structural proteins will not have had time to degrade, significant alterations to mechanical properties will not occur during that period[231,276,288,292,293,298,299,428]. To monitor protein degradation over time, pooled mouse brain slices (4 animals, approx. 4 slices of 400 µm thickness per time point) were incubated in 300 mOsm/l aCSF at 4°C for 0.5 h and 4 h, or at room temperature for 48 h. Western blots were then performed to observe changes to protein integrity at these time-points, as seen in Figure 21.

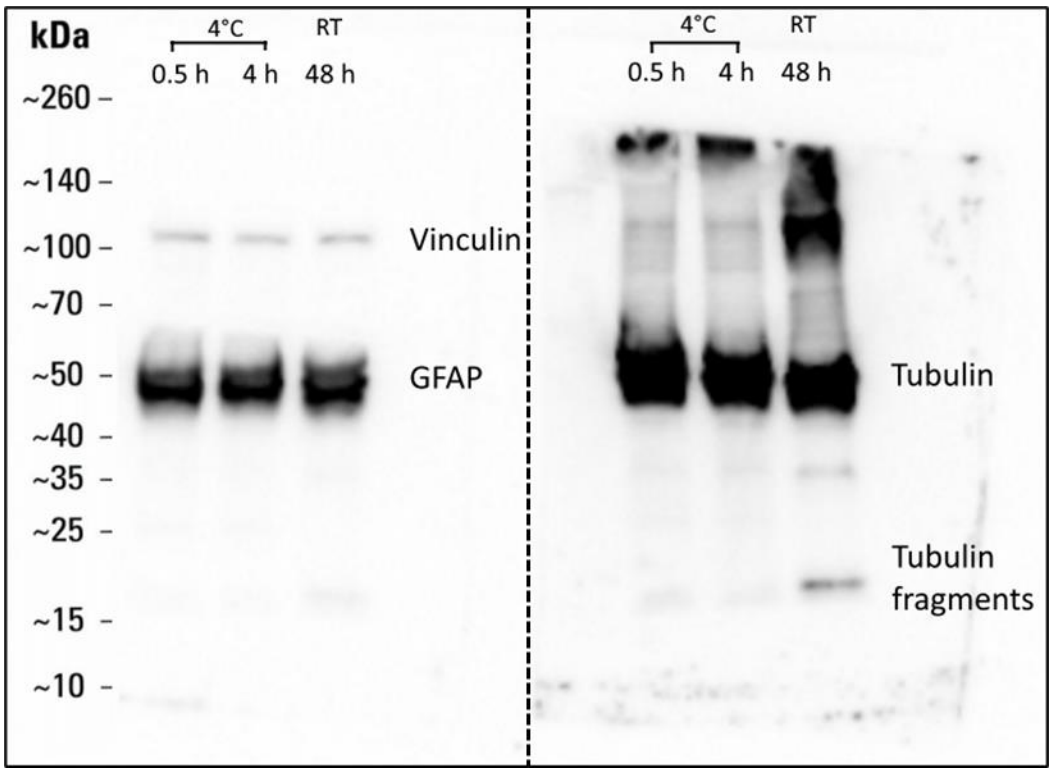

Figure 21: Western blot of vinculin, GFAP and α-tubulin does not show substantial protein degradation after 4 h at 4°C. Acute mouse brain slices incubated at 4°C for 0.5 or 2 h do not show fragments of vinculin, GFAP or tubulin, indicating there is not substantial degradation of these proteins. Slices incubated at RT show fragmentation of tubulin, but not of vinculin or GFAP. The left panel shows a single full-length membrane probed simultaneously with Vinculin and GFAP antibodies. The right panel shows a duplicate single full-length membrane probed with a-tubulin antibody.

Glial fibrillary acidic protein (GFAP) and α-tubulin were selected as they were some of the first proteins to show significant degradation in previous studies of post mortem brain[314,429], and vinculin was included as another cytoskeletal protein that is abundant in brain tissue.

Consistent with previous studies, after 48 h at room temperature, two distinct fragment bands of tubulin were observed as seen, and possibly minor degradation of GFAP — suggesting that degradation was occurring. All subsequent experiments were carried out over a period of 4 h, when it is reasonable to assume that protein degradation is not a significant factor in any mechanical changes observed.

5.2.2. AFM analysis of acute brain slice elastic modulus

Donnan swelling of brain tissue is caused by the fixed charge density of the tissue; when cells are damaged by trauma and their plasma membrane is compromised, charged molecules inside are exposed to the external environment. Since the cells can no longer maintain effective osmotic homeostasis via active pumping, water enters the tissue and causes swelling. Since the elastic components of the cells, cell debris and ECM are now distributed throughout a larger volume, the elastic modulus of the tissue decreases. This process is not instantaneous, and can occur over a period of hours or days, depending on the degree of tissue trauma[275,313]. Since Donnan swelling is a progressive phenomenon that increases over time, it follows that any alteration to tissue mechanical properties would increase as a function of the degree to which swelling has occurred.

To establish whether brain tissue elastic modulus changed significantly post-slicing, AFM indentation tests were performed on acute coronal brain slices in normal (300 mOsm/l) aCSF (see a representative force-distance curve in Figure 22). To test whether increasing aCSF osmolarity prevented changes to tissue elastic modulus, these measurements were repeated with aCSF adjusted to 400 mOsm/l. To investigate the potential effect of degrading fixed-charge density (in the form of

chondroitin sulphate proteoglycans) on changes to elastic modulus post-slicing, measurements were repeated with aCSF supplemented with 0.1 U/ml chondroitinase ABC enzyme.

Six mice were used per condition. Mice were sacrificed & brains were sliced coronally into 400 µm thick slices. One slice per animal was used for the whole time-course, measuring a square grid of ~60 points separated by 10 µm for each timepoint. At each timepoint, a new grid was measured near to the last, to avoid error that might arise from taking multiple measurements in the same location. All measurements were taken in the cortex (approximately central between the pial surface and the white matter, layer 3-5, bordering the hippocampus – Appendix B, green), since it is a large region that has been reported to be relatively consistent in elastic modulus across its volume[292]. All operations were carried out in fresh aCSF bubbled with carbogen. The aCSF was chilled (~4°C) to reduce metabolic rate and therefore oxygen and glucose consumption. To avoid potential vibration or noise from a perfusion system, aCSF was replaced via pipette every 10 min to maintain temperature between measurements.

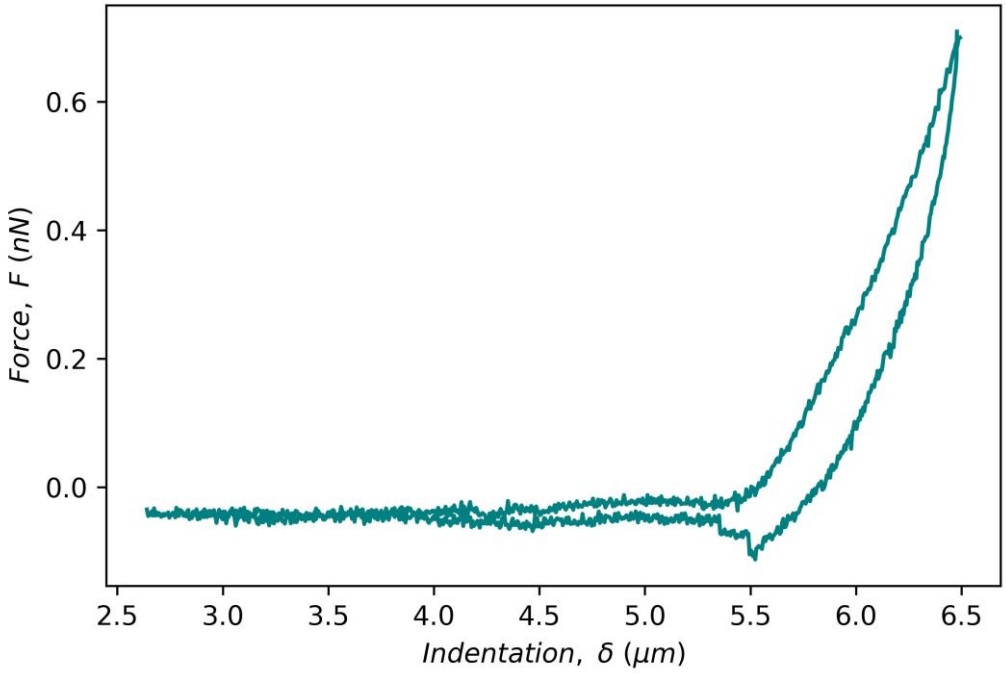

Figure 22: A representative AFM force-displacement curve for acute mouse brain slices. The negative force during unloading is due to strong adhesion between the AFM probe and tissue.

As seen in Figure 23, the elastic moduli of slices decreased with time in all conditions (300 mOsm/l: 330 ± 130 Pa at 0.5 h to 122 ± 49 Pa 4 h, 400 mOsm/l: 159 ± 52 Pa at 0.5 h to 101 ± 62 Pa at 4 h, ChABC: 246 ± 135 at 0.5 h to 152 ± 68 Pa at 3.5 h) and reached a plateau at ~2 h. However, the least variation across timepoints was seen at 400 mOsm/l. The overall reduction was modest, and it was the only condition in which elastic modulus increased above its starting value (between 2 and 3 h). At 2 h, the 400mOsm condition's elastic modulus was significantly higher than the 300 mOsm (p = 0.03) and ChABC-treated (p = 0.036) conditions, suggesting that the higher osmolarity may produce a more mechanically-stable sample across this timescale. However, the elastic modulus at 0.5 h was substantially lower than that in the 300 mOsm and ChABC conditions and was approximately the same as the 300 mOsm/l condition at ≥ 2 h, suggesting that whilst this condition may equilibrate at a higher elastic modulus, the initial changes may occur more rapidly than in other conditions. A post-hoc Tukey analysis of the three treatment conditions at 0.5 h

supports this, indicating that the 400 mOsm condition was significantly softer than either 300 mOsm or ChABC-treated samples (p = 0.0310). The ChABC treated samples showed similar values to the 300 mOsm samples until 3.5 h, when its stiffness increased.

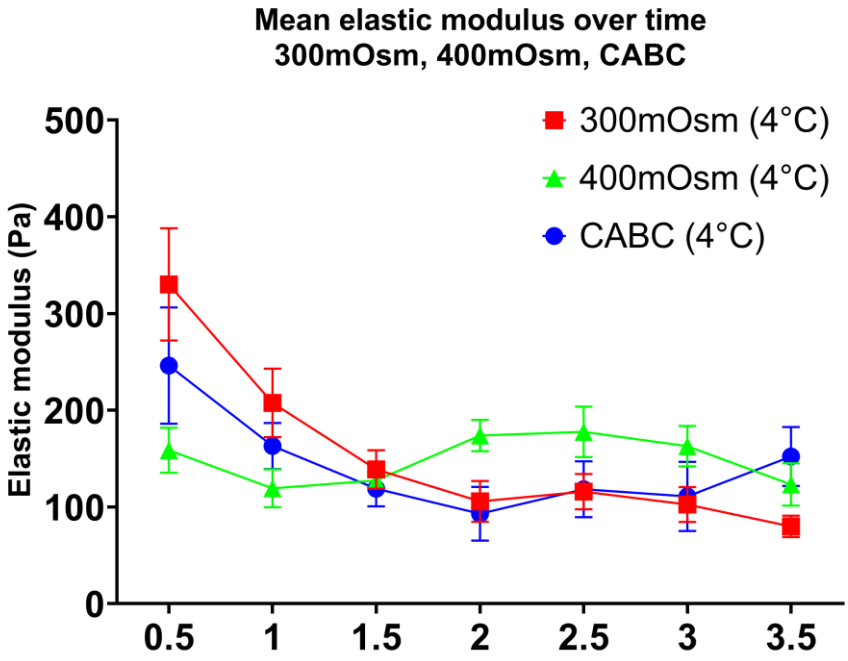

Figure 23: Acute brain slice elastic modulus as measured with AFM decreases rapidly after slicing. Elastic modulus decreases with time in 300 mOsm/l and ChABC conditions, plateauing at ~2 h. 400 mOsm/l condition begins at a lower elastic modulus than other conditions, but remains relatively stable. Bars show +/- standard error of the mean. N = 6 animals per condition.

Two-way mixed-effects model analysis of the elastic modulus results returned a significant ($p < 0.0001$) relationship of time to elastic modulus, indicating that acute mouse brain slices are not mechanically stable across this timeframe. Mouse-to-mouse variation was however high, accounting for 30.88% of the total variation.

5.2.3. Acute brain slice hydration analysis

If the observed changes to acute brain slice elastic modulus were due to Donnan swelling or other osmotic factors, it would be expected that tissue hydration would have an inverse relationship to elastic modulus. To investigate this, the hydration level of samples immersed in 300 mOsm/l, 400 mOsm/l, ChABC-treated 300 mOsm/l (all at 4°C) and ChABC-treated 300 mOsm/l (at RT) was compared over a 4 h period post-slicing (Figure 24). Six mice were used per condition. Brain tissue hydration

increased over time post-slicing (300 mOsm/l: 88% ± 1.6 to 89% ± 1.4, 400 mOsm/l: 86% ±1.0 to 89% ± 0.5, ChABC 4°C: 85% ±0.4 to 89% ± 0.3, ChABC RT: 87% ± 1.4 to 92% ±0.8), tending to stabilise at approximately 2 - 2.5 h as in the elastic modulus data.

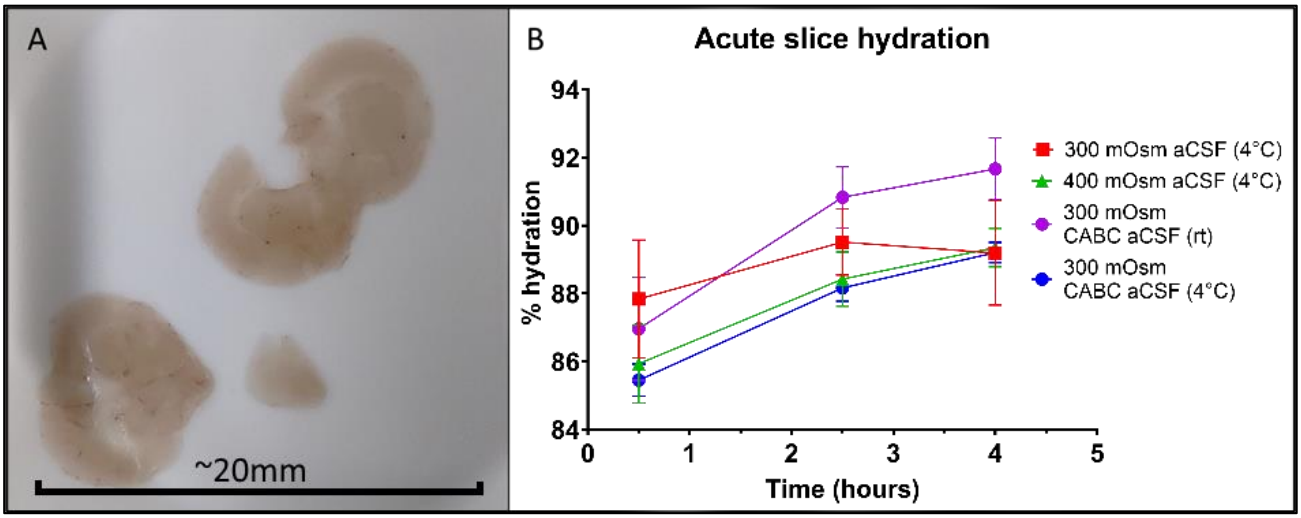

Figure 24: Acute brain slice hydration increases over time. (A) A representative image of an acute mouse brain slice air dried at 37°C for 48 h. (B) Brain slice hydration tends to increase over time. Bars show mean +/- standard deviation. N = 6 animals per condition.

Two-way mixed-effects model analysis of the hydration data showed a significant relationship of time ($p < 0.0001$) and treatment ($p = 0.0007$) to tissue hydration, with no significant mouse-to-mouse variation ($p = 0.5037$). Increases in tissue hydration were significantly delayed in the 400 mOsm/l aCSF and the 4°C ChABC-treated samples, but reached approximately the same peak hydration at 4 h, whilst the water content of the room temperature ChABC-treated samples climbed throughout, ending with higher hydration than the other two conditions.

Multiple comparisons results from the mixed-effects analysis showed that the room temperature ChABC-treated tissue was significantly more hydrated than the 300 mOsm/l ($p = 0.0223$ at 4 h) and 400 mOsm/l ($p = 0.0017$ at 1.5 h and $p = 0.0016$ at 4 h) conditions. This more rapid and extensive hydration of the room temperature ChABC-treated samples is likely to be due to the increased temperature causing more rapid consumption of oxygen and glucose as well as accelerating apoptosis, outweighing the effect of the enzyme.

In summary, increasing aCSF osmolarity had a significant delaying effect on increases to tissue hydration but did not prevent the changes from occurring. Temperature was a major factor; room temperature ChABC-treated samples experienced a substantially larger increase in hydration than the other three conditions at 4°C. ChABC treatment at 4°C had the largest delaying effect, but eventually reached the same hydration level as 300 mOsm/l and 400 mOsm/l aCSF conditions. This suggests that temperature and time are the two most important variables for minimising increases in brain slice hydration, followed by ChABC treatment and osmolarity.

5.2.4. Acute brain slice volume analysis

If changes to the elastic modulus of the tissue were primarily caused by osmotic swelling rather than degradation of structural proteins, it would be expected that tissue whose elastic modulus decreases over time will see a concomitant increase in volume. To investigate whether acute brain slices swell over time, 400 µm thick acute coronal brain slices were obtained from 16 mice (4 animals per condition) and incubated in 300 mOsm/l, 400 mOsm/l and ChABC-treated 300 mOsm/l oxygenated aCSF at 4°C, and ChABC-treated 300 mOsm/l aCSF at room temperature. The slices were photographed from a fixed camera at 0.5 h increments. The change in planar area (XY plane) was measured as XY swelling. As brain tissue swelling can be assumed to be approximately isotropic[443], XY swelling data were transformed into approximate volumetric swelling values by raising to a power of 3/2. The volume swelling ratio was obtained by dividing the original volume of each slice by its final volume.

As seen in Figure 25, brain tissue volume increased over time post-slicing (volume swelling ratio at 4 h of 300 mOsm/l: 1.3 ± 0.1, 400 mOsm/l: 1.3 ± 0.1, ChABC 4°C: 1.0 ± 0.2, ChABC RT: 1.4 ± 0.2 respectively). Swelling was lower for the 400 mOsm/l condition than the 300 mOsm/l condition until 4 h, where the two conditions converge. Room-temperature ChABC-treated tissue swelled rapidly and more

extensively than in other conditions, stabilising at approximately 2 h, whereas chilled ChABC-treated samples showed similar swelling rates to the 300- and 400 mOsm/l conditions but stabilised quickly and recovered to approximately their original size by 4 h. Two-way mixed-effects analysis of the data shows that tissue volume is significantly associated with time ($p < 0.0001$) and treatment ($p < 0.0001$). Although there was mouse-to-mouse variation, this did not reach a high level of significance ($p = 0.139$).

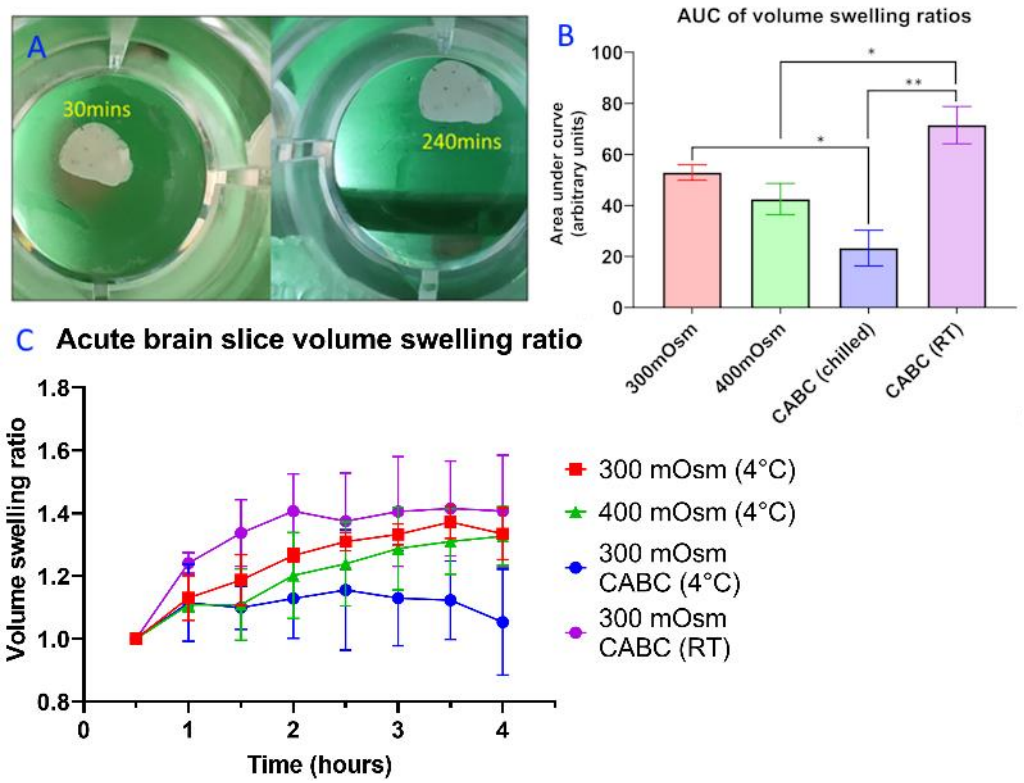

Figure 25: Acute brain slices swell over time. (A) A representative acute brain slice at 0.5 and 4 h post-slicing. (B) A comparison of area-under-curve (AUC) values for brain slices at different conditions. (C) Temporal change of volume swelling ratio at different conditions. Results presented were averaged values +/- standard deviation, n = 4 animals per condition.

A one-way ANOVA indicates that there is significant influence from the different conditions on area-under-curve (AUC), where a higher AUC represents greater swelling across the course of the experiment ($p = 0.001$). Multiple comparison tests suggest that the chilled ChABC condition had a significantly lower AUC than the 300 mOsm/l samples ($p = 0.0224$) and that the room-temperature ChABC-treated samples had significantly higher AUC than the 400 mOsm/l and chilled ChABC samples ($p = 0.0256$ and $p = 0.0006$, respectively).

In summary, increasing aCSF osmolarity delayed — but did not prevent — brain slice swelling. Room-temperature ChABC-treated brain slices swelled substantially more than other conditions, and 4°C ChABC-treated slices both experienced delayed and reduced swelling than the other three conditions. This suggests that — as with slice hydration — temperature and time are the most important factors for brain slice swelling, followed by ChABC treatment and osmolarity.

5.3. Conclusion

Swelling of sliced brain tissue has been described previously in studies of brain oedema[313], however the effect of this on elastic modulus has not been widely considered in the brain mechanics literature. Here we show that considerable changes in the mechanical properties of mouse brain slices occur within time frames during which such properties are typically assumed to be stable.

Garo *et al.* (2007) suggest that the elastic modulus of porcine brain tissue remains stable for ~6 h *post mortem*, after which the tissue begins to stiffen[444]. Whilst this may be true, the samples used by Garo *et al.* were subject to delays of up to 3 h prior to slicing and measurement, and measurements were conducted from 2.5 to 10 h *post mortem*. This puts their findings mostly outside the 0.5 - 4 h time window investigated in this study, and certainly beyond the period up to 2 h during which we observed the most substantial changes. Additionally, samples were stored as whole brain in unoxygenated saline without glucose, raising the concern that they were no longer alive at the point of measurement, and will likely behave differently from brain slices kept in oxygenated aCSF. Our study extends understanding of *ex vivo* brain tissue mechanics into an earlier period *post mortem*.

Since brain slice oedema has been largely attributed to the Donnan effect[313] (where a compromised cell containing fixed negative charge is flooded with water when it can no longer actively maintain osmotic homeostasis), it might be assumed that brain slices sufficiently provided with oxygen and glucose will not swell or soften over time.

However, damage caused by slicing — and resultant Donnan swelling — is likely to occur at depths beyond that reached by an atomic force microscope. Indeed, we demonstrate progressive changes in the swelling, hydration, and elastic modulus of brain tissue — even when provided with oxygen and glucose — immediately after slicing, progressing rapidly within the first few hours.

The swelling data implicate CSPGs as contributors to fixed charge density in swelling of acute brain slices, since digesting them enzymatically has a limited but significant mitigating effect – predominantly in the first hour after slicing. However, it is questionable whether this method would be usefully applicable to experimental study of brain tissue mechanics since the enzyme alters extracellular matrix and intracellular architecture, complicating the interpretation of data from ChABC-treated samples. ChABC activity increases at higher temperatures. However, since temperature also appears to be a major factor in brain slice swelling (a relationship supported by existing literature on brain oedema[445]), any benefit from temperature increase on ChABC activity would need to exceed the resultant increase in swelling rate due to this temperature increase.

Adjusting aCSF osmolarity to 400 mOsm/l did not prevent changes to hydration or swelling but did serve to delay these changes. It would be expected from these results that there would be a similar delay in reductions of tissue elastic modulus. However, the fact that the elastic modulus of the 400 mOsm/l-treated tissue was already lower at the first measured time point (0.5 h) than in other conditions suggests that an additional unknown mechanism rapidly alters the mechanical properties of the slices in these conditions.

Aside from treatment with ChABC, the factors that most greatly affected tissue hydration, swelling and elastic modulus were time and temperature. Slices swelled, softened and became more hydrated rapidly from the moment of slicing, and slices incubated at room temperature showed substantially more rapid changes. There

appears to be some correlation between elastic modulus, hydration and volume in 300 mOsm, 400 mOsm and ChABC, as shown in Figure 26.

These results suggest that when carrying out indentation analysis of acute brain slices, measurements must be carried out as rapidly as possible, at a consistent time, and in chilled conditions. Whilst use of non-physiological temperatures is non-ideal, the strong relationship of temperature to brain tissue oedema means that at higher temperatures, variation in post-sacrifice delay of as little as minutes can dramatically affect elastic modulus. Considering this, use of lower temperatures with consistent outcomes is preferable to use of physiological temperatures with unreliable outcomes. Alternatively, measurements can be made when ongoing changes in tissue properties are less pronounced (e.g. 2 to 4 h post slicing), with the understanding that these measurements will be less reflective of those found in the intact tissue. The common assumption that elastic modulus is stable for up to 8 h post-slicing is inaccurate.

To fully eliminate osmotic swelling and other *ex vivo* changes from an experiment, measurements must be carried out *in vivo* using non-invasive methods such as magnetic resonance elastography, which allows measurement at physiological temperatures and in fully intact brain. As such, this method is strongly recommended as the ideal approach for measuring mouse brain elastic modulus.

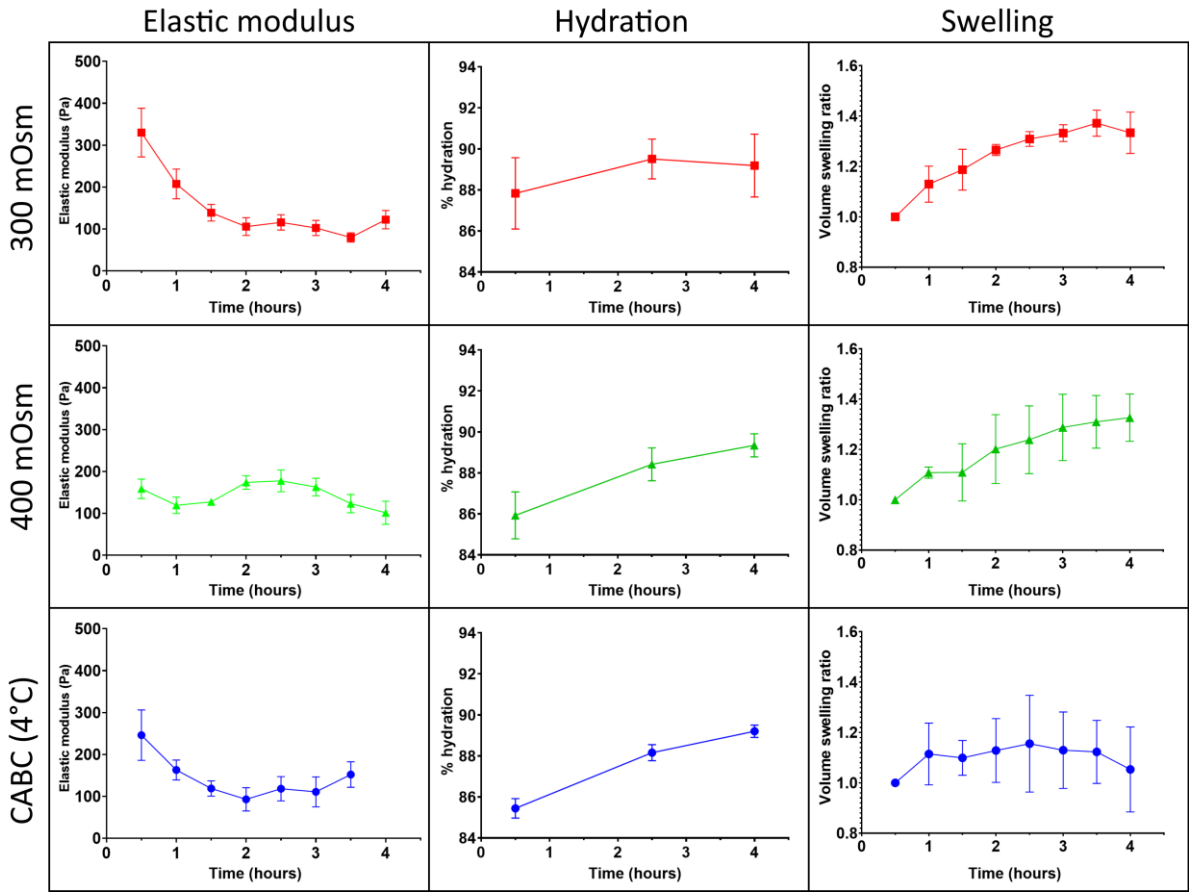

Figure 26: Changes in acute mouse brain slice elastic modulus, hydration and volume appear to correlate with time across each treatment (300 mOsm, 400 mOsm and ChABC-treated).

Chapter 6. Results: Optical Toxicity in Brain

6.1. Introduction

It is clear that further research into the effects of light exposure (in both acute and chronic timescales) on brain tissue is required in order to effectively assess the safety of emerging optogenetic medical devices.

A major goal of such work should be to establish a scale for wavelength, intensity and duration of light exposure and its relation to brain tissue toxicity. Such data (similar to that presently used by regulatory agencies for assessment of light hazard to skin and retina) would allow more confident evaluation of novel optogenetic medical devices and their suitability for human trials.

Ideally, experiments to quantify optical toxicity in brain would be carried out *in vivo*, in a system as similar as possible to that of human patient brain. The ideal model system would therefore be a chronic, *in vivo* optrode insertion into nonhuman primate (NHP) brain tissue, using illumination intensity, wavelength and pulse pattern similar to that which might be employed for therapeutic applications.

Such work has obvious ethical considerations that must be addressed; NHPs are intelligent and capable of suffering, and justification of experiments involving chronic transcranial implantation of an optrode must be backed with robust proof-of-concept experiments in a simpler and less ethically expensive model. Additionally, NHPs and their upkeep are costly; development of an experimental protocol on a simpler model with less stringent ethical demands is indicated before moving on to this type of model.

Whilst optogenetics employs a wide range of wavelengths for stimulation, toxicity arising from blue-wavelength visible light exposure has been documented in multiple studies with multiple types of cells and tissue. 470 nm blue light occupies the higher-

energy portion of the visible spectrum and is likely to be more damaging than longer wavelengths.

As such, preliminary experiments were carried out using a 470 nm LED with intensities ranging from 0 to 16 mW, emitted from a 400 µm diameter glass optical fibre. This emitter was used to illuminate acute cortical mouse brain slices which were then fixed and stained for markers of cell death. Early results with one marker (TUNEL) were promising, however a reliable protocol could not be developed – additional markers were trialled in an attempt to identify a reliable method for quantifying light-induced cell death.

After several failed attempts to develop a reliable method, it was decided to move to a simpler model and to identify what factor(s) may be preventing successful detection of light-induced cell death. Monolayer cultures of CRL2541 immortalised cerebellar mouse astrocytes were exposed to light and stained with Live-Dead NIR (Thermo Fisher) and it was determined that successful detection of light-induced cell death relies on allowing sufficient time for apoptosis to occur after light exposure. A modified protocol was developed to account for this requirement and was used to quantify the relationship of 470 nm light intensity with cell death in acute mouse brain slices.

6.2. Results and discussion

6.2.1. Optical fibre spot analysis

Before light exposure experiments could commence, it was necessary to determine the illumination pattern that the fibre-coupled LED produced. A camera chip was arranged with the optical fibre (and thus the emitted light cone) oriented at 90° to it, with approximately 100 µm of separation. Ximea software was used to record the illumination spot and intensity (Figure 27). The illumination intensity was approximately consistent across the 400 µm diameter of the emitted light spot, and rapidly decreased with lateral distance from the fibre edge. This suggests that provided the optical fibre tip is within 100 µm of the sample surface, illumination at the surface will approximate this pattern – any scattering will be due to the properties of the sample as opposed to the optical fibre.

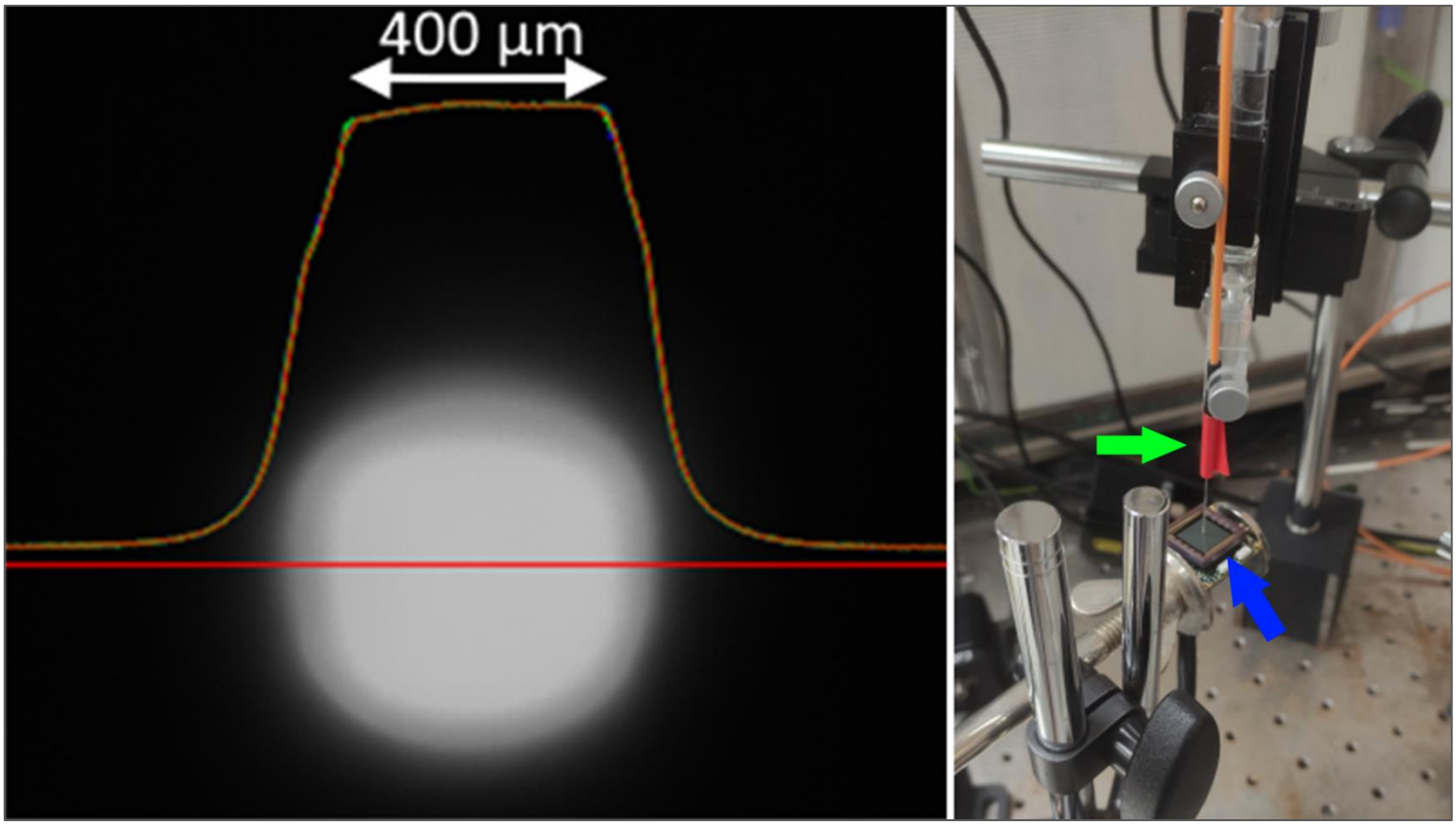

Figure 27: Apparatus for measurement of light spot intensity. A camera chip (blue arrow) was arranged with the optical fibre (green arrow) oriented at 90°, with approximately 100 µm of separation. Ximea software was used to record the spot.

6.2.2. TUNEL staining of light-exposed acute mouse brain slices

A 14-week old male SOM-CRE mouse[446] was sacrificed via cervical dislocation, its brain dissected and cut into 200 µm thick slices with a vibratome (methods). Twelve acute brain slices were obtained. This mouse was selected as it was scheduled for culling, and it was determined that since the knock-in cre recombinase activity is inducible – and by default inactive – the model would be suitably similar to wild-type for initial feasibility experiments. The slices were exposed to 15.94 mW light at 470 nm, with a 50% duty cycle and a pulse duration of 100 ms. Six slices were exposed for 30 min and the remaining six for 60 min, then were fixed in paraformaldehyde, sectioned with a sled microtome with freezing stage and stained with TUNEL (an enzymatic staining method that attaches fluorescently-tagged nucleotides to the ends of fragmented DNA, used as a marker for apoptosis) and a propidium iodide nuclear counterstain (methods).

TUNEL staining showed clear circular regions of punctate staining in the exposed locations (Figure 28 A & B). This is not the usual expected staining pattern of TUNEL, which will typically localise to affected cell nuclei and would thus be expected to colocalise with the propidium iodide. It is possible that the TUNEL stained only DNA fragments from cells that had been lysed, or that the fluorescent label bound non-specifically to necrotic cell fragments[447].

TUNEL intensity was low at the edges of the exposed region, increasing as it approached the centre. Whilst the optical fibre output was relatively consistent across the 400 µm surface illumination spot, slices from deeper into the sample will have experienced light scattering, making the absolute centre of the illuminated region brighter than the edges. The intensity of staining was higher across the whole exposed region in 60 min samples than in those exposed for 30 min (Figure 28 C).

Additional slices from another SOM-CRE mouse (male, 15 weeks) were exposed to lower intensity light (4.7 mW) for a longer period of 180 min, resulting in a substantially brighter spot whose intensity was consistent across the full 400 µm site, fading rapidly with lateral distance beyond this region (Figure 28 D). This matches the illumination spot of the optical fibre much more closely, suggesting that almost all cells in the exposed region had died and that scattered light was insufficient to cause toxicity in cells outside the illuminated region.

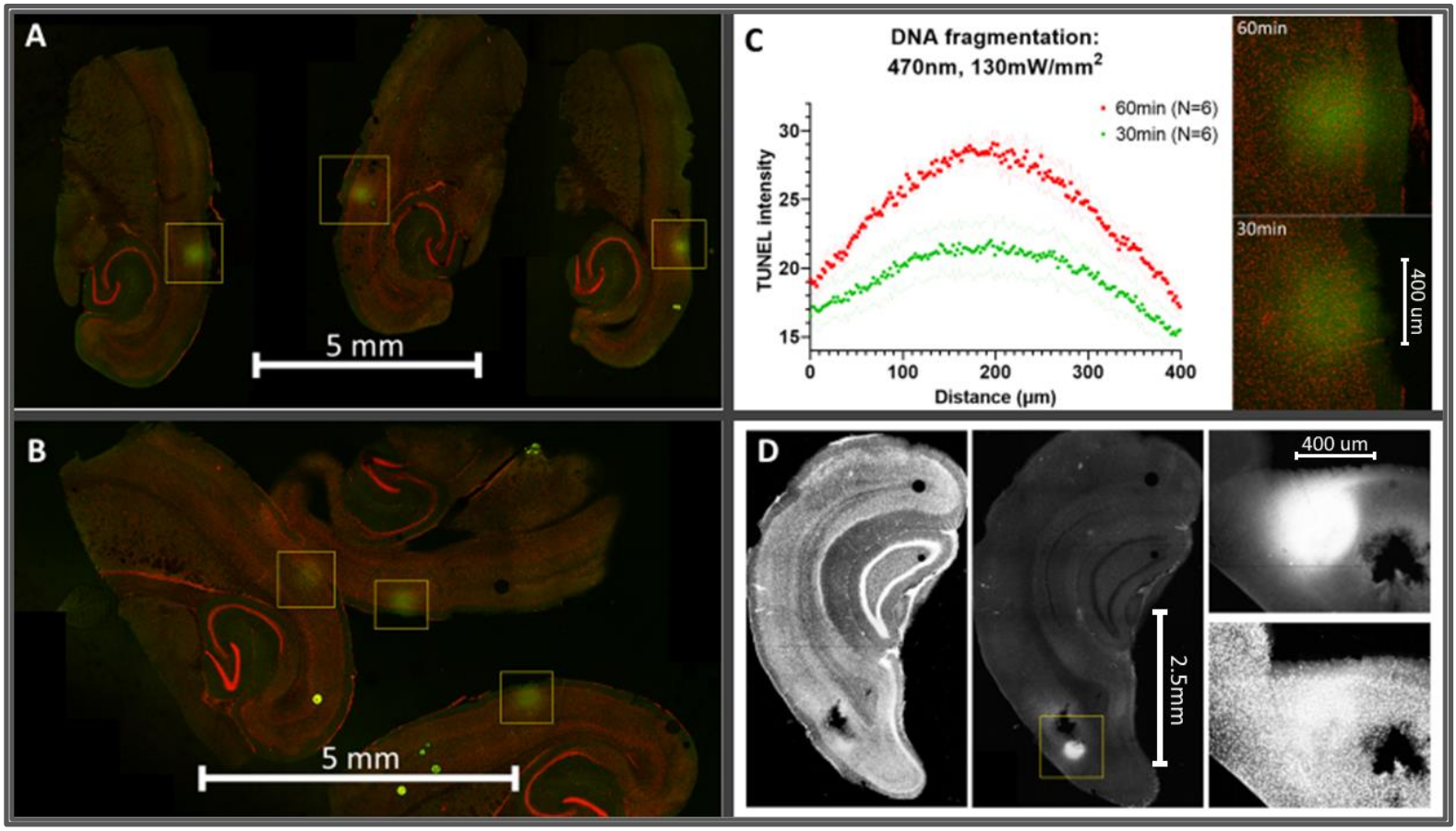

Figure 28: Early TUNEL staining results. Initial TUNEL staining presented as punctate green fluorescence without nuclear resolution (A, B and D). Mean TUNEL intensity (N = 6 slices per condition) was higher in regions exposed to 470 nm light for a longer period (C).

Subsequent experiments with TUNEL staining on unmodified C57BL/6 and EMX-1 ChR channelrhodopsin-expressing mice were unable to replicate these results, producing either no detectable signal or broad staining across the whole sample. Several potential issues were identified with the staining protocol, permitting iterative improvement to be made over several attempts. These test samples were prepared using benzonase – a DNase enzyme with broad specificity and high activity – as a positive control to simulate DNA damage, and untreated samples as negative controls.

It was identified that the use of proteinase K as a permeabilisation step was too harsh for fresh brain samples, causing extensive damage and making the resultant slices extremely fragile. This was substituted for Triton X-100, resulting in improved cell permeabilisation and reagent penetration without the associated damage. Additionally, the inclusion of ethylenediamine tetra-acetic acid (EDTA) to halt benzonase activity (TUNEL can only stain DNA fragments longer than 200 base pairs[447], so benzonase activity must be halted before DNA is excessively fragmented) was identified as a potential issue since the activity of the terminal deoxynucleotidyl transferase (TdT) in the TUNEL stain relies on the presence of Mg^{2+}, Mn^{2+}, Zn^{2+} or Co^{2+}as a cofactor[448]. Since EDTA is an effective chelating agent, it acted to inhibit the TdT enzyme until the protocol was modified to include 10 mM MgCl in wash buffers.

Other changes were implemented including adjustments to incubation periods for various steps, reagent concentrations, use of thinner tissue slices (reducing from 40 µm to 20 µm) and addition of dimethyl sulphoxide (DMSO) to aid reagent penetration. Several TUNEL kits were also tested alongside one another to eliminate the possibility of batch-to-batch variation.

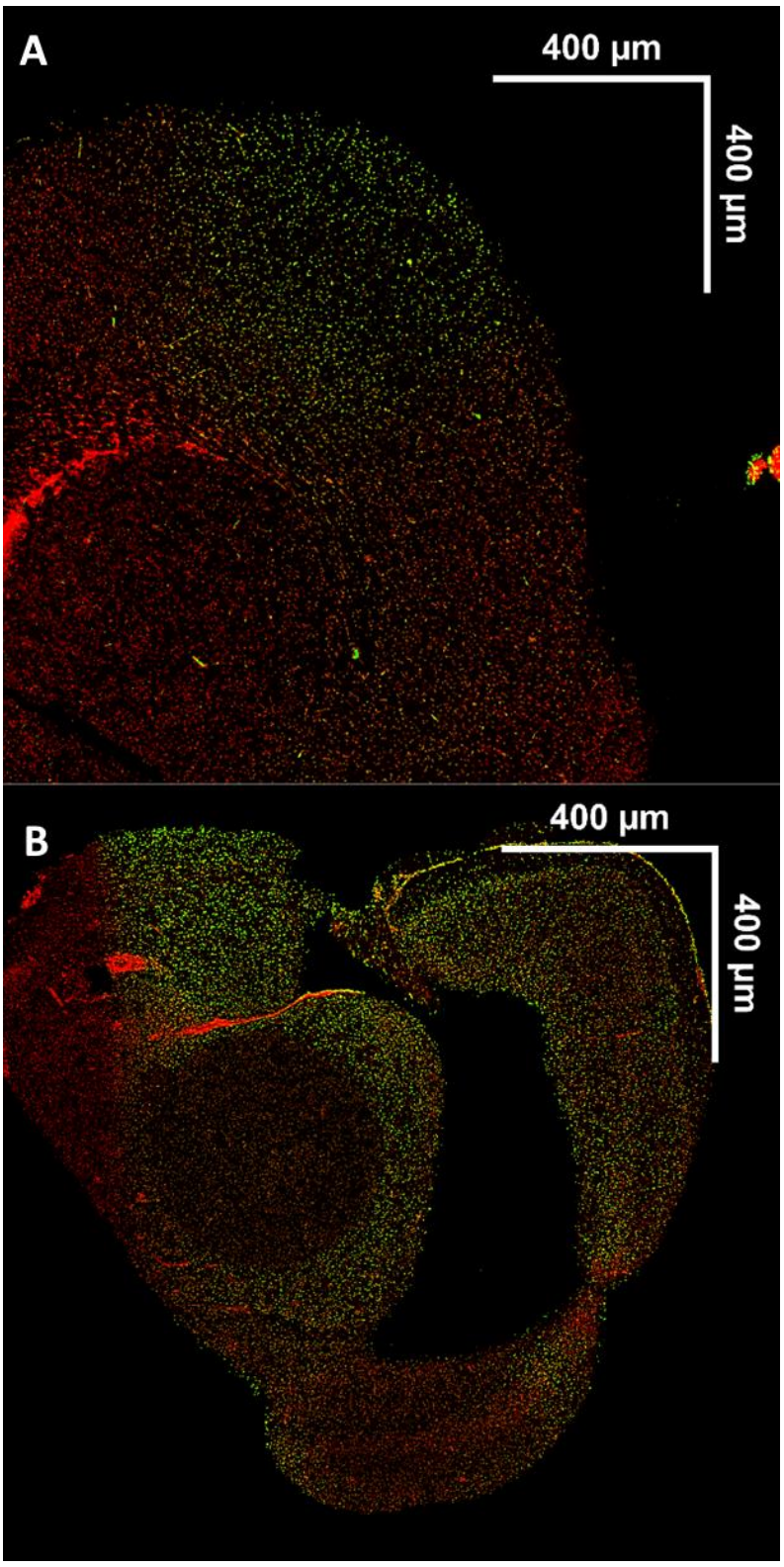

Figure 29: Results of modified TUNEL protocol. The stain now shows nuclear resolution, however there is extensive background staining, requiring additional digital processing steps to mitigate.

Acute brain slices from a C57BL/6 mouse, exposed at 470 nm, 7 mW for 60 min (A) or unexposed and treated with benzonase (a DNA-degrading enzyme) for a positive control (B). Slices are stained with TUNEL (green) and Propidium Iodide (red).

These modifications resulted in more consistently successful staining and better nuclear resolution of the TUNEL stain (Figure 29). However the protocol remained unpredictable, succeeding in some cases and failing in others without an obvious cause. Further investigation suggested that TUNEL signal may not develop immediately, requiring 6-24 hr after apoptosis to emerge[449]. Because of this, it was determined that alternative markers of cell death should be tested.

Additionally, fluorescent images of the samples exhibited significant background signal stemming from brain tissue's strong autofluorescence in the green channel.

Brain tissue contains a range of fluorescent molecules that can contribute to autofluorescent signal in microscopy, however the most common is lipofuscin; a range of oxidised liposomal remnants that accumulates in brain tissue (and other tissues) over time. Whilst lipofuscin accumulates with age, it is still present in young organisms and can interfere significantly with fluorescence microscopy[89].

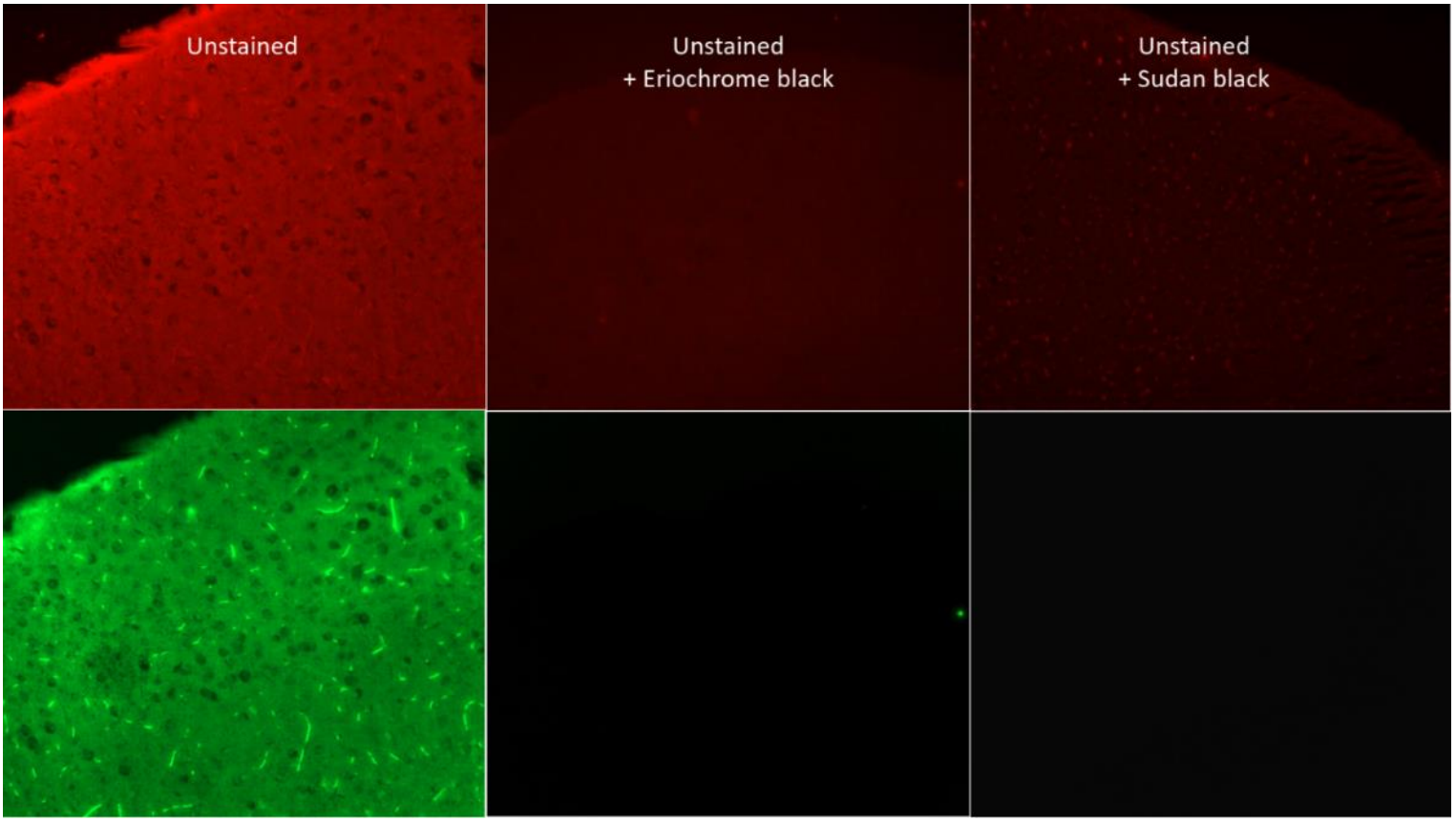

Figure 30: Autofluorescence suppression with Sudan black and Eriochrome black dyes. Green-channel autofluorescence was entirely quenched and red-channel was substantially suppressed by both treatments.

Multiple methods exist in the literature to quench lipofuscin-derived autofluorescent signal, typically involving a chromophore that binds to the fluorescent molecules and absorbs emitted photons, re-emitting them at a longer wavelength. Two of the most popular and cost-efficient reagents used for this purpose are Sudan black (a diazo dye also known as solvent black 3) and eriochrome black T (an azo dye)[450]. These two dyes were applied to unstained fresh frozen brain sections, which were imaged in the red and green channels to assess their efficacy in reducing mouse brain tissue autofluorescence (Figure 30). Both dyes were effective at diminishing red-channel autofluorescence intensity, with eriochrome black producing blurred but greatly dimmed signal and Sudan black producing sharp images of similarly reduced intensity. Eriochrome black was marginally less effective than Sudan black in the green channel, however both dyes almost completely quenched green channel autofluorescence.

Subsequently, both dyes were tested on TUNEL and propidium iodide-stained mouse brain tissue treated with benzonase. The benzonase-free control exhibited the greatest amount of green-channel autofluorescence, which unexpectedly reduced substantially after benzonase treatment. The Sudan black-treated sample showed the lowest green-channel autofluorescence, showing signal only in TUNEL-positive nuclei. The eriochrome black performed poorly and inconsistently, eliminating autofluorescence, propidium iodide and TUNEL signal across much of the sample but leaving only autofluorescent signal in other regions (Figure 31). Consequently, Sudan black treatment was adopted as an autofluorescence quenching step for future experiments.

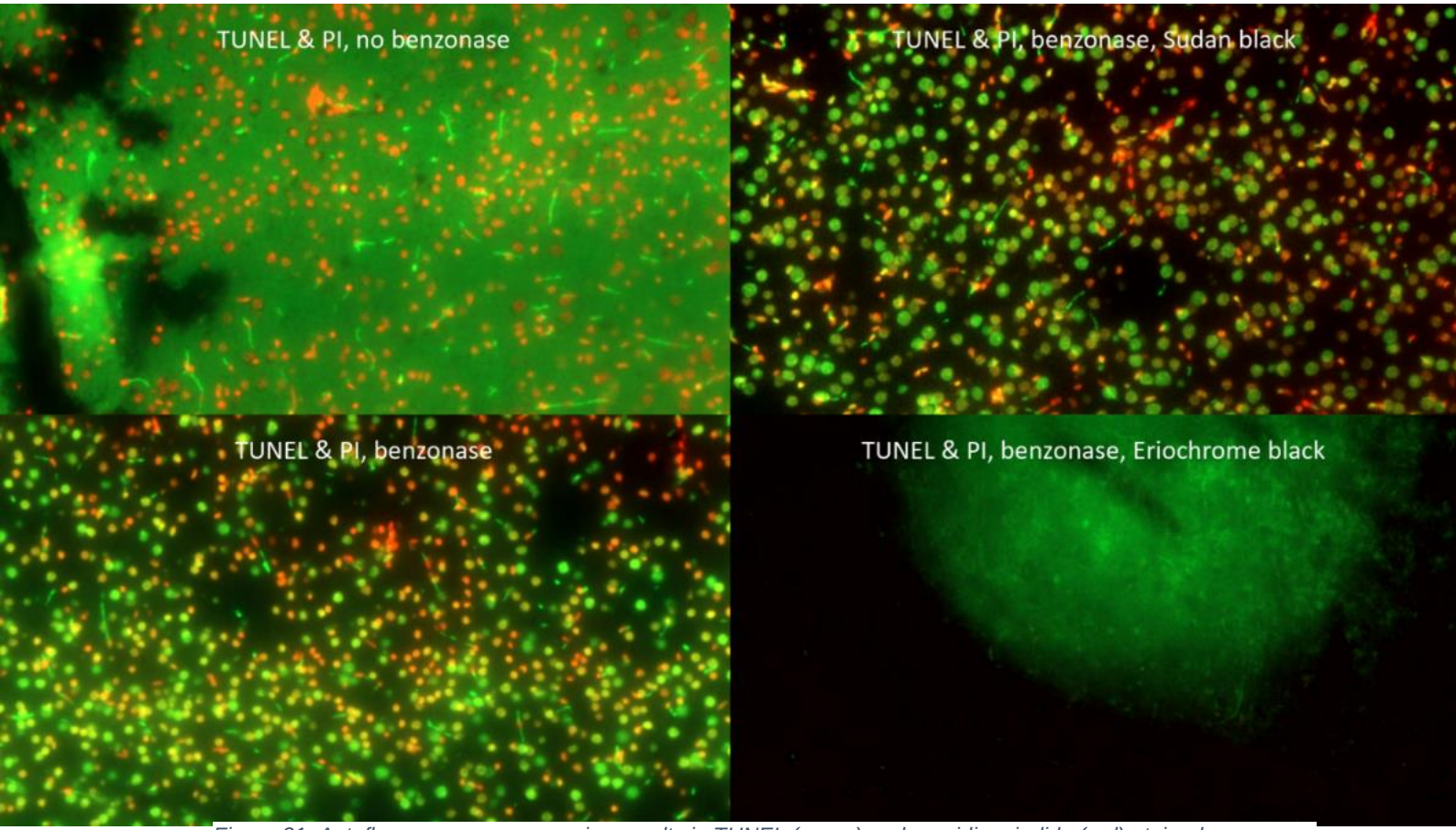

Figure 31: Autofluorescence suppression results in TUNEL (green) and propidium iodide (red) stained, benzonase-treated positive control brain slices. Sudan black greatly suppressed green- and red-channel autofluorescence, whilst eriochrome black suppressed TUNEL signal entirely.

6.2.3. Testing of alternative cell death and oxidative stress markers

A range of alternative markers for cell death – either apoptosis or necrosis – were tested for suitability in phototoxicity experiments. Each was tested on 20 µm thick sections of acute brain slices from C57BL/6 mice (male or female depending on availability of animals, typically ~8-10 weeks of age except for animals scheduled for culling, which may be as old as 12 months) exposed to 470 nm light of various intensities and for various durations (noted in discussion of each marker).

Cleaved caspase-3 and p53

Caspase-3 is a protein responsible for terminal signalling of many (but not all) apoptotic pathways. It begins as an inactive proto-enzyme that is cleaved by other caspases (8, 9 and 10) into two subunits, which dimerise into the active enzyme. The active enzyme goes on to activate downstream caspases (6 and 7) and its activation is considered a “point of no return” in the apoptotic process. Consequently, increases in detected levels of the large or small subunit of caspase-3 are considered to be indicative of increases in the rate of apoptosis.

p53 is a cancer-regulating protein that binds to DNA, detecting damage and arresting the cell cycle to allow DNA-repairing enzymes to work. If damage is sufficient, p53 can trigger apoptosis. DNA damage is a potential consequence of photochemical trauma, either from oxidative damage or direct photochemical alteration of the DNA molecule itself. Ordinarily, P53 is inactivated by mdm2, whose dissociation is triggered by a range of pathways. Increases in detected p53 levels (via an antibody specific to dissociated p53) would indicate increased levels of DNA damage and apoptosis arising from such, though it is possible for p53 activity to be triggered by other factors[451].

The anti-cleaved caspase antibody used in this experiment (methods) binds specifically to the large subunit of caspase-3, and is not reactive to the un-cleaved proto-enzyme or other caspase proteins or fragments. Acute mouse brain slices (C57BL/6, 9 weeks old, female) were exposed to 470 nm light (4, 5, 6, 7, 8, 9 and 10 mW intensity) for 1 h, fixed, sectioned and stained for caspase-3 and DAPI.

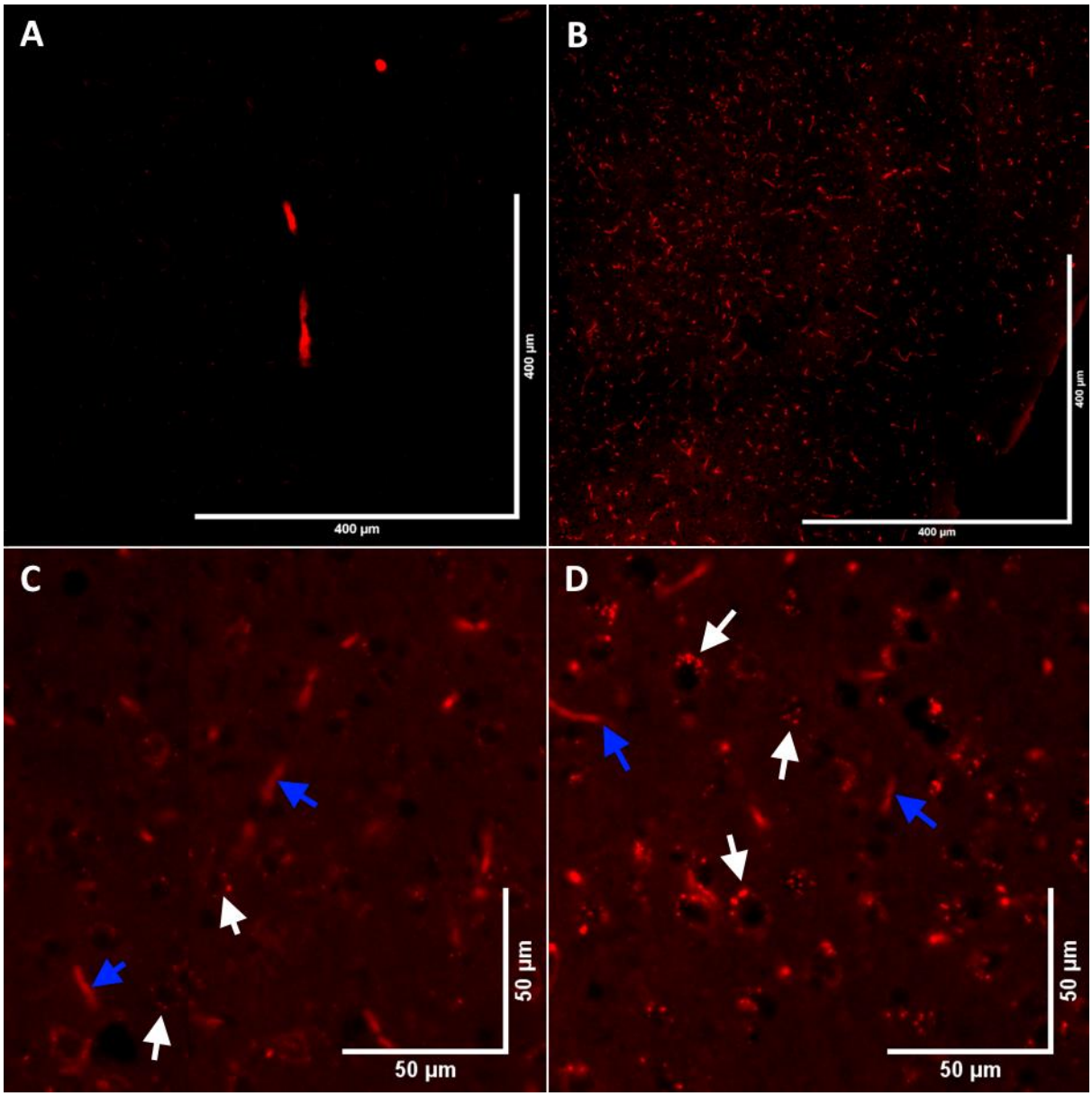

Figure 32: Top - an unstained (A) and caspase-3 stained (B) C57BL/6 acute brain slice. Caspase-3 staining (red, white arrows) can be seen. However there is extensive non-specific blood vessel staining, visible as lines (blue arrows). Bottom - a low (C) and high (D) region of caspase-3 expression.

Caspase-3 staining of these samples showed no difference in cleaved caspase-3 levels between exposure intensities; all samples showed inconsistent levels with regions of high and low staining thought to be from normal cell death that occurs in acute brain slices due to inadequate delivery of glucose and oxygen (Figure 32). Light-exposed regions did not exhibit increased caspase-3 signal compared to unexposed regions. Slices also exhibited strong blood vessel autofluorescence, making it difficult to count dying cells; treatment with Sudan black did reduce this signal but also suppressed caspase-3 signal.

A Western blot for p53 and caspase-3 (with vinculin – a cytoskeletal protein used as a loading control) showed increased p53 levels in both light-exposed samples and in positive controls (deprived of oxygen and glucose for 1 hr) compared to negative controls (Figure 33). No caspase-3 signal was detected in any condition. Vinculin levels were strong and relatively consistent across the conditions, indicating that the blot was successful.

Communication with Cell Signalling Technology suggested that cell death in brain does not commonly follow conventional apoptotic pathways, and that brain tissue has low caspase-3 expression. Instead, it was suggested that much of the cell death occurring may be via necroptosis; a recently characterised pathway which Cell Signalling Technology's own scientists have successfully (but with difficulty) detected in monolayer cell culture, but had not yet been successful at detecting in tissue samples. Whilst they did sell a range of necroptosis-specific antibodies, they recommended against considering them as a candidate for these experiments due to the extreme difficulty they experienced with detecting the process.

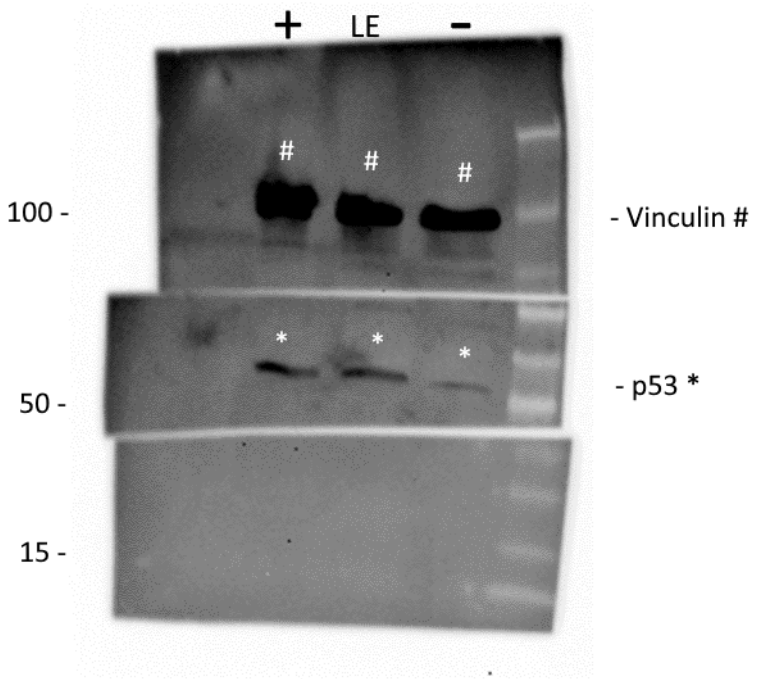

Figure 33: A Western blot with Vinculin (# - 117 kDa), P53 (- 53 kDa) and cleaved caspase-3 (no visible band – 17 and 19 kDa). Samples are positive control (oxygen & glucose-deprived for 1hr, left lane marked +), 470nm light-exposed at ~16mW, 3hrs (middle lane marked LE) and untreated control (right lane marked -). Vinculin signal was strong in all samples, indicating that the blot was successful. P53 signal appears marginally higher in the positive control and treated samples, however signal can be seen in the untreated control. No caspase-3 signal can be seen in any sample.*

γ-H2AX

Ser-139 is a histone protein that becomes phosphorylated after DNA double-strand breaks (e.g. after photochemical DNA damage or during DNA fragmentation in apoptosis), generating foci of γ-H2AX at the damaged site. If light exposure were to cause DNA damage or apoptosis, it would be expected that detectable γ-H2AX levels would increase.

Acute mouse brain slices (C57BL/6, 10 weeks old, male) were exposed to 470 nm light (4, 5, 6, 7, 8, 9 and 10 mW intensity) for 1 h, fixed, sectioned and stained for γ-H2AX and DAPI. Staining did not exhibit any γ-H2AX signal (though DAPI signal was strong and readily detected).

γ-H2AX foci do not appear immediately; whilst signal can be detected in radiation-damaged tissue by as little as a few minutes post-exposure, peak signal development occurs approximately 30 min after DNA breakage[452]. If DNA fragmentation occurs due to apoptosis rather than direct photochemical damage to DNA, development of γ-H2AX signal may be delayed by several hours as, whilst morphological signs of apoptosis appear inside a couple of hours post-insult, the whole process can take 12-24 h to complete[453]. Since acute brain slices are fixed immediately after light exposure (to avoid cell death from oxygen and glucose starvation), γ-H2AX signal may not have had sufficient time to develop.

8-OXO-DG

The primary route via which light exposure causes toxicity at intensities used for optogenetics is photochemical damage via production of ROS. If this ROS production caused oxidative damage to nuclear DNA, it should result in a measurable increase in DNA oxidation. If the primary site of oxidative stress is another structure (for instance the mitochondria), nuclear DNA in exposed tissue regions should experience a similar level of oxidative stress to unexposed regions.

8-Oxo-2'-deoxyguanosine (8-OXO-DG) is a product of deoxyguanosine oxidation, and is a major component of oxidised DNA. Acute mouse brain slices (C57BL/6, 10 weeks old, male) were exposed to 470 nm light (4, 5, 6, 7, 8, 9 and 10 mW intensity) for 1 h, fixed, sectioned and stained for 8-OXO-DG and NucBlue.

Clear 8-OXO-DG staining was observed across all samples (Figure 34), with no increase in exposed regions of tissue. Whilst some regions stained more brightly than others (primarily due to increased cell density in those locations), staining did not differ across different illumination intensities. An unstained control showed no red fluorescent signal aside from autofluorescence (which was largely suppressed with Sudan black treatment), indicating that the red fluorescence seen in the stained samples was 8-OXO-DG.

Since oxidation products form almost immediately upon light exposure (ROS do not last very long after production, reacting with nearby molecules extremely rapidly), this would suggest that the majority of ROS arising from phototoxicity in mouse brain are not produced in the nucleus (where close proximity would enable nuclear DNA damage) but instead must be formed elsewhere. This aligns with existing literature for retina and skin, where ROS formation from visible-light phototoxicity is primarily confined to the mitochondria.

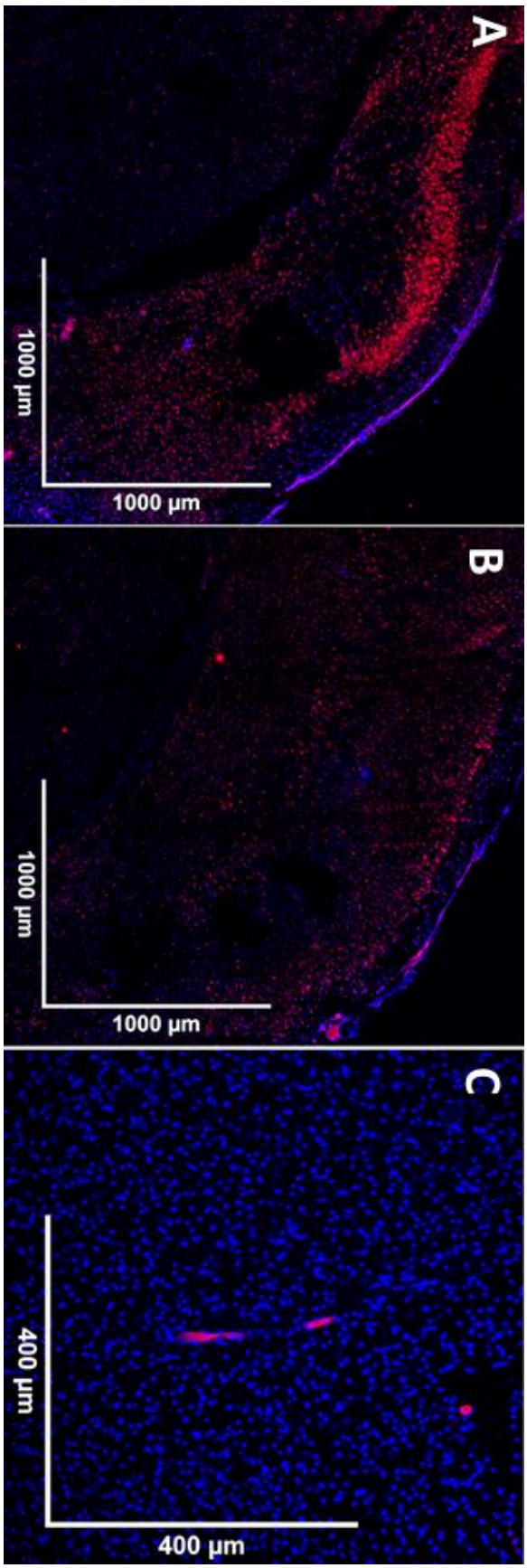

Figure 34: C57BL/6 brain stained with 8-OXO-DG (red) and NucBlue nuclear stain (blue). Exposed samples (A = 10 mW, B = 9 mW) showed no difference in 8-oxo-dg staining between exposed and unexposed regions, suggesting that optical insult does not increase DNA oxidation levels. An unstained control (C) indicates that the 8-oxo-dg staining was successful.

Fluoro-jade C

Fluoro-jade C is one of three variants of fluorescein (a green-fluorescent organic dye widely used in biological staining) that stains degenerating neurons via an as-yet unknown mechanism. Despite the lack of understanding of how the stain binds to degenerating neurons, validation studies have demonstrated that it is as or more reliable than traditional stains such as silver nitrate, H&E and nissl stain for identifying degenerating neurons[454,455].

Fluoro-jade C was developed as a modified version of the original stain, intended to increase signal-to-noise ratio. Despite this, it still exhibits a large amount of background staining, which is usually mitigated with potassium permanganate background suppression treatments.

Acute mouse brain slices (C57BL/6, 12 months old, female) were exposed to 470 nm light (4, 7, 9, 14 mW intensity) for 1 h, fixed, sectioned and stained for fluoro-jade C. All sections showed degenerating neurons throughout the tissue, with no increase in exposed regions relative to the rest of the sample (Figure 35). Signal-to-noise ratio was poor and cells were blurred; treatment with Sudan black or eriochrome black did not alleviate this background signal; nor did adjusting potassium permanganate incubation time.

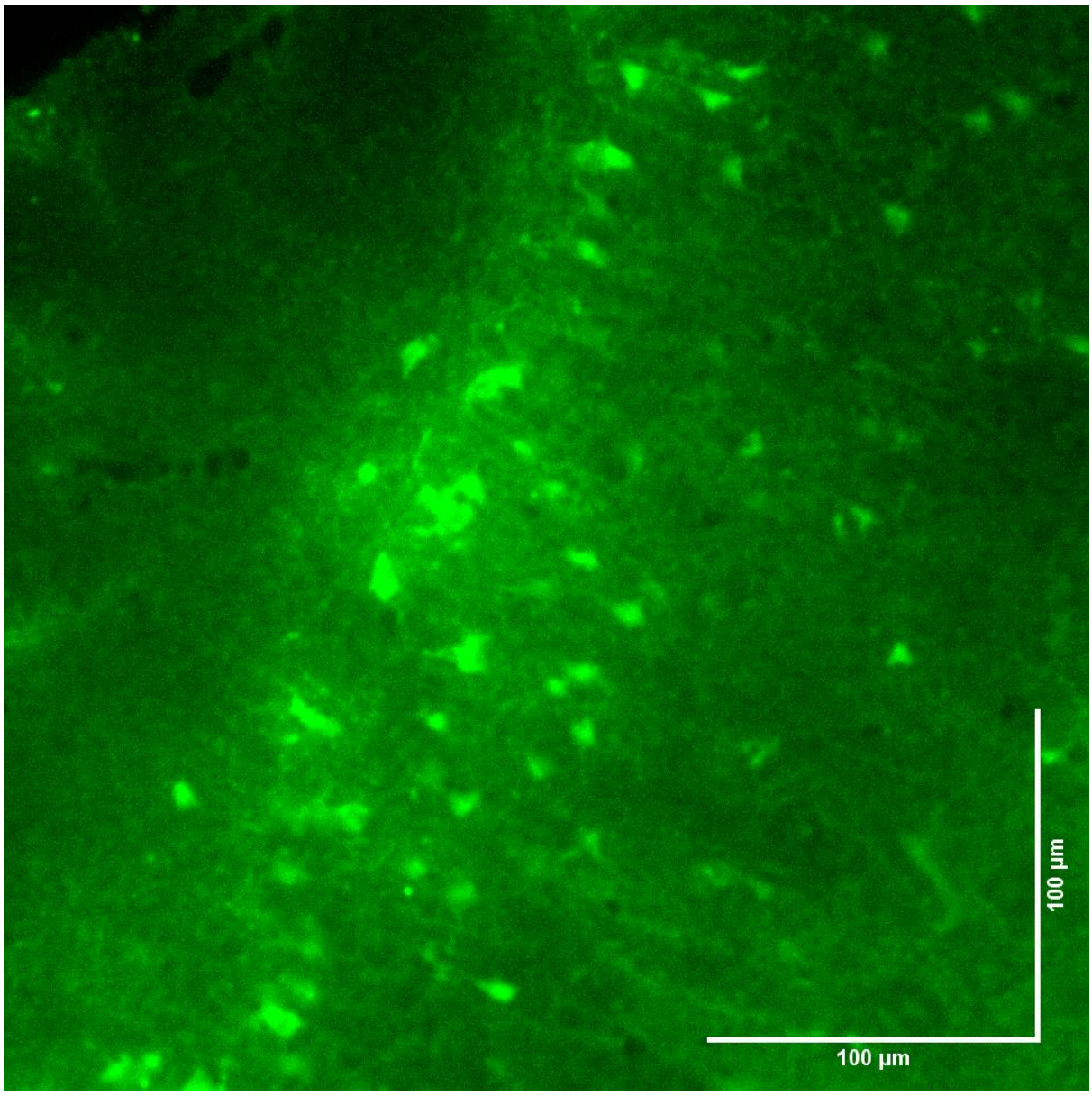

Figure 35: A C57BL/6 brain slice stained with fluoro-jade C. Whilst degenerating neurons were successfully stained, signal-noise ratio was poor and neurons were stained throughout the tissue (rather than being concentrated at the illumination site), suggesting widespread toxicity either due to overlong incubation or some other source of toxicity.

Propidium iodide

Propidium iodide is a red-fluorescent intercalating dye used to stain DNA. Whilst it is fluorescent under most conditions its quantum yield increases 20-30 fold when bound to DNA, causing DNA in samples (usually cell nuclei) to fluoresce brightly relative to background.

Propidium iodide is often used as a nuclear counterstain in fixed cell and tissue samples. However, if applied to living samples the dye cannot penetrate the cell membrane, resulting in only dead cells (which are unable to actively transport dye out of their cytoplasm and may have ruptured cell membranes) being stained.

Acute mouse brain slices (C57BL/6, 12 months old, female) were exposed to 470 nm light (14 mW intensity) for 3 h. The slices were stained with propidium iodide and imaged live in a Nikon upright widefield fluorescent microscope with immersion lenses. Samples exhibited high background signal (attributed to dead tissue on the top and bottom surfaces of the samples, which stained positively for propidium iodide due to damage from slicing). However, illuminated regions did show increased staining intensity indicative of higher rates of cell death in those regions (Figure 36). Illuminated regions also appeared out of focus compared to the rest of the sample, suggesting that sample swelling had occurred at these locations. This swelling could be attributed to Donnan swelling due to cell death. Difficulty focusing on the exposed site combined with high background made propidium iodide staining an impractical method for measuring optical toxicity.

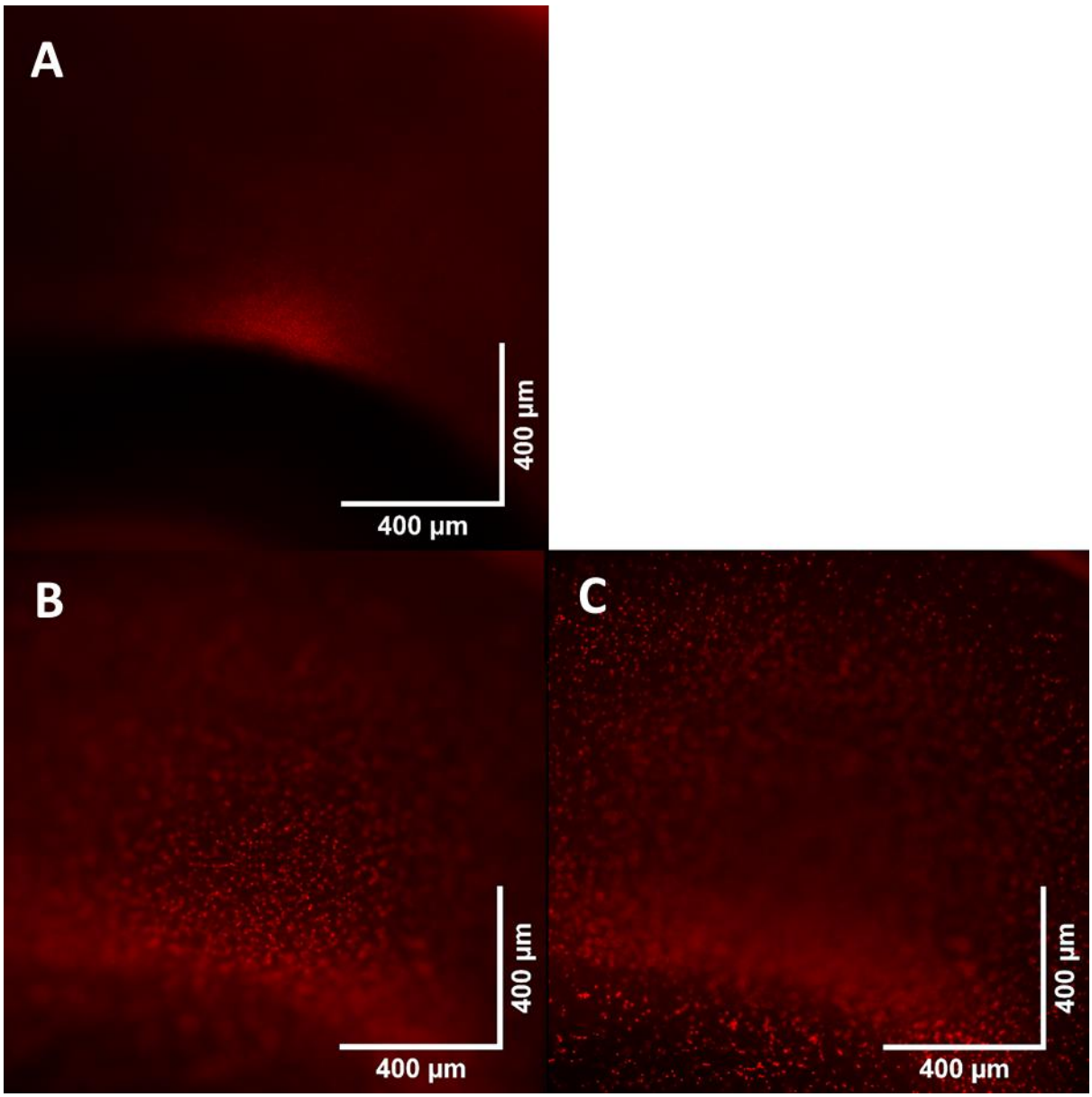

Figure 36: (A) C57BL/6 acute brain slice exposed to 470 nm light (~16 mW) for 3 h with 100 ms pulse, 50% duty cycle, live-stained with propidium iodide. A crescent of PI staining can be seen where the optical fibre overlapped a region of white matter. There is extensive background signal. (B) and (C) PI staining of an exposed region of a C57BL/6 acute coronal brain slice. The exposed region is out of focus with the rest of the slice, indicating substantial swelling has occurred, but making imaging difficult.

Calcein-AM

Calcein is a green fluorescent protein with an excitation/emission profile similar to that of fluorescein. Its acetomethoxy derivative – calcein-AM – is able to permeate cell membranes, allowing it to pass into live cells without the need for permeabilisation or fixation. In living cells, the molecule is altered, removing the acetomethoxy group and thus removing this membrane-permeant property whilst also allowing the molecule to chelate Ca^{2+}, Mg^{2+} or Zn^{2+} ions required for its fluorescence. The result is that living cells fluoresce green under fluorescent imaging, whilst dead cells (which lack the esterase activity to remove the acetomethoxy group) do not. Calcein-AM is also available in a red-shifted form with altered excitation and emission behaviour, though with the disadvantage of retaining a small level of fluorescent activity before removal of the AM-group, worsening the signal-to-noise ratio.

Acute mouse brain slices (C57BL/6, 12 months old, female) were exposed to 470 nm light (14 mW intensity) for 2 h. After exposure they were stained with either calcein-AM green or red and imaged with a Nikon upright microscope with immersion lens.

Both red and green calcein-AM successfully stained living cells in the acute brain slices (Figure 37 A). No live cells were observed in the illuminated regions, indicating that these cells did not have esterase activity sufficient to modify the calcein-AM molecule and were dying or dead (Figure 37 D). Green calcein-AM exhibited substantially lower levels of background signal than red, which provided sufficiently poor contrast to be unusable. Both stains were highly sensitive to elapsed time post-exposure; live-cell signal dropped significantly over approximately 20 minutes after imaging was commenced (Figure 37 A vs C).

Both green and red calcein-AM stained samples showed significant bleaching of autofluorescent background in the light-exposed regions, resulting in dark circles where neither cell staining nor autofluorescence could be observed. This complicated image processing, since the variance in autofluorescent background intensity between the exposed and unexposed regions made automated counting of positively-stained (live) cells difficult. The green stain was judged as viable for use in assessment of photochemical toxicity in acute mouse brain samples, however several complicating factors (short imaging window, high sensitivity to variation in experimental timing, low signal-to-noise ratio, varied autofluorescent background between exposed and unexposed regions) combined with the inability to fix calcein-AM signal indicated that other options should be assessed before settling on this method.

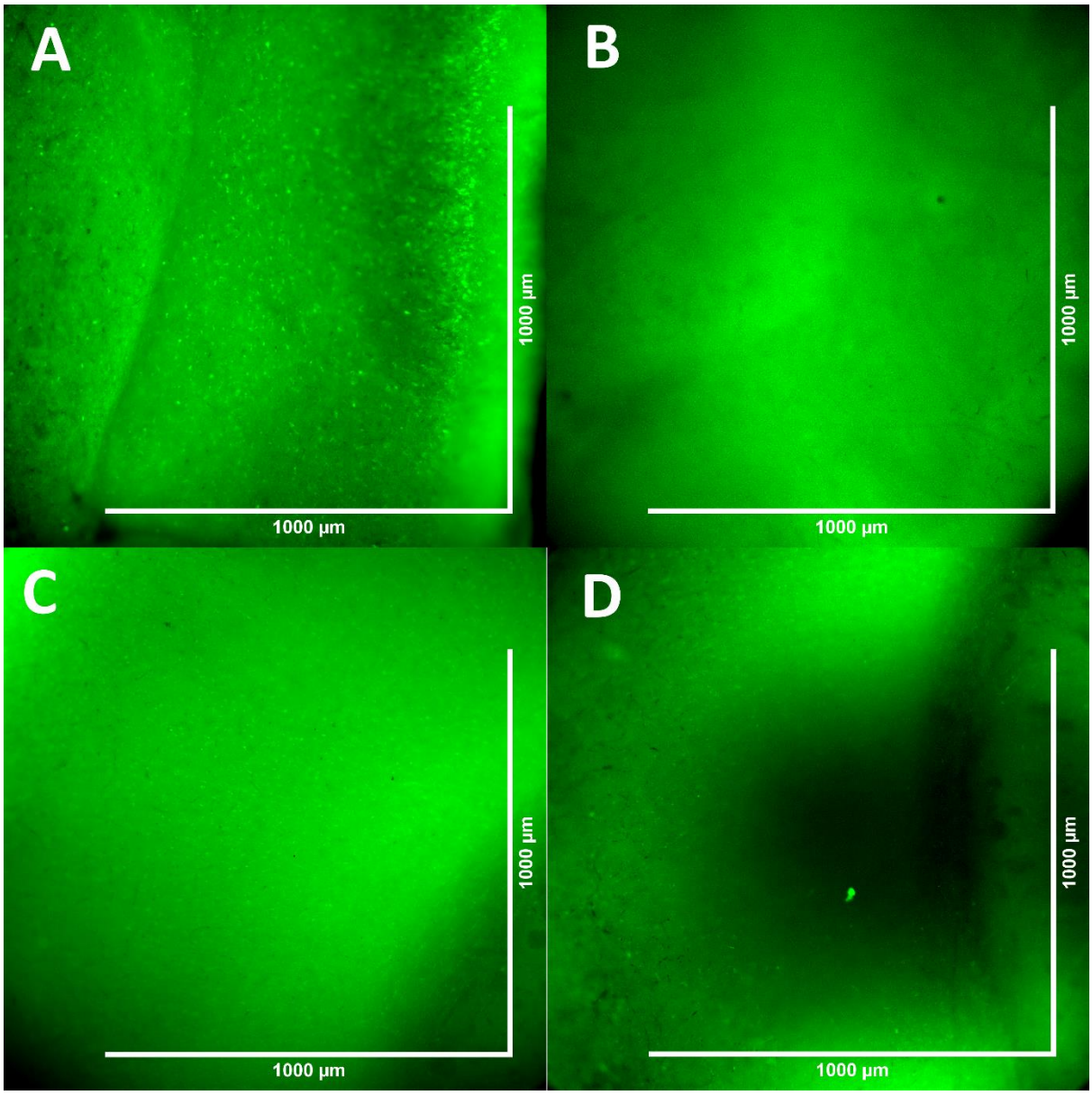

Figure 37: Calcein-AM staining of acute mouse brain slices exposed to 470 nm light (14 mW, 100 ms pulse, 50% duty cycle, 2 h). (A) Unexposed negative control, stained with calcein-AM. Bright spots denote live cells. (B) Unstained negative control – no bright spots are visible. (C) Unexposed region of light-exposed slice. Bright dots of calcein-AM stained cells are much less bright compared to background however they are visible. Differences compared to the negative control are likely due to sensitivity in timings for calcein-AM imaging. (D) Light-exposed region of a calcein-AM stained slice. Bright dots of live cells stained with calcein-AM are visible outside the exposed region. Inside the exposed region, autofluorescent background signal has been bleached and no calcein-AM stained cells are visible.

Optical coherence tomography

Optical coherence tomography (OCT) is an optical technique used to produce images of (typically) biological samples at micron resolution. It is a type of interferometry, typically using long-wavelength light for better sample penetration; this light is split into two paths, one of which passes through the sample and the other which passes into a reference pathway. When the reference path is set to the correct length (approximately the same distance that the sample path travels), the two beams will produce interference patterns when recombined; the greater the difference in the path length of the reflected photons (due to scattering by the sample), the greater the resulting interference. This difference is recorded as pixel intensity, allowing an image to be produced that depicts the reflectivity of the sample.

In biological tissue, changes in this property may indicate changes in density or structure; tumour tissue may be detectable with OCT due to differences in the density of the tumour compared to the healthy tissue surrounding it.

Attempts were made to image light-exposed acute brain slices (C57BL/6, female, ~10 wks. 470 nm, 12 mW, 50% duty cycle, 100 ms pulse length, 1 hr exposure) with OCT to determine if there were changes to tissue density in exposed regions. Samples were transported from the laboratory where slicing was performed to the location of the OCT, immersed in chilled, oxygenated aCSF – this took approximately 5 minutes.

Initial imaging attempts were unsuccessful due to insufficient contrast with the sample container; this was resolved by changing from a standard white weighing boat to black.

Several difficulties arose whilst attempting to image brain slices with OCT; setting the correct distance for the reference path was time-consuming and difficult to perform repeatably. Adjusting the distance is achieved by tightening or loosening the threaded connector of the reference path tube; as such there is no scale or other method for obtaining repeatable and precise settings. Since the brain slices were immersed in aCSF, they did not lie flat on the bottom of the sample container, instead floating or sitting at different heights due to bending of the slice. Slices would also swell during the experiment, causing their thickness to vary substantially across the measurement period. It was therefore difficult to achieve a suitable calibration before the sample had experienced extensive cell death.

Despite these challenges, some images were successfully obtained. Identification of the exposed site was difficult, suggesting that either the amount of cell death and consequent swelling was small, or that sufficient swelling had occurred across the sample to obscure the illuminated spot. One image (Figure 38) clearly shows the exposed site as a “pit” in the sample surface with a bright layer of tissue beneath. However it is likely that the bright white region is tissue that has been compressed by accidental contact with the optical fibre rather than the result of phototoxicity.

Due to the difficulty in obtaining OCT images rapidly and reliably, use of the technique was not pursued further.

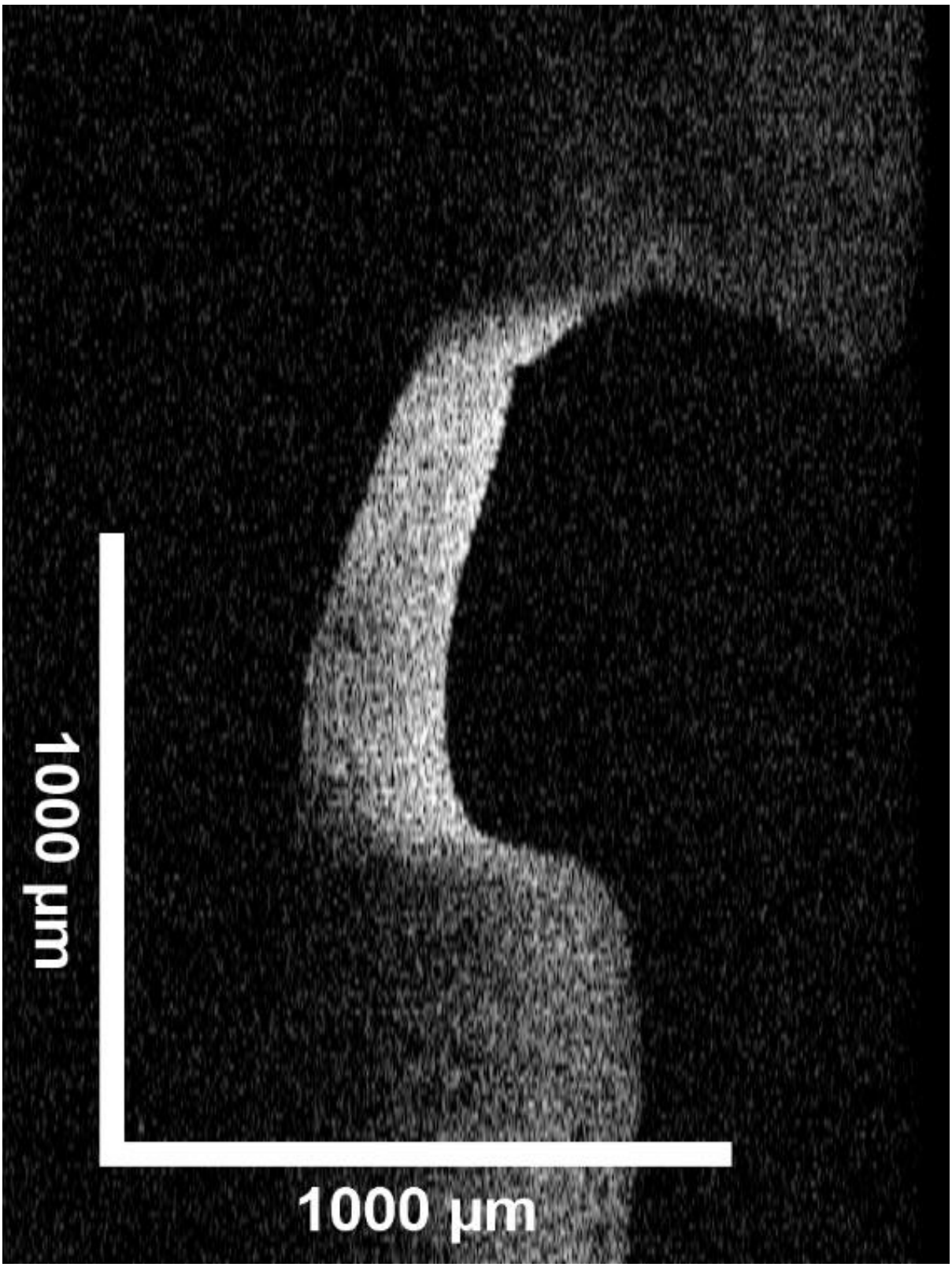

Figure 38: OCT image of an acute mouse brain slice (longitudinal section). A crater is visible in the tissue surface, above a bright white area of tissue, indicating increased light scattering. This was likely caused by accidental mechanical damage from the optical fibre.

6.2.4. Autofluorescence bleaching in light-exposed acute mouse brain slices

Tissue autofluorescence arises from stimulation of endogenous fluorophores when carrying out fluorescence microscopy. Changes to autofluorescent signal can indicate photochemical modification of these fluorophores; either molecules which were originally not fluorescent under the wavelength in question gain fluorescence due to photochemical modification, or ordinarily fluorescent molecules lose this property (they are “bleached”).

Changes to retinal autofluorescence are used as a diagnostic factor for light-induced retinal damage[173,190,194,195]. The principal source of retinal autofluorescence is lipofuscin, a mixture of liposomal products that cannot be cleared by the cell, accumulating with age[89]. Lipofuscin is also present in brain tissue, and is similarly responsible for most of the tissue’s autofluorescent signal in the green channel. The oxidation products of lipofuscin produced by photochemical modification can be toxic, or can act as further photosensitising agents that accelerate phototoxicity[85,174,193]. Lipofuscin formation and accumulation is linked to mitochondrial stress, meaning that tissue may become progressively more susceptible to phototoxicity with chronic light exposure[91]. It follows that changes to autofluorescence may be similarly indicative of phototoxicity in brain as in retina.

250 µm thick acute brain slices from each of C57BL/6, HALO (a mouse genetically modified to express a halorhodopsin/enhanced yellow fluorescent protein fusion in cre- expressing cells[264]) and EMX-ChR (a mouse genetically modified to express a channelrhodopsin/enhanced yellow fluorescent protein fusion in cre-expressing cells[265]) mice were exposed to 6, 9 and 12 mW of 470 nm light for 1 h at a 50% duty cycle and 100 ms pulse length (10 slices per condition). Slices were fixed in PFA, re-sectioned to 20 µm via cryostat and mounted for widefield fluorescent imaging in a Zeiss AxioExplorer upright microscope.

Images were processed with the Fiji software package (ImageJ version 1.35T). A linear histogram of pixel intensity was acquired across the centre of the exposed region on each tissue section, and the mean of these curves plotted for each condition.

C57BL/6 slices showed an increase in tissue autofluorescence in light-exposed regions. This increase was most prominent in slices exposed to 6 mW light, and decreased with intensity (arbitrary intensity units: ~400 in non-illuminated regions, increasing to ~750 when illuminated with 6 mW and decreasing with increased intensity to ~650 when illuminated with 12 mW). This suggests that whilst endogenous fluorophores are initially modified by light exposure into products with higher green-channel fluorescence, continued photochemical modification further alters these products into non-fluorescent forms (Figure 39).

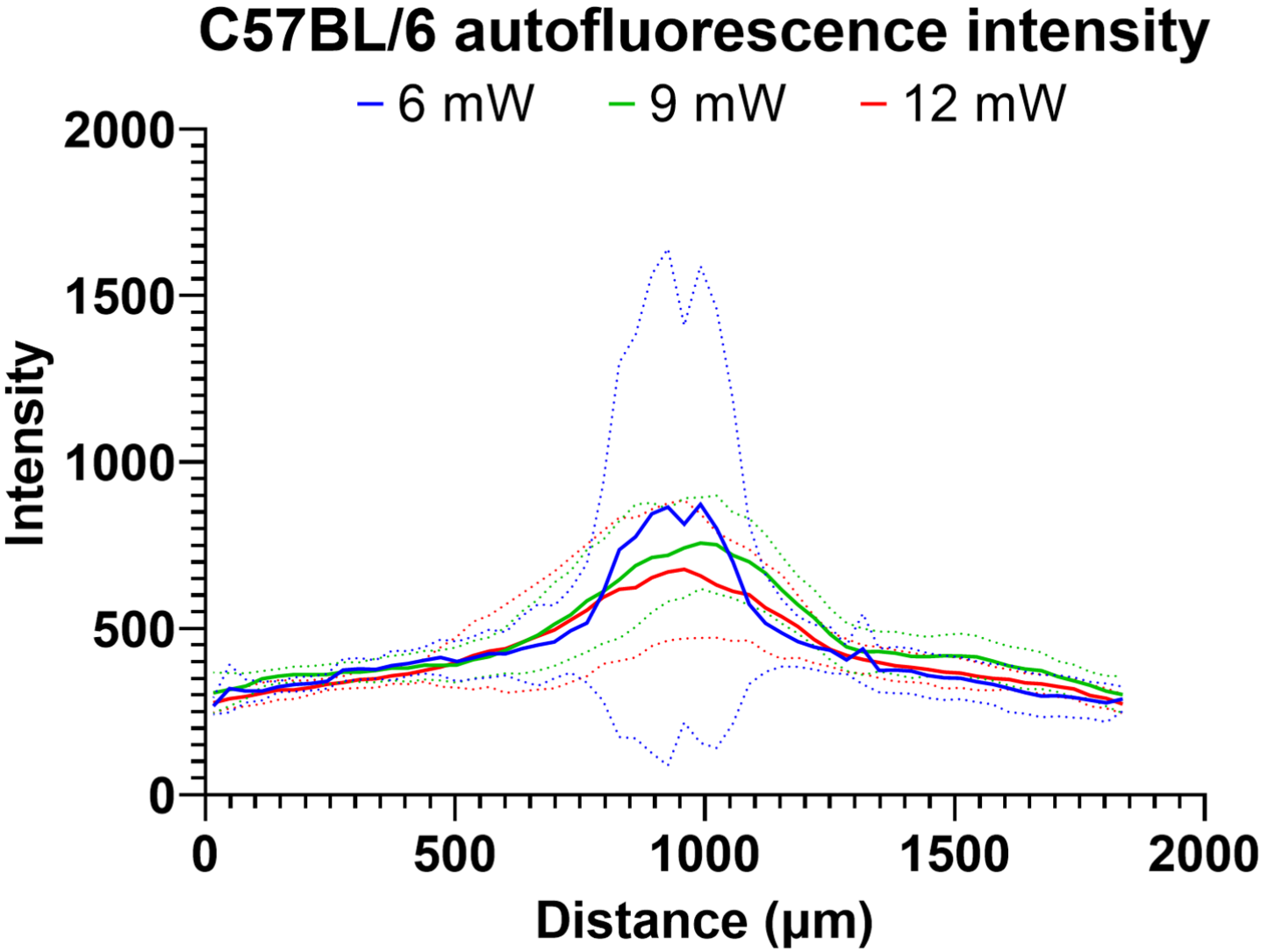

Figure 39: Pixel intensity of green-channel autofluorescence of acute mouse brain slices exposed to 470 nm light. Intensity is higher in exposed regions than in background, and decreases with increased exposure intensity. Solid lines are mean values, dotted lines are standard deviation.

Both the HALO and EMX mice express enhanced yellow fluorescent protein (EYFP) as a confirmational marker of successful genome editing; if the channelrhodopsin molecule is successfully inserted into the animal's genome, EYFP will also be expressed. The channelrhodopsin proteins encoded in both lines are targeted to cre-expressing neurons. However, whilst this promoter produces animals with high expression of both channelrhodopsin and EYFP in pyramidal neurons, lower levels of expression are promoted throughout the brain[456]. This can be seen in the histograms

for both HALO and EMX where, even after similar exposures, some regions of the brain showed relatively low background fluorescence (~200-600 intensity, Figure 40 B) and increased intensity in light-exposed regions (due to low YFP expression, fluorescence from endogenous proteins is dominant) whilst others showed relatively intense background fluorescence (~1000-2000, Figure 40 A) and the exposed region was bleached relative to background (YFP expression causes higher background fluorescence, and is bleached by light exposure).

In both EMX and HALO slices, the difference between high-YFP and low-YFP regions can be seen clearly in plots where either background fluorescence is higher (“light” – Figure 40, A & B) or lower (“dark” – Figure 40, C & D) are excluded.

If sites with lower background fluorescence are excluded, both EMX and HALO curves show a distinct drop in fluorescence signal after light exposure (EMX autofluorescence intensity was ~2000 in non-exposed regions, decreasing to ~900 in exposed regions — Figure 41 C). HALO autofluorescence intensity was ~800 in non-exposed regions, decreasing to ~500 in exposed regions — Figure 42 C), suggesting that EYFP is causing higher background fluorescence in the region and has been bleached in the exposed site.

If sites with low background fluorescence are excluded from the EMX data, the remaining curve shows an increase in fluorescence in the exposed region (from ~400 in non-exposed regions to ~500 with 9 mw exposure, and ~600 at 12 mW exposure — Figure 41 B), suggesting that endogenous fluorophores have been photochemically altered into more fluorescent products. This increase is most pronounced with 12 mW exposures, suggesting that the presence of YFP may have a protective effect (compared to the C57BL/6 samples, in which autofluorescence was most intense at 6 mW and was then bleached as intensity increased).

Similarly, if regions with low background fluorescence are excluded in the HALO plots, intensity in the exposed region increases between 6 and 9 mW, and shows a “shoulder” of increased signal at 12 mW exposure (~500 unexposed, ~700 at 9 mW and a “shoulder” of ~1000 at 12 mW, with a bleached centre of ~600 — Figure 42 B), but the centre of the exposed region is bleached – suggesting that the 12 mW exposure is sufficiently intense to bleach the endogenous fluorophores in the same way as in the C57BL/6 samples.

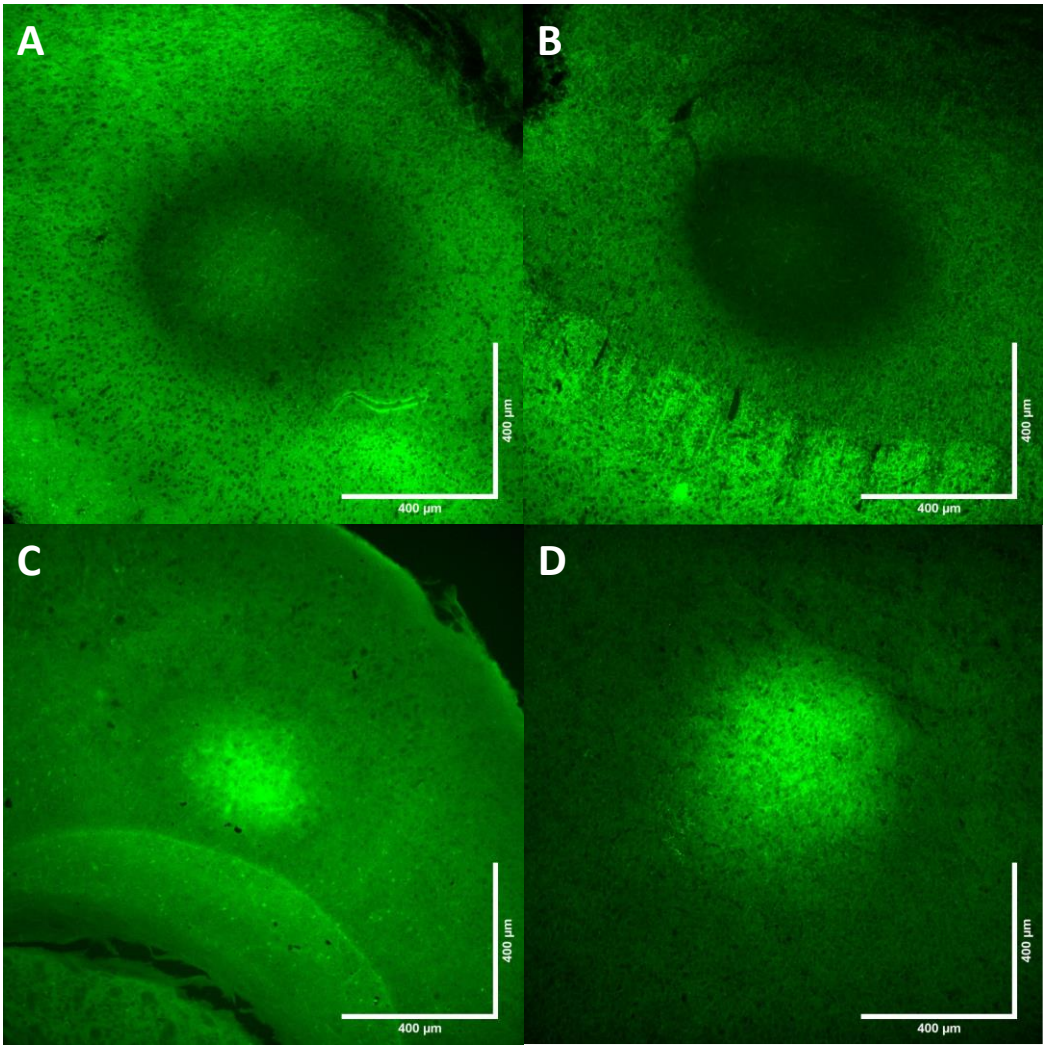

Figure 40: Representative examples of autofluorescence imaging results. Some sites exposed to 470 nm light in acute brain slices exhibit decreases in autofluorescence (A, B) whilst others exhibit increases in autofluorescence intensity (C, D).

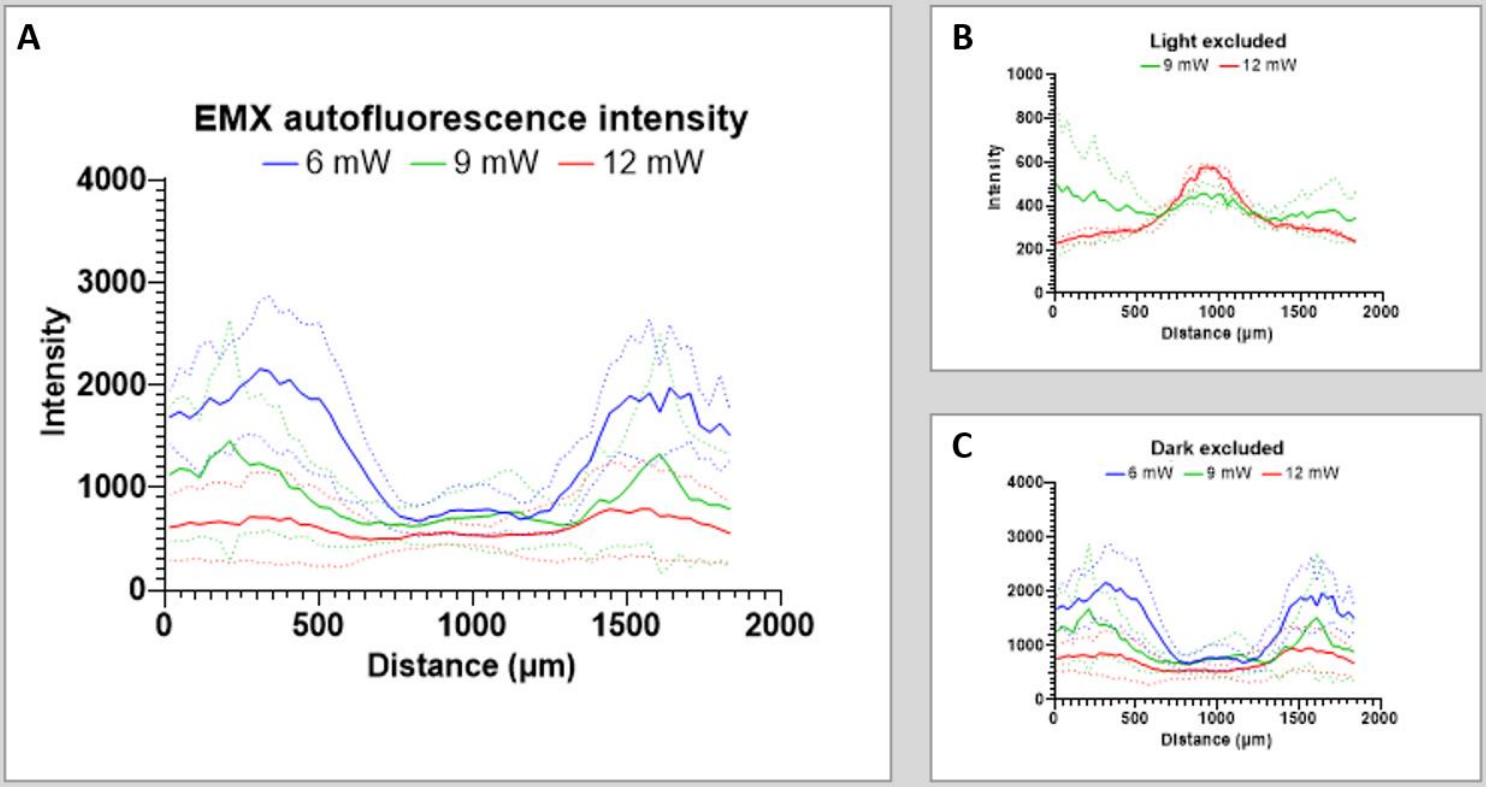

Figure 41: EMX samples show a decrease in autofluorescence intensity in 470 nm light-exposed regions (A). If regions with high background fluorescence are excluded, the remaining regions show a similar increase in intensity to C57BL/6 samples (B). If areas with low background fluorescence are excluded, the bleaching effect is more pronounced (C).

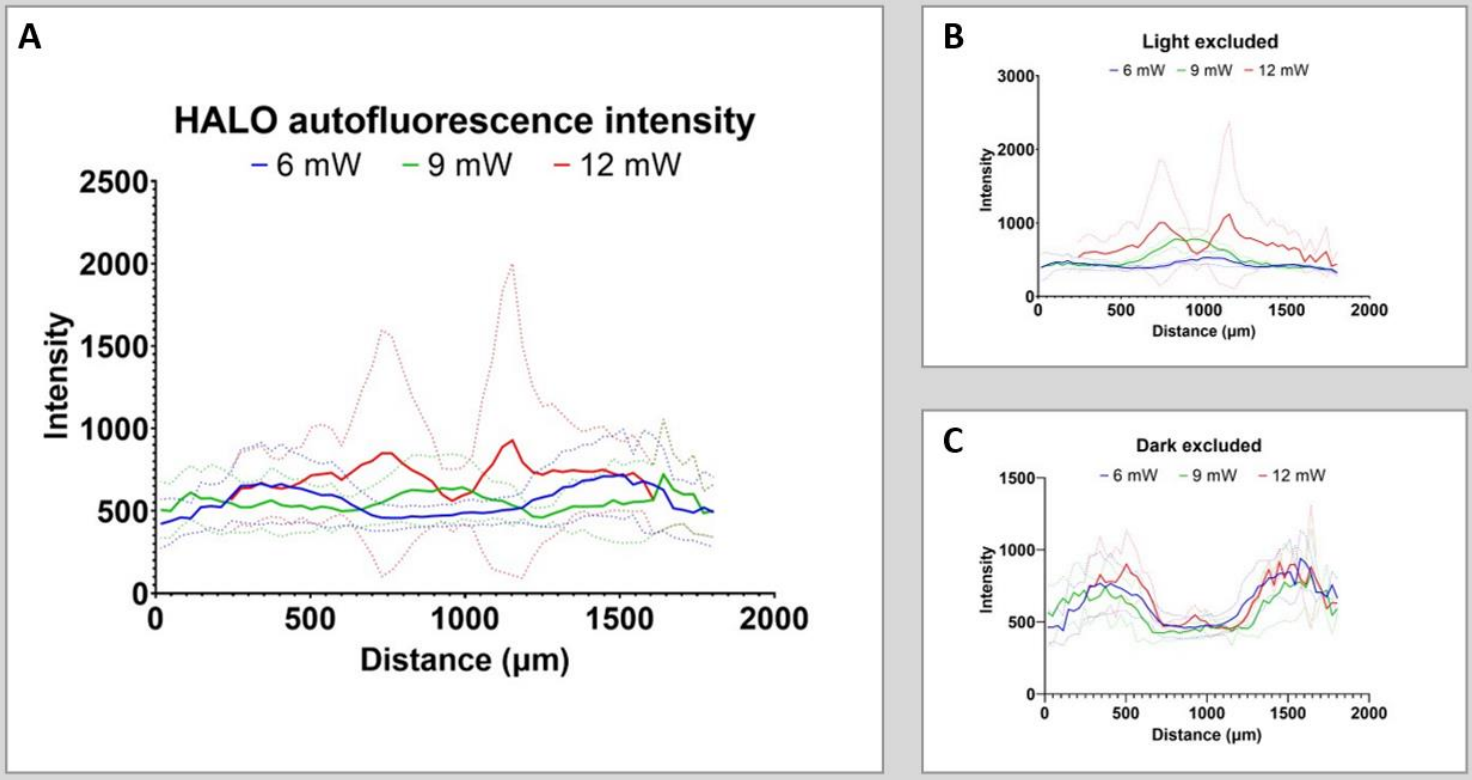

Figure 42: HALO samples show an overall increase in autofluorescence intensity in 470 nm light-exposed regions, except at 12 mW where the "shoulder" of the exposed region continues to increase in intensity whilst the centre is bleached (A). If regions with high background fluorescence are excluded, this pattern remains (B). If areas with low background fluorescence are excluded, a similar bleaching pattern to EMX samples emerges (C).

All samples experienced changes to autofluorescence intensity at all exposure intensities; this suggests that 470 nm light exposure at intensities of 6 mW or higher for 1 h or more are sufficient to produce photochemical changes to brain tissue in a similar manner to light-damaged retina.

6.2.5. CRL2541 immortalised astrocyte light exposure

Previous attempts to visualise phototoxicity in acute mouse brain slices had largely failed, or possessed complications or limitations that precluded use of a given method. To better identify potential methodological issues, it was decided to move to a simpler model which could be iterated more rapidly and ethically.

The ideal model would be a neural culture, however existing neural cell models are either primary cultures extracted from acute tissue (a process with a significant learning curve to achieve high yields, and which still requires primary tissue to accomplish, negating any potential ethical advantage) or – since mature neurons do not divide – are pluripotent cell lines that can be triggered to transform into a neural phenotype[457]. Such models are costly, require specialised culture media and cannot be guaranteed to behave similarly to neurons *in vivo.*

CRL2541 cells (ATCC) are immortalised mouse cerebellar astrocytes. Whilst we established that these cells may not behave like wild-type astrocytes (chapter 4), they have several advantages over primary or pluripotent cell-derived neural cultures: they require no specialised culture conditions, grow rapidly, their growth can be arrested via serum deprivation (allowing consistent confluence between dishes and preventing regions of interest from being overgrown after light exposure), and are inexpensive (and already in stock from previous experiments). Astrocytes are a major component of brain tissue, and the activated phenotype is the most likely to interact with light stimulation proximally to an optrode implant *in vivo* since surgical trauma would trigger gliosis.

Additionally, blue-light phototoxicity and oxidative damage in astrocytes has been studied in the past, indicating that it should be possible to develop a method for quantifying phototoxicity in this model[160,161].

Dishes were illuminated via an optical fibre held in a retort stand such that the fibre contacted the underside of the dish at 90° (Figure 43) and the circumference of the dish marked on the incubator shelf to facilitate repeatable illumination of the precise centre of each sample.

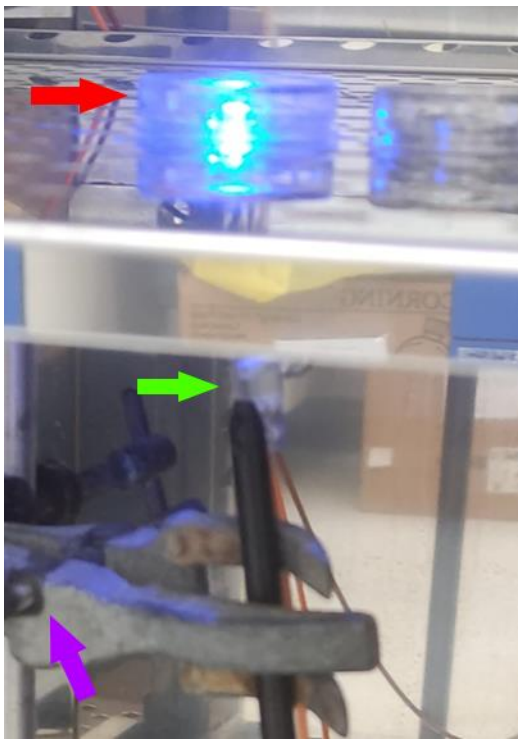

Figure 43: Dishes (red arrow) were illuminated from beneath via a 400 µm diameter optical fibre (green arrow) held in a retort stand (purple arrow). The fibre position was adjusted to 90° from the dish after this image was acquired.

Culture medium was aspirated and replaced with oxygenated aCSF prior to illumination as many culture media contain photosensitising agents[158,175]. Medium was replaced with serum-free high-glucose DMEM after exposure, and dishes were incubated overnight before simultaneous staining and fixation, preventing potential errors from normal cell death accumulating should samples have been stained and fixed at different times.

Samples were stained with live-dead NIR stain (Thermo Fisher Scientific), fixed in paraformaldehyde and mounted under cover slips with ProLong glass antifade mountant with NucBlue (Thermo Fisher Scientific).

Dishes were imaged with a Zeiss AxioObserver upright fluorescent microscope. The total cell count (using the NucBlue channel) and the dead cell count (using the Live/Dead NIR channel) was obtained using a macro in Fiji image analysis software (full macro is provided in the appendix).

The macro used carried out the following steps:

- The “enhance contrast” function was used with the default saturation value of 0.35 to aid differentiation between background signal and stained cells (brightness and contrast settings were not standardised across all images as relative intensity of stained cells was unimportant).
- An automatic thresholding step was applied to segment the stained cells by creating a mask comprising only pixels above a particular intensity value; several of Fiji’s built-in thresholding settings were tested on the NucBlue and NIR channels to establish which would be most accurate on each channel.
    - “Moments” was selected for the NucBlue channel and “Intermodes” for the NIR.
- The “watershed” function was applied to separate cells which overlapped, ensuring that they were counted as two cells rather than a single feature.
- Finally, the “analyze particles” function was used to count the number of cells, using a size range of 20-800 square microns (since the thresholding steps do not always segment the entire cell, some cells will appear smaller than their “true” size, whilst others will appear larger due to segmentation picking up a larger region; 20 square microns was sufficiently large to exclude small thresholding artefacts and 800 square microns excluded any large artefacts such as dust or bubbles.

Whilst there is a risk that this will also exclude large clusters of very closely packed cells, this was judged to be unlikely since Live/Dead staining was less bright at the cell periphery, allowing effective segmentation even when cells were very closely positioned to one another).

- The macro performed these steps separately for the two channels in each image, outputting them to a results table.

Exposure duration

To establish reasonable values for light exposure to be used in acute brain slice experiments, 10 replicate 35mm diameter polystyrene cell culture dishes were cultured to ~80% confluence with CRL2541 astrocytes and exposed for each of 20, 40 and 60 min with 470 nm light at 12 mW, 50% duty cycle with a 100 ms pulse from a 400 µm diameter optical fibre. Each exposure duration also included a control dish that was unexposed, for a total of 33 dishes.

Percentage cell death increased with exposure duration (0 min: 7.6 ± 4.5%, 20 min: 8.2 ± 3.5%, 40 min: 30.5 ± 10.1%, 60 min: 36 ± 12.1% - Figure 45); a one-way ANOVA indicates significant association of cell death with exposure time ($p = 0.000007$). A circular region of dead cells is clearly visible in higher duration exposures (Figure 44). Existing literature on retinal phototoxicity describes photochemical damage as time-dependent and cumulative, which is consistent with these results. From this experiment it can be established that >40 min is a reasonable exposure time within which to detect phototoxicity from illumination of this intensity and pulse pattern.

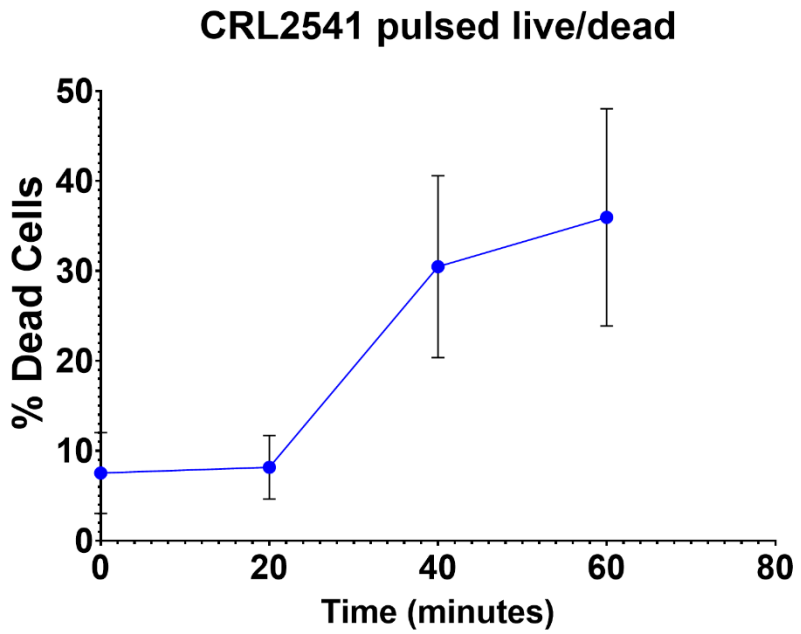

Figure 45: Percentage cell death is associated with exposure duration in CRL2541 cells exposed to pulsed 470 nm light. N = 10 per exposure time. Error bars are standard deviation.

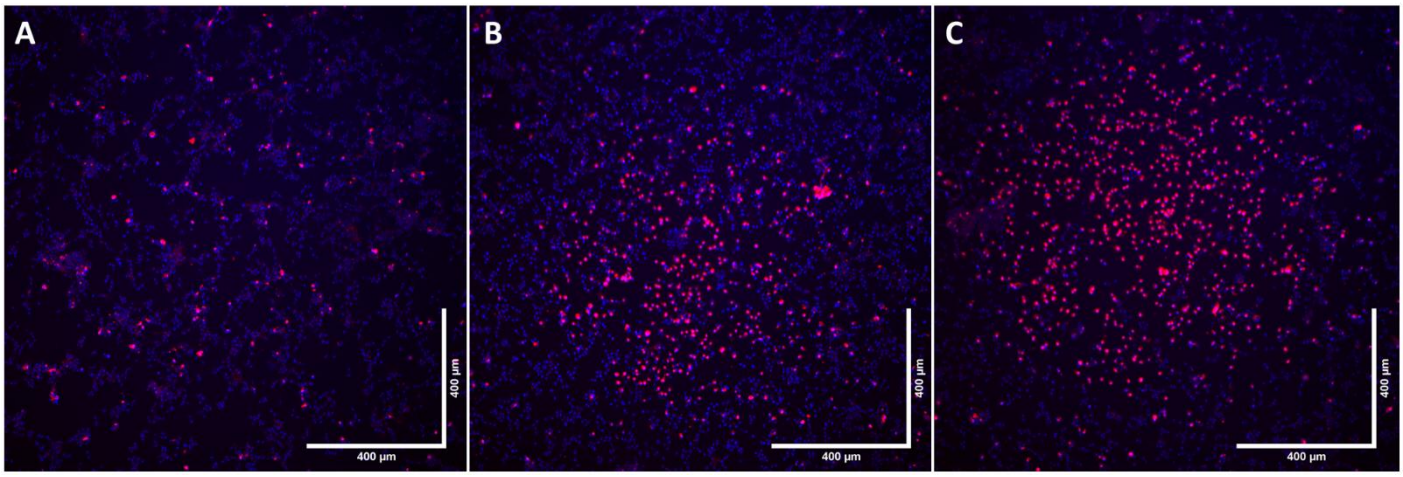

Figure 44: A clear circular region of dead CRL2541 cells becomes visible as 470 nm light exposure duration increases. The ratio of dead cells (red) to total cells (blue) increases with exposure time (A = 20 min, B = 40 min, C = 60 min).

Duty cycle

To compare the effect of continuous-wave light exposure to pulsed, 6 replicate 35mm diameter polystyrene cell culture dishes were cultured to ~80% confluence with CRL2541 astrocytes and exposed for each of 10, 20 and 30 min with 470 nm light at 12 mW, continuous wave from a 400 µm diameter optical fibre, such that total exposure time is equal to that of the 20, 40 and 60 min exposures at a 50% duty cycle. 6 replicate control dishes were also measured, for a total of 24 dishes.

Illuminated samples exhibited a similar pattern to those exposed to pulsed exposure: % cell death was approximately similar to control dishes at 10 minutes exposure (0 min = 9.1 ± 3%, 10 min = 8.0 ± 2.2%) and increased at 20 and 30 minutes (20 min = 15.1 ± 11.3%, 30 min = 28 ± 16.9% — Figure 47) A similar region of cell death to the pulsed samples is visible at longer exposure durations (Figure 46). A one-way ANOVA indicated a significant relationship of exposure time to cell death ($p = 0.0003$).

A two-way mixed-effects analysis comparing continuous wave to pulsed exposure found no significant difference at any time point (0 min $p = 0.2252$, 10 min $p = >0.9999$, 20 min $p = 0.1428$, 30 min $p = 0.8268$), indicating that pulse pattern had no significant effect on cell death.

Thermal effects from visible light exposure are strongly related to the duty cycle of exposure[100], with a long period of illumination relative to darkness resulting in higher risk of photothermal effects. Increases in temperature of >3 °C are normal in brain tissue for short periods, but can become hazardous if elevated for extended periods[98,99] (Chapter 1.7.3 and 1.8.4). The lack of difference between pulsed (50% duty cycle) and continuous (100% duty cycle) exposure suggests that no major thermal effects are experienced by samples illuminated at this intensity and wavelength; if thermal effects were significant, it would be expected that the

continuously exposed samples would exhibit higher rates of cell death than those subjected to pulsed exposure.

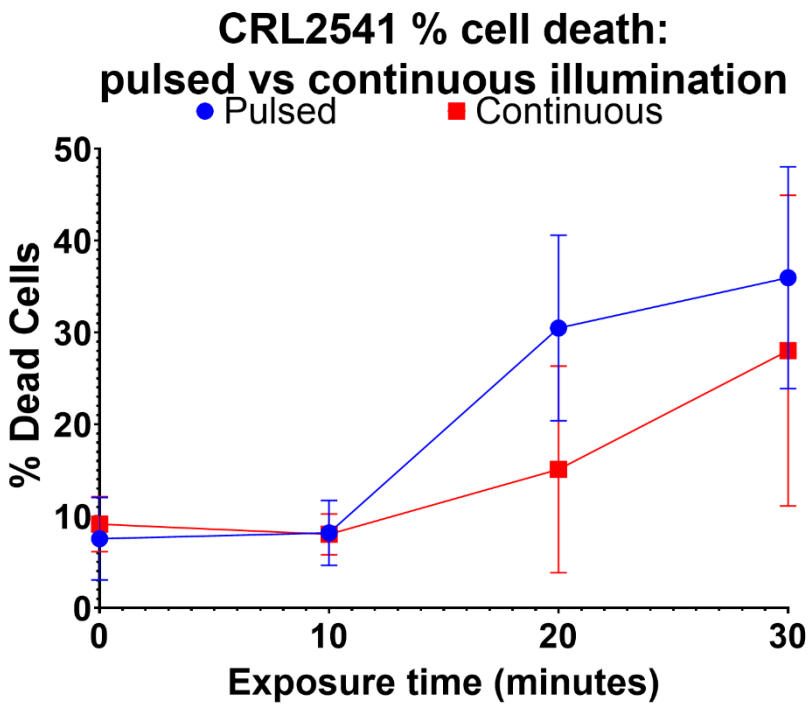

Figure 47: Continuous-wave 470 nm light exposure in CRL2541 cells has a similar relationship with cell death as in pulsed samples. N = 6 per exposure time. Error bars show standard deviation.

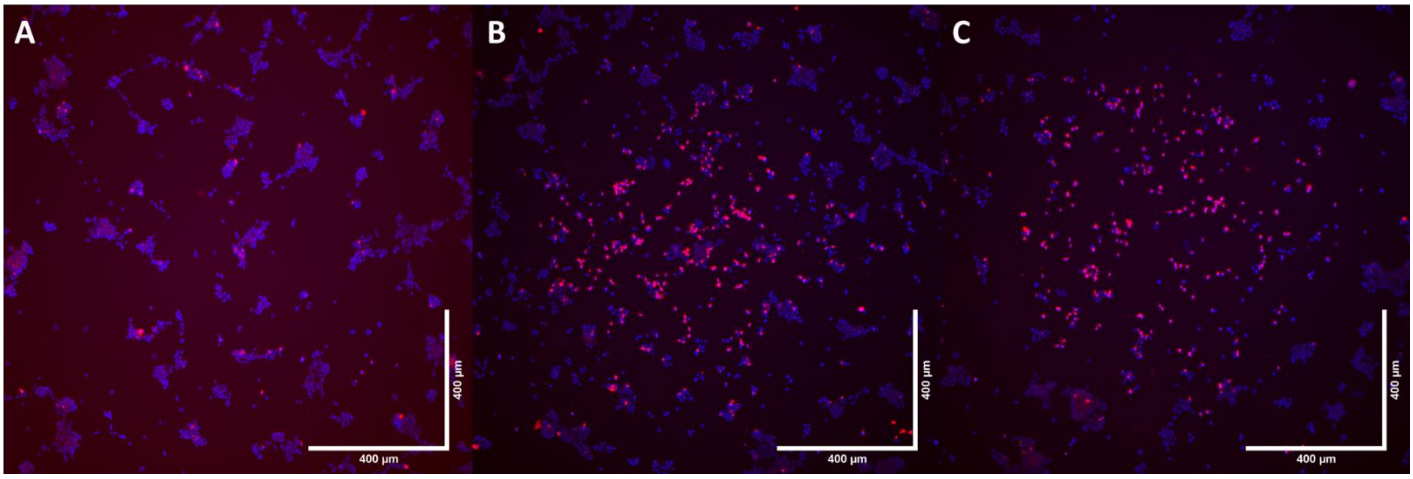

Figure 46: A clear circular region of dead CRL2541 cells forms at longer exposures to continuous-wave 470 nm light. The ratio of dead cells (red) to total cells (blue) increases with exposure time (A = 10 min, B = 20 min, C = 30 min).

Wavelength

Whilst there is substantial precedent for blue-light phototoxicity in retina and other tissue types, there are far fewer studies on longer wavelengths and potential photochemical hazard. To explore the effect of longer wavelength visible light exposure, a 595 nm LED was used. Due to its lower photon energy, the maximum power of this LED was ~4 mW through a 400 µm diameter optical fibre. Since photochemical toxicity appears to be cumulative with time, it is necessary to adjust the exposure time to account for the lower power density available. Unfortunately, the long exposure duration limited the number of samples that could be produced.

Two replicate 35 mm diameter polystyrene cell culture dishes were cultured to ~80% confluence with CRL2541 astrocytes and exposed for each of 6, 18 and 24 h with 595 nm light at 4 mW, pulsed with a 50% duty cycle and 100 ms duration from a 400 µm diameter optical fibre.

Percentage cell death did not increase between 6 and 18 h exposure, but approximately doubled by 24 h (6 h: 8 ± 1%, 16 h: 7.5 ± 0%, 24 h: 16 ± 3.7% - Figure 49); a one-way ANOVA indicates significant association of cell death with exposure time ($P = 0.0461$). Unlike in cells exposed to brighter 470 nm light for shorter periods, there is not a clear circular region of cell death – possibly due to the longer time that is available for cells to migrate in and out of the exposed site (Figure 48). Since all samples were cultured, fixed and stained simultaneously, there should be no error due to cell death from other sources.

This preliminary experiment suggests that despite the substantially lower energy per-photon, further investigation of 595 nm light exposure is warranted; optogenetic implants are chronically implanted devices intended to function for multiple years, raising the possibility of long-term phototoxicity from even longer wavelengths. Further experiments with a brighter illumination source capable of matching the output of the 470 nm LED on a larger sample population may reveal as-yet unknown hazard from these longer wavelengths.

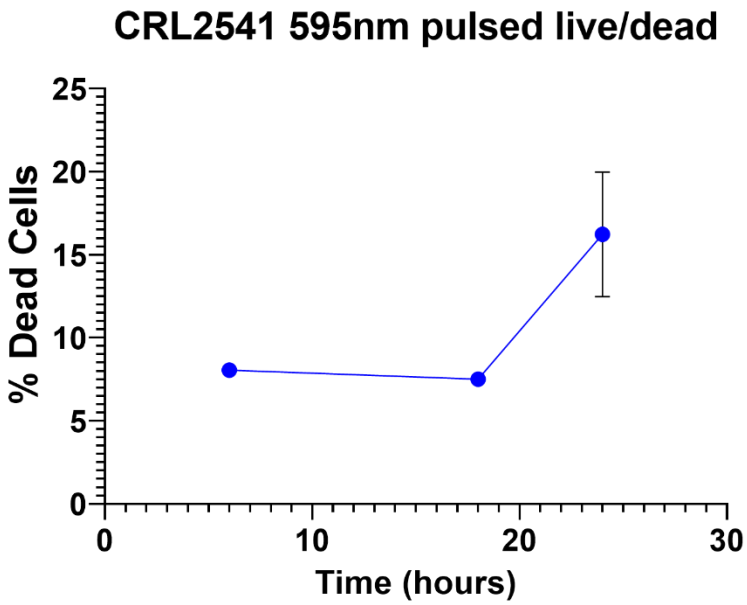

Figure 49: CRL2541 cell death increases after 24 h of exposure to 595 nm light.

N = 2 for each exposure time. Error bars are standard deviation.

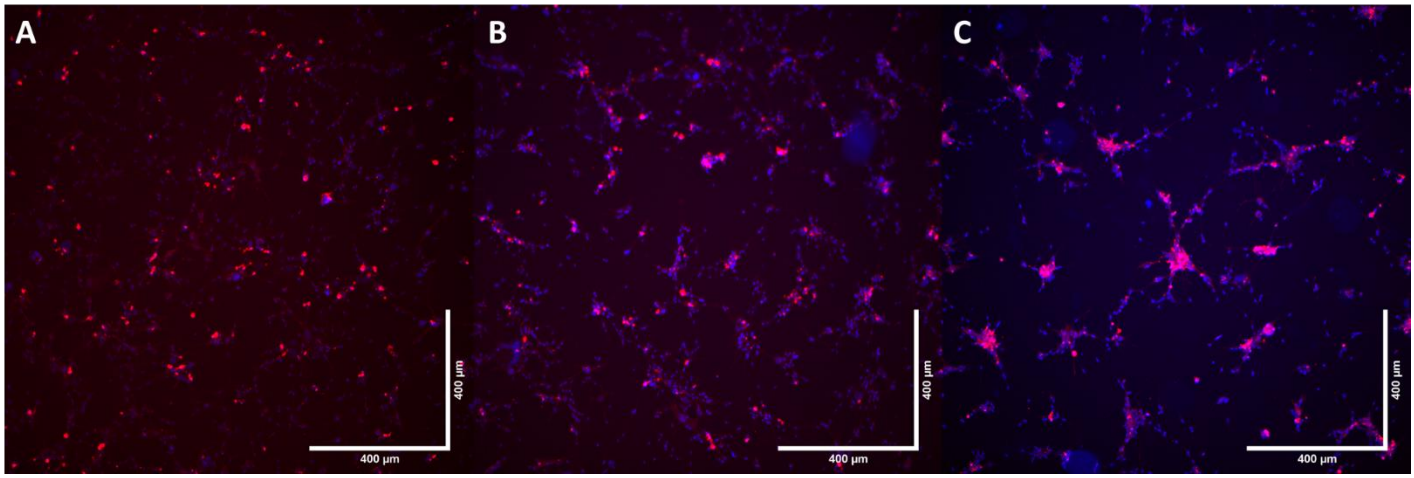

Figure 48: Exposure of CRL2541 cells to 595 nm light does not produce as clear a region of cell death as with 470 nm exposure. The ratio of dead cells (red) to total cells (blue) does not with exposure time between 6 h (A) and 18 h (B) but does increase at 24 h exposure (C).

Recovery time post-exposure: time course experiment

The main factor that differs between the successful CRL2541 cell experiments and the failed attempts to stain for light-induced cell death in acute brain slices is that the cell cultures were stained and fixed after an overnight incubation post-exposure, whereas the acute brain slices were fixed and stained immediately after light exposure. This difference was necessary; the perfusion chambers used to sustain acute brain slices can keep slices viable for only 2-3 hrs, with cell death due to oxygen and glucose deprivation accumulating rapidly after this point.

Since apoptosis can take many hours to complete (revealing different biomarkers at different stages of the process), it seemed likely that the chief cause of failure in previous trials of cell death stains in these samples was that insufficient time was afforded for the affected cells to die.

To pinpoint the amount of time required for dying CRL2541 astrocytes to be detectable via the Live/Dead NIR staining method, six 35 mm diameter polystyrene cell culture dishes were cultured to ~80% confluence with CRL2541 astrocytes and exposed for 1 h with 470 nm light at 12 mW, pulsed with a 50% duty cycle and 100 ms duration from a 400 µm diameter optical fibre. Dishes were illuminated in a staggered manner such that one dish was left for each of 30, 60, 90, 120, 240 or 360 min between illumination and simultaneous staining and fixation of all dishes. Six control dishes were also treated identically, omitting the light exposure step.

Percentage cell death was similar to control samples for 30, 60 and 90 min, but increased substantially from 120 min onwards (from 9.4% at 90 min to 23.3 % at 120 min – Figure 50) until its maximum at 360 min (29.7%) and exhibited a clear circular region of cell death (Figure 51), suggesting that cell death induced by exposure to 470 nm light requires approximately 120 min before it is detectable with the Live/Dead NIR assay.

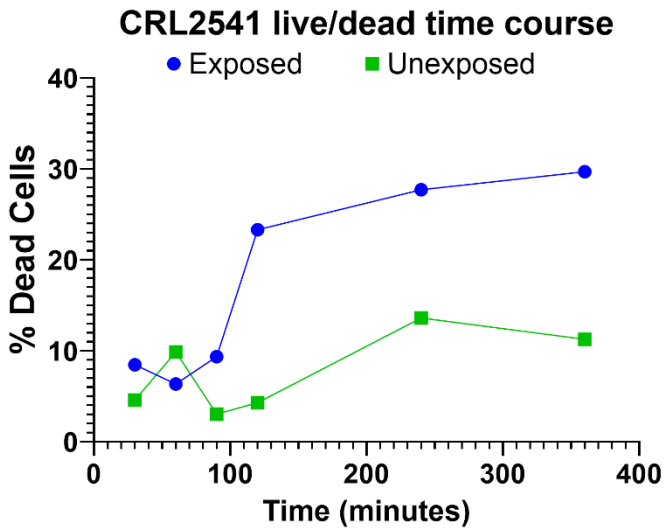

Figure 50: Detectable CRL2541 death increases sharply 120 min after light exposure. Due to long exposure time requirements, N=1 for each time point.

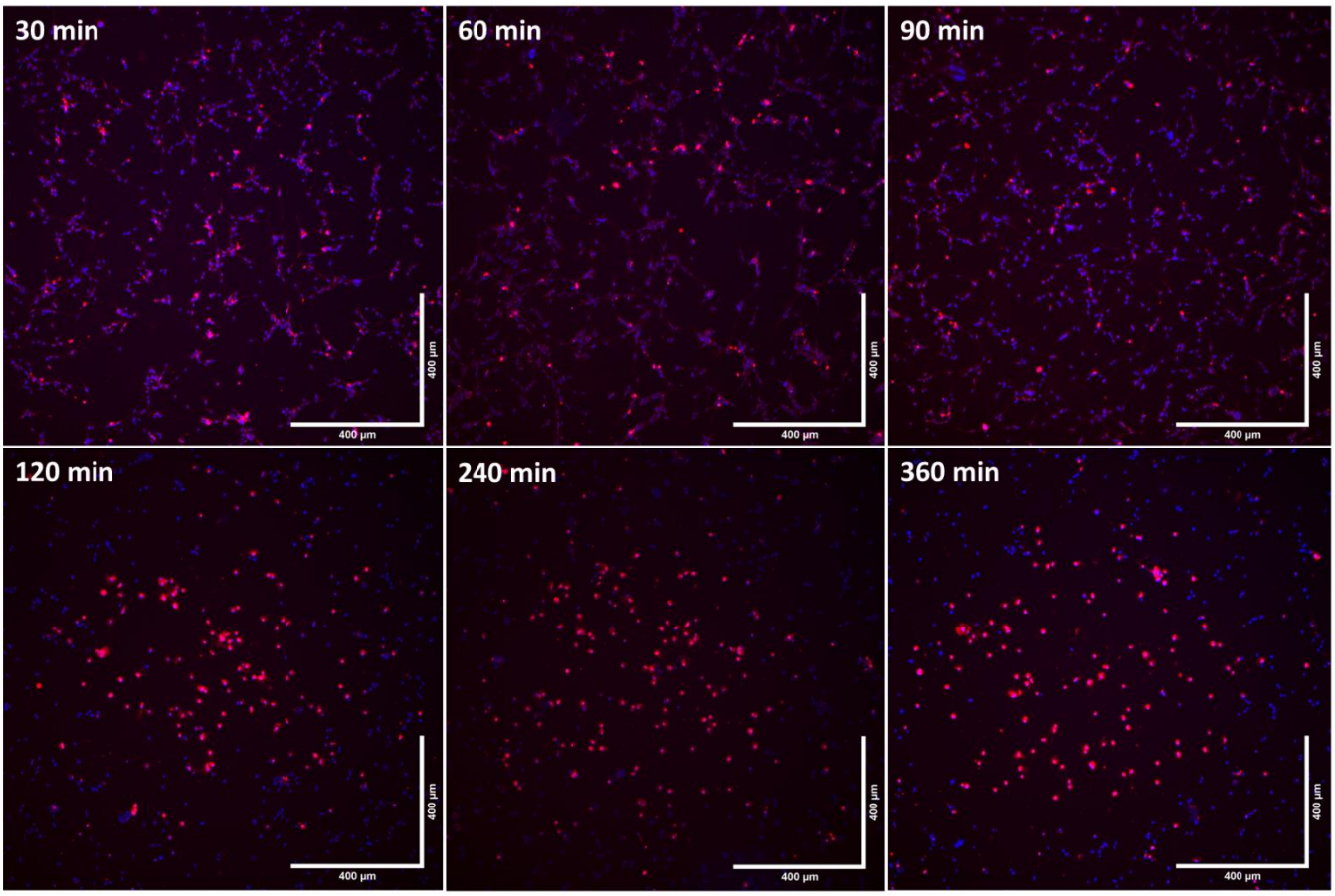

Figure 51: A distinct circular region of CRL2541 cell death is detectable only if cells are allowed to incubate for 120 min or longer after 470 nm light exposure. The ratio of dead cells (red) to total cells (blue) does not increase between dishes left 30 min after exposure and those incubated for 90 min, but does increase if dishes are incubated for 120 min or longer post-exposure.

6.2.6. Acute mouse brain slices with 3 h at RT after light exposure

Following the time-course experiment with CRL2541 astrocyte cells, it was necessary to test whether a similar delay post-exposure would be sufficient to visualise blue light-triggered cell death in acute mouse brain slices. To achieve this, a method must be employed to slow or prevent cell death from glucose and oxygen deprivation, which would normally occur soon after light exposure in slices kept in a perfusion chamber. A possible approach would be to return the slices to a lower temperature environment after exposure; cells with damaged mitochondria may continue to apoptose in such an environment whilst healthy cells may remain healthy for a longer period due to metabolic suppression in the cooler conditions, allowing light-induced damage to be more readily visualised.

Three 250 µm thick acute brain slices were prepared from a C57BL/6 female mouse of approximately 1 year of age (scheduled for culling). The slices were exposed to 470 nm light at 12 mW intensity, with a 50% duty cycle and 100 ms pulse length for 1 h in the perfusion chamber (set to 37 °C) before being returned to the recovery chamber (maintained at room temperature, ~20-22 °C) for 3 h. Slices were then stained with Live/Dead NIR, fixed, sectioned and mounted with ProLong Glass with NucBlue as normal.

Fluorescent images of the samples showed clearly resolved circular (or ovoid, in cases where the optical fibre was not perfectly placed at 90° to the tissue surface) regions of cell death, with little Live/Dead signal in the surrounding tissue that had not been exposed (Figure 52). This suggests that reducing the temperature of acute mouse brain slices to room temperature after exposure is sufficient to prevent excessive cell death that would ordinarily occur at 37°C in a perfusion chamber, whilst allowing cell death arising from phototoxicity to continue.

Since the tissue is being maintained at non-physiological temperatures, it is possible that the mechanisms of cell death may be altered from that which might occur *in vivo.*

Despite this drawback, this method has facilitated detection of light-induced cell death where other approaches have failed.

An alternative approach could be to produce brain slice organotypic cultures; when acute brain slices are maintained in the correct conditions it is possible to keep them alive for up to 6 months[458]. However, these organotypic cultures undergo substantial structural and behavioural changes from tissue *in vivo*, including “spreading” onto their growth substrate, changes in opacity and altered cell behaviour. Additionally, they must be obtained from young mouse pups (P8-9), and further differences have not been fully characterised compared to acute samples. Many of these issues can be mitigated in laboratories with sufficient experience and resources[459], however learning to reliably culture brain slices with confidence that they would be comparable to brain tissue *in vivo* was considered out-of-scope for this project. It was judged that the potential effect of temperature reduction is likely less substantial than the changes incurred during organotypic slice culture.

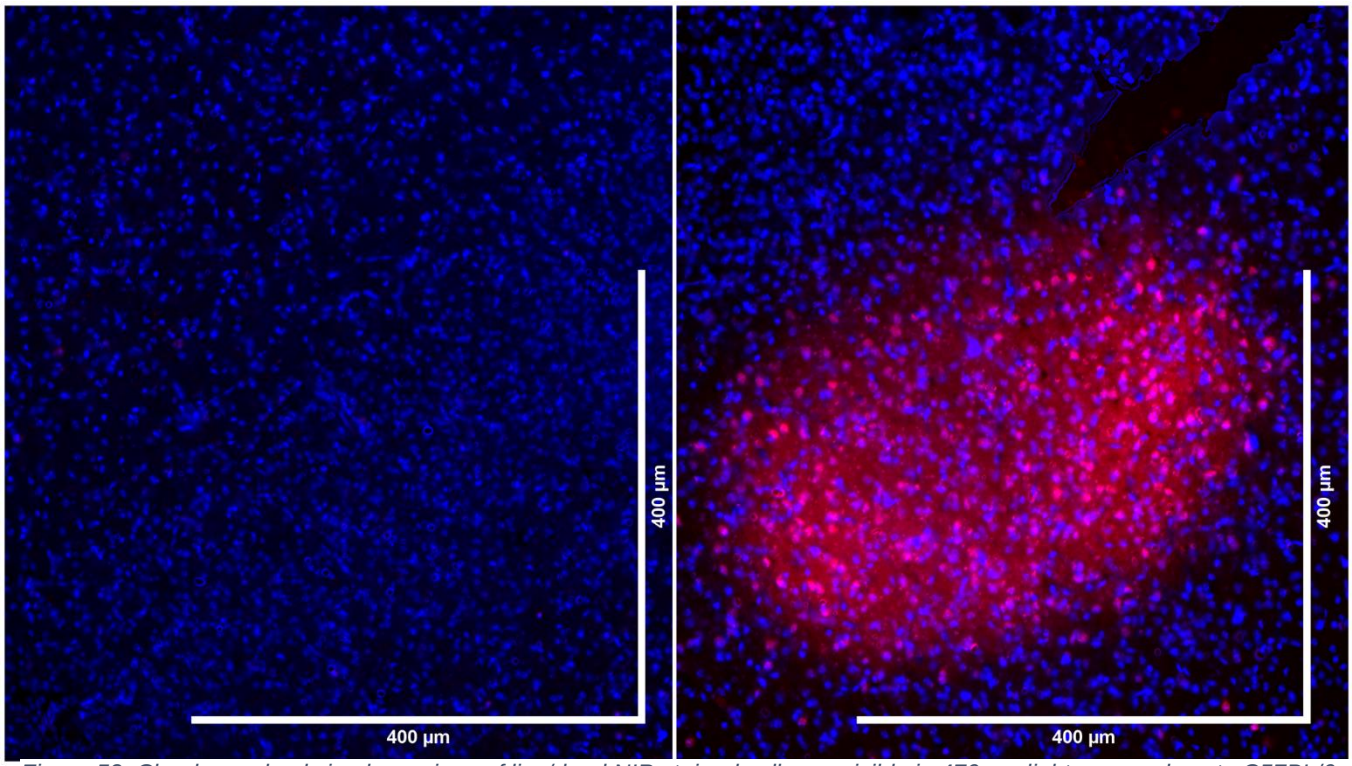

Figure 52: Clearly resolved circular regions of live/dead NIR stained cells are visible in 470 nm light-exposed acute C57BL/6 mouse brain slices when incubated at room temperature for 3 hrs post-exposure before fixation and staining.

6.2.7. Live/Dead Fixable NIR staining of light-exposed acute mouse brain slices

Following the trial experiment, acute mouse brain slices were obtained from HALO, EMX-ChR and C57BL/6 mice: 10 slices from each of three female HALO mice, ~8 wks old; 30 slices total. 10 slices from each of three EMX-ChR mice, ~10 wks old; 30 slices total. 10 slices from each of six C57BL/6 mice, age ranging from 8 wks to 1 year; 60 slices total. Excess slices were used as controls.

Slices were exposed to 470 nm light at 6, 9 and 12 mW with a 50% duty cycle and 100 ms pulse length for 1 h (10 slices per intensity value; 20 for C57BL/6) before being transferred to the recovery chamber for 2 h (this reduced time at room temperature was selected as a compromise, to reduce potential changes arising from the reduced temperature whilst providing sufficient time for cell death to become detectable). Slices were then stained with Live/Dead NIR, fixed, resectioned into 20 µm slices via cryostat and mounted with ProLong glass with NucBlue.

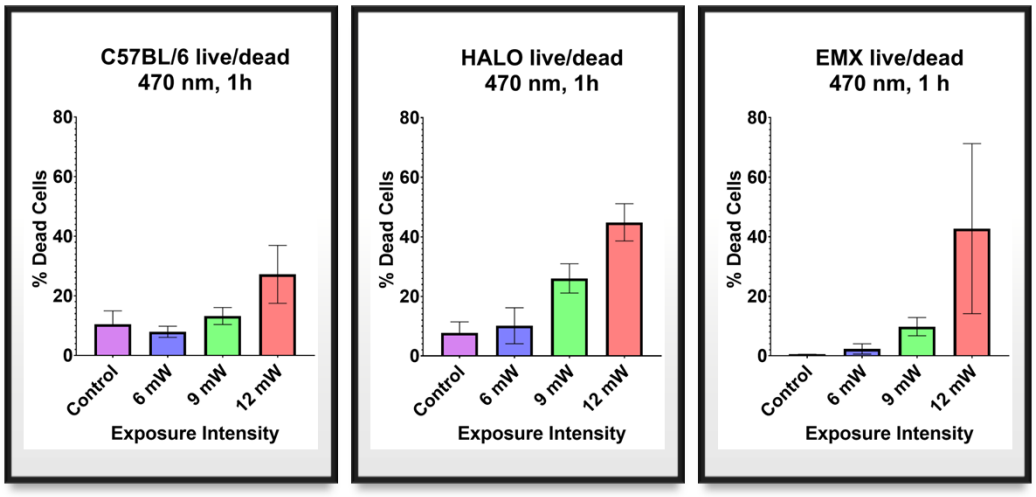

Figure 53: C57BL/6, HALO and EMX acute brain slices all show a positive relationship of 470 nm light exposure intensity to percentage cell death. N = 10 for EMX and HALO, 20 for C57BL/6. Error bars are standard deviation.

All three models exhibited increases in percentage cell death with increased light exposure intensity (Figure 53). The C57BL/6 slices did not experience significant increases between control and 6 mW exposure (Control: 10.5 ± 4.5%, 6 mW = 7.9 ± 1.9%. One-way ANOVA comparing control to 6 mW returns $p = 0.82$) however increased significantly between 6, 9 and 12 mW exposure (9 mW = 13.2 ± 2.9, 12 mW = 27.2 ± 9.7. One-way ANOVA comparing 6 to 9 mW returns $p = 0.03$ and 9 to 12 mW $p < 0.0001$). Overall, C57BL/6 samples show a strong association between exposure intensity and cell death ($p < 0.0001$).

The HALO slices did not experience significant increases between control and 6 mW exposure (Control: 7.7 ± 3.7%, 6 mW = 10.1 ± 6%. One-way ANOVA comparing control to 6 mW returns $p = 0.74$) however increased significantly between 6, 9 and 12 mW exposure (9 mW = 26 ± 4.9, 12 mW = 44.9 ± 6.3. One-way ANOVA comparing 6 to 9 mW returns $p < 0.0001$ and 9 to 12 mW $p < 0.0001$). Overall, HALO samples show a strong association between exposure intensity and cell death ($p < 0.0001$).

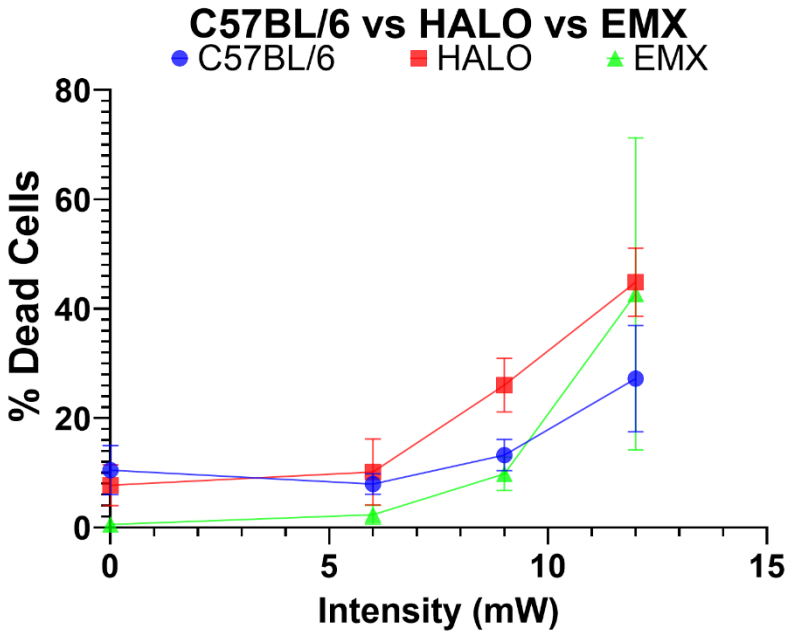

Figure 54: HALO mice experience significantly higher rates of 470 nm light-induced cell death than do C57BL/6 mice. EMX and C57BL/6 mice appear to experience similar levels of phototoxicity from this exposure. N = 10 per intensity value. Error bars are standard deviation.

The EMX-ChR slices did not experience significant increases between control and 6 mW exposure (Control: 0.5 ± 0.01%, 6 mW = 2.3 ± 1.7%. One-way ANOVA comparing control to 6 mW returns p = 0.99) or 6 to 9 mW (9 mW = 9.8 ± 3.1. One-way ANOVA comparing 6 to 9 mW returns p = 0.74) however increased significantly between 9 and 12 mW exposure (12 mW = 42.7 ± 28.5. One-way ANOVA comparing 9 to 12 mW returns p = 0.0006). Overall, EMX-ChR samples show a strong association between exposure intensity and cell death ($p < 0.0001$).

Mixed-effects analysis comparing the three mouse types returns a significant effect on cell death from mouse strain ($p < 0.0001$). Tukey's multiple comparisons analysis suggests that this difference is primarily between C57BL/6 and HALO mice (comparison of EMX and HALO animals returns p = 0.26 and comparison of C57BL/6 with EMX returns p = 0.87 whereas comparison of C57BL/6 with HALO returns p = 0.0004, indicating that HALO mice experience significantly higher rates of cell death after light exposure than do C57BL/6 animals – Figure 54 & Figure 55).

This difference could be due to the presence of YFP in the HALO animals; absorption and re-emission of incident light may increase the number of photons that interact with cells in the exposed regions. However, the EMX animals also express YFP and do not appear to experience significantly higher rates of cell death than C57BL/6 animals; as the relative expression level of YFP between the two models is unknown it is not possible to determine whether HALO expression of YFP is higher than EMX. Another possible explanation could be that the HALO neurons experience overstimulation and become stressed when exposed to 470 nm light, making them more susceptible to phototoxicity. This is unlikely since halorhodopsin has a red-shifted action spectrum compared to ChR2, with a peak absorption of ~570 nm compared to ChR2's peak of ~460 nm (ref [460]), meaning that unless the HALO animals expressed significantly higher levels of halorhodopsin than the EMX animals do ChR2, the EMX neurons are likely to experience greater stimulation of action potentials than will the HALO.

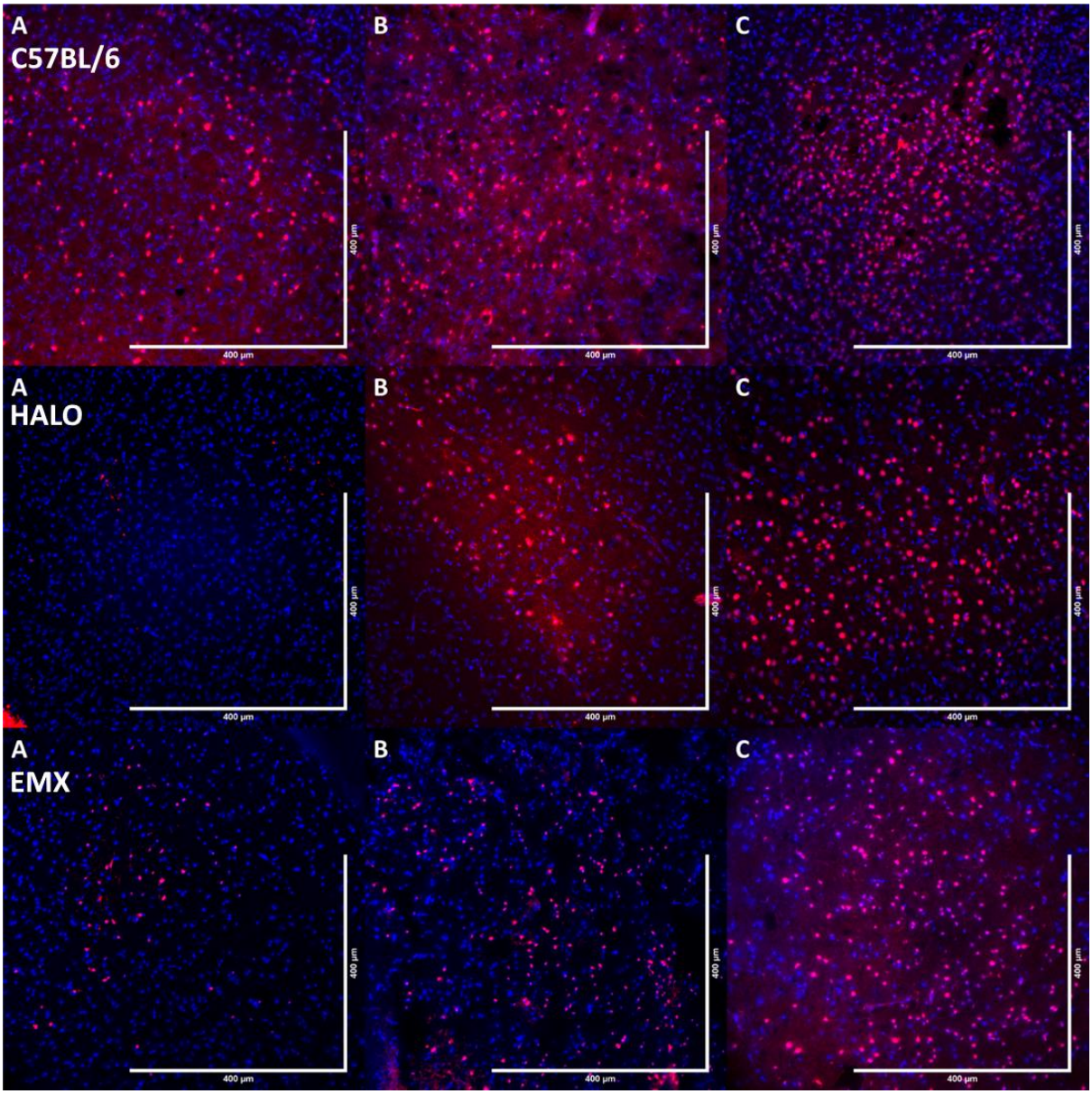

Figure 55: All three mouse lines tested show a positive relationship of cell death to 470 nm illumination intensity. A = 6 mW, B = 9 mW, C = 12 mW. Red = dead cells stained with Live/Dead NIR, blue = all cells stained with NucBlue.

6.3. Discussion and future prospects

Successful deployment of an optogenetic brain implant to clinical settings requires extensive validation by regulatory organisations; this process can be extremely difficult – if not impossible – if regulatory bodies lack sufficient information to make informed decisions about safety and efficacy of a given device.

Whilst data regarding optical toxicity in skin and retina are available, the action of visible light exposure on brain is poorly understood; whilst studies exist that demonstrate the “blue light hazard” in brain tissue or brain-derived cells, a comprehensive action spectrum for visible light exposure in brain has yet to be developed. Retina, skin and brain contain different chromophores at different levels of expression, and possess differing defences against this type of insult; it has not been demonstrated whether levels of antioxidants and protective/reparative enzymes differ between these tissues. However it would seem likely that tissue that is not routinely exposed to light — such as brain — may not possess the same level of protection as those adapted to light exposure.

Consequently, it is necessary to develop an action spectrum for photochemical damage in brain tissue in the visible spectrum if optogenetic devices are to be brought into clinical practice. This project sought to develop methods for establishing hazard thresholds for visible light exposure in brain, and if possible to begin collecting the data required.

Method development for detection of light-induced phototoxicity in acute mouse brain slices was hampered by difficulty detecting cell death after exposure; 470 nm light was chosen for this developmental process since the “blue light hazard” has been firmly established in the literature for a range of tissues (though not thoroughly described for brain).

It was hypothesised that these difficulties in detection of cell death were due to the process having not progressed to a detectable stage before tissue fixation and staining. Experimentation has established that a post-exposure incubation period of 2 h facilitates detection by providing sufficient time for cell death to occur; this incubation period can be carried out at room temperature to prevent cell death from other sources without interfering with detecting of light-induced damage. With this knowledge, it was possible to develop a method that reliably detects light-induced cell death in acute mouse brain slices. The Thermo Fisher Live/Dead NIR assay is relatively inexpensive, has a simple protocol and clearly labels dead cells, allowing it to be used in conjunction with a nuclear counterstain to determine a rate of cell death in a light-exposed region of tissue or cell culture. Whilst this stain has many advantages, it may be possible to re-test other cell death markers that were discarded in earlier stages of this project to identify a more optimal stain for future work, or to expand the information gained.

Both CRL2541 astrocytes and acute mouse brain models experience increased rates of cell death when exposed to 470 nm light at intensities, durations and pulse patterns similar to those used in optogenetics literature. Whilst the illumination intensity was higher than that used in some (but not all) mouse studies, this reflects the need for more intense illumination in non-human primate models and – ultimately – humans.

Acute brain slice autofluorescence is altered by 470 nm light exposure, indicating that photochemical processes are occurring in exposed regions. In retina, these changes correlate with phototoxicity; this link cannot yet be confirmed in brain but alterations to brain tissue autofluorescence are a potential diagnostic marker for photochemical trauma arising from optogenetic implant use.

We found that CRL2541 astrocytes may experience phototoxicity from 595 nm light. However, lack of a suitably intense light source and insufficient time limited the degree to which this could be explored. Literature investigating the effect of visible light at longer than 470 nm on brain tissue is sparse, and further investigation is required for wavelengths in the green, yellow-orange and red regions of the visible spectrum.

There was no difference in death rate of CRL-2541 cells exposed to continuous-wave or pulsed 470 nm light, suggesting that photothermal effects are not strong at this wavelength. However, these experiments must be repeated and expanded for different pulse patterns, intensities and wavelengths in acute brain slice models to establish at what point photothermal effects may become significant. It is still advisable to use pulsed light to allow cooling of samples and avoid errors from thermal effects when measuring photochemical toxicity.

A method for inducing and detecting phototoxicity in acute mouse brain slices has been successfully developed. This method can be used to investigate a wider range of wavelengths, intensities, exposure durations, pulse patterns and models to develop a phototoxic action spectrum for visible light in brain. These data would be useful to regulatory organisations responsible for assessing novel optogenetic technologies for clinical deployment.

Newcastle University BioImaging Facility has recently constructed a wide-field microscope equipped with a Polygon digital mirror device, allowing precise illumination of defined sample regions with a range of light sources. The system is equipped with a heated perfusion system, allowing acute brain slices to be exposed in this manner.

Whilst there was insufficient time to explore the possibilities of this system during this project, it could facilitate exposing a single sample to multiple wavelengths or intensities of light in clearly delineated regions during the same experiment, allowing a wide range of wavelengths to be investigated in a much shorter period than was possible with illumination via optical fibre.

In addition to light-induced cell death, other possible consequences of visible light exposure in brain must be considered and investigated: alterations to gene expression, inflammatory status, electrical activity, oxidative stress and other aspects of tissue health may be negatively affected by chronic light exposure; further experiments will be needed to produce a comprehensive picture of the effects of light on brain tissue before optogenetic devices can be confidently approved for clinical use.

Chapter 7. Conclusions and Future Direction

The original objective of this project was to develop a better understanding of the effects of optogenetic implants on brain tissue, both in an acute sense (immediately during and after implantation) and after chronic use in a patient. The effects of mechanical, thermal and optical trauma were to be measured and a hazard spectrum for light exposure in brain produced.

Whilst some progress was made on these goals — including successful quantification of the effect of blue light exposure on acute mouse brain slices — the project has primarily highlighted the difficulty of measuring the properties and responses of brain tissue in a repeatable and robust manner. Brain is an inhomogeneous, anisotropic biological tissue that varies with species and strain, presenting great challenges for measurement of mechanical properties. Chapter 3 shows that current reports of mouse brain mechanical properties are highly variable, with substantial differences in mouse age and strain, frequency and strain size of mechanical measurement, temperature and slice orientation of samples and the method in which samples were handled and stored.

This highlights a need for a comprehensive study that determines the mechanical behaviour of healthy mouse brain (and that of other common research organisms such as porcine and bovine brain) and accounts for common causes of unreliability in the literature so far. Use of magnetic resonance elastography (or similarly non-invasive methods such as shear wave elastography) — or failing that, AFM measurements on chilled, freshly-sliced brain tissue — would allow for errors arising from Donnan swelling of brain tissue to be avoided, and comparisons of multiple popular mouse strains (such as BALB-C, C57BL/6 and CD1) would establish whether there are significant differences between the models currently used in brain mechanics research.

In Chapter 4, cell-derived extracellular matrix (ECM) samples were successfully produced from the CRL-2541 immortalised astrocyte cell line. These ECM samples were intended to serve as a model platform for exploring the effect of mechanical, thermal and optical insult on the composition and mechanical properties of ECM in brain. Whilst production of these models was successful, they proved to be extremely difficult to measure, and their low stiffness when measured with both atomic force microscopy and shear rheology suggest that the contribution of ECM to brain tissue mechanical behaviour is only a small part of the question; it seems likely that the contribution of cellular components of the tissue and their bonds with each other and the surrounding ECM contribute substantially to the overall picture. This is supported by later AFM measurement of acute mouse brain slices in Chapter 5, whose stiffness was several orders of magnitude higher than that of the ECM gels. However, it is possible that these results are specific to the CRL-2541 cell line, or that that 3-dimensional models or co-cultures of multiple cell types might produce substantially stiffer ECM.

Whilst it seems likely that ECM in brain contributes minimally to overall tissue mechanics, this does not mean that there is no value in exploring the effects of mechanical, thermal and photochemical insult in these samples. The effect of these types of insult on ECM composition are not well understood, and use of models such as the one produced in this project would provide a consistent platform that does not suffer the damage that decellularised whole tissue experiences. Exploring alterations to astrocyte-derived ECM composition and structure could reveal novel insights into the brain's response to trauma.

Further highlighting the need for a re-assessment of methods used for the measurement and reporting of brain mechanical properties, Chapter 5 demonstrates that a commonly reported assumption in brain mechanics literature — that acute brain slices remain mechanically stable provided they are measured within 8 hrs of death — is false, and that studies in which this assumption is made are likely to

possess significant inaccuracies in their reported data. Whilst this chapter does suggest ways in which these samples can be measured more reliably (namely measuring as rapidly as possible after tissue is sliced, maintaining samples at a low temperature and using less invasive methods such as magnetic resonance elastography rather than *ex vivo* methods in which brain tissue is susceptible to osmotic swelling), these samples remain extremely challenging to measure mechanically in a manner that is consistent and reliable.

Similarly challenging was the detection and quantification of optical toxicity in acute mouse brain slices. Chapter 6 concluded with an effective protocol for the exposure of acute mouse brain slices to visible light and measurement of the resulting toxicity, but it also highlighted the importance of time in these experiments. Living brain is dynamic and its response to insult is not necessarily immediate; if it is fixed immediately after light exposure, cell death cannot be adequately quantified.

In brief, the new protocol involves exposure of an acute mouse brain slice to visible light via an optical fibre in a perfusion chamber. Exposure times can vary from 0 to ~2 h; after this point the perfusion chamber cannot adequately support the brain slices, though this limit is heavily influenced by operator skill and the precise perfusion setup used. Exposed slices are returned to a recovery chamber at room temperature for ~2 h to allow cell death to occur and are then stained and/or fixed as normal. The protocol uses a Live/Dead NIR stain to highlight dead cells, though in theory many other stains for cell death or toxicity should work, and those which were initially trialled in this project should be reassessed in light of the new post-exposure room temperature incubation step. The protocol can be readily adjusted for different wavelengths, intensities, pulse patterns and staining targets, and can be scaled up for use in non-human primate tissue prior to *in-vivo* experiments if desired.

The ”blue light hazard” is a well-known phenomenon in retina and skin, and for this reason 470 nm light was selected as a proof of principle. However, whilst the effect of blue light exposure had been quantified in cell models this is the first time (to my knowledge) that the phototoxic effect of blue light has been directly measured in *ex vivo* acute brain tissue; previous studies of blue light phototoxicity have been limited to *in vitro* cultures of immortalised or primary cells. Amongst those studies, most concern retinal cells with only four studies using glial or neural cultures from brain. The results support the hypothesis that 470 nm light is toxic to brain tissue at intensities relevant to optogenetic implants, and that this toxicity is both time- and intensity-dependent.

Optical toxicity experiments in this project investigated the effects of only one wavelength; establishing a reliable protocol for measuring cell death in cells and tissue exposed to 470 nm light was more challenging than expected, leaving little time for analysis of other wavelengths. Similarly, a wider range of pulse patterns, intensities and cell death detection methods require attention. Once a hazard spectrum of visible light has been produced for acute mouse brain slices, these experiments can be repeated *in vivo,* at first in both acute and chronic exposures of mouse brain and ultimately in non-human primate models. A visible hazard spectrum for non-human primate brain would be a powerful tool for both research groups developing optogenetic devices for clinical applications and the regulatory authorities responsible for assessing their safety and efficacy.

Due to ethical and financial constraints, the number of mice used in this project was limited; repeats of these experiments with greater numbers of samples would be prudent to increase the reliability of the conclusions drawn.

This project highlights several ways in which our understanding of optogenetic device safety can be improved. If experimental approaches to mechanical and phototoxic experimentation on brain tissue consider the insights from this work, it will serve to improve the reliability and utility of novel data going forward. This work paves the way to establishing regulatory guidelines for introduction of optogenetic implant technologies into the clinical market, potentially improving the lives of patients suffering from a wide range of conditions.

Appendix

Appendix A: ImageJ Macro

```
/*
 * Macro template to process multiple images in a folder
 */

#@ File (label = "Input directory", style = "directory") input
#@ File (label = "Output directory", style = "directory") output
#@ String (label = "File suffix", value = ".czi") suffix

// See also Process_Folder.py for a version of this code
// in the Python scripting language.

//Process files using below functions
processFolder(input);

// function to scan folders/subfolders/files to find files with correct suffix
function processFolder(input) {
    list = getFileList(input);
    list = Array.sort(list);
    for (i = 0; i < list.length; i++) {
        if(File.isDirectory(input + File.separator + list[i]))
            processFolder(input + File.separator + list[i]);
        if(endsWith(list[i], suffix))
            processFile(input, output, list[i]);
    }
}

function processFile(input, output, file){
setBatchMode(true); //prevents image windows from opening up when the script is running
run("Bio-Formats", "open=[" + input + "/" + file +"] autoscale");
name = getTitle();
run("Split Channels");
Ch1 = "C1-"+name;
Ch2 = "C2-"+name;
Ch3 = "C3-"+name;
selectWindow(Ch1);
run("Enhance Contrast", "saturation=0.35");
setAutoThreshold("Moments dark no-reset"); //run("Threshold…");
setOption("BlackBackground", true);
run("Convert to Mask");
run("Watershed");
run("Analyze Particles...", "size=20-800 circularity=0.20-1.00 summarize overlay");
selectWindow(Ch2);
run("Enhance Contrast", "saturation=0.35");
setAutoThreshold("Intermodes dark no-reset"); //run("Threshold…");
setOption("BlackBackground", true);
run("Convert to Mask");
run("Watershed");
run("Analyze Particles...", "size=20-800 circularity=0.20-1.00 summarize overlay");
close("*");
}
```

Appendix B: Mouse brain AFM measurement region

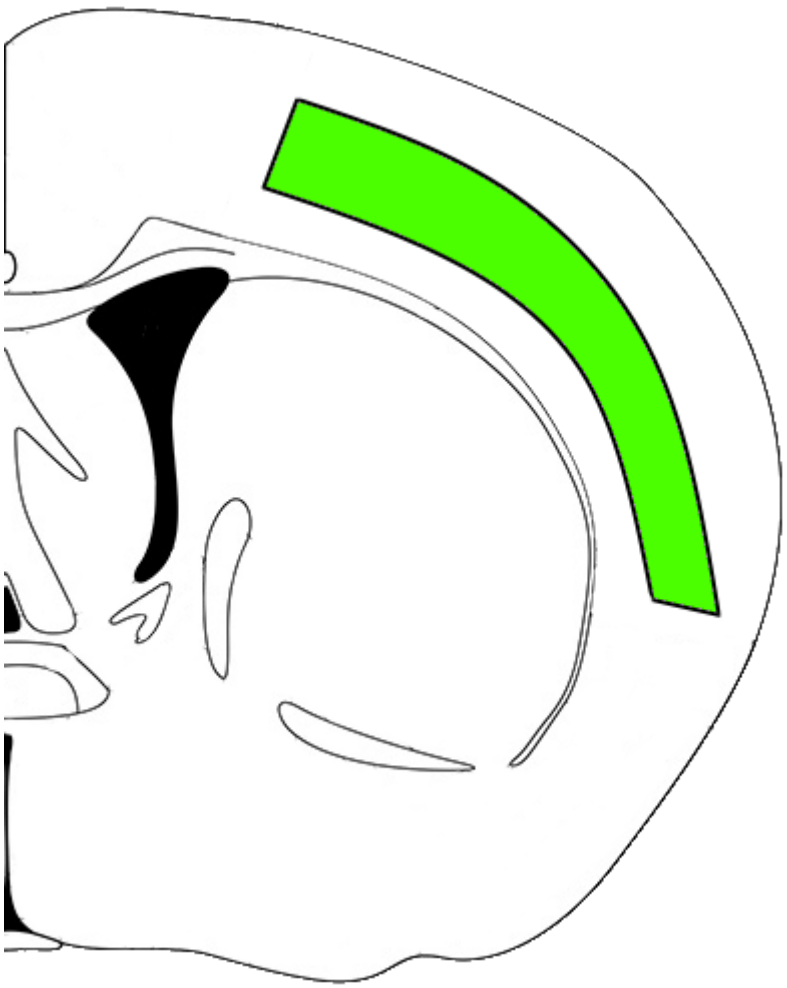

Bibliography

1. Coffey, R. J. Deep Brain Stimulation Devices: A Brief Technical History and Review. *Artif. Organs* **33**, 208–220 (2009).
2. Benabid, A. L., Pollak, P., Hoffmann, D., Gervason, C., Hommel, M., Perret, J. E., de Rougemont, J. & Gao, D. M. Long-term suppression of tremor by chronic stimulation of the ventral intermediate thalamic nucleus. *The Lancet* **337**, 403–406 (1991).
3. Mayberg, H. S., Lozano, A. M., Voon, V., McNeely, H. E., Seminowicz, D., Hamani, C., Schwalb, J. M. & Kennedy, S. H. Deep Brain Stimulation for Treatment-Resistant Depression. *Neuron* **45**, 651–660 (2005).
4. Larson, P. S. Deep Brain Stimulation for Movement Disorders. *Neurotherapeutics* **11**, 465–474 (2014).
5. Frizon, L. A., Yamamoto, E. A., Nagel, S. J., Simonson, M. T., Hogue, O. & Machado, A. G. Deep Brain Stimulation for Pain in the Modern Era: A Systematic Review. *Neurosurgery* **86**, 191–202 (2020).
6. Casagrande, S. C. B., Cury, R. G., Alho, E. J. L. & Fonoff, E. T. Deep brain stimulation in Tourette's syndrome: evidence to date. *Neuropsychiatr. Dis. Treat.* **15**, 1061–1075 (2019).
7. Vyas, D. B., Ho, A. L., Dadey, D. Y., Pendharkar, A. V., Sussman, E. S., Cowan, R. & Halpern, C. H. Deep Brain Stimulation for Chronic Cluster Headache: A Review. *Neuromodulation J. Int. Neuromodulation Soc.* **22**, 388–397 (2019).
8. Magown, P. & Burchiel, K. J. Complications of Deep Brain Stimulation (DBS). in *Complications in Neurosurgery* 189–195 (Elsevier, 2019). doi:10.1016/B978-0-323-50961-9.00033-5.

9. Beric, A., Kelly, P. J., Rezai, A., Sterio, D., Mogilner, A., Zonenshayn, M. & Kopell, B. Complications of deep brain stimulation surgery. *Stereotact. Funct. Neurosurg.* **77**, 73–78 (2001).
10. Falowski, S., Ooi, Y. C., Smith, A., Verhargen Metman, L. & Bakay, R. A. E. An Evaluation of Hardware and Surgical Complications with Deep Brain Stimulation Based on Diagnosis and Lead Location. *Stereotact. Funct. Neurosurg.* **90**, 173–180 (2012).
11. Boyden, E. S., Zhang, F., Bamberg, E., Nagel, G. & Deisseroth, K. Millisecond-timescale, genetically targeted optical control of neural activity. *Nat. Neurosci.* **8**, 1263–1268 (2005).
12. Han, X. Optogenetics in the nonhuman primate. *Prog. Brain Res.* **196**, 215–233 (2012).
13. Favre-Bulle, I. A. Light Scattering in Brain Tissue Using Monte Carlo Method. in *Imaging, Manipulation and Optogenetics in Zebrafish* (ed. Favre-Bulle, I. A.) 9–20 (Springer International Publishing, 2018). doi:10.1007/978-3-319-96250-4_2.
14. Favre-Bulle, I. A., Preece, D., Nieminen, T. A., Heap, L. A., Scott, E. K. & Rubinsztein-Dunlop, H. Scattering of Sculpted Light in Intact Brain Tissue, with implications for Optogenetics. *Sci. Rep.* **5**, 11501 (2015).
15. Yona, G., Meitav, N., Kahn, I. & Shoham, S. Realistic Numerical and Analytical Modeling of Light Scattering in Brain Tissue for Optogenetic Applications. *eNeuro* **3**, ENEURO.0059-15.2015 (2016).
16. Fenno, L., Yizhar, O. & Deisseroth, K. The Development and Application of Optogenetics. *Annu. Rev. Neurosci.* **34**, 389–412 (2011).
17. Cogan, S. F., Ludwig, K. A., Welle, C. G. & Takmakov, P. Tissue damage thresholds during therapeutic electrical stimulation. *J. Neural Eng.* **13**, 021001 (2016).

18. Mohammed Ali, H. A., Abdullah, S. S. & Faraj, M. An In-vitro Study of Electrodes Impedance in Deep Brain Stimulation. *J. Phys. Conf. Ser.* **1829**, 012019 (2021).
19. Govorunova, E. G., Sineshchekov, O. A. & Spudich, J. L. Emerging Diversity of Channelrhodopsins and Their Structure-Function Relationships. *Front. Cell. Neurosci.* **15**, (2022).
20. Govorunova, E. G., Sineshchekov, O. A., Janz, R., Liu, X. & Spudich, J. L. Natural light-gated anion channels: A family of microbial rhodopsins for advanced optogenetics. *Science* **349**, 647–650 (2015).
21. Stahlberg, M. A., Ramakrishnan, C., Willig, K. I., Boyden, E. S., Deisseroth, K. & Dean, C. Investigating the feasibility of channelrhodopsin variants for nanoscale optogenetics. *Neurophotonics* **6**, 015007 (2019).
22. Ross, S., Faraday, M. & Hartley, H. B. Faraday consults the scholars: the origins of the terms of electrochemistry. *Notes Rec. R. Soc. Lond.* **16**, 187–220 (1997).
23. Hoad, T. F. & Oxford University Press. *The concise Oxford dictionary of English etymology [electronic resource]*. ([Oxford] : Oxford University Press, 2002).
24. Nagatsu, T., Nakashima, A., Watanabe, H., Ito, S. & Wakamatsu, K. Neuromelanin in Parkinson's Disease: Tyrosine Hydroxylase and Tyrosinase. *Int. J. Mol. Sci.* **23**, 4176 (2022).
25. D'Amato, R. J., Alexander, G. M., Schwartzman, R. J., Kitt, C. A., Price, D. L. & Snyder, S. H. Evidence for neuromelanin involvement in MPTP-induced neurotoxicity. *Nature* **327**, 324–326 (1987).
26. Pu, Y., Chen, J., Wang, W. & Alfano, R. R. 11 - Basic Optical Scattering Parameter of the Brain and Prostate Tissues in the Spectral Range of 400–2400nm. in *Neurophotonics and Biomedical Spectroscopy* (eds. Alfano, R. R. & Shi, L.) 229–252 (Elsevier, 2019). doi:10.1016/B978-0-323-48067-3.00011-1.

27. Ariel, P. A beginner's guide to tissue clearing. *Int. J. Biochem. Cell Biol.* **84**, 35–39 (2017).
28. Richardson, D. S. & Lichtman, J. W. Clarifying Tissue Clearing. *Cell* **162**, 246–257 (2015).
29. Feng, Z. *et al.* Perfecting and extending the near-infrared imaging window. *Light Sci. Appl.* **10**, 197 (2021).
30. Ruiz, O., Lustig, B. R., Nassi, J. J., Cetin, A., Reynolds, J. H., Albright, T. D., Callaway, E. M., Stoner, G. R. & Roe, A. W. Optogenetics through windows on the brain in the nonhuman primate. *J. Neurophysiol.* **110**, 1455–1467 (2013).
31. Cramer, S. W., Carter, R. E., Aronson, J. D., Kodandaramaiah, S. B., Ebner, T. J. & Chen, C. C. Through the looking glass: A review of cranial window technology for optical access to the brain. *J. Neurosci. Methods* **354**, 109100 (2021).
32. Sahel, J.-A. *et al.* Partial recovery of visual function in a blind patient after optogenetic therapy. *Nat. Med.* **27**, 1223–1229 (2021).
33. McClements, M. E., Staurenghi, F., MacLaren, R. E. & Cehajic-Kapetanovic, J. Optogenetic Gene Therapy for the Degenerate Retina: Recent Advances. *Front. Neurosci.* **14**, 570909 (2020).
34. Stefanov, A. & Flannery, J. G. A Systematic Review of Optogenetic Vision Restoration: History, Challenges, and New Inventions from Bench to Bedside. *Cold Spring Harb. Perspect. Med.* a041304 (2022) doi:10.1101/cshperspect.a041304.
35. Chernov, M. M., Friedman, R. M., Chen, G., Stoner, G. R. & Roe, A. W. Functionally specific optogenetic modulation in primate visual cortex. *Proc. Natl. Acad. Sci.* **115**, 10505–10510 (2018).

36. Yazdan-Shahmorad, A., Diaz-Botia, C., Hanson, T. L., Kharazia, V., Ledochowitsch, P., Maharbiz, M. M. & Sabes, P. N. A Large-Scale Interface for Optogenetic Stimulation and Recording in Nonhuman Primates. *Neuron* **89**, 927–939 (2016).
37. Soltan, A. *et al.* A Head Mounted Device Stimulator for Optogenetic Retinal Prosthesis. *J. Neural Eng.* (2018) doi:10.1088/1741-2552/aadd55.
38. McAlinden, N. *et al.* Multisite microLED optrode array for neural interfacing. *Neurophotonics* **6**, 035010 (2019).
39. Rajalingham, R., Sorenson, M., Azadi, R., Bohn, S., DiCarlo, J. J. & Afraz, A. Chronically implantable LED arrays for behavioral optogenetics in primates. 2020.09.10.291583 Preprint at https://doi.org/10.1101/2020.09.10.291583 (2020).
40. Komatsu, M., Sugano, E., Tomita, H. & Fujii, N. A Chronically Implantable Bidirectional Neural Interface for Non-human Primates. *Front. Neurosci.* **11**, (2017).
41. Steude, A., Witts, E. C., Miles, G. B. & Gather, M. C. Arrays of microscopic organic LEDs for high-resolution optogenetics. *Sci. Adv.* **2**, e1600061 (2016).
42. Grossman, N. *et al.* Multi-site optical excitation using ChR2 and micro-LED array. *J. Neural Eng.* **7**, 016004 (2010).
43. Azadi, R., Bohn, S., Eldridge, M. A. G. & Afraz, A. *Surgical procedure for implantation of Opto-Array in nonhuman primates*. http://biorxiv.org/lookup/doi/10.1101/2022.10.04.510884 (2022) doi:10.1101/2022.10.04.510884.
44. Zhou, Y. *et al.* A silk-based self-adaptive flexible opto-electro neural probe. *Microsyst. Nanoeng.* **8**, 1–12 (2022).

45. Ozden, I. *et al.* A coaxial optrode as multifunction write-read probe for optogenetic studies in non-human primates. *J. Neurosci. Methods* **219**, 142–154 (2013).
46. Acker, L., Pino, E. N., Boyden, E. S. & Desimone, R. FEF inactivation with improved optogenetic methods. *Proc. Natl. Acad. Sci.* **113**, E7297–E7306 (2016).
47. Modified toolbox for optogenetics in the nonhuman primate. https://www.spiedigitallibrary.org/journals/neurophotonics/volume-2/issue-3/031202/Modified-toolbox-for-optogenetics-in-the-nonhuman-primate/10.1117/1.NPh.2.3.031202.full.
48. Sileo, L. *et al.* Tapered Fibers Combined With a Multi-Electrode Array for Optogenetics in Mouse Medial Prefrontal Cortex. *Front. Neurosci.* **12**, (2018).
49. Chuong, A. S. *et al.* Noninvasive optical inhibition with a red-shifted microbial rhodopsin. *Nat. Neurosci.* **17**, 1123–1129 (2014).
50. Yizhar, O. *et al.* Neocortical excitation/inhibition balance in information processing and social dysfunction. *Nature* **477**, 171–178 (2011).
51. Pisanello, F., Sileo, L., Oldenburg, I. A., Pisanello, M., Martiradonna, L., Assad, J. A., Sabatini, B. L. & De Vittorio, M. Multipoint-Emitting Optical Fibers for Spatially Addressable In Vivo Optogenetics. *Neuron* **82**, 1245–1254 (2014).
52. Wang, J. & Dong, J. Optical Waveguides and Integrated Optical Devices for Medical Diagnosis, Health Monitoring and Light Therapies. *Sensors* **20**, 3981 (2020).
53. Shim, E., Chen, Y., Masmanidis, S. & Li, M. Multisite silicon neural probes with integrated silicon nitride waveguides and gratings for optogenetic applications. *Sci. Rep.* **6**, 22693 (2016).

54. Kwon, K. & Li, W. Integrated multi-LED array with three-dimensional polymer waveguide for optogenetics. in *2013 IEEE 26th International Conference on Micro Electro Mechanical Systems (MEMS)* 1017–1020 (2013). doi:10.1109/MEMSYS.2013.6474421.

55. Sekiguchi, H., Yasunaga, H., Tsuchiyama, K. & Nitta, R. Neural optical probe with monolithically integrated intensity-monitoring μLED and polymer waveguide for optogenetics. *Electron. Lett.* **55**, 619–621 (2019).

56. Yamagiwa, S., Ishida, M. & Kawano, T. *Flexible optrode array: Parylene-film waveguide arrays with microelectrodes for optogenetics*. *2015 Transducers - 2015 18th International Conference on Solid-State Sensors, Actuators and Microsystems (TRANSDUCERS)* doi:10.1109/TRANSDUCERS.2015.7180915.

57. Scharf, R. *et al.* A compact integrated device for spatially-selective optogenetic neural stimulation based on the Utah Optrode Array. in *Optogenetics and Optical Manipulation 2018* (eds. Mohanty, S. K., Thakor, N. V. & Jansen, E. D.) 15 (SPIE, 2018). doi:10.1117/12.2299296.

58. Luo, J. *et al.* The Neural Engine: A Reprogrammable Low Power Platform for Closed-loop Optogenetics. *IEEE Trans. Biomed. Eng.* (2020) doi:10.1109/TBME.2020.2973934.

59. Goncalves, S. B., Palha, J. M., Fernandes, H. C., Souto, M. R., Pimenta, S., Dong, T., Yang, Z., Ribeiro, J. F. & Correia, J. H. LED Optrode with Integrated Temperature Sensing for Optogenetics. *Micromachines* **9**, 473 (2018).

60. Yue, S., Yuan, M., Zhang, Y., Wang, X. & Wang, S. [Development of An Implantable Optrode for Optogenetic Stimulation]. *Sheng Wu Yi Xue Gong Cheng Xue Za Zhi J. Biomed. Eng. Shengwu Yixue Gongchengxue Zazhi* **33**, 337–342 (2016).

61. Rossi, M. A., Go, V., Murphy, T., Fu, Q., Morizio, J. & Yin, H. H. A wirelessly controlled implantable LED system for deep brain optogenetic stimulation. *Front. Integr. Neurosci.* **9**, (2015).

62. 李亚民王阳 & Yamin Li, Y. W. **植入式光**电极器件发展. **物理化学学**报 **36**, 1912054 (2020).

63. Yasunaga, H. *et al.* MicroLED neural probe for effective in vivo optogenetic stimulation. *Opt. Express* **30**, 40292–40305 (2022).

64. Pycroft, L., Stein, J. & Aziz, T. Deep brain stimulation: An overview of history, methods, and future developments. *Brain Neurosci. Adv.* **2**, 239821281881601 (2018).

65. Rolston, J. D., Englot, D. J., Starr, P. A. & Larson, P. S. An unexpectedly high rate of revisions and removals in deep brain stimulation surgery: Analysis of multiple databases. *Parkinsonism Relat. Disord.* **33**, 72–77 (2016).

66. Kluger, B. M., Foote, K. D., Jacobson, C. E. & Okun, M. S. Lessons learned from a large single center cohort of patients referred for DBS management. *Parkinsonism Relat. Disord.* **17**, 236–239 (2011).

67. Okun, M. S., Tagliati, M., Pourfar, M., Fernandez, H. H., Rodriguez, R. L., Alterman, R. L. & Foote, K. D. Management of referred deep brain stimulation failures: a retrospective analysis from 2 movement disorders centers. *Arch. Neurol.* **62**, 1250–1255 (2005).

68. Pawela, C., DeYoe, E. & Pashaie, R. Intracranial Injection of an Optogenetics Viral Vector Followed by Optical Cannula Implantation for Neural Stimulation in Rat Brain Cortex. in *Optogenetics* (ed. Kianianmomeni, A.) vol. 1408 227–241 (Springer New York, 2016).

69. Mohr, J. P. *Stroke: pathophysiology, diagnosis, and management*. (Churchill Livingstone, 2004).

70. Vedam-Mai, V., Rodgers, C., Gureck, A., Vincent, M., Ippolito, G., Elkouzi, A., Yachnis, A. T., Foote, K. D. & Okun, M. S. Deep Brain Stimulation associated gliosis: A post-mortem study. *Parkinsonism Relat. Disord.* **54**, 51–55 (2018).
71. Polikov, V. S., Tresco, P. A. & Reichert, W. M. Response of brain tissue to chronically implanted neural electrodes. *J. Neurosci. Methods* **148**, 1–18 (2005).
72. Stichel, C. C. & Müller, H. W. The CNS lesion scar: new vistas on an old regeneration barrier. *Cell Tissue Res.* **294**, 1–9 (1998).
73. Chew, D. J., Fawcett, J. W. & Andrews, M. R. The challenges of long-distance axon regeneration in the injured CNS. *Prog. Brain Res.* **201**, 253–294 (2012).
74. Silver, J. & Miller, J. H. Regeneration beyond the glial scar. *Nat. Rev. Neurosci.* **5**, 146–156 (2004).
75. Davies, S. J. A., Fitch, M. T., Memberg, S. P., Hall, A. K., Raisman, G. & Silver, J. Regeneration of adult axons in white matter tracts of the central nervous system. *Nature* **390**, 680–683 (1997).
76. Silver, J., Schwab, M. E. & Popovich, P. G. Central nervous system regenerative failure: role of oligodendrocytes, astrocytes, and microglia. *Cold Spring Harb. Perspect. Biol.* **7**, a020602 (2014).
77. WAYNE, C. E. A. & WAYNE, R. P. A. *Photochemistry*. (Oxford University Press, Incorporated, 1996).
78. Davies, M. J. Reactive species formed on proteins exposed to singlet oxygen. *Photochem. Photobiol. Sci.* **3**, 17–25 (2004).
79. Michaeli, A. & Feitelson, J. Reactivity of Singlet Oxygen Toward Amino Acids and Peptides. *Photochem. Photobiol.* **59**, 284–289 (1994).
80. Dougherty, T. J., Gomer, C. J., Henderson, B. W., Jori, G., Kessel, D., Korbelik, M., Moan, J. & Peng, Q. Photodynamic Therapy. *J. Natl. Cancer Inst.* **90**, 889–905 (1998).

81. Kim, W. B., Shelley, A. J., Novice, K., Joo, J., Lim, H. W. & Glassman, S. J. Drug-induced phototoxicity: A systematic review. *J. Am. Acad. Dermatol.* **79**, 1069–1075 (2018).

82. Marek, V. *et al.* Blue light exposure in vitro causes toxicity to trigeminal neurons and glia through increased superoxide and hydrogen peroxide generation. *Free Radic. Biol. Med.* **131**, 27–39 (2019).

83. Mahalingam, S. M., Ordaz, J. D. & Low, P. S. Targeting of a Photosensitizer to the Mitochondrion Enhances the Potency of Photodynamic Therapy. *ACS Omega* **3**, 6066–6074 (2018).

84. Passarella, S. & Karu, T. Absorption of monochromatic and narrow band radiation in the visible and near IR by both mitochondrial and non-mitochondrial photoacceptors results in photobiomodulation. *J. Photochem. Photobiol. B* **140**, 344–358 (2014).

85. Santacruz-Perez, C., Tonolli, P. N., GustavoRavagnani, F., Baptista, M. S., Santacruz-Perez, C., Tonolli, P. N., GustavoRavagnani, F. & Baptista, M. S. *Photochemistry of Lipofuscin and the Interplay of UVA and Visible Light in Skin Photosensitivity*. *Photochemistry and Photophysics - Fundamentals to Applications* (IntechOpen, 2018). doi:10.5772/intechopen.76641.

86. Cooke, M. S., Evans, M. D., Dizdaroglu, M. & Lunec, J. Oxidative DNA damage: mechanisms, mutation, and disease. *FASEB J.* **17**, 1195–1214 (2003).

87. Elfawy, H. A. & Das, B. Crosstalk between mitochondrial dysfunction, oxidative stress, and age related neurodegenerative disease: Etiologies and therapeutic strategies. *Life Sci.* **218**, 165–184 (2019).

88. Guo, C., Sun, L., Chen, X. & Zhang, D. Oxidative stress, mitochondrial damage and neurodegenerative diseases. *Neural Regen. Res.* **8**, 2003–2014 (2013).

89. Gray, D. A. & Woulfe, J. Lipofuscin and Aging: A Matter of Toxic Waste. *Sci. Aging Knowl. Environ.* **2005**, re1–re1 (2005).
90. Atamna, H. Heme, iron, and the mitochondrial decay of ageing. *Ageing Res. Rev.* **3**, 303–318 (2004).
91. König, J., Ott, C., Hugo, M., Jung, T., Bulteau, A.-L., Grune, T. & Höhn, A. Mitochondrial contribution to lipofuscin formation. *Redox Biol.* **11**, 673–681 (2017).
92. Benaroya, H. Brain energetics, mitochondria, and traumatic brain injury. *Rev. Neurosci.* **31**, 363–390 (2020).
93. Misgeld, T. & Schwarz, T. L. Mitostasis in neurons: Maintaining mitochondria in an extended cellular architecture. *Neuron* **96**, 651–666 (2017).
94. Koester, H. J., Baur, D., Uhl, R. & Hell, S. W. Ca2+ fluorescence imaging with pico- and femtosecond two-photon excitation: signal and photodamage. *Biophys. J.* **77**, 2226–2236 (1999).
95. Blázquez-Castro, A. Optical Tweezers: Phototoxicity and Thermal Stress in Cells and Biomolecules. *Micromachines* **10**, (2019).
96. Glickman, R. D. Phototoxicity to the Retina: Mechanisms of Damage. *Int. J. Toxicol.* **21**, 473–490 (2002).
97. Peng, Q., Juzeniene, A., Chen, J., Svaasand, L., Warloe, T., Giercksky, K.-E. & Moan, J. Lasers in medicine. *Rep. Prog. Phys.* **71**, 056701 (2008).
98. Kiyatkin, E. A. Brain temperature: from physiology and pharmacology to neuropathology. in *Handbook of Clinical Neurology* vol. 157 483–504 (Elsevier, 2018).
99. Kiyatkin, E. A. Physiological and pathological brain hyperthermia. in *Progress in Brain Research* vol. 162 219–243 (Elsevier, 2007).

100. Senova, S., Scisniak, I., Chiang, C.-C., Doignon, I., Palfi, S., Chaillet, A., Martin, C. & Pain, F. Experimental assessment of the safety and potential efficacy of high irradiance photostimulation of brain tissues. *Sci. Rep.* **7**, 43997 (2017).
101. Deng, W., Goldys, E. M., Farnham, M. M. & Pilowsky, P. M. Optogenetics, the intersection between physics and neuroscience: light stimulation of neurons in physiological conditions. *Am. J. Physiol.-Regul. Integr. Comp. Physiol.* **307**, R1292–R1302 (2014).
102. *Directive 2006/25/EC of the European Parliament and of the Council of 5 April 2006 on the minimum health and safety requirements regarding the exposure of workers to risks arising from physical agents (artificial optical radiation) (19th individual Directive within the meaning of Article 16(1) of Directive 89/391/EEC)*. (2019).
103. Solano, F. Photoprotection and Skin Pigmentation: Melanin-Related Molecules and Some Other New Agents Obtained from Natural Sources. *Mol. Basel Switz.* **25**, 1537 (2020).
104. Kobat, S. G. & Turgut, B. Importance of Müller Cells. *Beyoglu Eye J.* **5**, 59–63 (2020).
105. Pandel, R., Poljšak, B., Godic, A. & Dahmane, R. Skin Photoaging and the Role of Antioxidants in Its Prevention. *ISRN Dermatol.* **2013**, 930164 (2013).
106. Tokarz, P., Kaarniranta, K. & Blasiak, J. Role of antioxidant enzymes and small molecular weight antioxidants in the pathogenesis of age-related macular degeneration (AMD). *Biogerontology* **14**, 461–482 (2013).
107. Youssef, P. N., Sheibani, N. & Albert, D. M. Retinal light toxicity. *Eye* **25**, 1–14 (2011).
108. Gardner, J. A history of deep brain stimulation: Technological innovation and the role of clinical assessment tools. *Soc. Stud. Sci.* **43**, 707–728 (2013).

109. Rajabian, A. *et al.* Accuracy, precision, and safety of stereotactic, frame-based, intraoperative MRI-guided and MRI-verified deep brain stimulation in 650 consecutive procedures. *J. Neurosurg.* 1–10 (2022) doi:10.3171/2022.8.JNS22968.
110. Park, C. K., Jung, N. Y., Kim, M. & Chang, J. W. Analysis of Delayed Intracerebral Hemorrhage Associated with Deep Brain Stimulation Surgery. *World Neurosurg.* **104**, 537–544 (2017).
111. Park, J. H., Chung, S. J., Lee, C. S. & Jeon, S. R. Analysis of hemorrhagic risk factors during deep brain stimulation surgery for movement disorders: comparison of the circumferential paired and multiple electrode insertion methods. *Acta Neurochir. (Wien)* **153**, 1573–1578 (2011).
112. Blomstedt, P. & Hariz, M. I. Are Complications Less Common in Deep Brain Stimulation than in Ablative Procedures for Movement Disorders? *Stereotact. Funct. Neurosurg.* **84**, 72–81 (2006).
113. Morishita, T., Okun, M. S., Burdick, A., Jacobson IV, C. E. & Foote, K. D. Cerebral Venous Infarction: A Potentially Avoidable Complication of Deep Brain Stimulation Surgery. *Neuromodulation Technol. Neural Interface* **16**, 407–413 (2013).
114. Bezchlibnyk, Y. B. *et al.* Clinical outcomes of globus pallidus deep brain stimulation for Parkinson disease: a comparison of intraoperative MRI– and MER-guided lead placement. *J. Neurosurg.* **134**, 1072–1082 (2020).
115. Seijo, F. J., Alvarez-Vega, M. A., Gutierrez, J. C., Fdez-Glez, F. & Lozano, B. Complications in subthalamic nucleus stimulation surgery for treatment of Parkinson's disease. Review of 272 procedures. *Acta Neurochir. (Wien)* **149**, 867–876 (2007).

116. Umemura, A., Jaggi, J. L., Hurtig, H. I., Siderowf, A. D., Colcher, A., Stern, M. B. & Baltuch, G. H. Deep brain stimulation for movement disorders: morbidity and mortality in 109 patients. *J. Neurosurg.* **98**, 779–784 (2003).
117. Tasker, R. R. Deep brain stimulation is preferable to thalamotomy for tremor suppression. *Surg. Neurol.* **49**, 145–153 (1998).
118. Voges, J. Deep-brain stimulation: long-term analysis of complications caused by hardware and surgery--experiences from a single centre. *J. Neurol. Neurosurg. Psychiatry* **77**, 868–872 (2006).
119. Sorar, M., Hanalioglu, S., Kocer, B., Eser, M. T., Comoglu, S. S. & Kertmen, H. Experience Reduces Surgical and Hardware-Related Complications of Deep Brain Stimulation Surgery: A Single-Center Study of 181 Patients Operated in Six Years. *Park. Dis.* **2018**, 1–7 (2018).
120. Terao, T., Takahashi, H., Yokochi, F., Taniguchi, M., Okiyama, R. & Hamada, I. Hemorrhagic complication of stereotactic surgery in patients with movement disorders. *J. Neurosurg.* **98**, 1241–1246 (2003).
121. Binder, D. K., Rau, G. & Starr, P. A. Hemorrhagic complications of microelectrode-guided deep brain stimulation. *Stereotact. Funct. Neurosurg.* **80**, 28–31 (2003).
122. Gorgulho, A., De Salles, A. A. F., Frighetto, L. & Behnke, E. Incidence of hemorrhage associated with electrophysiological studies performed using macroelectrodes and microelectrodes in functional neurosurgery. *J. Neurosurg.* **102**, 888–896 (2005).
123. Sansur, C. A., Frysinger, R. C., Pouratian, N., Fu, K.-M., Bittl, M., Oskouian, R. J., Laws, E. R. & Elias, W. J. Incidence of symptomatic hemorrhage after stereotactic electrode placement. *J. Neurosurg.* **107**, 998–1003 (2007).

124. Schuurman, P. R., Bosch, D. A., Merkus, M. P. & Speelman, J. D. Long-term follow-up of thalamic stimulation versus thalamotomy for tremor suppression. *Mov. Disord.* **23**, 1146–1153 (2008).

125. Zrinzo, L., Foltynie, T., Limousin, P. & Hariz, M. I. Reducing hemorrhagic complications in functional neurosurgery: a large case series and systematic literature review: Clinical article. *J. Neurosurg.* **116**, 84–94 (2012).

126. Ben-Haim, S., Asaad, W. F., Gale, J. T. & Eskandar, E. N. RISK FACTORS FOR HEMORRHAGE DURING MICROELECTRODE-GUIDED DEEP BRAIN STIMULATION AND THE INTRODUCTION OF AN IMPROVED MICROELECTRODE DESIGN. *Neurosurgery* **64**, 754–763 (2009).

127. Binder, D. K., Rau, G. M. & Starr, P. A. Risk factors for hemorrhage during microelectrode-guided deep brain stimulator implantation for movement disorders. *Neurosurgery* **56**, 722–732; discussion 722-732 (2005).

128. Fenoy, A. J. & Simpson, R. K. Risks of common complications in deep brain stimulation surgery: management and avoidance. *J. Neurosurg.* **120**, 132–139 (2014).

129. Xiaowu, H., Xiufeng, J., Xiaoping, Z., Bin, H., Laixing, W., Yiqun, C., Jinchuan, L., Aiguo, J. & Jianmin, L. Risks of intracranial hemorrhage in patients with Parkinson's disease receiving deep brain stimulation and ablation. *Parkinsonism Relat. Disord.* **16**, 96–100 (2010).

130. Kenney, C., Simpson, R., Hunter, C., Ondo, W., Almaguer, M., Davidson, A. & Jankovic, J. Short-term and long-term safety of deep brain stimulation in the treatment of movement disorders. *J. Neurosurg.* **106**, 621–625 (2007).

131. Broggi, G., Dones, I., Ferroli, P., Franzini, A., Genitrini, S. & Micon, B. M. Surgery for Movement Disorders: Complications and Complication Avoidance. *Semin. Neurosurg.* **12**, 225–232 (2001).

132. Chou, Y.-C. *et al.* Surgical and hardware complications in subthalamic nucleus deep brain stimulation. *J. Clin. Neurosci.* **14**, 643–649 (2007).
133. Lyons, K. E., Wilkinson, S. B., Overman, J. & Pahwa, R. Surgical and hardware complications of subthalamic stimulation: A series of 160 procedures. *Neurology* **63**, 612–616 (2004).
134. Voges, J. *et al.* Thirty days complication rate following surgery performed for deep-brain-stimulation. *Mov. Disord.* **22**, 1486–1489 (2007).
135. Kimmelman, J., Duckworth, K., Ramsay, T., Voss, T., Ravina, B. & Emborg, M. E. Risk of surgical delivery to deep nuclei: a meta-analysis. *Mov. Disord. Off. J. Mov. Disord. Soc.* **26**, 1415–1421 (2011).
136. Liu, J. K. C., Soliman, H., Machado, A., Deogaonkar, M. & Rezai, A. R. Intracranial hemorrhage after removal of deep brain stimulation electrodes: Clinical article. *J. Neurosurg.* **116**, 525–528 (2012).
137. Hariz, M. I., Rehncrona, S., Quinn, N. P., Speelman, J. D. & Wensing, C. Multicenter study on deep brain stimulation in Parkinson's disease: An independent assessment of reported adverse events at 4 years. *Mov. Disord.* **23**, 416–421 (2008).
138. Deogaonkar, M., Nazzaro, J. M., Machado, A. & Rezai, A. Transient, symptomatic, post-operative, non-infectious hypodensity around the deep brain stimulation (DBS) electrode. *J. Clin. Neurosci. Off. J. Neurosurg. Soc. Australas.* **18**, 910–915 (2011).
139. Lu, Y., Qiu, C., Chang, L., Luo, B., Dong, W., Zhang, W. & Sun, H.-H. Development of Unilateral Peri-Lead Edema Into Large Cystic Cavitation After Deep Brain Stimulation: A Case Report. *Front. Neurol.* **13**, (2022).
140. Sharma, V. D. *et al.* Cystic Lesions as a Rare Complication of Deep Brain Stimulation. *Mov. Disord. Clin. Pract.* **3**, 87–90 (2015).

141. Schoen, N. B., Jermakowicz, W. J., Luca, C. C. & Jagid, J. R. Acute symptomatic peri-lead edema 33 hours after deep brain stimulation surgery: a case report. *J. Med. Case Reports* **11**, 103 (2017).
142. Gupta, H. V., Lyons, M. K. & Mehta, S. H. Teaching Neuro *Images* : Noninfectious cyst as an unusual complication of deep brain stimulation. *Neurology* **87**, e223–e224 (2016).
143. Staudt, M. D. & MacDougall, K. W. Spontaneous Regression of an Intraparenchymal Cyst Following Deep Brain Stimulator Electrode Implantation: Case Report and Literature Review. *World Neurosurg.* **117**, 249–254 (2018).
144. Deep brain stimulation peri-lead edema: Common or uncommon complication? *MDS Abstracts* https://www.mdsabstracts.org/abstract/deep-brain-stimulation-peri-lead-edema-common-or-uncommon-complication/.
145. Tian, Y., Wang, J., Jiang, L., Feng, Z., Shi, X. & Hao, Y. The need to be alert to complications of peri-lead cerebral edema caused by deep brain stimulation implantation: A systematic literature review and meta-analysis study. *CNS Neurosci. Ther.* **28**, 332–342 (2022).
146. Chen, I.-W., Ronzitti, E., Lee, B. R., Daigle, T. L., Dalkara, D., Zeng, H., Emiliani, V. & Papagiakoumou, E. In Vivo Submillisecond Two-Photon Optogenetics with Temporally Focused Patterned Light. *J. Neurosci.* **39**, 3484–3497 (2019).
147. Thunemann, M. *et al.* Deep 2-photon imaging and artifact-free optogenetics through transparent graphene microelectrode arrays. *Nat. Commun.* **9**, 2035 (2018).
148. Adesnik, H. & Abdeladim, L. Probing neural codes with two-photon holographic optogenetics. *Nat. Neurosci.* **24**, 1356–1366 (2021).
149. Chen, S. *et al.* Near-infrared deep brain stimulation via upconversion nanoparticle–mediated optogenetics. *Science* **359**, 679–684 (2018).

150. Liu, X. *et al.* Near-infrared manipulation of multiple neuronal populations via trichromatic upconversion. *Nat. Commun.* **12**, 5662 (2021).
151. Noell, W. K., Walker, V. S., Kang, B. S. & Berman, S. Retinal damage by light in rats. **5**, (1966).
152. Miralles de Imperial-Ollero, J. A., Gallego-Ortega, A., Ortín-Martínez, A., Villegas-Pérez, M. P., Valiente-Soriano, F. J. & Vidal-Sanz, M. Animal Models of LED-Induced Phototoxicity. Short- and Long-Term In Vivo and Ex Vivo Retinal Alterations. *Life* **11**, 1137 (2021).
153. Godley, B. F., Shamsi, F. A., Liang, F.-Q., Jarrett, S. G., Davies, S. & Boulton, M. Blue Light Induces Mitochondrial DNA Damage and Free Radical Production in Epithelial Cells *. *J. Biol. Chem.* **280**, 21061–21066 (2005).
154. Rózanowska, M., Jarvis-Evans, J., Korytowski, W., Boulton, M. E., Burke, J. M. & Sarna, T. Blue Light-induced Reactivity of Retinal Age Pigment: IN VITRO GENERATION OF OXYGEN-REACTIVE SPECIES (∗). *J. Biol. Chem.* **270**, 18825–18830 (1995).
155. Marek, V., Mélik-Parsadaniantz, S., Villette, T., Montoya, F., Baudouin, C., Brignole-Baudouin, F. & Denoyer, A. Blue light phototoxicity toward human corneal and conjunctival epithelial cells in basal and hyperosmolar conditions. *Free Radic. Biol. Med.* **126**, 27–40 (2018).
156. Arnault, E. *et al.* Phototoxic Action Spectrum on a Retinal Pigment Epithelium Model of Age-Related Macular Degeneration Exposed to Sunlight Normalized Conditions. *PLOS ONE* **8**, e71398 (2013).
157. Wenzel, A., Grimm, C., Samardzija, M. & Remé, C. E. Molecular mechanisms of light-induced photoreceptor apoptosis and neuroprotection for retinal degeneration. *Prog. Retin. Eye Res.* **24**, 275–306 (2005).

158. Stockley, J. H., Evans, K., Matthey, M., Volbracht, K., Agathou, S., Mukanowa, J., Burrone, J. & Káradóttir, R. T. Surpassing light-induced cell damage in vitro with novel cell culture media. *Sci. Rep.* **7**, 849 (2017).

159. Cheng, K. P., Kiernan, E. A., Eliceiri, K. W., Williams, J. C. & Watters, J. J. Blue Light Modulates Murine Microglial Gene Expression in the Absence of Optogenetic Protein Expression. *Sci. Rep.* **6**, 21172 (2016).

160. Jou, M.-J., Jou, S.-B., Chen, H.-M., Lin, C.-H. & Peng, T.-I. Critical role of mitochondrial reactive oxygen species formation in visible laser irradiation-induced apoptosis in rat brain astrocytes (RBA-1). *J. Biomed. Sci.* **9**, 507–516 (2002).

161. Jou, M.-J., Jou, S.-B., Guo, M.-J., Wu, H.-Y. & Peng, T.-I. Mitochondrial reactive oxygen species generation and calcium increase induced by visible light in astrocytes. *Ann. N. Y. Acad. Sci.* **1011**, 45–56 (2004).

162. Khoshakhlagh, P., Bowser, D. A., Brown, J. Q. & Moore, M. J. Comparison of visible and UVA phototoxicity in neural culture systems micropatterned with digital projection photolithography. *J. Biomed. Mater. Res. A* **107**, 134–144 (2019).

163. Roberts, J. E. Ocular phototoxicity. *J. Photochem. Photobiol. B* **64**, 136–143 (2001).

164. Jaadane, I. *et al.* Retinal phototoxicity and the evaluation of the blue light hazard of a new solid-state lighting technology. *Sci. Rep.* **10**, 6733 (2020).

165. Wolffe, M. How safe is the light during ophthalmic diagnosis and surgery. *Eye* **30**, 186–188 (2016).

166. Biesen, P. R. van den, Berenschot, T., Verdaasdonk, R. M., Weelden, H. van & Norren, D. van. Endoillumination during vitrectomy and phototoxicity thresholds. *Br. J. Ophthalmol.* **84**, 1372–1375 (2000).

167. Zhang, J., Wang, X., Vikash, V., Ye, Q., Wu, D., Liu, Y. & Dong, W. ROS and ROS-Mediated Cellular Signaling. *Oxid. Med. Cell. Longev.* **2016**, e4350965 (2016).

168. Forrester, S. J., Kikuchi, D. S., Hernandes, M. S., Xu, Q. & Griendling, K. K. Reactive Oxygen Species in Metabolic and Inflammatory Signaling. *Circ. Res.* **122**, 877–902 (2018).

169. Duke, C. G., Savell, K. E., Tuscher, J. J., Phillips, R. A. & Day, J. J. Blue Light-Induced Gene Expression Alterations in Cultured Neurons Are the Result of Phototoxic Interactions with Neuronal Culture Media. *eneuro* **7**, ENEURO.0386-19.2019 (2020).

170. Wojtovich, A. P. & Foster, T. H. Optogenetic control of ROS production. *Redox Biol.* **2**, 368–376 (2014).

171. Ouyang, X., Yang, J., Hong, Z., Wu, Y., Xie, Y. & Wang, G. Mechanisms of blue light-induced eye hazard and protective measures: a review. *Biomed. Pharmacother. Biomedecine Pharmacother.* **130**, 110577 (2020).

172. Miyamoto, Y., Umebayashi, Y. & Nishisaka, T. Comparison of phototoxicity mechanism between pulsed and continuous wave irradiation in photodynamic therapy. *J. Photochem. Photobiol. B* **53**, 53–59 (1999).

173. Hunter, J. J., Morgan, J. I. W., Merigan, W. H., Sliney, D. H., Sparrow, J. R. & Williams, D. R. The susceptibility of the retina to photochemical damage from visible light. *Prog. Retin. Eye Res.* **31**, 28–42 (2012).

174. Różanowska, M. B., Pawlak, A. & Różanowski, B. Products of Docosahexaenoate Oxidation as Contributors to Photosensitising Properties of Retinal Lipofuscin. *Int. J. Mol. Sci.* **22**, 3525 (2021).

175. Zabolocki, M. *et al.* BrainPhys neuronal medium optimized for imaging and optogenetics in vitro. *Nat. Commun.* **11**, 5550 (2020).

176. Grzelak, A., Rychlik, B. & Bartosz, G. Light-dependent generation of reactive oxygen species in cell culture media. *Free Radic. Biol. Med.* **30**, 1418–1425 (2001).

177. Frigault, M. M., Lacoste, J., Swift, J. L. & Brown, C. M. Live-cell microscopy - tips and tools. *J. Cell Sci.* **122**, 753–767 (2009).

178. Magidson, V. & Khodjakov, A. Circumventing photodamage in live-cell microscopy. *Methods Cell Biol.* **114**, 545–560 (2013).

179. Dixit, R. & Cyr, R. Cell damage and reactive oxygen species production induced by fluorescence microscopy: effect on mitosis and guidelines for non-invasive fluorescence microscopy. *Plant J.* **36**, 280–290 (2003).

180. Icha, J., Weber, M., Waters, J. C. & Norden, C. Phototoxicity in live fluorescence microscopy, and how to avoid it. *BioEssays News Rev. Mol. Cell. Dev. Biol.* **39**, (2017).

181. Peak, J. G. & Peak, Meyrick. J. INDUCTION OF SLOWLY DEVELOPING ALKALI-LABILE SITES IN HUMAN P3 CELL DNA BY UVA AND BLUE- AND GREEN-LIGHT PHOTONS: ACTION SPECTRUM. *Photochem. Photobiol.* **61**, 484–487 (1995).

182. Peraza, A. V., Guzmán, D. C., Brizuela, N. O., Herrera, M. O., Olguín, H. J., Silva, M. L., Tapia, B. J. & Mejía, G. B. Riboflavin and pyridoxine restore dopamine levels and reduce oxidative stress in brain of rats. *BMC Neurosci.* **19**, 71 (2018).

183. Cardoso, D. R., Libardi, S. H. & Skibsted, L. H. Riboflavin as a photosensitizer. Effects on human health and food quality. *Food Funct.* **3**, 487–502 (2012).

184. de La Rochette, A., Silva, E., Birlouez-Aragon, I., Mancini, M., Edwards, A. M. & Morlière, P. Riboflavin photodegradation and photosensitizing effects are highly

dependent on oxygen and ascorbate concentrations. *Photochem. Photobiol.* **72**, 815–820 (2000).

185. Coimbra, C. G. & Junqueira, V. B. C. High doses of riboflavin and the elimination of dietary red meat promote the recovery of some motor functions in Parkinson's disease patients. *Braz. J. Med. Biol. Res. Rev. Bras. Pesqui. Medicas E Biol.* **36**, 1409–1417 (2003).
186. Marashly, E. T. & Bohlega, S. A. Riboflavin Has Neuroprotective Potential: Focus on Parkinson's Disease and Migraine. *Front. Neurol.* **8**, 333 (2017).
187. Wu, T., Chiang, S. K. S., Chau, F. Y. & Tso, M. O. M. Light-induced photoreceptor degeneration may involve the NFκB/caspase-1 pathway in vivo. *Brain Res.* **967**, 19–26 (2003).
188. Organisciak, D. T., Darrow, R. A., Barsalou, L., Darrow, R. M. & Lininger, L. A. Light-induced Damage in the Retina: Differential Effects of Dimethylthiourea on Photoreceptor Survival, Apoptosis and DNA Oxidation. *Photochem. Photobiol.* **70**, 261–268 (1999).
189. Ni, J. D., Baik, L. S., Holmes, T. C. & Montell, C. A rhodopsin in the brain functions in circadian photoentrainment in Drosophila. *Nature* **545**, 340–344 (2017).
190. Morgan, J. I. W., Hunter, J. J., Masella, B., Wolfe, R., Gray, D. C., Merigan, W. H., Delori, F. C. & Williams, D. R. Light-Induced Retinal Changes Observed with High-Resolution Autofluorescence Imaging of the Retinal Pigment Epithelium. *Investig. Opthalmology Vis. Sci.* **49**, 3715 (2008).
191. Wang, Y., Lan, B., He, H., Hu, M., Cao, Y. & Wang, C. Laser stimulation can activate autophagy in HeLa cells. *Appl. Phys. Lett.* **105**, 173703 (2014).

192. Dasgupta, R., Ahlawat, S., Verma, R. S., Uppal, A. & Gupta, P. K. Hemoglobin degradation in human erythrocytes with long-duration near-infrared laser exposure in Raman optical tweezers. *J. Biomed. Opt.* **15**, 055009 (2010).
193. Różanowska, M. B. & Różanowski, B. Photodegradation of Lipofuscin in Suspension and in ARPE-19 Cells and the Similarity of Fluorescence of the Photodegradation Product with Oxidized Docosahexaenoate. *Int. J. Mol. Sci.* **23**, 922 (2022).
194. Meleth, A. D. & Nida, H. Use of Fundus Autofluorescence in the Diagnosis and Management of Uveitis. *Int. Ophthalmol. Clin.* **52**, 45–54 (2012).
195. Hunter, J. J., Morgan, J. I. W., Merigan, W. H. & Williams, D. R. Retinal phototoxicity observed using high-resolution autofluorescence imaging. *Int. Laser Saf. Conf.* **2009**, 61–65 (2009).
196. Grossman, N., Simiaki, V., Martinet, C., Toumazou, C., Schultz, S. & Nikolic, K. The spatial pattern of light determines the kinetics and modulates backpropagation of optogenetic action potentials. *J. Comput. Neurosci.* **34**, (2012).
197. Yizhar, O., Fenno, L. E., Davidson, T. J., Mogri, M. & Deisseroth, K. Optogenetics in Neural Systems. *Neuron* **71**, 9–34 (2011).
198. Acker, L. C., Pino, E. N., Boyden, E. S. & Desimone, R. Large Volume, Behaviorally-relevant Illumination for Optogenetics in Non-human Primates. *J. Vis. Exp. JoVE* 56330 (2017) doi:10.3791/56330.
199. Franklin, A. M., Marshall, N. J. & Lewis, S. M. Multimodal signals: ultraviolet reflectance and chemical cues in stomatopod agonistic encounters. *R. Soc. Open Sci.* **3**, 160329 (2016).
200. ICNIRP Guidelines on Limits of Exposure to Incoherent Visible and Infrared Radiation. *Health Phys.* **105**, 74–96 (2013).

201. Broser, M. *et al.* NeoR, a near-infrared absorbing rhodopsin. *Nat. Commun.* **11**, 5682 (2020).

202. Owen, S. F., Liu, M. H. & Kreitzer, A. C. Thermal constraints on in vivo optogenetic manipulations. *Nat. Neurosci.* **22**, 1061–1065 (2019).

203. Picot, A. *et al.* Temperature Rise under Two-Photon Optogenetic Brain Stimulation. *Cell Rep.* **24**, 1243-1253.e5 (2018).

204. Fankhauser, F., Giger, H., Niederer, P. & Seiler, T. Transpupillary laser phototherapy of tumors and vascular anomalies of retina and choroid: theoretical approach and clinical implications. *Technol. Health Care Off. J. Eur. Soc. Eng. Med.* **8**, 93–112 (2000).

205. Journée-de Korver, J. G. & Keunen, J. E. E. Thermotherapy in the management of choroidal melanoma. *Prog. Retin. Eye Res.* **21**, 303–317 (2002).

206. Stujenske, J. M., Spellman, T. & Gordon, J. A. Modeling the Spatiotemporal Dynamics of Light and Heat Propagation for In Vivo Optogenetics. *Cell Rep.* **12**, 525–534 (2015).

207. Arias-Gil, G., Ohl, F. W., Takagaki, K. & Lippert, M. T. Measurement, modeling, and prediction of temperature rise due to optogenetic brain stimulation. *Neurophotonics* **3**, 045007 (2016).

208. Christie, I. N., Wells, J. A., Southern, P., Marina, N., Kasparov, S., Gourine, A. V. & Lythgoe, M. F. fMRI response to blue light delivery in the naïve brain: Implications for combined optogenetic fMRI studies. *NeuroImage* **66**, 634–641 (2013).

209. Wells, J. D., Thomsen, S., Whitaker, P., Jansen, E. D., Kao, C. C., Konrad, P. E. & Mahadevan-Jansen, A. Optically mediated nerve stimulation: Identification of injury thresholds. *Lasers Surg. Med.* **39**, 513–526 (2007).

210. Chernov, M. M., Chen, G. & Roe, A. W. Histological Assessment of Thermal Damage in the Brain Following Infrared Neural Stimulation. *Brain Stimulat.* **7**, 476–482 (2014).

211. Cayce, J. M., Friedman, R. M., Chen, G., Jansen, E. D., Mahadevan-Jansen, A. & Roe, A. W. Infrared neural stimulation of primary visual cortex in non-human primates. *NeuroImage* **84**, 181–190 (2014).

212. Philips. All in 1 LED Lighting Solutions Guide. http://www.philipslumileds.com/uploads/221/PG01-pdf (2012).

213. Wang, J. H.-C., Thampatty, B. P., Lin, J.-S. & Im, H.-J. Mechanoregulation of gene expression in fibroblasts. *Gene* **391**, 1–15 (2007).

214. Steward, R. L., Cheng, C.-M., Ye, J. D., Bellin, R. M. & LeDuc, P. R. Mechanical stretch and shear flow induced reorganization and recruitment of fibronectin in fibroblasts. *Sci. Rep.* **1**, 147 (2011).

215. Jaalouk, D. E. & Lammerding, J. Mechanotransduction gone awry. *Nat. Rev. Mol. Cell Biol.* **10**, 63–73 (2009).

216. Martino, F., Perestrelo, A. R., Vinarský, V., Pagliari, S. & Forte, G. Cellular Mechanotransduction: From Tension to Function. *Front. Physiol.* **9**, (2018).

217. Moeendarbary, E., Weber, I. P., Sheridan, G. K., Koser, D. E., Soleman, S., Haenzi, B., Bradbury, E. J., Fawcett, J. & Franze, K. The soft mechanical signature of glial scars in the central nervous system. *Nat. Commun.* **8**, 14787 (2017).

218. Mohammadkarim, A., Tabatabaei, M., Parandakh, A., Mokhtari-Dizaji, M., Tafazzoli-Shadpour, M. & Khani, M.-M. Radiation therapy affects the mechanical behavior of human umbilical vein endothelial cells. *J. Mech. Behav. Biomed. Mater.* **85**, 188–193 (2018).

219. Alhalhooly, L., Mamnoon, B., Kim, J., Mallik, S. & Choi, Y. Dynamic cellular biomechanics in responses to chemotherapeutic drug in hypoxia probed by atomic force spectroscopy. *Oncotarget* **12**, 1165–1177 (2021).
220. Fan, Y., Sun, Q., Li, X., Feng, J., Ao, Z., Li, X. & Wang, J. Substrate Stiffness Modulates the Growth, Phenotype, and Chemoresistance of Ovarian Cancer Cells. *Front. Cell Dev. Biol.* **9**, (2021).
221. Zhang, C., Tan, Y., Feng, J., Huang, C., Liu, B., Fan, Z., Xu, B. & Lu, T. Exploration of the Effects of Substrate Stiffness on Biological Responses of Neural Cells and Their Mechanisms. *ACS Omega* **5**, 31115–31125 (2020).
222. Yi, B., Xu, Q. & Liu, W. An overview of substrate stiffness guided cellular response and its applications in tissue regeneration. *Bioact. Mater.* **15**, 82–102 (2022).
223. Aregueta-Robles, U. A., Woolley, A. J., Poole-Warren, L. A., Lovell, N. H. & Green, R. A. Organic electrode coatings for next-generation neural interfaces. *Front. Neuroengineering* **7**, (2014).
224. Group, S. M. Bioactive Coating Camouflages Implants for Deep Brain Stimulation. https://www.medicaldesignbriefs.com/component/content/article/mdb/pub/features/global-innovations/14904 (2012).
225. Hyakumura, T., Aregueta-Robles, U., Duan, W., Villalobos, J., Adams, W. K., Poole-Warren, L. & Fallon, J. B. Improving Deep Brain Stimulation Electrode Performance in vivo Through Use of Conductive Hydrogel Coatings. *Front. Neurosci.* **15**, (2021).
226. Sridharan, A. & Muthuswamy, J. Soft, Conductive, Brain-Like, Coatings at Tips of Microelectrodes Improve Electrical Stability under Chronic, In Vivo Conditions. *Micromachines* **12**, 761 (2021).

227. Banks, H., Hu, S. & Kenz, Z. A Brief Review of Elasticity and Viscoelasticity. *Adv. Appl. Math. Mech.* **3**, (2011).

228. Coleman, B. D. & Noll, W. Foundations of Linear Viscoelasticity. *Rev. Mod. Phys.* **33**, 239–249 (1961).

229. Chakraborty, B. C. & Ratna, D. Chapter 3 - Viscoelasticity. in *Polymers for Vibration Damping Applications* (eds. Chakraborty, B. C. & Ratna, D.) 69–141 (Elsevier, 2020). doi:10.1016/B978-0-12-819252-8.00003-3.

230. Elasticity in Biological Materials (all content). https://www.doitpoms.ac.uk/tlplib/bioelasticity/printall.php.

231. MacManus, D. B., Pierrat, B., Murphy, J. G. & Gilchrist, M. D. Dynamic mechanical properties of murine brain tissue using micro-indentation. *J. Biomech.* **48**, 3213–3218 (2015).

232. Rashid, B., Destrade, M. & Gilchrist, M. D. Mechanical characterization of brain tissue in tension at dynamic strain rates. *J. Mech. Behav. Biomed. Mater.* **33**, 43–54 (2014).

233. Rashid, B., Destrade, M. & Gilchrist, M. D. Mechanical characterization of brain tissue in compression at dynamic strain rates. *J. Mech. Behav. Biomed. Mater.* **10**, 23–38 (2012).

234. Bianchi, L., Cavarzan, F., Ciampitti, L., Cremonesi, M., Grilli, F. & Saccomandi, P. Thermophysical and mechanical properties of biological tissues as a function of temperature: a systematic literature review. *Int. J. Hyperthermia* **39**, 297–340 (2022).

235. Liu, Z., Zhang, Z. & Ritchie, R. O. Structural Orientation and Anisotropy in Biological Materials: Functional Designs and Mechanics. *Adv. Funct. Mater.* **30**, 1908121 (2020).

236. Feng, Y., Lee, C.-H., Sun, L., Ji, S. & Zhao, X. Characterizing white matter tissue in large strain via asymmetric indentation and inverse finite element modeling. *J. Mech. Behav. Biomed. Mater.* **65**, 490–501 (2017).
237. Eskandari, F., Rahmani, Z. & Shafieian, M. The effect of large deformation on Poisson's ratio of brain white matter: An experimental study. *Proc. Inst. Mech. Eng. [H]* **235**, 401–407 (2021).
238. Janmey, P. A., Georges, P. C. & Hvidt, S. Basic Rheology for Biologists. in *Methods in Cell Biology* vol. 83 1–27 (Academic Press, 2007).
239. Selecting the correct accessories for rheology and viscosity testing. http://www.rheologyschool.com/advice/rheology-tips/73-selecting-the-correct-accessories-for-rheology-and-viscosity-testing.
240. Cirka, H. A., Koehler, S. A., Farr, W. W. & Billiar, K. L. Eccentric rheometry for viscoelastic characterization of small, soft, anisotropic, and irregularly shaped biopolymer gels and tissue biopsies. *Ann. Biomed. Eng.* **40**, 1654–1665 (2012).
241. Deptuła, P. *et al.* Tissue Rheology as a Possible Complementary Procedure to Advance Histological Diagnosis of Colon Cancer. *ACS Biomater. Sci. Eng.* **6**, 5620–5631 (2020).
242. Relative Stiffness Measurements of Tumour Tissues by Shear Rheology. https://en.bio-protocol.org/en/bpdetail?id=2265&type=0.
243. Atomic Force Microscopy for Biologists. https://www.worldscientific.com/doi/epdf/10.1142/p674.
244. Chang, K.-C., Chiang, Y.-W., Yang, C.-H. & Liou, J.-W. Atomic force microscopy in biology and biomedicine. *Tzu Chi Med. J.* **24**, 162–169 (2012).
245. Carvalho, F. A. & Santos, N. C. Atomic force microscopy-based force spectroscopy — biological and biomedical applications. *IUBMB Life* **64**, 465–472 (2012).

246. Efremov, Y. M., Okajima, T. & Raman, A. Measuring viscoelasticity of soft biological samples using atomic force microscopy. *Soft Matter* **16**, 64–81 (2020).
247. Gavara, N. A beginner's guide to atomic force microscopy probing for cell mechanics. *Microsc. Res. Tech.* **80**, 75–84 (2017).
248. Viji Babu, P. K. & Radmacher, M. Mechanics of Brain Tissues Studied by Atomic Force Microscopy: A Perspective. *Front. Neurosci.* **13**, (2019).
249. Kalcioglu, Z. I., Qu, M., Strawhecker, K. E., Shazly, T., Edelman, E., VanLandingham, M. R., Smith, J. F. & Van Vliet, K. J. Dynamic impact indentation of hydrated biological tissues and tissue surrogate gels. *Philos. Mag.* **91**, 1339–1355 (2011).
250. Mijailovic, A. S., Qing, B., Fortunato, D. & Van Vliet, K. J. Characterizing viscoelastic mechanical properties of highly compliant polymers and biological tissues using impact indentation. *Acta Biomater.* **71**, 388–397 (2018).
251. Atay, S. M., Kroenke, C. D., Sabet, A. & Bayly, P. V. Measurement of the Dynamic Shear Modulus of Mouse Brain Tissue In Vivo by Magnetic Resonance Elastography. *J. Biomech. Eng.* **130**, (2008).
252. Gao, X. & Gu, W. A New Constitutive Model for Hydration-Dependent Mechanical Properties in Biological Soft Tissues and Hydrogels. *J. Biomech.* **47**, 3196–3200 (2014).
253. Grant, C. A., Brockwell, D. J., Radford, S. E. & Thomson, N. H. Effects of hydration on the mechanical response of individual collagen fibrils. *Appl. Phys. Lett.* **92**, 233902 (2008).
254. Haut, T. L. & Haut, R. C. The state of tissue hydration determines the strain-rate-sensitive stiffness of human patellar tendon. *J. Biomech.* **30**, 79–81 (1997).

255. Hoffman, A. H., Robichaud, D. R., Duquette, J. J. & Grigg, P. Determining the effect of hydration upon the properties of ligaments using pseudo Gaussian stress stimuli. *J. Biomech.* **38**, 1636–1642 (2005).

256. Ntim, M., Bembey, A., Ferguson, V. & Bushby, A. Hydration Effects on the Viscoelastic Properties of Collagen. *MRS Proc.* **898**, (2011).

257. Kalra, A. An Overview of Factors Affecting the Skin's Young's Modulus. **4**, 5 (2016).

258. Chimich, D., Shrive, N., Frank, C., Marchuk, L. & Bray, R. Water content alters viscoelastic behaviour of the normal adolescent rabbit medial collateral ligament. *J. Biomech.* **25**, 831–837 (1992).

259. Haut, T. L. & Haut, R. C. The state of tissue hydration determines the strain-rate-sensitive stiffness of human patellar tendon. *J. Biomech.* **30**, 79–81 (1997).

260. Lozano, P. F., Scholze, M., Babian, C., Scheidt, H., Vielmuth, F., Waschke, J., Ondruschka, B. & Hammer, N. Water-content related alterations in macro and micro scale tendon biomechanics. *Sci. Rep.* **9**, 7887 (2019).

261. Kerch, G. Role of Changes in State of Bound Water and Tissue Stiffness in Development of Age-Related Diseases. *Polymers* **12**, 1362 (2020).

262. Thornton, G. M., Shrive, N. G. & Frank, C. B. Altering ligament water content affects ligament pre-stress and creep behaviour. *J. Orthop. Res. Off. Publ. Orthop. Res. Soc.* **19**, 845–851 (2001).

263. Atkinson, T. S., Ewers, B. J. & Haut, R. C. The tensile and stress relaxation responses of human patellar tendon varies with specimen cross-sectional area. *J. Biomech.* **32**, 907–914 (1999).

264. 014539 - Ai39 or Ai39(RCL-eNpHR3.0/EYFP) Strain Details. https://www.jax.org/strain/014539.

265. 005628 - Emx1[IRES cre] , Emx1-Cre Strain Details. https://www.jax.org/strain/005628.
266. Shcholok, T. & Eftekharpour, E. Cre-recombinase systems for induction of neuron-specific knockout models: a guide for biomedical researchers. *Neural Regen. Res.* **18**, 273–279 (2022).
267. Papouin, T. & Haydon, P. G. Obtaining Acute Brain Slices. *Bio-Protoc.* **8**, (2018).
268. High Resolution Mouse Brain Atlas. https://www.hms.harvard.edu/research/brain/atlas.html.
269. Maugis, D. Extension of the Johnson-Kendall-Roberts Theory of the Elastic Contact of Spheres to Large Contact Radii. *Langmuir* **11**, 679–682 (1995).
270. Sneddon, I. N. The relation between load and penetration in the axisymmetric boussinesq problem for a punch of arbitrary profile. *Int. J. Eng. Sci.* **3**, 47–57 (1965).
271. Hermanowicz, P., Sarna, M., Burda, K. & Gabryś, H. AtomicJ: An open source software for analysis of force curves. *Rev. Sci. Instrum.* **85**, 063703 (2014).
272. Chen, J. & Lu, G. Finite element modelling of nanoindentation based methods for mechanical properties of cells. *J. Biomech.* **45**, 2810–2816 (2012).
273. Schindelin, J. *et al.* Fiji: an open-source platform for biological-image analysis. *Nat. Methods* **9**, 676–682 (2012).
274. Li, W., Shepherd, D. E. T. & Espino, D. M. Frequency dependent viscoelastic properties of porcine brain tissue. *J. Mech. Behav. Biomed. Mater.* **102**, 103460 (2020).
275. Elkin, B. S., Shaik, M. A. & Morrison, B. Chondroitinase ABC Reduces Brain Tissue Swelling In Vitro. *J. Neurotrauma* **28**, 2277–2285 (2011).
276. Mijailovic, A. S. Methods to measure and relate the viscoelastic properties of brain tissue. (Massachusetts Institute of Technology, 2016).

277. Prange, M. T. & Margulies, S. S. Regional, directional, and age-dependent properties of the brain undergoing large deformation. *J. Biomech. Eng.* **124**, 244–252 (2002).

278. Rohatgi, A. WebPlotDigitizer. (2022).

279. Riek, K., Millward, J. M., Hamann, I., Mueller, S., Pfueller, C. F., Paul, F., Braun, J., Infante-Duarte, C. & Sack, I. Magnetic resonance elastography reveals altered brain viscoelasticity in experimental autoimmune encephalomyelitis. *NeuroImage Clin.* **1**, 81–90 (2012).

280. Clayton, E. H., Garbow, J. R. & Bayly, P. V. Frequency-dependent viscoelastic parameters of mouse brain tissue estimated by MR elastography. *Phys. Med. Biol.* **56**, 2391 (2011).

281. Murphy, M. C., Curran, G. L., Glaser, K. J., Rossman, P. J., Huston, J., Poduslo, J. F., Jack, C. R., Felmlee, J. P. & Ehman, R. L. Magnetic resonance elastography of the brain in a mouse model of Alzheimer's disease: initial results. *Magn. Reson. Imaging* **30**, 535–539 (2012).

282. Diguet, E. High Resolution MR-Elastography Mouse Brain Study: Towards a Mechanical Atlas. *Int. Soc. Magn. Reson. Med. Proc.* **2009**, (2009).

283. Klein, C., Hain, E. G., Braun, J., Riek, K., Mueller, S., Steiner, B. & Sack, I. Enhanced Adult Neurogenesis Increases Brain Stiffness: In Vivo Magnetic Resonance Elastography in a Mouse Model of Dopamine Depletion. *PLOS ONE* **9**, e92582 (2014).

284. Freimann, F. B. *et al.* MR elastography in a murine stroke model reveals correlation of macroscopic viscoelastic properties of the brain with neuronal density. *NMR Biomed.* **26**, 1534–1539 (2013).

285. Feng, Y., Clayton, E. H., Okamoto, R. J., Engelbach, J., Bayly, P. V. & Garbow, J. R. A longitudinal magnetic resonance elastography study of murine brain tumors following radiation therapy. *Phys. Med. Biol.* **61**, 6121 (2016).
286. Boulet, T. IMPLEMENTATION OF MAGNETIC RESONANCE ELASTOGRAPHY FOR THE INVESTIGATION OF TRAUMATIC BRAIN INJURIES.
287. Boulet, T., Kelso, M. L. & Othman, S. F. Long-Term In Vivo Imaging of Viscoelastic Properties of the Mouse Brain after Controlled Cortical Impact. *J. Neurotrauma* **30**, 1512–1520 (2013).
288. Pogoda, K. *et al.* Compression stiffening of brain and its effect on mechanosensing by glioma cells. *New J. Phys.* **16**, 075002 (2014).
289. Eberle, D. *et al.* Acute but not inherited demyelination in mouse models leads to brain tissue stiffness changes. 449603 Preprint at https://doi.org/10.1101/449603 (2018).
290. Urbanski, M. M., Brendel, M. B. & Melendez-Vasquez, C. V. Acute and chronic demyelinated CNS lesions exhibit opposite elastic properties. *Sci. Rep.* **9**, 999 (2019).
291. Iwashita, M., Kataoka, N., Toida, K. & Kosodo, Y. Systematic profiling of spatiotemporal tissue and cellular stiffness in the developing brain. *Dev. Camb. Engl.* **141**, 3793–3798 (2014).
292. Antonovaite, N., Beekmans, S. V., Hol, E. M., Wadman, W. J. & Iannuzzi, D. Regional variations in stiffness in live mouse brain tissue determined by depth-controlled indentation mapping. *Sci. Rep.* **8**, (2018).
293. Antonovaite, N., Hulshof, L. A., Hol, E. M., Wadman, W. J. & Iannuzzi, D. *Viscoelastic mapping of mouse brain tissue: relation to structure and age*.

http://biorxiv.org/lookup/doi/10.1101/2020.05.11.089144 (2020) doi:10.1101/2020.05.11.089144.

294. Tang, C. *et al.* A fiber-shaped neural probe with alterable elastic moduli for direct implantation and stable electronic–brain interfaces. *J. Mater. Chem. B* **8**, 4387–4394 (2020).

295. Zhao, W., Cui, W., Xu, S., Cheong, L.-Z. & Shen, C. Examination of Alzheimer's disease by a combination of electrostatic force and mechanical measurement. *J. Microsc.* **275**, 66–72 (2019).

296. Feng, Y., Gao, Y., Wang, T., Tao, L., Qiu, S. & Zhao, X. A longitudinal study of the mechanical properties of injured brain tissue in a mouse model. *J. Mech. Behav. Biomed. Mater.* **71**, 407–415 (2017).

297. Jorba, I. *et al.* Ageing and chronic intermittent hypoxia mimicking sleep apnea do not modify local brain tissue stiffness in healthy mice. *J. Mech. Behav. Biomed. Mater.* **71**, 106–113 (2017).

298. MacManus, D. B., Pierrat, B., Murphy, J. G. & Gilchrist, M. D. Mechanical characterization of the P56 mouse brain under large-deformation dynamic indentation. *Sci. Rep.* **6**, (2016).

299. MacManus, D. B., Pierrat, B., Murphy, J. G. & Gilchrist, M. D. A viscoelastic analysis of the P56 mouse brain under large-deformation dynamic indentation. *Acta Biomater.* **48**, 309–318 (2017).

300. Strain Survival Information | National Institute on Aging. https://web.archive.org/web/20220714072032/https://www.nia.nih.gov/research/dab/aged-rodent-colonies-handbook/strain-survival-information.

301. Life-span and the inheritance of longevity of inbred mice - PubMed. https://pubmed.ncbi.nlm.nih.gov/1120887/.

302. Mihai, L. A., Chin, L., Janmey, P. A. & Goriely, A. A comparison of hyperelastic constitutive models applicable to brain and fat tissues. *J. R. Soc. Interface* **12**, 20150486 (2015).
303. Clarke, E. C., Cheng, S., Green, M., Sinkus, R. & Bilston, L. E. Using static preload with magnetic resonance elastography to estimate large strain viscoelastic properties of bovine liver. *J. Biomech.* **44**, 2461–2465 (2011).
304. Tirella, A., Mattei, G. & Ahluwalia, A. Strain rate viscoelastic analysis of soft and highly hydrated biomaterials. *J. Biomed. Mater. Res. A* **102**, 3352–3360 (2014).
305. Poon, B., Rittel, D. & Ravichandran, G. An analysis of nanoindentation in linearly elastic solids. *Int. J. Solids Struct.* **45**, 6018–6033 (2008).
306. Alcaraz, J., Buscemi, L., Grabulosa, M., Trepat, X., Fabry, B., Farré, R. & Navajas, D. Microrheology of Human Lung Epithelial Cells Measured by Atomic Force Microscopy. *Biophys. J.* **84**, 2071–2079 (2003).
307. Hecht, F. M., Rheinlaender, J., Schierbaum, N., Goldmann, W. H., Fabry, B. & Schäffer, T. E. Imaging viscoelastic properties of live cells by AFM: power-law rheology on the nanoscale. *Soft Matter* **11**, 4584–4591 (2015).
308. Rother, J., Nöding, H., Mey, I. & Janshoff, A. Atomic force microscopy-based microrheology reveals significant differences in the viscoelastic response between malign and benign cell lines. *Open Biol.* **4**, 140046 (2014).
309. Bartolini, L., Iannuzzi, D. & Mattei, G. Comparison of frequency and strain-rate domain mechanical characterization. *Sci. Rep.* **8**, 13697 (2018).
310. Huang, C.-Y., Wang, V. M., Flatow, E. L. & Mow, V. C. TEMPERATURE-DEPENDENT VISCOELASTIC PROPERTIES OF THE HUMAN SUPRASPINATUS TENDON. *J. Biomech.* **42**, 546–549 (2009).
311. Franck, A. Viscoelasticity and dynamic mechanical testing.

312. Species Specific Information: Mouse. https://web.jhu.edu/animalcare/procedures/mouse.html.
313. Elkin, B. S., Shaik, M. A. & Morrison, B. Fixed negative charge and the Donnan effect: a description of the driving forces associated with brain tissue swelling and oedema. *Philos. Transact. A Math. Phys. Eng. Sci.* **368**, 585–603 (2010).
314. Ferrer, I. *et al.* Brain Protein Preservation Largely Depends on the Postmortem Storage Temperature: Implications for Study of Proteins in Human Neurologic Diseases and Management of Brain Banks: A BrainNet Europe Study. *J. Neuropathol. Exp. Neurol.* **66**, 35–46 (2007).
315. Feng, Y., Okamoto, R. J., Namani, R., Genin, G. M. & Bayly, P. V. Measurements of mechanical anisotropy in brain tissue and implications for transversely isotropic material models of white matter. *J. Mech. Behav. Biomed. Mater.* **23**, 117–132 (2013).
316. Kovalev, V. & Kruggel, F. Texture anisotropy of the brain's white matter as revealed by anatomical MRI. *IEEE Trans. Med. Imaging* **26**, 678–685 (2007).
317. Xing, M. Tensile behavior and mechanical anisotropy of branched cerebral vasculature within gray matter. (Rutgers University - Graduate School - New Brunswick, 2015). doi:10.7282/T3JW8GXZ.
318. Alba-Ferrara, L. M. & de Erausquin, G. A. What does anisotropy measure? Insights from increased and decreased anisotropy in selective fiber tracts in schizophrenia. *Front. Integr. Neurosci.* **7**, 9 (2013).
319. Giordano, C., Cloots, R. J. H., van Dommelen, J. a. W. & Kleiven, S. The influence of anisotropy on brain injury prediction. *J. Biomech.* **47**, 1052–1059 (2014).

320. Ling, Y., Li, C., Feng, K., Duncan, R., Eisma, R., Huang, Z. & Nabi, G. Effects of fixation and preservation on tissue elastic properties measured by quantitative optical coherence elastography (OCE). *J. Biomech.* **49**, 1009–1015 (2016).
321. Metz, H., McElhaney, J. & Ommaya, A. K. A comparison of the elasticity of live, dead, and fixed brain tissue. *J. Biomech.* **3**, 453–458 (1970).
322. Rouleau, L., Delorme, S., Thibault, F., Mongrain, R. & Leask, R. L. Effect of Formalin Fixation on the Local Mechanical Properties of Aortic Tissue.
323. Iwashita, M., Nomura, T., Suetsugu, T., Matsuzaki, F., Kojima, S. & Kosodo, Y. Comparative Analysis of Brain Stiffness Among Amniotes Using Glyoxal Fixation and Atomic Force Microscopy. *Front. Cell Dev. Biol.* **8**, (2020).
324. Xu, Z. S., Yao, A., Chu, S. S., Paun, M. K., McClintic, A. M., Murphy, S. P. & Mourad, P. D. Detection of Mild Traumatic Brain Injury in Rodent Models Using Shear Wave Elastography: Preliminary Studies. *J. Ultrasound Med.* **33**, 1763–1771 (2014).
325. Choi, B. H. & Lapham, L. W. Radial glia in the human fetal cerebrum: A combined golgi, immunofluorescent and electron microscopic study. *Brain Res.* **148**, 295–311 (1978).
326. Levison, S. W. & Goldman, J. E. Both oligodendrocytes and astrocytes develop from progenitors in the subventricular zone of postnatal rat forebrain. *Neuron* **10**, 201–212 (1993).
327. Young, J. K. & McKenzie, J. C. GLUT2 Immunoreactivity in Gomori-positive Astrocytes of the Hypothalamus. *J. Histochem. Cytochem.* **52**, 1519–1524 (2004).
328. Zerlin, M., Levison, S. W. & Goldman, J. E. Early patterns of migration, morphogenesis, and intermediate filament expression of subventricular zone

cells in the postnatal rat forebrain. *J. Neurosci. Off. J. Soc. Neurosci.* **15**, 7238–7249 (1995).

329. Beattie, R. & Hippenmeyer, S. Mechanisms of radial glia progenitor cell lineage progression. *Febs Lett.* **591**, 3993–4008 (2017).
330. Raff, M., Abney, E., Cohen, J., Lindsay, R. & Noble, M. Two types of astrocytes in cultures of developing rat white matter: differences in morphology, surface gangliosides, and growth characteristics. *J. Neurosci.* **3**, 1289–1300 (1983).
331. Venkatesh, K., Srikanth, L., Vengamma, B., Chandrasekhar, C., Sanjeevkumar, A., Prasad, B. C. M. & Sarma, P. V. G. K. In vitro differentiation of cultured human CD34+ cells into astrocytes. *Neurol. India* **61**, 383 (2013).
332. Mollet, G. A. Fundamentals of Human Neuropsychology, 6th Edition. *J. Undergrad. Neurosci. Educ.* **6**, R3–R4 (2008).
333. Clark, J. A., Cheng, J. C., Leung, K. S. & Leung, P. C. Mechanical characterisation of human postburn hypertrophic skin during pressure therapy. *J. Biomech.* **20**, 397–406 (1987).
334. Dingal, P. C. D. P., Bradshaw, A. M., Cho, S., Raab, M., Buxboim, A., Swift, J. & Discher, D. E. Fractal heterogeneity in minimal matrix models of scars modulates stiff-niche stem-cell responses via nuclear exit of a mechanorepressor. *Nat. Mater.* **14**, 951–960 (2015).
335. Georges, P. C. *et al.* Increased stiffness of the rat liver precedes matrix deposition: implications for fibrosis. *Am. J. Physiol. Gastrointest. Liver Physiol.* **293**, G1147-1154 (2007).
336. Hinz, B. Tissue stiffness, latent TGF-beta1 activation, and mechanical signal transduction: implications for the pathogenesis and treatment of fibrosis. *Curr. Rheumatol. Rep.* **11**, 120–126 (2009).

337. Moyssakis, I., Gialafos, E., Vassiliou, V., Taktikou, E., Katsiari, C., Papadopoulos, D. P. & Sfikakis, P. P. Aortic stiffness in systemic sclerosis is increased independently of the extent of skin involvement. *Rheumatol. Oxf. Engl.* **44**, 251–254 (2005).

338. Berry: Mesenchymal stem cell injection after myocardial... - Google Scholar. https://scholar.google.com/scholar_lookup?title=Mesenchymal%20stem%20cell%20injection%20after%20myocardial%20infarction%20improves%20myocardial%20compliance&author=Berry%2CM.%20F.&journal=Am.%20J.%20Physiol.&volume=290&pages=H2196-H2203&publication_year=2006.

339. Moeendarbary, E., Weber, I. P., Sheridan, G. K., Koser, D. E., Soleman, S., Haenzi, B., Bradbury, E. J., Fawcett, J. & Franze, K. The soft mechanical signature of glial scars in the central nervous system. *Nat. Commun.* **8**, 14787 (2017).

340. Jiang, F. X., Yurke, B., Firestein, B. L. & Langrana, N. A. Neurite outgrowth on a DNA crosslinked hydrogel with tunable stiffnesses. *Ann. Biomed. Eng.* **36**, 1565–1579 (2008).

341. Koser, D. E. *et al.* Mechanosensing is critical for axon growth in the developing brain. *Nat. Neurosci.* **19**, 1592–1598 (2016).

342. Pathak, M. M., Nourse, J. L., Tran, T., Hwe, J., Arulmoli, J., Le, D. T. T., Bernardis, E., Flanagan, L. A. & Tombola, F. Stretch-activated ion channel Piezo1 directs lineage choice in human neural stem cells. *Proc. Natl. Acad. Sci. U. S. A.* **111**, 16148–16153 (2014).

343. Miller, W. J., Leventhal, I., Scarsella, D., Haydon, P. G., Janmey, P. & Meaney, D. F. Mechanically induced reactive gliosis causes ATP-mediated alterations in astrocyte stiffness. *J. Neurotrauma* **26**, 789–797 (2009).

344. Li, G., Cao, Y., Shen, F., Wang, Y., Bai, L., Guo, W., Bi, Y., Lv, G. & Fan, Z. Mdivi-1 Inhibits Astrocyte Activation and Astroglial Scar Formation and Enhances Axonal Regeneration after Spinal Cord Injury in Rats. *Front. Cell. Neurosci.* **10**, (2016).

345. Tian, D., Xie, M., Yu, Z., Zhang, Q., Wang, Y., Chen, B., Chen, C. & Wang, W. Cell cycle inhibition attenuates microglia induced inflammatory response and alleviates neuronal cell death after spinal cord injury in rats. *Brain Res.* **1135**, 177–185 (2007).

346. Tian, D.-S., Yu, Z.-Y., Xie, M.-J., Bu, B.-T., Witte, O. W. & Wang, W. Suppression of astroglial scar formation and enhanced axonal regeneration associated with functional recovery in a spinal cord injury rat model by the cell cycle inhibitor olomoucine. *J. Neurosci. Res.* **84**, 1053–1063 (2006).

347. Yew, W. P., Djukic, N. D., Jayaseelan, J. S. P., Woodman, R. J., Muyderman, H. & Sims, N. R. Differential effects of the cell cycle inhibitor, olomoucine, on functional recovery and on responses of peri-infarct microglia and astrocytes following photothrombotic stroke in rats. *J. Neuroinflammation* **18**, 168 (2021).

348. Dahl, D., Rueger, D. C., Bignami, A., Weber, K. & Osborn, M. Vimentin, the 57 000 molecular weight protein of fibroblast filaments, is the major cytoskeletal component in immature glia. *Eur. J. Cell Biol.* **24**, 191–196 (1981).

349. Yabe, J. T., Chan, W. K.-H., Wang, F.-S., Pimenta, A., Ortiz, D. D. & Shea, T. B. Regulation of the transition from vimentin to neurofilaments during neuronal differentiation. *Cell Motil.* **56**, 193–205 (2003).

350. Tate, C. C., Tate, M. C. & LaPlaca, M. C. Fibronectin and laminin increase in the mouse brain after controlled cortical impact injury. *J. Neurotrauma* **24**, 226–230 (2007).

351. Bradbury, E. J., Moon, L. D. F., Popat, R. J., King, V. R., Bennett, G. S., Patel, P. N., Fawcett, J. W. & McMahon, S. B. Chondroitinase ABC promotes functional recovery after spinal cord injury. *Nature* **416**, 636–640 (2002).
352. Keough, M. B. *et al.* An inhibitor of chondroitin sulfate proteoglycan synthesis promotes central nervous system remyelination. *Nat. Commun.* **7**, 11312 (2016).
353. Yue, B. Biology of the Extracellular Matrix: An Overview. *J. Glaucoma* S20–S23 (2014) doi:10.1097/IJG.0000000000000108.
354. Frantz, C., Stewart, K. M. & Weaver, V. M. The extracellular matrix at a glance. *J. Cell Sci.* **123**, 4195–4200 (2010).
355. Karamanos, N. K. *et al.* A guide to the composition and functions of the extracellular matrix. *FEBS J.* **288**, 6850–6912 (2021).
356. Brauchle, E., Kasper, J., Daum, R., Schierbaum, N., Falch, C., Kirschniak, A., Schäffer, T. E. & Schenke-Layland, K. Biomechanical and biomolecular characterization of extracellular matrix structures in human colon carcinomas. *Matrix Biol.* **68–69**, 180–193 (2018).
357. Levental, K. R. *et al.* Matrix Crosslinking Forces Tumor Progression by Enhancing Integrin signaling. *Cell* **139**, 891–906 (2009).
358. Ahn, S., Lee, K. Y., Parker, K. K. & Shin, K. Formation of Multi-Component Extracellular Matrix Protein Fibers. *Sci. Rep.* **8**, 1913 (2018).
359. Sophia Fox, A. J., Bedi, A. & Rodeo, S. A. The Basic Science of Articular Cartilage. *Sports Health* **1**, 461–468 (2009).
360. Franchi, M., Trirè, A., Quaranta, M., Orsini, E. & Ottani, V. Collagen structure of tendon relates to function. *ScientificWorldJournal* **7**, 404–420 (2007).
361. DeQuach, J. A., Mezzano, V., Miglani, A., Lange, S., Keller, G. M., Sheikh, F. & Christman, K. L. Simple and High Yielding Method for Preparing Tissue Specific Extracellular Matrix Coatings for Cell Culture. *PLOS ONE* **5**, e13039 (2010).

362. Yu, Y., Alkhawaji, A., Ding, Y. & Mei, J. Decellularized scaffolds in regenerative medicine. *Oncotarget* **7**, 58671–58683 (2016).
363. Kyburz, K. A. & Anseth, K. S. Synthetic Mimics of the Extracellular Matrix: How Simple is Complex Enough? *Ann. Biomed. Eng.* **43**, 489–500 (2015).
364. Advanced BioMatrix. ECM Select® Array Kit Ultra-36 #5170-1EA. https://www.advancedbiomatrix.com/extracellular-matrix-screening-array/ecm-select-array-kit-ultra-36/ (2018).
365. Corning. Matrigel Matrix | Extracellular Matrix | Corning. https://www.corning.com/emea/en/products/life-sciences/products/surfaces/matrigel-matrix.html (2018).
366. R&D Systems. Cultrex Basement Membrane Extract (BME) and Extracellular Matrices (ECM): R&D Systems. https://www.rndsystems.com/products/cultrex-basement-membrane-extract-bme-and-extracellular-matrices-ecm (2018).
367. Taylor, A. J., Ratner, B. D., Buttery, L. D. & Alexander, M. R. Revealing cytokine-induced changes in the extracellular matrix with secondary ion mass spectrometry. *Acta Biomater.* **14**, 70–83 (2015).
368. White, L. J. *et al.* The impact of detergents on the tissue decellularization process: a ToF-SIMS study. *Acta Biomater.* **50**, 207 (2017).
369. Carvalho, M. S., Silva, J. C., Udangawa, R. N., Cabral, J. M. S., Ferreira, F. C., da Silva, C. L., Linhardt, R. J. & Vashishth, D. Co-culture cell-derived extracellular matrix loaded electrospun microfibrous scaffolds for bone tissue engineering. *Mater. Sci. Eng. C Mater. Biol. Appl.* **99**, 479–490 (2019).
370. Assunção, M., Dehghan-Baniani, D., Yiu, C. H. K., Später, T., Beyer, S. & Blocki, A. Cell-Derived Extracellular Matrix for Tissue Engineering and Regenerative Medicine. *Front. Bioeng. Biotechnol.* **8**, (2020).

371. Zahmatkesh, E., Khoshdel-Rad, N., Mirzaei, H., Shpichka, A., Timashev, P., Mahmoudi, T. & Vosough, M. Evolution of organoid technology: Lessons learnt in Co-Culture systems from developmental biology. *Dev. Biol.* **475**, 37–53 (2021).
372. Carvalho, M. S., Silva, J. C., Cabral, J. M. S., da Silva, C. L. & Vashishth, D. Cultured cell-derived extracellular matrices to enhance the osteogenic differentiation and angiogenic properties of human mesenchymal stem/stromal cells. *J. Tissue Eng. Regen. Med.* **13**, 1544–1558 (2019).
373. Jeong, W., Kim, M. K. & Kang, H.-W. Effect of detergent type on the performance of liver decellularized extracellular matrix-based bio-inks. *J. Tissue Eng.* **12**, 2041731421997091 (2021).
374. White, L. J. *et al.* The impact of detergents on the tissue decellularization process: a ToF-SIMS study. *Acta Biomater.* **50**, 207 (2017).
375. Youngstrom, D. W., Barrett, J. G., Jose, R. R. & Kaplan, D. L. Functional Characterization of Detergent-Decellularized Equine Tendon Extracellular Matrix for Tissue Engineering Applications. *PLOS ONE* **8**, e64151 (2013).
376. Kawamura, R., Hayashi, Y., Murakami, H. & Nakashima, M. EDTA soluble chemical components and the conditioned medium from mobilized dental pulp stem cells contain an inductive microenvironment, promoting cell proliferation, migration, and odontoblastic differentiation. *Stem Cell Res. Ther.* **7**, 77 (2016).
377. Pattabhi, S. rao, Martinez, J. S. & Keller, T. C. S. Decellularized ECM Effects on Human Mesenchymal Stem Cell Stemness and Differentiation. *Differ. Res. Biol. Divers.* **88**, 131–143 (2014).
378. Shakoor, A., Gao, W., Zhao, L., Jiang, Z. & Sun, D. Advanced tools and methods for single-cell surgery. *Microsyst. Nanoeng.* **8**, 1–21 (2022).

379. Furihata, T., Ito, R., Kamiichi, A., Saito, K. & Chiba, K. Establishment and characterization of a new conditionally immortalized human astrocyte cell line. *J. Neurochem.* **136**, 92–105 (2016).

380. Langley, R. R., Fan, D., Guo, L., Zhang, C., Lin, Q., Brantley, E. C., McCarty, J. H. & Fidler, I. J. Generation of an Immortalized Astrocyte Cell Line from H-2Kb-tsA58 Mice to Study the Role of Astrocytes in Brain Metastasis. *Int. J. Oncol.* **35**, 665–672 (2009).

381. Cahoy, J. D. *et al.* A Transcriptome Database for Astrocytes, Neurons, and Oligodendrocytes: A New Resource for Understanding Brain Development and Function. *J. Neurosci.* **28**, 264–278 (2008).

382. Pekny, M. & Nilsson, M. Astrocyte activation and reactive gliosis. *Glia* **50**, 427–434 (2005).

383. Parmentier-Batteur, S. *et al.* Attenuation of scratch-induced reactive astrogliosis by novel EphA4 kinase inhibitors. *J. Neurochem.* **118**, 1016–1031 (2011).

384. Cullen, D. K., Simon, C. M. & LaPlaca, M. C. Strain rate-dependent induction of reactive astrogliosis and cell death in three-dimensional neuronal-astrocytic co-cultures. *Brain Res.* **1158**, 103–115 (2007).

385. Thelin, E. P. *et al.* Delineating Astrocytic Cytokine Responses in a Human Stem Cell Model of Neural Trauma. *J. Neurotrauma* **37**, 93–105 (2020).

386. Canchi, S., Sarntinoranont, M., Hong, Y., Flint, J. J., Subhash, G. & King, M. A. Simulated blast overpressure induces specific astrocyte injury in an ex vivo brain slice model. *PloS One* **12**, e0175396 (2017).

387. Katsel, P., Byne, W., Roussos, P., Tan, W., Siever, L. & Haroutunian, V. Astrocyte and Glutamate Markers in the Superficial, Deep, and White Matter Layers of the Anterior Cingulate Gyrus in Schizophrenia. *Neuropsychopharmacology* **36**, 1171–1177 (2011).

388. Bao, Y., Qin, L., Kim, E., Bhosle, S., Guo, H., Febbraio, M., Haskew-Layton, R. E., Ratan, R. & Cho, S. CD36 is involved in astrocyte activation and astroglial scar formation. *J. Cereb. Blood Flow Metab.* **32**, 1567–1577 (2012).

389. Benfenati, V., Caprini, M., Dovizio, M., Mylonakou, M. N., Ferroni, S., Ottersen, O. P. & Amiry-Moghaddam, M. An aquaporin-4/transient receptor potential vanilloid 4 (AQP4/TRPV4) complex is essential for cell-volume control in astrocytes. *Proc. Natl. Acad. Sci. U. S. A.* **108**, 2563–2568 (2011).

390. Chen, Y.-J., Hsu, C.-C., Shiao, Y.-J., Wang, H.-T., Lo, Y.-L. & Lin, A. M. Y. Anti-inflammatory effect of afatinib (an EGFR-TKI) on OGD-induced neuroinflammation. *Sci. Rep.* **9**, (2019).

391. Folck, A. F. A CELL-BASED MODEL TO STUDY FACTORS THAT DRIVE DIFFUSE ASTROCYTOMA DEVELOPMENT. 65 (2016).

392. Gunnarson, E., Axehult, G., Baturina, G., Zelenin, S., Zelenina, M. & Aperia, A. Lead induces increased water permeability in astrocytes expressing aquaporin 4. *Neuroscience* **136**, 105–114 (2005).

393. Han, D., Jin, J., Woo, J., Min, H. & Kim, Y. Proteomic analysis of mouse astrocytes and their secretome by a combination of FASP and StageTip-based, high pH, reversed-phase fractionation. *PROTEOMICS* **14**, 1604–1609 (2014).

394. Katakowski, M., Jiang, F., Zheng, X., Gutierrez, J. A., Szalad, A. & Chopp, M. Tumorigenicity of cortical astrocyte cell line induced by the protease ADAM17. *Cancer Sci.* **100**, 1597–1604 (2009).

395. Lee, M. R., Ruby, C. L., Hinton, D. J., Choi, S., Adams, C. A., Young Kang, N. & Choi, D.-S. Striatal Adenosine Signaling Regulates EAAT2 and Astrocytic AQP4 Expression and Alcohol Drinking in Mice. *Neuropsychopharmacology* **38**, 437–445 (2013).

396. Leoni, G., Rattray, M., Fulton, D., Rivera, A. & Butt, A. M. Immunoablation of cells expressing the NG2 chondroitin sulphate proteoglycan. *J. Anat.* **224**, 216–227 (2014).

397. Mulvihill, J. J. E., Raykin, J., Snider, E. J., Schildmeyer, L. A., Zaman, I., Platt, M. O., Kelly, D. J. & Ethier, C. R. Development of a Platform for Studying 3D Astrocyte Mechanobiology: Compression of Astrocytes in Collagen Gels. *Ann. Biomed. Eng.* **46**, 365–374 (2018).

398. Oka, M. S. & Rupp, R. G. *Cell Biology and Biotechnology: Novel Approaches to Increased Cellular Productivity*. (Springer Science & Business Media, 2012).

399. Phamduong, E. *et al.* Acute and Chronic Mu Opioids Differentially Regulate Thrombospondins 1 and 2 Isoforms in Astrocytes. *ACS Chem. Neurosci.* **5**, 106–114 (2013).

400. Radany, E. H., Brenner, M., Besnard, F., Bigornia, V., Bishop, J. M. & Deschepper, C. F. Directed establishment of rat brain cell lines with the phenotypic characteristics of type 1 astrocytes. *Proc. Natl. Acad. Sci. U. S. A.* **89**, 6467–6471 (1992).

401. Shen, Y., Tenney, A. P., Busch, S. A., Horn, K. P., Cuascut, F. X., Liu, K., He, Z., Silver, J. & Flanagan, J. G. PTPσ Is a Receptor for Chondroitin Sulfate Proteoglycan, an Inhibitor of Neural Regeneration. *Science* **326**, 592–596 (2009).

402. Ku, W.-C. *et al.* A comparative proteomic study of secretomes in kaempferitrin-treated CTX TNA2 astrocytic cells. *Phytomedicine Int. J. Phytother. Phytopharm.* **36**, 137–144 (2017).

403. Ridge, K. M., Eriksson, J. E., Pekny, M. & Goldman, R. D. Roles of vimentin in health and disease. *Genes Dev.* **36**, 391–407 (2022).

404. Liesi, P. & Kauppila, T. Induction of Type IV Collagen and Other Basement-Membrane-Associated Proteins after Spinal Cord Injury of the Adult Rat May Participate in Formation of the Glial Scar. *Exp. Neurol.* **173**, 31–45 (2002).
405. Balasubramanian, S., Packard, J. A., Leach, J. B. & Powell, E. M. Three-Dimensional Environment Sustains Morphological Heterogeneity and Promotes Phenotypic Progression During Astrocyte Development. *Tissue Eng. Part A* **22**, 885–898 (2016).
406. Delgado-Rivera, R., Harris, S. L., Ahmed, I., Babu, A. N., Patel, R. P., Ayres, V., Flowers, D. & Meiners, S. Increased FGF-2 secretion and ability to support neurite outgrowth by astrocytes cultured on polyamide nanofibrillar matrices. *Matrix Biol. J. Int. Soc. Matrix Biol.* **28**, 137–147 (2009).
407. Oakes, R. S., Polei, M. D., Skousen, J. L. & Tresco, P. A. An astrocyte derived extracellular matrix coating reduces astrogliosis surrounding chronically implanted microelectrode arrays in rat cortex. *Biomaterials* **154**, 1–11 (2018).
408. Wiese, S., Karus, M. & Faissner, A. Astrocytes as a Source for Extracellular Matrix Molecules and Cytokines. *Front. Pharmacol.* **3**, 120 (2012).
409. Wujek, J. R. & Akeson, R. A. Extracellular matrix derived from astrocytes stimulates neuritic outgrowth from PC12 cells in vitro. *Brain Res.* **431**, 87–97 (1987).
410. Yu, P., Wang, H., Katagiri, Y. & Geller, H. M. An In Vitro Model of Reactive Astrogliosis and Its Effect on Neuronal Growth. *Methods Mol. Biol. Clifton NJ* **814**, 327–340 (2012).
411. Gómez-Pinilla, F., Vu, L. & Cotman, C. W. Regulation of astrocyte proliferation by FGF-2 and heparan sulfate in vivo. *J. Neurosci. Off. J. Soc. Neurosci.* **15**, 2021–2029 (1995).

412. Kang, W., Balordi, F., Su, N., Chen, L., Fishell, G. & Hébert, J. M. Astrocyte activation is suppressed in both normal and injured brain by FGF signaling. *Proc. Natl. Acad. Sci. U. S. A.* **111**, E2987-2995 (2014).
413. Zou, L.-H., Shi, Y.-J., He, H., Jiang, S.-M., Huo, F.-F., Wang, X.-M., Wu, F. & Ma, L. Effects of FGF2/FGFR1 Pathway on Expression of A1 Astrocytes After Infrasound Exposure. *Front. Neurosci.* **13**, (2019).
414. Goddard, D. R., Berry, M., Kirvell, S. L. & Butt, A. M. Fibroblast growth factor-2 induces astroglial and microglial reactivity in vivo. *J. Anat.* **200**, 57–67 (2002).
415. Isolation and culturing of primary mouse astrocytes for the analysis of focal adhesion dynamics. https://star-protocols.cell.com/protocols/1220#limitations.
416. Lattke, M., Goldstone, R., Ellis, J. K., Boeing, S., Jurado-Arjona, J., Marichal, N., MacRae, J. I., Berninger, B. & Guillemot, F. Extensive transcriptional and chromatin changes underlie astrocyte maturation in vivo and in culture. *Nat. Commun.* **12**, 4335 (2021).
417. Schildge, S., Bohrer, C., Beck, K. & Schachtrup, C. Isolation and Culture of Mouse Cortical Astrocytes. *J. Vis. Exp. JoVE* 50079 (2013) doi:10.3791/50079.
418. Stewart, D. C., Rubiano, A., Dyson, K. & Simmons, C. S. Mechanical characterization of human brain tumors from patients and comparison to potential surgical phantoms. *PLoS ONE* **12**, e0177561 (2017).
419. Walter, C., Crawford, L., Lai, M., Toonen, J. A., Pan, Y., Sakiyama-Elbert, S., Gutmann, D. H. & Pathak, A. Increased Tissue Stiffness in Tumors from Mice with Neurofibromatosis-1 Optic Glioma. *Biophys. J.* **112**, 1535–1538 (2017).
420. Pong, A. C., Jugé, L., Bilston, L. E. & Cheng, S. Development of acute hydrocephalus does not change brain tissue mechanical properties in adult rats, but in juvenile rats. *PLOS ONE* **12**, e0182808 (2017).

421. Moazen, M., Alazmani, A., Rafferty, K., Liu, Z.-J., Gustafson, J., Cunningham, M. L., Fagan, M. J. & Herring, S. W. Intracranial pressure changes during mouse development. *J. Biomech.* **49**, 123–126 (2016).

422. Oshio, K., Watanabe, H., Song, Y., Verkman, A. S. & Manley, G. T. Reduced cerebrospinal fluid production and intracranial pressure in mice lacking choroid plexus water channel Aquaporin-1. *FASEB J.* **19**, 76–78 (2005).

423. Feiler, S., Friedrich, B., Schöller, K., Thal, S. C. & Plesnila, N. Standardized induction of subarachnoid hemorrhage in mice by intracranial pressure monitoring. *J. Neurosci. Methods* **190**, 164–170 (2010).

424. Yang, B., Zador, Z. & Verkman, A. S. Glial Cell Aquaporin-4 Overexpression in Transgenic Mice Accelerates Cytotoxic Brain Swelling*. *J. Biol. Chem.* **283**, 15280–15286 (2008).

425. Sphere AFM Tips and Colloidal AFM Probes - NanoAndMore. https://www.nanoandmore.com/Sphere-Nanomechanics-AFM-Probes.

426. Rambani, K., Vukasinovic, J., Glezer, A. & Potter, S. M. Culturing thick brain slices: An interstitial 3D microperfusion system for enhanced viability. *J. Neurosci. Methods* **180**, 243–254 (2009).

427. De Simoni, A. & MY Yu, L. Preparation of organotypic hippocampal slice cultures: interface method. *Nat. Protoc.* **1**, 1439–1445 (2006).

428. Atay, S. M., Kroenke, C. D., Sabet, A. & Bayly, P. V. Measurement of the Dynamic Shear Modulus of Mouse Brain Tissue In Vivo by Magnetic Resonance Elastography. *J. Biomech. Eng.* **130**, (2008).

429. Fountoulakis, M., Hardmeier, R., Höger, H. & Lubec, G. Postmortem Changes in the Level of Brain Proteins. *Exp. Neurol.* **167**, 86–94 (2001).

430. Steffensen, A. B., Oernbo, E. K., Stoica, A., Gerkau, N. J., Barbuskaite, D., Tritsaris, K., Rose, C. R. & MacAulay, N. Cotransporter-mediated water

transport underlying cerebrospinal fluid formation. *Nat. Commun.* **9**, 2167 (2018).

431. Bandaranayake, N. M., Nemoto, E. M. & Stezoski, S. W. Rat brain osmolality during barbiturate anesthesia and global brain ischemia. *Stroke* **9**, 249–254 (1978).
432. Hatashita, S., Hoff, J. T. & Salamat, S. M. Ischemic Brain Edema and the Osmotic Gradient between Blood and Brain. *J. Cereb. Blood Flow Metab.* **8**, 552–559 (1988).
433. Oernbo, E. K. *et al.* Cerebrospinal fluid formation is controlled by membrane transporters to modulate intracranial pressure. 2021.12.10.472067 Preprint at https://doi.org/10.1101/2021.12.10.472067 (2021).
434. Wibroe, E. A., Yri, H. M., Jensen, R. H., Wibroe, M. A. & Hamann, S. Osmolality of Cerebrospinal Fluid from Patients with Idiopathic Intracranial Hypertension (IIH). *PLOS ONE* **11**, e0146793 (2016).
435. GOLDBERG, N. B., SAWINSKI, V. J. & GOLDBERG, A. F. Human Cerebrospinal Fluid Osmolality at 37° C. *Anesthesiology* **26**, 829 (1965).
436. Artificial Cerebrospinal Fluid (ACSF) for Synaptic Plasticity Studies. *Cold Spring Harb. Protoc.* **2016**, pdb.rec092353 (2016).
437. Finan, J. D., Cho, F. S., Kernie, S. G. & Morrison, B. Intracerebroventricular administration of chondroitinase ABC reduces acute edema after traumatic brain injury in mice. *BMC Res. Notes* **9**, 160 (2016).
438. Aquino, D. A., Margolis, R. U. & Margolis, R. K. Immunocytochemical localization of a chondroitin sulfate proteoglycan in nervous tissue. I. Adult brain, retina, and peripheral nerve. *J. Cell Biol.* **99**, 1117–1129 (1984).

439. Margolis, R. K., Thomas, M. D., Crockett, C. P. & Margolis, R. U. Presence of chondroitin sulfate in the neuronal cytoplasm. *Proc. Natl. Acad. Sci. U. S. A.* **76**, 1711–1715 (1979).

440. Mukherjee, N., Nandi, S., Garg, S., Ghosh, S., Ghosh, S., Samat, R. & Ghosh, S. Targeting Chondroitin Sulfate Proteoglycans: An Emerging Therapeutic Strategy to Treat CNS Injury. *ACS Chem. Neurosci.* **11**, 231–232 (2020).

441. Kawamata, T., Mori, T., Sato, S. & Katayama, Y. Tissue hyperosmolality and brain edema in cerebral contusion. *Neurosurg. Focus* **22**, E5 (2007).

442. Lang, G. E., Stewart, P. S., Vella, D., Waters, S. L. & Goriely, A. Is the Donnan effect sufficient to explain swelling in brain tissue slices? *J. R. Soc. Interface* **11**, 20140123 (2014).

443. Kuroiwa, T., Ueki, M., Chen, Q., Ichinose, S. & Okeda, R. Is the swelling in brain edema isotropic or anisotropic? *Acta Neurochir. Suppl. (Wien)* **60**, 155–157 (1994).

444. Garo, A., Hrapko, M., van Dommelen, J. a. W. & Peters, G. W. M. Towards a reliable characterisation of the mechanical behaviour of brain tissue: The effects of post-mortem time and sample preparation. *Biorheology* **44**, 51–58 (2007).

445. Du, T. *et al.* Cerebrospinal fluid is a significant fluid source for anoxic cerebral oedema. *Brain* **145**, 787–797 (2022).

446. 013044 - Sst-IRES-Cre (SOM-IRES-Cre) Strain Details. https://www.jax.org/strain/013044.

447. King, T. C. 1 - Cell Injury, Cellular Responses to Injury, and Cell Death. in *Elsevier's Integrated Pathology* (ed. King, T. C.) 1–20 (Mosby, 2007). doi:10.1016/B978-0-323-04328-1.50007-3.

448. Chang, L. M. S. & Bollum, F. J. Deoxynucleotide-Polymerizing Enzymes of Calf Thymus Gland, IV. Inhibition of Terminal Deoxynucleotidyl Transferase by Metal Ligands*. *Proc. Natl. Acad. Sci. U. S. A.* **65**, 1041–1048 (1970).

449. Namura, S., Zhu, J., Fink, K., Endres, M., Srinivasan, A., Tomaselli, K. J., Yuan, J. & Moskowitz, M. A. Activation and Cleavage of Caspase-3 in Apoptosis Induced by Experimental Cerebral Ischemia. *J. Neurosci.* **18**, 3659–3668 (1998).

450. Davis, A. S., Richter, A., Becker, S., Moyer, J. E., Sandouk, A., Skinner, J. & Taubenberger, J. K. Characterizing and Diminishing Autofluorescence in Formalin-fixed Paraffin-embedded Human Respiratory Tissue. *J. Histochem. Cytochem.* **62**, 405–423 (2014).

451. Information (US), N. C. for B. *The p53 tumor suppressor protein*. *Genes and Disease [Internet]* (National Center for Biotechnology Information (US), 1998).

452. Mah, L.-J., El-Osta, A. & Karagiannis, T. C. γH2AX: a sensitive molecular marker of DNA damage and repair. *Leukemia* **24**, 679–686 (2010).

453. Saraste, A. Morphologic criteria and detection of apoptosis. *Herz* **24**, 189–195 (1999).

454. Ikenari, T., Kurata, H., Satoh, T., Hata, Y. & Mori, T. Evaluation of Fluoro-Jade C Staining: Specificity and Application to Damaged Immature Neuronal Cells in the Normal and Injured Mouse Brain. *Neuroscience* **425**, 146–156 (2020).

455. Schmued, L. C., Albertson, C. & Slikker, W. Fluoro-Jade: a novel fluorochrome for the sensitive and reliable histochemical localization of neuronal degeneration. *Brain Res.* **751**, 37–46 (1997).

456. Wang, X., Zhang, C., Szábo, G. & Sun, Q.-Q. Distribution of CaMKIIα expression in the brain in vivo, studied by CaMKIIα-GFP mice. *Brain Res.* **1518**, 9–25 (2013).

457. Silva, T. P., Bekman, E. P., Fernandes, T. G., Vaz, S. H., Rodrigues, C. A. V., Diogo, M. M., Cabral, J. M. S. & Carmo-Fonseca, M. Maturation of Human Pluripotent Stem Cell-Derived Cerebellar Neurons in the Absence of Co-culture. *Front. Bioeng. Biotechnol.* **8**, (2020).
458. Croft, C. L. & Noble, W. Preparation of organotypic brain slice cultures for the study of Alzheimer's disease. *F1000Research* **7**, 592 (2018).
459. Schwarz, N. *et al.* Long-term adult human brain slice cultures as a model system to study human CNS circuitry and disease. *eLife* **8**, e48417 (2019).
460. Zhang, F. *et al.* Multimodal fast optical interrogation of neural circuitry. *Nature* **446**, 633–639 (2007).